

Methane Oxidation on Platinum Catalysts Investigated by Spatially Resolved Methods

vorgelegt von
Diplom Chemiker
Oliver Korup
aus Perleberg

von der Fakultät II – Mathematik und Naturwissenschaften
der Technischen Universität Berlin
zur Erlangung des akademischen Grades
Doktor der Naturwissenschaften
- Dr. rer. nat. -

genehmigte Dissertation

Promotionsausschuss:

Vorsitzender: Prof. Dr. Thorsten Ressler
Berichter/Gutachter: Prof. Dr. Robert Schlögl
Berichter/Gutachter: Prof. Dr. Reinhard Schomäcker
Berichter/Gutachter: Prof. Dr. Thomas Risse

Tag der wissenschaftlichen Aussprache: 07.08.2012

Berlin 2012

D 83

Kurzfassung

Die katalytische Partialoxidation von Methan stellt eine reizvolle Reaktion zur Herstellung von Synthesegas, einer Vorstufe zur Synthese verschiedener Basischemikalien wie Methanol, Dimethylether oder Formaldehyd, dar. Die Reaktion ist mild exotherm und kann autotherm bei Temperaturen von etwa 1000 °C, sowie Raumgeschwindigkeiten bis zu 500000 h⁻¹ durchgeführt werden. Bei der Verwendung von Edelmetallkatalysatoren wie Rhodium- oder Platin-beschichteten Aluminiumoxid-Schaummonolithen können Gleichgewichtsausbeuten an Synthesegas in Kontaktzeiten in der Größenordnung von Millisekunden erzielt werden [1].

Betrachtet man den Reaktionsverlauf entlang des Katalysatorbettes beobachtet man zwei Reaktionszonen. Im vorderen Teil des Katalysators, in Anwesenheit von Sauerstoff in der Reaktionsmischung, wird eine Kombination aus direkter Methan-Partial- und Methan-Totaloxidation beobachtet. Nachdem der Sauerstoff vollständig umgesetzt wurde, wird die Bildung von Synthesegas fortgesetzt, jetzt jedoch durch Dampfreformierung des verbleibenden Methans und des in der ersten Reaktionszone gebildeten Wasserdampfes. Die beobachteten Reaktionsgeschwindigkeiten von Oxidation und Dampfreformierung über Platin-beschichteten Schaummonolithen sind deutlich niedriger als die über den äquivalenten Rhodiumkatalysatoren.

Für die Reaktion über Rhodiumkatalysatoren wurde eine Anzahl hochentwickelter mikrokinetischer Modelle entwickelt, welche die Eduktumsetzung und Produktbildung mit großer Genauigkeit vorhersagen können [2–4]. Mit Hilfe dieser Modelle konnte ein gutes Verständnis über den Reaktionsmechanismus und die Transportprozesse in Rhodium-beschichteten Schaummonolithen erlangt werden. Im zurückliegenden Jahrzehnt wurde es dann auch möglich die mikrokinetischen Modelle mit experimentellen Daten zu validieren. Ermöglicht wurde dies durch die Entwicklung von speziellen Reaktoren, welche die Gradienten von Spezieskonzentrationen und der Temperatur innerhalb eines arbeitenden Katalysators hoch auflösen konnten.

Die Pionierarbeiten von Horn et al. [2, 3, 5–10] mit Schwerpunkt auf Rhodiumkatalysatoren finden in der vorliegenden Arbeit ihre Fortführung, wobei Platinkatalysatoren untersucht werden. In einem weiterentwickelten Reaktorsystem wurde eine Serie von Reaktorprofilen gemessen und systematisch die Reaktanzzusammensetzung, die Kontaktzeit und der Reaktordruck variiert. Neben Schaummonolithen wurden Experimente mit Kugelbetten und katalytischen Wandreaktoren durchgeführt.

Mit mikrokinetischen Simulationen, welche ein pseudo-zweidimensional-heterogenes Reaktormodell mit der detaillierten Kinetik zweier unterschiedlicher State-of-the-Art-Reaktionsmechanismen verbinden, wurden die experimentell erhaltenen Reaktorprofile in Platin-beschichteten Schaummonolithen modelliert. Die Ergebnisse der Modellierung zeigen signifikante Abweichungen in den Speziesprofilen von Simulation und Experiment. Durch Charakterisierung der verwendeten Katalysatoren vor und nach der katalytischen Testung (geometrische Oberfläche, BET- und Platinoberfläche, Metalldispersion, Platinkristallitgröße, Raman-Spektroskopie, Elektronenmikroskopie, u.a.) konnte eine Umverteilung der Platinpartikel entlang des Katalysatorschaumes, sowie eine signifikante Verkokung der Katalysatoroberfläche als Ursache der Abweichungen zwischen Modellierung und Experiment nachgewiesen werden. Die führenden, aktuellen mikrokinetischen Modelle vernachlässigen bislang eine inhomogene Verteilung der aktiven Zentren, und Reaktionspfade zum Aufbau von langkettigen Kohlenwasserstoffen wurden bislang nicht berücksichtigt. Die beobachtete Verkokung der Platin-beschichteten Schaummonolithe wurde durch in-situ-Raman-spektroskopische Experimente an einer polykristallinen Platinfolie bestätigt. Es konnte die Bildung und Modifikation von kohleartigen Ablagerungen auf der Platinfolie mit wachsender Reaktionszeit und/oder steigender Reaktionstemperatur dokumentiert werden [11].

Die Ergebnisse dieser Arbeit geben neue Impulse für die Weiterentwicklung von bestehenden Reaktionsmechanismen für die katalytische Partialoxidation von Methan über Platin.

Abstract

Catalytic partial oxidation (CPO) of methane is an attractive technology for industrial production of synthesis gas, an important precursor for the production of diverse basic chemicals, e.g. methanol, dimethyl ether, and formaldehyde. The exothermic reaction operates autothermally at temperatures around 1000 °C and gas hourly space velocity (GHSV) values up to 500000 h⁻¹. On noble metal catalysts such as rhodium and platinum coated alumina foams, equilibrium synthesis gas yields are reached within millisecond contact time [1]. The CPO reaction proceeds in two steps along the catalyst bed. First a combination of direct methane partial oxidation coupled with methane deep oxidation is observed in the catalyst entrance section, where gas phase oxygen is present. After the oxygen is converted, product formation continues by a change in the reaction mechanism to steam reforming chemistry. Quantitative analysis reveals that the rates of oxidation and steam reforming are much lower on platinum than on rhodium coated foam catalysts.

For rhodium catalysts sophisticated microkinetic models are available in literature, which can predict the reactant conversion and product formation with high accuracy [2–4]. These models allow a good understanding of the reaction mechanism and transport properties in rhodium coated foam monoliths. Within the last decade it became possible to validate the microkinetic models, due to the development of high resolution spatial profile measurement techniques, that can measure species and temperature gradients inside the catalyst foams.

The pioneering work by Horn et al. [2,3,5–10], mainly focused on rhodium catalysts, is in this work extended to platinum catalysts. In a next generation reactor setup a set of reactor profiles was measured, systematically varying gas feed composition, contact time and reactor pressure. Besides foam monoliths, sphere beds and catalytic wall reactors have been tested.

Microkinetic simulations applying a pseudo-2D heterogeneous reactor model that couples heat and mass transport limitations with detailed chemical kinetics of two different state-of-the-art microkinetic models taken from the literature have been used to simulate the experimentally measured reactor profiles through platinum coated foam monoliths. The reaction mechanisms predict species profiles considerably different from the measured profiles. By pre- and post-catalytic characterization of the catalyst by means of geometric, BET and platinum surface area, as well as metal dispersion and platinum crystallite size in combination with spatially resolved Raman spectroscopy and electron microscopy it was possible to identify significant metal redistribution and carbon formation on the catalyst surface as missing reaction pathways in the existing state-of-the-art microkinetic models. These findings are supported by in-situ Raman experiments on a polycrystalline platinum foil that follow the transition of the carbonaceous deposits with time on stream and reaction temperature [11]. The results presented in this thesis give new impulses for ongoing mechanism development.

Contents

1	Introduction	11
1.1	Methane Conversion to Synthesis Gas	12
1.1.1	Methane Steam Reforming	12
1.1.2	Methane Dry Reforming	12
1.1.3	Methane Catalytic Partial Oxidation	13
1.2	Discussion on the Reaction Mechanism of Methane CPO	13
1.3	Steady State Kinetic Modeling for Reaction Mechanism Development	14
1.4	Steady State Spatial Reactor Profiles for Reaction Mechanism Validation	15
1.5	Thesis Aim	15
1.6	Outline of the Thesis	16
2	Summary of Results and Future Perspective	17
3	Methodology	21
3.1	Adsorption Methods	21
3.1.1	Specific Surface Area by Nitrogen Physisorption	21
3.1.2	Specific Surface Area by Krypton Physisorption	23
3.1.3	Chemisorption	23
3.1.4	Microcalorimetry	25
3.2	Catalytic Testing - Profile Measurements	25
3.3	Electron Microscopy	25
3.3.1	Scanning Electron Microscopy	25
3.3.2	Transmission Electron Microscopy	26
3.4	IR Thermography	27
3.5	Mass Spectrometry	28
3.5.1	Electron Ionization	28
3.5.2	Quadrupole Mass Filter	28
3.5.3	Secondary Electron Multiplier	29
3.6	Microkinetic Modeling	30
3.7	Raman Spectrometry	30
3.8	Thermogravimetry	31
3.9	Ultraviolet-Visible-Near Infrared Spectrometry	31
3.10	X-ray Diffraction	32
3.11	X-ray Microtomography	33
4	Microwave-Assisted Self-Propagating Combustion Synthesis for Uniform Deposition of Metal Nanoparticles on Ceramic Monoliths	37
4.1	Introduction	37
4.2	Experimental Methods	38
4.2.1	Materials	38
4.2.2	Deposition of Metal Nanoparticles on Ceramic Foams	38
4.2.3	Characterization	39
4.3	Results and Discussion	39
4.3.1	Ignition of Self-Propagating Combustion Synthesis by Microwave Irradiation	39
4.4	Synthesis Mechanism	41
4.4.1	Characterization of the Prepared Pt-Coated Foam Catalysts	44
4.5	Conclusion	49

5	Reactor for In-Situ Measurements of Spatially Resolved Kinetic Data in Heterogeneous Catalysis	51
5.1	Introduction	51
5.2	Reactor Design	52
5.2.1	Reactor Body	52
5.2.2	Gas Flow Control, Pressure Control, Heater and Safety	53
5.2.3	Measurement of Gas Species Profiles	53
5.2.4	Measurement of Gas and Surface Temperature Profiles	54
5.3	Application Examples	54
5.3.1	Methane Oxidation on Pt Coated α -Al ₂ O ₃ Foam Catalysts from 1.4 bar to 15 bar	54
5.3.2	Methane Oxidative Coupling on Li/MgO Coated α -Al ₂ O ₃ Foam Catalysts at Atmospheric Pressure	57
5.4	Summary and Conclusions	58
6	Catalytic Partial Oxidation of Methane on Autothermally Operated Pt Catalysts: Reaction Pathways, Zoning Effects, and Impact of Mass and Heat Transport	59
6.1	Introduction	59
6.2	Experimental	59
6.3	Results and Discussion	60
6.4	Conclusions	61
7	Measurement and Analysis of Spatial Reactor Profiles in High Temperature Catalysis Research	65
7.1	Introduction	65
7.2	Measurement of Species, Fluid and Solid Temperature Profiles, and the Principle of Spatially Resolved Fiber Spectroscopy	67
7.2.1	Species Profiles	67
7.2.2	High Pressure Measurements	69
7.2.3	Temperature Profiles	69
7.2.4	Spatially Resolved Spectroscopy	69
7.3	Application Examples	69
7.3.1	Catalytic Partial Oxidation (CPO) of Methane on Rh and Pt Foam Catalysts	69
7.3.2	Spatial Profiles on Rh and Mechanistic Discussion	70
7.3.3	Recent Work on Pt	70
7.3.4	Possible Origin of Reduced CPO Reactivity of Pt Compared to Rh	76
7.3.5	Gas Phase Methane Oxidative Coupling	76
7.3.6	Oxidative Dehydrogenation of Ethane to Ethylene on Molybdenumoxide Catalysts	79
7.4	Spatially Resolved Fiber Spectroscopy	81
7.5	Conclusions	84
8	Carbon formation in catalytic partial oxidation of methane on platinum: Model studies on a polycrystalline Pt foil	85
8.1	Introduction	85
8.2	Experimental	86
8.3	Results and Discussion	88
8.3.1	Raman Spectra of Defective Carbon	88
8.3.2	In-situ Raman Spectra During Temperature Programmed Reaction	90
8.4	In-situ Raman x,y-Mapping of Platinum Foil During Methane CPO	95
8.5	Conclusions	97
9	Catalytic Partial Oxidation of Methane on Platinum Investigated by Spatial Reactor Profiles, Spatially Resolved Spectroscopy, and Microkinetic Modeling	99
9.1	Introduction	99
9.2	Experimental	100
9.2.1	Catalyst Preparation	100
9.2.2	Catalytic Testing	101
9.2.3	Catalyst Characterization	101
9.3	Numerical Modeling	102
9.3.1	Model Equations	102
9.3.2	Microkinetic Models	105
9.4	Results and Discussion	106

9.4.1	Microkinetic Modeling Results Compared with Experimental Reactor Profiles	106
9.4.2	Spatially Resolved Raman spectroscopy	107
9.4.3	Spatially Resolved SEM	113
9.5	Conclusion	115
9.6	Acknowledgements	116
9.7	Appendix: Reaction Mechanisms	118
Appendix		122
A IR Thermography: Pyrometer Calibration		123
B Quantitative Mass Spectrometry: MS Calibration		127
C Spatially Resolved Reactor Profiles: Data Evaluation		131
D Raman Spectroscopy: Continuum Background Correction		143
D.1	Screening for Best Parameter Set	145
D.2	Removing Background Fraction from Raman Spectra	146
E Reactor Profile Library		149
E.1	Reactor Profiles Through Catalyst Foam #10253	150
E.1.1	$\dot{V}_{total} = 2000 \text{ mln min}^{-1}$ - C/O Variation	151
E.1.2	$\dot{V}_{total} = 4000 \text{ mln min}^{-1}$ - C/O Variation	155
E.2	Reactor Profiles Through Catalyst Foam #10255	159
E.2.1	$\dot{V}_{total} = 2000 \text{ mln min}^{-1}$ - C/O Variation	159
E.2.2	$\dot{V}_{total} = 4000 \text{ mln min}^{-1}$ - C/O Variation	163
E.2.3	$\dot{V}_{total} = 2000 \text{ mln min}^{-1}$ - Pressure Variation	167
E.3	Reactor Profiles Through Catalyst Foam #10256	169
E.3.1	$\dot{V}_{total} = 4000 \text{ mln min}^{-1}$ - Pressure Variation	170
E.4	Reactor Profiles Through Catalyst Foam #10774	172
E.4.1	$\dot{V}_{total} = 2000 \text{ mln min}^{-1}$ - C/O Variation	172
E.4.2	$\dot{V}_{total} = 4000 \text{ mln min}^{-1}$ - C/O Variation	176
E.4.3	$\dot{V}_{total} = 2000 \text{ mln min}^{-1}$ - Pressure Variation	180
E.4.4	$\dot{V}_{total} = 4000 \text{ mln min}^{-1}$ - Pressure Variation	182
E.5	Reactor Profiles Through Catalyst Foam #12036	184
E.5.1	$\dot{V}_{total} = 500 \text{ mln min}^{-1}$ - C/O Variation	184
E.5.2	$\dot{V}_{total} = 1000 \text{ mln min}^{-1}$ - C/O Variation	188
List of Abbreviations		193
List of Symbols		195
List of Figures		198
List of Tables		204
Bibliography		206
Acknowledgment		219
Curriculum Vitae		221
List of Publications		221
List of Conference Talks as Presenter or Co-Author		222
List of Posters as Presenter or Co-Author		224

Chapter 1

Introduction

Since the industrial revolution starting in the late 18th century, our society has become hungrier for energy and changed after extensive deforestation from the renewable energy carrier wood to fossil fuels as primary energy source. First coal, later petroleum and gas became main energy carriers for heating, electricity, transportation, and advanced materials production. A growing chemical industry developed pervading today's everyday life and depending on petroleum as chemical feedstock. It is common sense that most carbon containing chemicals start their synthesis in a refinery. Basic chemical building blocks like ethylene or propylene are produced from crude oil, for example by catalytic or steam cracking of naphtha [12]. Another important chemical building block is synthesis gas ($\text{CO} + \text{H}_2$) produced by hydrocarbon steam reforming. It is a precursor for the production of diverse basic chemicals, such as methanol, dimethyl ether, formaldehyd, etc. Despite continuous enhancement of the petroleum production from different oil wells and progress in the manufacturing process by the petroleum industry [13] a production plateau and shortfall can be foreseen soon [14] or is already present [15]. Due to an increasing demand worldwide the upward trend of the oil price in the last decades is just consistent. Additionally the oil price is fluctuating because of political instabilities in some oil-producing countries and the strong speculative interest on the stock markets [16]. With increasing tension from multiple political parties to reduce green house gas emission [17] natural gas attracts growing interest as alternative energy carrier and chemical feedstock.

Natural gas, a mixture of methane (80 – 90 %) and C_2 - C_4 alkanes (5 – 15 %), is available in similar amounts on earth as petroleum but remains less exploited [16]. Unfortunately most of the natural gas is found in remote areas, far away from consumer markets. As a gas its energy density is much smaller than that of crude oil (see Tab. 1.1) and for transportation expensive pipelines or liquefaction facilities have to be built, which is gainless for small gas fields. Furthermore a LNG carrier for transportation of liquid natural gas at temperatures lower than $-162\text{ }^\circ\text{C}$ is more expensive than an oil tanker and has to deal somehow with the methane boil-off problem until the consumer markets are reached. In lack of economic transportation natural gas is therefore often flared or pumped back into the oil fields when it is produced as byproduct of the crude oil production. A process right at the gas field to convert methane into transportable liquid chemicals could reduce these costs.

Methane is also a product from fermentation of organic material. The biogas production is one politically favored technology capable to contribute to a carbon-neutral society in the future. Still, up to now methane is mainly used as clean fuel for heat and electricity production.

Using methane as an alternative chemical feedstock is hindered by the fact that the functionalization of the smallest alkane methane is difficult because of its stability. The tetrahedron-shaped molecule has an almost spherical electron cloud and weak polarization in the C–H bonds. The dissociation energy of the first CH_3 -H bond is comparably high (439.3 kJ mol^{-1} [18]) and high reaction temperatures are required to activate the molecule. An example for direct conversion of methane to a higher value chemical at high reaction temperatures is oxidative coupling of methane (OCM) to ethane and even more interesting to ethylene. The OCM reaction is typically done in a temperature range between 700 to 800 $^\circ\text{C}$ on various catalytic materials [19]. Unfortunately, the reaction suffers from low C_2 yields even at low methane conversion [19] and at high methane conversion the selectivity to the desired products is insufficient. A recent review of hundreds of different catalyst materials for OCM [20] allowed to confine the active materials but so far no high performance material with economic relevance is available. If homogeneous reactions become relevant the situation becomes even more complex, because the desired products are more rapidly consumed at these reaction conditions than methane itself, because of thermodynamics.

In principle the activation and partial oxidation of methane can be done under mild conditions, too. However the adaption of the biocatalytic pathway using oxygenases, as done in nature, is still in an initial stage [21,22] and homogeneous catalytic strategies like the mercury catalyzed oxidation of methane to methanol in concentrated sulfuric acid as described by Periana et al. [23] or a heterogeneous catalytic route by bromination

Table 1.1: Energy density of some important fuels taken from [35, 36].

diesel	33600 kJ l ⁻¹
gasoline	30240 kJ l ⁻¹
LPG	25200 kJ l ⁻¹
ethanol	21924 kJ l ⁻¹
methanol	15834 kJ l ⁻¹
natural gas (50 bar)	1344 kJ l ⁻¹

of methane followed by metathesis to methanol based on Lorkovic et al. [24] suffer from a complicated feasibility and the application of toxic or corrosive reactants. In industrial scale the handling of hundreds of tons of mercury or bromine could cause hazardous environmental risks and costly safety precautions.

It could be more promising to choose a synthesis route from methane to synthetic petroleum via synthesis gas, with the synthetic petroleum fitting in the existing customer infrastructure. The strategy is technically well-feasible by Fischer-Tropsch synthesis [25–28] or the Mobil process [29–31]. Its economic success depends on the availability of cheap natural gas and high performance synthesis gas production as demonstrated by the Shell Pearl GTL plant in Qatar offering a daily production of 140 kBOE¹ of gas-to-liquids products [34].

1.1 Methane Conversion to Synthesis Gas

About 60 to 70 % of the overall cost of a methanol, Fisher-Tropsch or ammonia production plant is associated with the synthesis gas production [37, 38]. At the same time the capital cost of a fuel oil based ammonia plant is approximately 50 % higher, a coal based plant even twice as high, as an ammonia plant using steam reforming of natural gas [39]. Synthesis gas generation using natural gas as feedstock is therefore of eminent industrial and scientific interest aiming both for cost reduction and process improvement.

1.1.1 Methane Steam Reforming

The state-of-the-art technology to convert methane in synthesis gas and for hydrogen production is since decades methane steam reforming [36, 39–43].



The first detailed study describing the reaction of methane with steam was published by Neumann and Jacob [44] in 1924. Shortly after that, numerous patents appeared utilizing different catalysts consisting of iron, nickel, and cobalt as metal compound [39]. The first commercial steam reformer was used for hydrogen production² by Standard Oil of New Jersey in their refinery in Baton Rouge, LA in 1930 [45, 46]. And ever since methane steam reforming dominates the market for hydrogen generation for ammonia synthesis [39]. Current industrial catalysts are usually nickel based.

The strongly endothermic reaction is operated in large and cost intensive tube reactors which are heated by fired furnaces surrounding the reactor tubes. The large reactor dimensions, i.e. several meters in length, result from the necessity to transfer large amounts of heat into the reactant feed. The operation temperature usually exceeds 900 °C. The energy demand is additionally increased because of the need of excess amounts of superheated steam to prevent coke formation on the utilized nickel catalyst [39]. Further drawbacks are the parallel formation of significant amounts of carbon dioxide in the product gas stream generated by water gas shift



and the too high H₂/CO ratio of three. For downstream synthesis gas conversion to methanol, acetic acid, or hydrocarbons low H₂/CO ratios of about two are desired. The carbon chain growth in Fischer-Tropsch synthesis for example is limited at high H₂/CO ratios.

1.1.2 Methane Dry Reforming

Methane dry reforming is another highly endothermic reaction for methane conversion to synthesis gas.



¹1 BOE = 5.8 × 10⁶ BTU = 6.1 GJ = 1.7 MWh [32, 33]

²Daily production capacity of 155746 m³ clean hydrogen (T = 16 °C, p = 1 atm, 97 % purity) per day. [45]

Though the reaction is of large ecological interest, because it consumes two greenhouse gases and it yields an interestingly low H₂/CO ratio of one, the application is hindered by catalyst deactivation problems. Origin of the deactivation is either methane decomposition



and/or carbon monoxide disproportionation (Boudouard reaction)



To address the coke formation problem main attempts are focused on catalyst development [38]. Noble metals and nickel were identified as highly active catalysts. On nickel it was found that the carbon formation is structure sensitive for Reaction 1.4 with preferential decomposition activity on Ni(100) and Ni(110) [47]. On noble metals it was found that the carbon deposition decreases in the order of Ni > Pd = Rh > Ir > Pt ≫ Ru [38, 48] at a reaction temperature of 650 °C. The noble metal catalysts exhibit lower coking tendency but carbon deposition also occurs on these metals.

From a thermodynamic point of view Reaction 1.5 is unfavored at high reaction temperatures, i.e. in excess of 700 °C [38]. Operation at CO₂/CH₄ ratios larger than one could further minimize carbon deposition, but from an industrial point of view lower reaction temperatures and a reactant ratio close to unity are desired [38].

1.1.3 Methane Catalytic Partial Oxidation

An elegant alternative reaction to methane reforming would be catalytic partial oxidation (CPO) of methane.



The methane partial oxidation reaction is mildly exothermic and could be run more energy efficiently compared to methane steam reforming or methane dry reforming. Non-catalytic autothermal partial oxidation has been successfully operated since the 1950s. The Shell Gasification Process (SGP) with typical reaction temperatures in the range of 1300 to 1500 °C and pressures up to 70 bar [49] gives high synthesis gas yields close to equilibrium. Application of a suitable catalyst would reduce the required reaction temperature significantly to make methane partial oxidation even more economical avoiding formation of soot or unwanted by-products. Another advantage of methane partial oxidation over methane steam reforming is the product H₂/CO ratio of two, which is optimal for methanol or Fischer-Tropsch downstream process integration.

Reviewing the literature [36, 43, 50–52] shows that methane CPO to synthesis gas has been intensively investigated on supported nickel and noble metals such as platinum, rhodium, and others. Both catalyst types have been shown to be highly active, and H₂ and CO yields close to thermodynamic equilibrium could be achieved.

1.2 Discussion on the Reaction Mechanism of Methane CPO

Regarding the reaction mechanism of methane conversion with oxygen to synthesis gas a debate developed in the literature (Fig. 1.1). There are arguments suggesting a combustion and reforming reactions (CRR) mechanism that proceeds in two steps via primary total oxidation of methane



followed by a consecutive step of steam (Reaction 1.1) and dry reforming (Reaction 1.3) [36, 52]. The other suggested reaction mechanism proceeds in one step directly from methane to synthesis gas (Reaction 1.6), i.e. direct partial oxidation (DPO) mechanism [36, 51].

There are strong indications that on nickel a two step mechanism is present. Prettre et al. [53] first proposed the CRR mechanism concluding it from temperature measurements along a nickel based catalyst bed showing strong temperature gradients between the catalyst entrance and exit section. While the catalyst front showed a higher temperature than the reactor furnace resulting from exothermic chemistry, the catalyst temperature dropped towards the end reflecting endothermic reforming reactions. Further evidence is given by several groups investigating the product selectivities under different reaction conditions. It could be shown that the CO₂ and H₂O selectivity can be increased with simultaneous synthesis gas loss by either increasing the space velocity or increase in the O₂/CH₄ ratio [36, 54, 55]. The situation on the noble metal catalysts is controversial. The direct formation of CO and H₂ was proposed by several groups [1, 37, 56–62] for platinum and rhodium at short contact times. For rhodium coated monoliths higher selectivities to synthesis gas have been observed than for platinum coated monoliths [58]. With the observation of lower catalyst bed

temperature in case of the rhodium catalyst compared to platinum it was suggested that rhodium is the better partial oxidation catalyst. Hickman and Schmidt [56,59] and later Heitnes Hofstad et al. [62,63] investigated methane CPO on Pt and Pt/10 % Rh gauzes in comparable reactor setups with millisecond contact time. Both groups found similarly low synthesis gas selectivities on the Pt gauzes, whereas the Pt/10 % Rh showed high H₂ and CO selectivities. Increasing synthesis gas selectivity with decreasing contact time was observed, which cannot be explained by the two step mechanism observed on nickel. On the other hand transient studies from Baerns et al. [64–66] performed in the Knudsen-diffusion regime, with negligible influence of consecutive gas-phase reaction, did not indicate a direct reaction pathway over γ -Al₂O₃-supported rhodium or MgO-supported platinum.

Qin et al. [61] do not sharply differentiate between both reaction mechanisms and argument that both reaction mechanisms proceed in parallel, strongly influenced by the concentration of reactants and the kinetics of oxygen adsorption on different metal surfaces. They conclude that “it is unlikely that the preferred reaction mechanism is via the two-step mechanism, at least on the active catalysts Rh/MgO or Ru/MgO. Pd/MgO or Pt/MgO, [...] may have a higher rate for the two-step mechanism”.

1.3 Steady State Kinetic Modeling for Reaction Mechanism Development

To address the mechanistic controversy several reaction mechanisms have been developed to simulate the different experimental data. The macrokinetic ansatz, as followed by Wolf et al. [67,68], applies a limited amount of a few kinetically relevant reaction steps fitting data from kinetic experiments, i.e. gas composition, temperature, and pressure. The models are based on power law or empirical Hougen-Watson kinetic expressions. Although the macrokinetic approach is very flexible and widely used in fitting kinetic data, it is virtually useless for deduction of mechanistic information [69], because the models do not describe elementary reaction steps at the microscopic level, which is crucial for a mechanistic understanding of the complex reaction networks in heterogeneous catalysis. An approach based on elementary step reactions is the microkinetic ansatz, such as the reaction mechanism of Deutschmann et al. [70,71] originating of the work of Hickman and Schmidt [57] or the work of Vlachos et al. [72,73]. Their approach applies a complex reaction network including surface reactions with adsorption and desorption steps, that allow for combination with homogeneous gas phase reaction mechanisms, which become relevant for reaction conditions at elevated pressure. Gas phase models like the comprehensive GRI mechanism for gas phase oxidation of methane [74] include even more reaction steps and reached a sophisticated level. The resulting reaction network of surface and gas phase reactions is coupled in a non-linear way by heat transport, mass transport and exchange of reactive intermediates.

During investigations of reactions under high conversion and steady state conditions the reactor itself is treated as a black box without information about the reaction pathway in conventional reactor setups. Whether parallel or consecutive reaction channels exist remains hidden, as well as possible reaction intermediates and the catalyst state adapting to the changing chemical potential along the catalyst bed. Except some rare reactor designs with a few fluid sampling ports [75] which allowed for species characterization at a given amount of discrete sampling positions or the application of multiple or movable thermo elements, which allowed for analysis of temperature gradients along the catalyst bed, the simulated species and temperature profiles by above mentioned mechanisms lack solid experimental validation. Most microkinetic models are

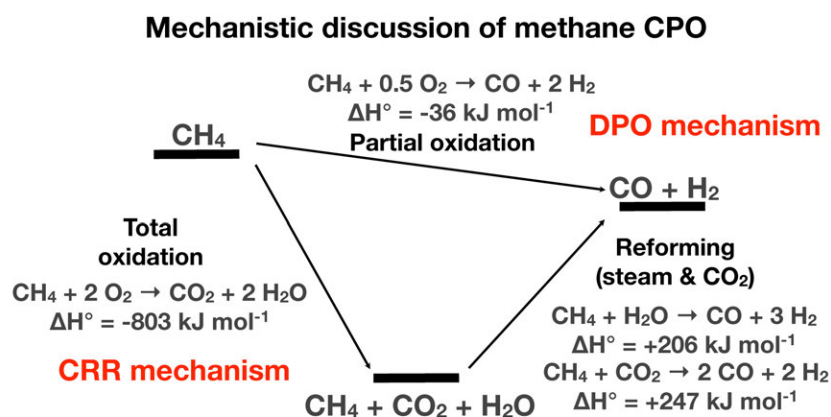


Figure 1.1: Suggested reaction pathways in methane CPO. Figure adapted from [52].

solely validated against integral catalytic data, i.e. the overall conversion and selectivity at the reactor exit. It turned out that this way of validation is not satisfactory, because even an incorrect microkinetic model can fit the integral reactor data well [76].

1.4 Steady State Spatial Reactor Profiles for Reaction Mechanism Validation

The situation changed with the pioneering parallel development of high resolution spatial reactor profiling techniques. Partridge et al. [77–79] at the Oak Ridge National Lab, Bosco and Vogel [80] at the Paul Scherrer Institute, and Horn et al. [5] at the University of Minnesota developed independently capillary sampling techniques allowing species reactor profile measurements with so far unreached resolution. The SpaciMS of Partridge et al. [77–79] applies a mass spectrometer for gas analytics connected with an array of open ended quartz capillaries to the reactor. The capillaries are placed in a channel monolith and it was demonstrated by CFD calculations that minimal fluid flow perturbations occur. By capillaries of different lengths, later by sliding the capillaries through the monolith block profiles along the channel monolith could be measured. By placing thermocouples in neighboring channels the monolith temperature can be measured. The Reactor of Bosco and Vogel [80] is a flat bed reactor with a catalyst coated metal plate and a flat quartz window on top. The cavity between catalyst plate and quartz window is a narrow slit with a flow field similar to that of a channel monolith. Through the window temperature measurements without perturbation of the fluid flow are possible by IR pyrometry. A thin stainless steel capillary can be slid through the cavity allowing for spatially resolved gas analytics by mass spectrometry. The reactor design by Horn et al. [5] is more flexible in terms of the investigated catalyst material. Experiments in foam monoliths, channel monoliths, packed sphere or granule beds, and catalytic wall reactors are possible. The reactor uses a quartz capillary with side sampling orifice, which slides through the centerline of the catalyst bed, mounted in a classical tubular reactor geometry. The sampling capillary accommodates a thermocouple or pyrometer fiber allowing for either gas phase or surface temperature measurement. A main advantage of the Horn design is the possibility to conduct profile measurements at elevated pressure. In the current reactor generation pressures up to 45 bar at reaction temperatures up to 1300 °C are possible. This reactor was also used in the present work and is described in detail in Chapter 5.

The work of Horn et al. [2, 3, 5–10] is continued in this thesis. In his previous work on methane CPO on rhodium and platinum supported on ceramic foam monoliths the novel reactor concept was developed, which gave high resolution spatial reactor profiles [5]. After first atmospheric pressure experiments the setup was improved to allow profile measurements at up to 11 bar reactor pressure [10]. The apparent reaction mechanism on both catalysts was found to be of CRR-like nature, with DPO participation in case of high reaction temperatures. Generally a zoning in two reaction sections was found. First a narrow zone of fast methane oxidation with high yields in carbon monoxide, hydrogen and water. Carbon dioxide is formed in less amounts. This narrow oxidation zone of a few millimeter length was followed by a reforming zone over the rest length of the catalyst bed, which showed steam reforming and water gas shift in the absence of CO₂ reforming. Over the investigated reaction time no catalyst deactivation was observed. Most of the previous work concentrates on rhodium catalysts. The studies found rhodium superior in synthesis gas selectivity over platinum [7, 10]. The high synthesis gas selectivity on the rhodium catalyst was investigated by microkinetic modeling with consideration of transport phenomena [2, 3]. A strong transport limitation within the oxidation zone was found. It was concluded that the coexistence of hydrogen and carbon monoxide in the oxidation zone in the presence of oxygen and at the high local temperatures is due to a strong oxygen deficit at the rhodium surface.

1.5 Thesis Aim

The work presented in this thesis is focused on platinum as a methane CPO catalyst. By application of the spatial profile measurement technique, different platinum based catalyst systems were investigated. The application range of the reactor profile technique should be extended from foam monoliths to packed beds and catalytic wall reactors. With a less active catalyst material the previously described zoning effect should be expanded, if possible allowing higher resolution in the narrow reaction zone in presence of oxygen. By microkinetic modeling and spatially resolved spectroscopic data the mechanistic insight in methane CPO on platinum should be improved by comparison to the reactor profile data and simulation.

1.6 Outline of the Thesis

After this short introduction, the major findings of the present work are summarized and discussed in context to the literature. Then a brief description of the applied characterization methods is given. Subsequently the cumulative part of this work is presented. The results of this work are presented in the chapter structure as follows:

Chapter 2 summarizes the work presented in this thesis and aims to link the different aspects of the papers in chapters 4 to 9. The chapter closes with a outlook for ongoing research in the field.

Chapter 3 summarizes briefly the methods applied in this work to characterize the catalyst material.

Chapter 4 adapts a paper describing a simple and energy-efficient synthesis technique for coating of ceramic foam monoliths with homogeneously distributed, thermally stable, and strongly adherent nanocrystalline Pt particles. The preparative work was developed by Ulyana Zavyalova and the method was later adapted by myself. In Chapter 6 results are presented that show profiles through a sphere bed prepared by the microwave assisted combustion synthesis method for coating of γ -alumina spheres. XRD data presented in this chapter are contributed by Frank Girgsdies.

Chapter 5 adapts a paper describing the reactor setup used in this thesis. The system components and operation parameters are presented. The described reactor is the third generation of the reactor design from [5]. The construction design was developed by Raimund Horn and the assembly was done by Michael Geske and myself. The initial reactor characterization, the development of operation procedures, as well as the development of evaluation routines for instantaneous raw data processing are done by myself. The paper concludes with examples of use to demonstrate the reactor capabilities.

Chapter 6 adapts a paper published as preprint to a presentation given at the 240th ACS National Meeting in Fall 2010 in Boston MA, USA [81]. It displays the various catalyst systems investigated by the reactor profile technique in this thesis. Reactor profiles through a platinum coated foam monolith are presented and the flexibility of the reactor setup to accommodate other heterogeneous catalysts is demonstrated on a platinum coated sphere bed and a platinum tube catalytic wall reactor. Reaction pathways and zoning effects are discussed comparing the three catalyst systems.

Chapter 7 adapts a paper discussing the application of the profile measurement technique. It is demonstrated how information about film transport limitation and reaction pathways can be extracted from reactor profiles. In a proof-of-principle experiment the possibility of spatially resolved Raman spectroscopy conducted inside the profile reactor is introduced. The paper contains preliminary results about significant carbon deposition on a platinum foil, which is worked out in more detail in Chapter 8. The paper contains additional reactor profiles measured through a molybdenum oxide coated sphere bed used for oxidative dehydrogenation of ethane. These results are from the work of Michael Geske. An other reactor profile measured through an empty reactor tube investigating the oxidative coupling of methane in homogeneous gas phase reaction was contributed from the work of Sardor Mavlyankariev.

Chapter 8 adapts a paper presenting a systematic characterization of carbon deposition during catalytic partial oxidation of methane on a polycrystalline platinum foil investigated by in-situ Raman spectroscopy. A structure-sensitive carbon deposition was observed.

Chapter 9 presents a paper in preparation comparing state-of-the-art microkinetic models for methane conversion with oxygen on platinum with high resolution spatial reactor profiles through platinum coated corundum foam monoliths. The microkinetic modeling is contributed by Claude Franklin Goldsmith. For the simulation part of the paper a precise foam solid body and void gas volume characterization is needed. Therefore X-ray micro-tomography was applied, which is contributed by Timur Kandemir. In an experiment with a catalyst stack consisting of two half monolith, carbon deposition and platinum transport along the catalyst bed is documented and correlated with deviations between the measured and simulated reactor profiles. The SEM pictures presented here are contributed by Gisela Weinberg.

Appendices Supporting material is presented to provide information of more practical and experimental relevance with respect to the thesis. These chapters are not necessary to understand the results of this thesis but are added to document important aspects of the data evaluation, including a list of the available reactor profile data, which would overstress the length of a peer reviewed paper.

Chapter 2

Summary of Results and Future Perspective

This thesis is concerned with methane catalytic partial oxidation to synthesis gas on platinum catalysts. The immediate objective was to contribute to the mechanistic understanding of this high temperature catalytic reaction by comparison of high-resolution spatial reactor profiles of species and temperature against state-of-the-art microkinetic models.

To approach the thesis aim, the capillary profile measurement technique developed by Horn et al. [5] was applied. A new reactor setup [82] improving the operation range of the original reactor setup [5] was built, which is described in detail in Chapter 5, e.g. [82]. The reactor allows simultaneous measurement of spatially resolved species and temperature profiles in heterogeneous catalytic reactions under industrially relevant reaction conditions, i.e. reactor pressures up to 45 bar and reaction temperatures up to 1300°C. In comparison to the original reactor setup sampling capillaries with laser drilled sampling orifice (50 – 100 μm inner diameter) have been used allowing increased spatial resolution in the sub-millimeter range.

The temperature sensor used in this work was a conical shaped fused silica fiber collecting the infra-red radiation emitted from the catalyst surface, which was analyzed by two-color ratio pyrometry. The pyrometer was calibrated against a K type thermocouple (cf. Appendix A). The accuracy of the temperature measurements was generally high ($\Delta T \leq 5$ K) but in reaction tests conducted at elevated pressure a measurement artifact was observed. The surface temperature profiles measured in autothermal methane CPO on platinum at reactor pressures higher than 10 bar showed temperature maxima prior the reaction zone in absence of any chemistry. This behavior was reproducibly observed. A potential explanation is that methane, which has a strong absorption band at 6096.4 cm^{-1} , absorbs selectively NIR radiation detected by the two color pyrometer at the longer pyrometer measurement wavelength, $\lambda_2 = 1.64 \mu\text{m}$ or $\tilde{\nu}_2 = 6097.6 \text{ cm}^{-1}$, but not at the shorter measurement wavelength, $\lambda_1 = 1.52 \mu\text{m}$ or $\tilde{\nu}_1 = 6578.9 \text{ cm}^{-1}$. As the temperature value is calculated from the intensity ratio $I(\lambda_1)/I(\lambda_2)$ erroneously high temperatures are measured if NIR absorption by methane becomes pronounced. This explanation needs experimental verification by future experiments and might allow for quantitative correction for such adsorption interference, because the gas phase composition at any axial position is known.

An optical fiber sensor similar to the pyrometer fiber probe used for temperature measurements was used to establish the possibility of spatially resolved spectroscopy in the profile reactor setup. By coupling a Raman spectrometer to the profile reactor setup it could be shown in an ex-situ demonstration experiment (cf. Section 7.4 in Chapter 7, e.g. [83]), that optical spectroscopy is principally feasible with the spatial profile reactor setup used in this work. First spatially resolved in-situ Raman studies in oxidative dehydrogenation of ethane to ethylene on molybdenum oxide model catalysts were successful [84, 85]¹ and extension to laser induced fluorescence is under development.

The investigated catalysts in this thesis are mainly platinum coated foam monoliths, which have been loaded with nominally 1 wt% platinum. The catalyst preparation has been done by two different methods. In addition to the classical incipient wetness method with an aqueous H_2PtCl_6 precursor solution, a new synthesis

¹This study is not subject of my work. A paper entitled "Resolving Kinetics and Dynamics of a Catalytic Reaction Inside a Packed Bed Reactor by Combining Kinetic and Spectroscopic Profiles" is currently in preparation by M. Geske, O. Korup, and R. Horn. Addendum (2012-08-16): The final manuscript entitled "Resolving Kinetics and Dynamics of a Catalytic Reaction Inside a Fixed Bed Reactor by Combined Kinetic and Spectroscopic Profiling" has been accepted by Catalysis Science & Technology for publication and is available online [86].

method has been applied (cf. Chapter 4, e.g. [87]). The new synthesis route proceeds via microwave-assisted self-propagating combustion of glycerol chelated metal precursors, such as the here utilized $(\text{NH}_3)_4\text{Pt}(\text{NO}_3)_2$. The synthesis method was applied to α -alumina foam monoliths and α - or γ -alumina spheres. By electron microscopy and powder X-ray diffraction it could be shown that the microwave synthesis is superior to the incipient wetness method by means of particle size and uniformity of particle distribution (cf. Chapter 4, e.g. [87], and Chapter 9, e.g. [83]). The microwave synthesis allows for homogeneous and strongly adherent deposition of nanocrystalline platinum on aluminas in a simple and energy-efficient way without the necessity of subsequent calcination and reduction treatment. Additionally catalytic wall reactors, i.e. pultruded platinum tubes of 4.4 mm inner diameter, and a polycrystalline platinum foil have been investigated.

A general observation in all measured foam profiles is a two-zone structure (cf. Appendix E). Analogous to profiles measured in rhodium coated foam monoliths [2,3,5–8,10] a catalyst section with fast and exothermic oxygen and methane conversion is followed by a section with more or less pronounced endothermic steam reforming chemistry, i.e. depending on the C/O ratio and linear velocity of the feed gas. The intersection between both zones is characterized by an abrupt change in reaction rates although the oxygen is still not fully converted. The intersection typically forms a kink in the species profiles of reactants and products. Prior the kink, in the oxidation zone, hydrogen and carbon monoxide are formed simultaneously, as well as water and small amounts carbon dioxide. In many profiles (cf. Appendix E) the oxidation zone shows linear shaped reactant profiles, i.e. constant reaction rates (cf. Chapter 5, e.g. [82], and Chapter 6, e.g. [88]). It was first speculated that this apparent zeroth-order reaction kinetics could be explained by a very low density of active sites (cf. Chapter 6, e.g. [88]) possibly due to blockage of the platinum sites by carbonaceous deposits. The existence and impact of carbonaceous deposits will be summarized later. After the kink the reaction rates are considerably slower. The carbon monoxide profiles now level off. In case of foam catalysts with a pore density of 45 ppi the hydrogen profiles follow this behavior. In case of foam catalysts with 80 ppi pore density two cases can be differentiated. If the gas feed C/O ratio is larger than 1.4 the same behavior is observed, but at C/O ratios smaller than 1.4 the hydrogen formation continues with lower formation rate under consumption of water and methane accompanied by carbon dioxide formation. This indicates that water gas shift and steam reforming are coupled in a way that carbon monoxide forms a plateau, whereas hydrogen and carbon dioxide are formed.

Compared to rhodium catalysts, the synthesis gas selectivities on platinum catalysts are lower. Both, in the oxidation zone as well as in the subsequent reforming zone lower synthesis gas yields are obtained. The superiority of rhodium over platinum is explained in literature by differences in the activation energy for the OH(s) formation from O(s) and H(s) (20 kcal mol⁻¹ for Rh vs 2.5 kcal mol⁻¹ for Pt) [57]. With respect to the high reaction temperatures around 1000°C this argumentation is not convincing. Furthermore it is claimed that strong film transport limitation in case of the rhodium catalyst explains the high synthesis gas selectivities in the oxidation zone of the catalyst [2,3]. By microkinetic simulations it could be shown, that the oxygen partial pressure at the rhodium surface is low. Hydrogen and carbon monoxide can be formed with high selectivity and are not oxidized, although oxygen is present in the bulk gas phase and the catalyst temperatures are high. The simulated transport control of the methane CPO on rhodium is additionally consistent with reactor profiles measured at different reactor pressures showing an invariance of the reactant conversion rates from reactor pressure, as would be expected in a transport controlled reaction regime [7,10]. In fact the results of this work suggest that a more important difference between both catalyst materials is related to transport phenomena.

On platinum as is carried out in Chapter 7, e.g. [83], the reaction is largely dominated by kinetic control, which implies that the concentration of oxygen at the platinum surface is not much lower than in the bulk gas phase [7,10,83]. Indeed, a comparison of the hydrogen selectivities measured on rhodium and on platinum at the same reactant stoichiometry C/O = 1.0 shows clearly that the pronounced film transport limitation as present on rhodium has a strong positive effect. But it also makes clear that even in full kinetic control, as on platinum, hydrogen can be formed in significant selectivities. Therefore, attributing the co-existence of hydrogen and oxygen in the oxidation zone solely to film transport limitations is not correct. Repeating the pressure variation experiments on rhodium with platinum showed an interesting and new result, in particular with respect to an industrial CPO process. Synthesis gas formation at elevated reactor pressures is not negatively influenced by pressure, at least under the investigated reaction conditions (C/O = 2.0). The increase in synthesis gas selectivity with increasing pressure is most likely due to the longer residence times at the higher reactor pressures. It would be very interesting to study methane CPO under pressure also at more favorable C/O ratios if a proper reactor design would prevent explosions.

Microkinetic simulations applying a pseudo-2D heterogeneous reactor model that couples heat and mass transport limitations with detailed chemical kinetics of two different state-of-the-art microkinetic models

taken from the literature have been used to simulate the experimentally measured reactor profiles of this work (cf. Chapter 9). The reaction mechanisms developed by Deutschmann et al. [70, 71, 89]) and Vlachos et al. [72, 73]) respectively are qualitatively correct with respect to the oxygen profiles, but the methane and product profiles however differ considerably. The linear reactant conversion in the oxidation zone and the abrupt change in reaction rates forming the kink are not reproduced by both reaction models. The same is true for the final product gas composition. Although both models predict a high concentration of vacant sites in the initial oxidation zone, the two models differ significantly in their prediction of the surface coverages. One mechanism predicts that CO(s) is the next most abundant surface species, whereas the other predicts high coverages of CH(s) and, to a lesser extent, C(s). Neither of the mechanism includes a submechanism for carbon growth, but post catalytic characterization of the catalyst by Raman spectroscopy and electron microscopy revealed that the kink position can be correlated with the formation of carbonaceous deposits. The morphology of the carbon material changes along the catalyst foam from filament-like at the kink and in the center of the foam to a mixture of thickened filaments and large roundish agglomerates towards the catalyst end. The platinum particles in the reforming zone are embedded in the carbon material. Carbon formation can be understood by taking into account that platinum is an excellent hydrogenation/dehydrogenation catalyst, which at high temperatures obviously leads to formation of surface carbon. The most likely explanation of the reduced platinum reactivity in the reforming zone is poisoning of the platinum particles by coke. In the oxidation zone no carbonaceous deposits could be detected. But it was found that the platinum distribution changed from islands of platinum particle agglomerates after preparation to re-dispersed much smaller particles in the oxidation zone after several hours time on stream. In the reforming zone of the catalyst foam, after the kink position and in an oxygen-lean/free environment the surface is enriched by larger spherical platinum particles covered with carbon deposits. It must be concluded that Pt is transported during operation from the hot catalyst front to the catalyst back.

In a model study on a polycrystalline platinum foil the carbon formation was investigated in-situ by Raman spectroscopy (cf. Chapter 8, e.g. [11]). A substantial surface carbon formation was found in methane CPO. Spectral analysis of the Raman spectra by curve fitting with five first-order Raman bands (G, D1, D2, D3, D4) according to Sadezky et al. [90] showed that after reaction light-off highly defective and inhomogeneous carbonaceous deposits are formed. This material transforms within several ten minutes up to approximately one hour to ordered oxidation resistant, graphite-like species. Surprisingly the carbon distribution at the platinum surface was found to be inhomogeneous and somehow related to the nature of the micro-crystals making up the polycrystalline platinum foil. The origin of this interesting phenomenon cannot be explained so far and needs further investigation. However the fact that some foil domains coke more strongly than others suggests that the reaction is structure-sensitive. It is well known from surface science literature that the activity for breaking H-H, C-H, and C-C bonds is controlled by surface irregularities, steps, and kinks. Their abundance and accessibility direct the selectivity and activity in hydrocarbon conversion. Dehydrogenation reactions on platinum are controlled by the step density of a platinum single crystal surface [91]. The step density is determined by the angle and orientation of the crystal phase. For this reason the observed inhomogeneous carbon distribution could reflect domains with higher and lower step density respectively. Furthermore surface additives are influencing the working catalyst. These additives are deposited reversibly or irreversibly by the catalyst pretreatment, by the reaction mixture under the conditions of reaction, by addition of a promotor, or by migration of bulk impurities to the surface. A contamination from the reactor cell itself can cause surface additives, too. These add species may also cause structural reconstruction or subsurface chemistry.

The linear shape of the oxidation zone still cannot be explained. A blockage by carbonaceous deposits was not observed. Possibly the linear zone is a consequence of the low platinum content in the oxidation zone due to platinum loss with time on stream, which needs to be quantified in future experiments.

The results presented in this work suggest that the lower synthesis gas selectivity of platinum compared to rhodium in methane CPO might originate from a loss in platinum active surface area in the oxidation zone and a blockage of almost all active platinum sites in the reforming zone. The accessible active platinum surface seems to be low in both reaction zones. Microkinetic models need to be revised to account for both observations. The non-uniform metal distribution needs to be considered. The reaction mechanism needs to be extended by a set of reactions, which account for the observed carbon species formation on the platinum surface. Without these important changes yielding in an advanced description of the catalyst deactivation, which was so far neglected, the models will fail to predict the species developments in the foam catalyst correctly.

Chapter 3

Methodology

3.1 Adsorption Methods

Knowledge of the surface area and pore structure of a solid catalyst is of crucial importance in heterogeneous catalysis. Factors like pore size, pore geometry, pore distribution, etc. are essential parameters controlling transport processes from and to the catalyst surface. In supported catalyst systems the surface area of the active component compared to the overall catalyst surface area has to be known. Using adsorption methods and adsorbates, which interact with different strength and selectivity allows to access above-named catalyst properties. Generally, sorption behavior is discriminated in physisorption and chemisorption [92]. Although frequently done, a classification in one of the sorption classes by bond strength only is not appropriate. In fact the limiting cases are as follows: In physisorption the forces between the sorptive and adsorbent are weak and of intermolecular nature, i.e. van der Waals forces or coulombic forces. The sorption process is reversible and species in the fluid and on the surface are chemically identical. The chemisorption process on the other hand is characterized by formation of strong bonds that change the electronic state of adsorbent and adsorbate. It is chemically specific, i.e. usually certain adsorption sites are occupied and only a monolayer of chemisorbed molecules is formed. The adsorption process may include surface dissociation and therefore can be irreversible. A sharp discrimination between both processes can be difficult, for example when strong hydrogen bonds are involved. The standard methods used in this work to determine specific surface areas are briefly described in the following section.

3.1.1 Specific Surface Area by Nitrogen Physisorption

The standard method to determine the specific surface area of a solid is nitrogen adsorption at its boiling point of 77 K, i.e. $-196\text{ }^\circ\text{C}$ [93–96]. The specific surface area is determined applying the Brunauer-Emmett-Teller (BET) method [97]. The sorption behavior and therefore the shape of the adsorption isotherm depend strongly on the pore structure of the probed solid. In literature six general types of physical adsorption isotherms are classified [98], of which five were originally proposed by Brunauer, Deming, Deming, and Teller [99]. The BET method is applicable to isotherms of type II and IV. Fig. 3.1 depicts both isotherm types, as they have been observed for the catalysts investigated in this work. A type II adsorption-desorption isotherm indicates a nonporous solid, whereas a type IV isotherm is characteristic for a mesoporous solid and shows the typical hysteresis loop. The pore nature can be characterized from the desorption branch of the isotherm by the Barrett-Joyner-Halenda (BJH) method [100–102].

To determine the specific surface area of a solid it is convenient to use the linearized form of the BET equation

$$\frac{p}{n_a(p_0 - p)} = \frac{1}{n_m C} + \frac{C - 1}{n_m C} \cdot \frac{p}{p_0} \quad (3.1)$$

where n_a is the amount of adsorbed gas at a relative pressure of p/p_0 , n_m is the monolayer capacity, and C is a constant depending on the isotherm shape. Attention has to be paid to finite linear part of the BET plot. Usually it is restricted to relative pressures of $0.05 \leq p/p_0 \leq 0.3$. Because of the simplifications of the BET method the isotherms need to have a fairly sharp knee to yield reliable values of n_m , i.e. the BET constant C shall be not smaller than 100. In a second step the specific surface area is calculated from n_m by

$$A_{\text{BET}} = n_m \cdot N_A \cdot a_m \quad (3.2)$$

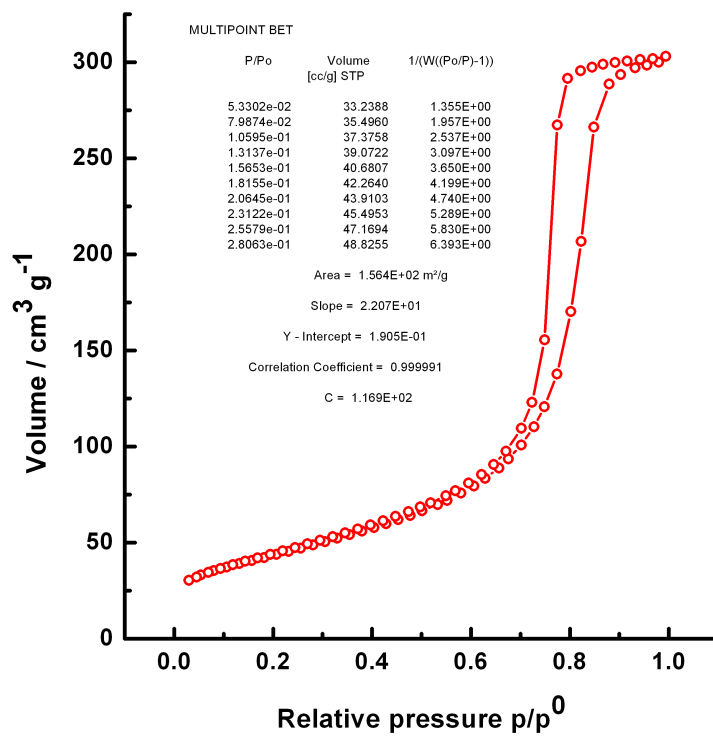
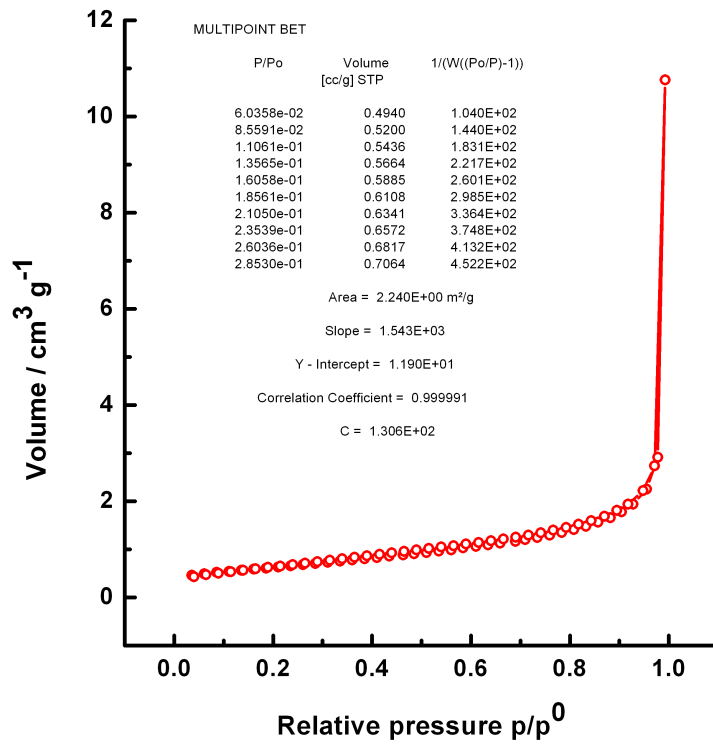


Figure 3.1: Nitrogen adsorption-desorption isotherms typical for the investigated catalyst systems. Top: A type II isotherm as it is observed for the α -Al₂O₃ supported catalysts. Bottom: A type IV isotherm as it is observed for γ -Al₂O₃ supported catalysts.

where N_A is the Avogadro constant¹ and a_m is the molecular cross-sectional area².

For nitrogen adsorption a Quantachrom apparatus, type Autosorb-6 or Autosorb-1 respectively was used.

3.1.2 Specific Surface Area by Krypton Physisorption

At very low surface areas, viz. $\approx 1 \text{ m}^2\text{g}^{-1}$, a determination of the specific surface area using nitrogen fails. Reason is the magnitude of correction for the unadsorbed gas remaining in the so-called “dead volume”, the intersection between sample cell at 77 K temperature and the pressure gauge at room temperature. Increasing inaccuracies with decreasing surface area make it unavoidable to substitute the adsorbate by a gas with lower saturation vapor pressure. The adsorption of krypton at 77 K is the common method to determine very small specific surface areas and permits the measurement of low enough amounts of gas with reasonable precision. It has to be mentioned that the benefit of the lower saturation vapor pressure is a mixed blessing, because there are some complications [95] such as the frequently nonlinear BET plot, selection of the proper molecular area and reference state. It is advised to calibrate against nitrogen adsorption, which is in practice difficult because the decision on krypton as sorptive is done in cases in which nitrogen adsorption yields only low accuracy results. It has to be accepted that in the absence of a nitrogen calibration uncertainties have to be estimated in the order of at least $\pm 20 \%$ [95].

In this thesis krypton adsorption was done with a Quantachrom apparatus, type Autosorb-1, located at the Technische Universität Berlin.

3.1.3 Chemisorption

The standard method to determine the metal surface area of a given catalyst is chemisorption [96, 103–106]. Generally three different measuring procedures are in use, viz. (I) the static-volumetric method [104], (II) the flow method [105], and (III) static-gravimetric method [106].

In this thesis the static-volumetric method is applied. The choice of the adsorptive is restricted by the investigated catalyst system. The interaction between adsorbate and probed metal shall be strong, but multilayer adsorption or dissolution in the metal bulk have to be avoided. Additionally, the adsorbate-support interaction shall be weak. The supported platinum catalysts used in this work were investigated by hydrogen and carbon monoxide chemisorption. Fig. 3.2 depicts as example a typical result of a CO chemisorption experiment. To determine the monolayer coverage of the platinum particles the samples were probed twice. In the first chemisorption isotherm (black trace) the platinum particles, the support and the sample cell were covered with the adsorbate. It is assumed that the hydrogen is adsorbed dissociatively on the metal, so that each molecule hydrogen is irreversibly bound to two platinum atoms. In the carbon monoxide experiments an one to one stoichiometry is assumed. Then the sample is evacuated at the adsorption temperature to remove all reversibly bound, not chemisorbed molecules. Subsequently the sample is again exposed to the adsorptive giving the second isotherm (red trace), which gives the amount of reversibly chemisorbed gas. The amount irreversible chemisorbed gas v_m can be read from the plateau of the difference isotherm (green trace). The specific metal surface area can be calculated with it applying the ideal gas law as

$$A_M = \left(\frac{v_m [\text{ml g}^{-1}]}{22414 [\text{ml mol}^{-1}]} \right) \cdot N_A \cdot \frac{1}{F} \cdot a_m, \quad (3.3)$$

as well as the metal dispersion

$$D = \left(\frac{v_m [\text{ml g}^{-1}]}{22414 [\text{ml mol}^{-1}]} \right) \cdot \frac{1}{F} \cdot \frac{M}{wt} \quad (3.4)$$

with v_m the volume of adsorbed probe molecules per gramm sample, N_A the Avogadro constant, F the chemisorption stoichiometry³, a_m the surface area occupied by a metal atom⁴, wt the metal loading ($0 < wt \leq 1$), and M the atomic mass of the metal.

Attention needs to be drawn to the selected stoichiometry coefficient. For CO adsorption on Pt it is known, that linear and bridged active sites of Pt coexist [107]. To discriminate between both Pt sites a microcalorimetric analysis of the chemisorption process is necessary. This method, which is described in the following

¹ $N_A = 6.02214129(27) \cdot 10^{23} \text{ mol}^{-1}$

² $a_m(\text{N}_2) = 0.162 \text{ nm}^2$, $a_m(\text{Kr}) = 0.202 \text{ nm}^2$ [93]

³Hydrogen chemisorption: $\text{Me} + \frac{1}{2} \text{H}_2 \rightarrow \text{Me-H}$ than $F = 0.5$ [103].

CO chemisorption: $\text{Me} + \text{CO} \rightarrow \text{Me-CO}$ than $F = 1$ or $2 \text{ Me} + \text{CO} \rightarrow \text{Me-CO-Me}$ than $F = 1$ [103].

⁴ $a_m(\text{Pt}) = 0.0800 \cdot 10^{-18} \text{ m}^2$ [103]

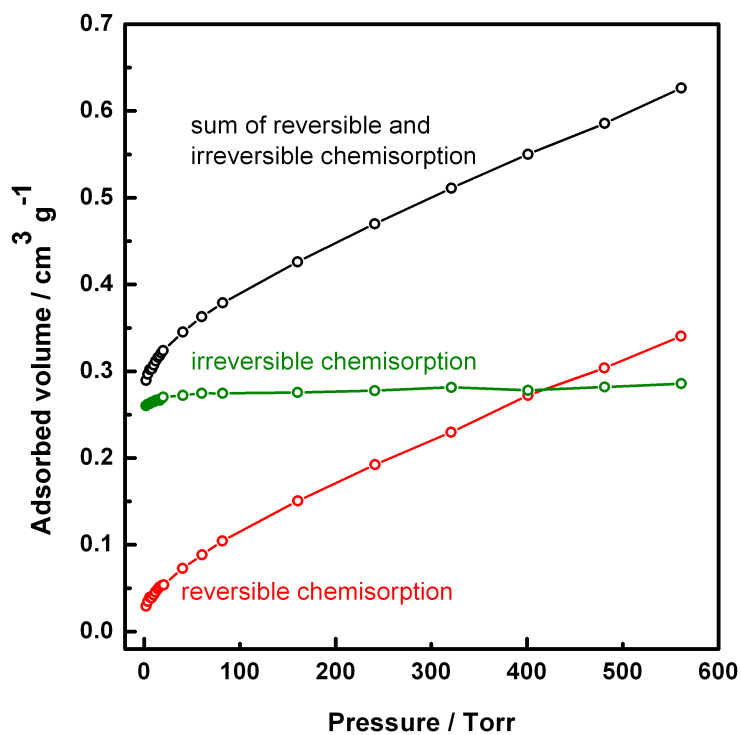


Figure 3.2: Typical chemisorption isotherms from CO adsorption at 40 °C. Black trace: first adsorption step (sum of reversible and irreversible chemisorption). Red trace: second adsorption step after evacuating at adsorption temperature (reversibly chemisorbed CO part). Green trace: irreversibly chemisorbed CO fraction, adsorbed volume can be read from the ordinate at the plateau.

section, was applied and confirmed the accuracy of the H₂ chemisorption experiments. The CO chemisorption was altered by a mixed adsorption stoichiometry.

In this thesis chemisorption experiments were done with a Quantachrom apparatus, type Autosorb-1.

3.1.4 Microcalorimetry

Calorimetry measures the heat of a chemical reaction or physical transformation. To discriminate between different reactive sites in catalysis, adsorption calorimetry is applied. To access the tiny amounts of heat released or consumed in a sorption experiment, a so-called heat flux or Tian-Calvet microcalorimeter [108] is used. This kind of calorimeter measures the heat flux between a micro calorimetric element, i.e. a cylindrical cell surrounded by an array of in-line connected thermocouples, and an isothermal reservoir, i.e. a large metal block at constant temperature. To calibrate the response of the calorimetric cell on a given heat portion (calorimeter constant), a small resistor can be introduced in the calorimeter cells and defined amounts of heat can be introduced. A microcalorimetric sorption experiment is conducted similar to the chemisorption experiment described above. The adsorbate is introduced stepwise at constant temperature, slowly increasing the cell pressure. For each dosing step the adsorbed gas amount is determined (isotherm). In comparison to the chemisorption experiment the differential heat of each dosing step can be determined by measuring the cell response of the calorimetric element and dividing it by the number of molecules adsorbed. The differential heats generated in each step can be interpreted by means of the nature of sites and allow a deeper understanding in the sorption experiment. As an example the bonding situation of CO on supported Pt can be mentioned [107]. All data sets consist of an isotherm and the corresponding heats of adsorption.

A SETARAM MS70 Calvet calorimeter with a custom-designed high vacuum and gas-dosing system was used in this thesis. The dosing manifold has a volume of 139 ml, and an absolute pressure transducer (MKS Baratron type 121) resolves pressure variations of 0.003 mbar, provided stabile laboratory air conditioning (± 1.5 °C). As conservative estimate probe gas amounts as small as 0.02 μmol can be dosed into the sample cell. The calorimeter has all metal cells, as described in [109] without the basket-like insert. The samples have been investigated using carbon monoxide as probe molecule.

3.2 Catalytic Testing - Profile Measurements

The catalytic testing was done in a dedicated reactor setup applying IR thermography (see Section 3.4) and quantitative mass spectrometry (see Section 3.5) in a spatially resolved manner. The reactor setup and its operation is described in detail in Chapter 5. For data evaluation it was necessary to convert the various time domains of all reactor components, i.e. mass spectrometer, thermocouples, pyrometer, and stepper motors, in a spatial coordinate, the reactor profile. For convenience reasons this was done in MATLAB script, which is elucidated in Appendix C.

3.3 Electron Microscopy

Electron microscopy (EM) is a powerful tool to investigate the topography and morphology of “very small” samples. By interaction of an electron beam with a specimen information about the nanostructure, size distribution, and composition of nano-materials and their agglomerates can be obtained. Because the wavelength of electrons is about five orders of magnitude shorter than that of visible light, magnification limits of light-optical microscopes are rescinded and images with atomic resolution are possible [110].

The most important interactions within an electron beam excited sample, q.v. Fig. 3.3, are backscattering of electrons, emission of secondary electrons, emission of Auger electrons, emission of characteristic X-ray radiation and bremsstrahlung, emission of visible light (cathodoluminescence), heat generation, and transmission of elastically and/or inelastically scattered electrons (if the sample thickness is appropriate). For detailed information about the subject the reader is referred to elaborated references such as [111–113].

3.3.1 Scanning Electron Microscopy

In scanning electron microscopy (SEM) a beam of electrons is probing the sample surface in a raster scan pattern, in vacuum. The sample responses of interest used in this thesis are the emission of secondary electrons, backscattering of electrons, and emission of characteristic X-rays. The information depth can be controlled by changing the acceleration voltage of the primary electron beam. It is usually in the range of 0.5 kV to 30 kV. An incident electron can interact with an electron in the sample and eject it with a certain amount of kinetic energy, which is then detected by a suitable detection device. By definition electrons

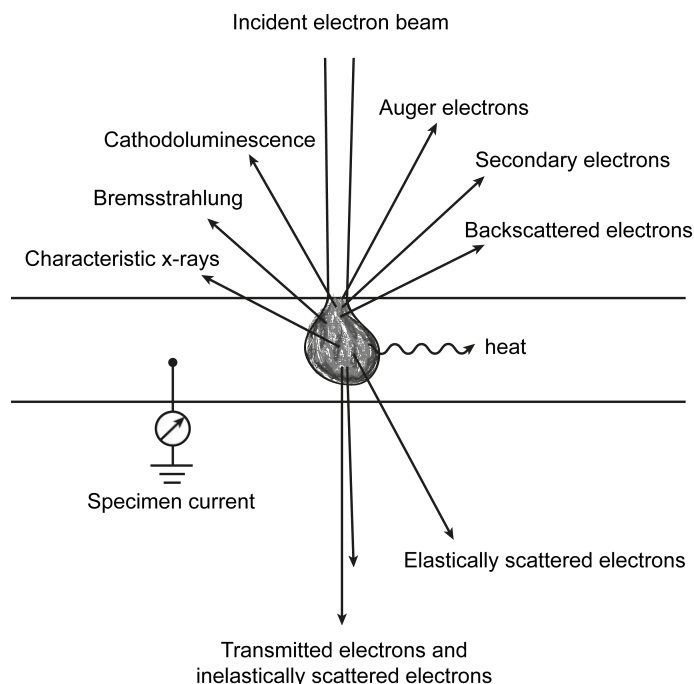


Figure 3.3: Schematic illustration of the principle responses of an electron beam interacting with a sample in an EM. Figure adapted from [112]

with kinetic energies smaller than 50 eV are referred as secondary electrons (SE). Due to their little energy SE can just escape from the sample if they are created in regions close to the sample surface. Generally speaking, SE carry surface topographic information. The image contrast can be interpreted as difference in object height. If the incident electrons interact with the nuclei of the sample it can be scattered back in any direction. Some of these electrons escape the sample, often after multiple scattering events. These backscattered electrons (BSE) are much richer in energy. The BSE signal emerges from deeper sample regions and depends strongly on the atomic number of the probed atom. Therefore BSE have lower spatial resolution, but carry additional information about the elemental composition of the sample, which is encoded in the BSE image contrast. Higher brightness can be interpreted as higher atomic weight. The elemental composition of the sample can be further characterized by analyzing the X-rays emitted from the electron excited sample. In modern SEM instruments an energy dispersive X-ray (EDX) detector is installed to detect X-ray radiation. X-rays are produced in cases, when an electron from the inner atomic shells is ejected from an atom and the resulting excited ion relaxes in its ground state under photon emission.

In this thesis a Hitachi S-4800 FEG (cold) with an energy dispersive X-ray sapphire detector, type EDAX Genesis 4000 System (Vers. 6.1) was used to characterize morphology and shape of the investigated Pt catalysts. Due to interference by charging of the mostly insulating catalyst foams a FEI Quanta 200 FEG (hot) ESEM with an EDAX Genesis 4000 System energy dispersive X-ray detector, was used to address these perturbations. A low vacuum with 30 mbar water pressure was applied.

3.3.2 Transmission Electron Microscopy

In transmission electron microscopy (TEM) a high energy and highly coherent electron beam is probing the sample specimen and electrons passing through the ultra thin sample are detected and analyzed. The typical specimen thickness is around 100 nm and electron energies in the range of 80 – 300 keV are applied. The instrument configuration and mode of operation go beyond the scope of this work and can be found elsewhere [113, 114]. Basically the contrast in a TEM, i.e. the features appearing in a TEM image are usually originating from electron transmittance variations from diffraction processes in the sample. Beside this “diffraction contrast” called phenomenon the electron beam is attenuated additionally by the sample thickness and density. Typically this “mass density contrast” is weaker and masked by the stronger diffraction contrast. It is distinguished between two imaging modes. By placing an objective aperture in the electron column to select undiffracted, transmitted electrons only results a so-called bright-field (BF) image. The image contains both diffraction and mass thickness contrast and thickness fringes or in crystalline samples grain boundaries, crystalline dislocations such as stacking faults, twins etc. may be observed. The second imaging mode yields dark-field (DF) images. In comparison to BF images only diffracted electrons contribute

to the image. The sample is therefore tilted and the objective aperture positioned in a way, that only a fraction of the crystallites in the sample fulfill the diffraction condition. Deviations from the perfect crystal as mentioned above do not fulfill the diffraction condition and appear dark in the image. Beside maximizing the image intensity with respect to the defect structures, DF images can be useful to determine shape, size and distribution of crystallite by selecting a fraction of crystallites from the sample. In both imaging modes it needs to be considered always that a TEM image is a two dimensional projection of a three dimensional object in electron beam direction.

In this thesis a Philips CM200 FEG with acceleration voltages up to 200 kV, a maximum resolution of 0.19 nm, STEM unit, an energy dispersive X-ray detector (EDAX Genesis 4000 System), and a Gatan Imaging Filter (Tridiem) was used.

3.4 IR Thermography

One of the most important parameters in catalysis research is the knowledge of temperature inside the catalyst bed. Many lab-scale reactor setups are designed in a way to be operated isothermally using strongly diluted reactant feeds and a few milligrams of catalyst. Typical reactant feed rates are in the order of a few milliliters per minute. In such cases the heat of reaction is usually small, and it is assumed that the furnace or heat bath temperature around the reactor equals the catalyst temperature, and that measuring the furnace temperature with a thermocouple gives good accuracy in the catalyst temperature measurement. In highly exothermic reactions, such as methane oxidation, operated on a several gram catalyst scale, converting a few liter reactants per minute typically builds up strong temperature gradients in the catalyst bed. Because of heat transport limitations the catalyst surface temperature can be easily 100 K or more above the temperature of the surrounding gas phase.

To measure the catalyst surface temperature an infrared pyrometer is used in this work. As described in Chapter 5 the pyrometer is connected to the reactor using a silica fiber with conical shaped tip. Fig. 7.4 depicts a silica fiber as it can be used to collect infrared radiation emitted by the catalyst material, which can be converted in an accurate solid temperature. The spectral, hemispherical emissive power $E_{\lambda, \text{blackbody}}(T)$ emitted of a black body is given by Planck's law

$$E_{\lambda, \text{blackbody}}(T) = \frac{c_1}{\lambda^5} \frac{1}{[\exp(\frac{c_2}{\lambda T}) - 1]} \quad (3.5)$$

with c_1 and c_2 Planck's radiation constants⁵, λ is the wavelength, and T is the temperature of the body. In practice no investigated material behaves like a black body, i.e. less radiation is emitted. Therefore the Planck equation can not be applied. The deviation from the black body can be expressed by the spectral emissivity $\epsilon(\lambda, T) = E_{\lambda}/E_{\lambda, \text{blackbody}}$. A special body is the so-called grey body, it has an emissivity that is independent of the wavelength. In reality the emissivity of many materials is a function of wavelength and temperature. Applying Wien's approximation⁶ on Eq. 3.5 and extending it by $\epsilon(\lambda, T)$ gives for the measured signal $I_{\lambda}(T)$

$$I_{\lambda}(T) = \frac{K\epsilon(\lambda, T)}{\lambda^5} \frac{1}{\exp(\frac{c_2}{\lambda T})}, \quad (3.6)$$

where K is pyrometer specific constant depending on the optical path, filter, the detector, etc. A calibration is required to determine K . The pyrometer temperature can be calculated from Eq. 3.6, the definition of $\epsilon(\lambda, T)$, and by approximation of a monochromatic pyrometer response [115] giving the following relation

$$\frac{1}{T_r} = \frac{1}{T} + \frac{\lambda}{c_2} \ln \epsilon_c(\lambda, T). \quad (3.7)$$

T_r is the so-called spectral radiance temperature and T the true object temperature. If the pyrometer is calibrated with a blackbody, as it was done in the present work, $\epsilon_c(\lambda, T)$ will be equal to 1 and the right part of the right term of Eq. 3.7 becomes zero. Than the measured spectral radiance temperature T_r equals the real object temperature T .

In practice it is impractical to calibrate the spectral radiation temperature to all operation conditions of the pyrometer, because of the temperature dependance of ϵ . To overcome this issue two-color ratio pyrometry is applied. In two-color ratio pyrometry two pyrometers operating at adjacent wavelengths are combined and the ratio Q between both spectral radiances is calculated. From Eq. 3.5 using Wien's approximation follows

$$Q = \frac{\epsilon(\lambda_1, T)}{\epsilon(\lambda_2, T)} \frac{\lambda_2^5 \exp(\frac{c_2}{\lambda_2 T})}{\lambda_1^5 \exp(\frac{c_2}{\lambda_1 T})}. \quad (3.8)$$

⁵ $c_1 = 2\pi hc^2 = 3.74177153(17) \cdot 10^{-16} \text{ W m}^2$ and $c_2 = hc/k_B = 1.4387770(13) \cdot 10^{-2} \text{ m K}$

⁶If $\frac{c_2}{\lambda T} \gg 1$ than $\exp\{\frac{c_2}{\lambda T}\} - 1 \approx \exp\{\frac{c_2}{\lambda T}\}$.

By approximating $\epsilon_1 = \epsilon_2$ for both close-by wavelengths gives a just temperature dependent relation between the ratio Q and the temperature T , $Q = Q(T)$. The relation between the measured ratio temperature T_R and the true temperature T is (derivation in [115])

$$T_R = \left(\frac{\ln Q - \ln(\epsilon_1/\epsilon_2) - \ln(K_1\lambda_2^5/K_2\lambda_1^5)}{c_2(\lambda_2^{-1} - \lambda_1^{-1})} \right)^{-1} \quad (3.9)$$

$$= \left(\frac{1}{T} + \frac{\ln(\epsilon_1/\epsilon_2)}{c_2(\lambda_2^{-1} - \lambda_1^{-1})} \right)^{-1} \quad (3.10)$$

However, in some cases the two emissivities are still not equal and the ratio $k = \epsilon_1/\epsilon_2$ needs to be corrected to derive the correct object temperature. Therefore it is recommended to calibrate the pyrometer, for example against a thermocouple.

In this work an IMPAC IGAR 12-LO:MB13 quotient pyrometer was used. It operates at $\lambda_1 = 1.52 \mu\text{m}$ and $\lambda_2 = 1.64 \mu\text{m}$, and in a temperature range of $350 \leq T \leq 1300 \text{ }^\circ\text{C}$. The pyrometer was calibrated against a type K thermocouple (details in appendix A).

3.5 Mass Spectrometry

Mass spectrometers are analytical devices that separate and analyze molecules and atoms in form of ions by means of their mass to charge ratio m/z . Principally a mass spectrometer has four main components: (I) An inlet system transferring the sample from atmospheric pressure into vacuum to the ion source. (II) An ion source converting the neutral sample molecule by removal or addition of an electron or proton into a gas-phase ions. The excess energy transferred during the ionization event may break the molecule to form characteristic fragments. (III) A mass analyzer separating the molecular ions for example in a magnetic sector, a quadrupole, by time-of-flight, a quadrupole ion trap, or an orbit trap. And (IV) an ion detector that records and amplifies the ion current passing the mass filter. The physical principles that are applied in each of the components are various and their choice is strongly related to the analysis task. Since it is not relevant to introduce a comprehensive image on the different mass spectrometer types and their working principle, the reader is referred to [116, 117] for detailed information. This section will briefly summarize basic aspects of a quadrupole mass spectrometer with electron ionization and secondary electron multiplier detector.

3.5.1 Electron Ionization

Electron ionization (EI) is the most common ionization principle for organic compounds with masses less than 600 amu. In the EI process the gaseous sample molecules are bombarded by accelerated electrons in vacuum (usually $10^{-5} - 10^{-6}$ mbar) forming molecular ions, i.e. radical cations.



In order to use EI, it is necessary that the kinetic energy of the electrons bombarding the sample molecule is larger than the ionization energy (IE) of the molecule. The excess energy, i.e. difference between electron energy and IE, remaining in the formed ion can subsequently induce fragmentation reactions. Characteristic smaller fragment ions are formed. The fragmentation pattern obtained is diagnostic of the structure of the probed molecule (fingerprint). The ionization and fragmentation probability increase with increasing electron energy, but goes through a maximum in the range of 50 to 100 eV. Usually electron energies of ≈ 70 eV are applied [116].

3.5.2 Quadrupole Mass Filter

A linear quadrupole mass filter consists of four cylindrical shaped rod electrodes arranged symmetrically in a square configuration. Ideally the rods should have hyperbolic shape. Fig. 3.4 depicts the assembly schematically for a cylindrical rod shape. At a time, a pair of opposite electrodes is held on the same potential Φ_0 creating the field within the square array. The potential is generated by superimposing a DC voltage U and a time-dependent radio frequency (RF) voltage V with the angular frequency ω , i.e. $\Phi_0 = U + V \cos(\omega t)$. The two pairs are set to the exact antipodal potential. These voltages create an oscillating field with in the electrodes that is given by

$$\Phi_{x,y} = \Phi_0 \frac{x^2 - y^2}{r_0^2} = (U + V \cos \omega t) \frac{x^2 - y^2}{r_0^2} \quad (3.12)$$

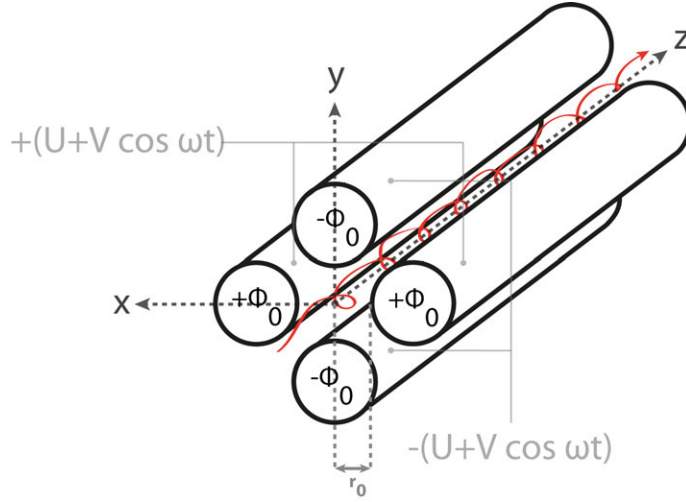


Figure 3.4: Schematic of a linear quadrupole mass analyzer. Red: Illustration of the wobbling ion trajectory of a transmitting ion. Figure adapted from [117] (modified).

where r_0 is one-half the distance between a electrode pair and x and y are the distances from the center of the xfield. An ion injected in the quadrupole, exposed to the oscillating field can be described by the Mathieu equation [118] in x- and y-direction

$$\frac{d^2x}{d\tau^2} + (a_x + 2q_x \cos 2\tau)x = 0 \quad (3.13)$$

$$\frac{d^2y}{d\tau^2} + (a_y + 2q_y \cos 2\tau)y = 0$$

with $\tau = \omega t/2$ and the dimensionless parameters a and q given by

$$a_x = -a_y = \frac{8eU}{m\omega^2 r_0^2} \quad (3.14)$$

$$q_x = -q_y = \frac{4eV}{m\omega^2 r_0^2} \quad (3.15)$$

Solutions of Eqs. 3.14 are either stable, i.e. $|x(\tau)|$ or $|y(\tau)|$ do not exceed r_0 at any τ , and the ion can pass the quadrupole in z direction or unstable, i.e. $|x(\tau)|$ or $|y(\tau)| > r_0$ at some time τ , and the ion is ejected from the quadrupole never arriving at the detector.

Speaking illustratively, the action of a quadrupole can be explained as follows [116]: Has a pair of electrodes a positive DC potential, positively charged ions are accelerated to the quadrupole center axis. The simultaneous RF modulated potential attracts the ions during its negative half-cycle towards the electrodes. Ions with low m/z ratio will be accelerated highest during each potential variation and finally leave the field-defining space. Ions with higher m/z ratio will respond much sluggardly on the RF modulated potential and will remain confined within the boundaries of the quadrupole. A pair of electrodes with negative DC potential accelerates all positively charged ions in electrode direction. The RF modulated potential again influences low m/z ratio ions strongest and rejects them inside the quadrupole, whereas higher m/z ratio ions will be lost. Summarizing the positive pair of electrodes behaves as a high-pass filter and the negative electrode pair acts as low-pass filter. The combination of both effects creates a stability window allowing a certain fraction of ions to the transit through the quadrupole in z direction, in a helical trajectory.

3.5.3 Secondary Electron Multiplier

The secondary electron multiplier (SEM) is the most common ion detector in mass spectrometry, because of its high sensitivity and speed in contrast to the simple Faraday cup detector which measures the ion current, the SEM provides a gain of $10^6 - 10^8$ [119] by pre-amplifying the ion current arriving at the detector. A variety of designs are in use, though the operational principle is always the same. A discrete dynode electron multiplier consists of a cascade of cup-shaped electrodes. Ions arriving from the mass filter are accelerated by a negative potential to hit the first electrode, i.e. the conversion dynode. The dynodes are made of a metal or semiconductor. The high energy ion impact induces secondary electron generation. The secondary electrons are attracted by a positive potential to the next dynode. The potential increases from one to the next dynode (usually ≈ 100 V) accelerating all emitted secondary electrons to hit the surface of the next

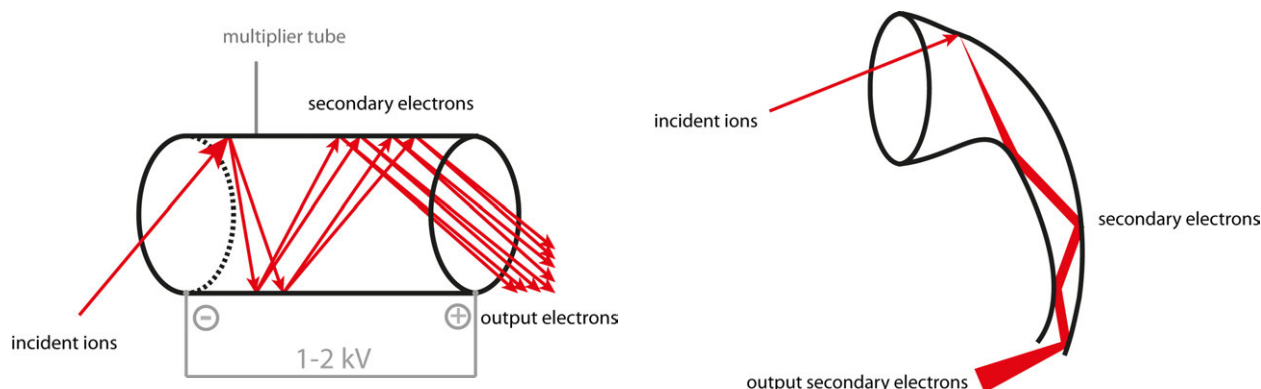


Figure 3.5: Schematic of a linear channel multiplier (single channel of a MCP) and a curved channel electron multiplier (channeltron). Figure adapted from [117] (modified).

dynode causing the release of several additional secondary electrons each.

An other version of the SEM is the so-called continuous dynode design with a horn-shaped tube. It is popularly known as channeltron and consists of a glass funnel coated with a semiconductor material on the inner surface. The conducting surface acts as an array of continuous dynodes. This variant is depicted in Fig. 3.5.

A third common variant is the multi channel plate (MCP) detector. It uses an array of millions of very short (μm range) linear electron multipliers. The gain of a MCP is in the order of $10^4 - 10^5$. To achieve a gain in the magnitude of SEMs or channeltrons, MCPs can be build as a stack of two or three single MCPs. MCPs are usually produced as round plates of various diameters allow very high temporal resolution. (ns regime) A typical application is single ion counting. In addition MCPs can be operated for imaging purposes, i.e. array detectors.

One complication of all SEMs is the fact, that the conversion yield of the first dynode depends on the impinging ions mass, charge, energy, and electronic configuration. The changing sensitivity to different analyte species complicates quantification of the SEM signal.

In this work a Balzers Prisma QME 200 with a QMA 200 M2 quadrupole mass filter equipped with Faraday cup and secondary electron multiplier (channeltron) detector and electron ionization was used for product quantification. The quantitative product analysis was done by using argon as internal standard. Details about the calibration procedure are presented in appendix B.

3.6 Microkinetic Modeling

The rate by which chemical reactions proceed is governed by chemical kinetics. In heterogeneous catalysis kinetic studies are conducted to derive rate equations of momentum, mass, and energy to design catalytic reactors. The rate equations for design purposes are usually very simple, e.g. power rate laws or Langmuir-Hinshelwood Hougen-Watson rate expressions, and provide non or only minimal mechanistic insight into the catalytic reaction. In recent years microkinetic models have been reported for many catalytic reactions, among them the catalytic partial oxidation of methane on platinum [70–73,89], which consist of a series of reversible elementary reaction steps at the catalyst surface and corresponding kinetic parameters. Many surface intermediates are explicitly included and no assumptions are made about rate determining steps, quasi-equilibrated steps, or most abundant surface species.

One of the goals of the present work was to validate the performance of the two most comprehensive microkinetic models for methane oxidation on platinum against the spatial reactor profiles measured in this work. The kinetic formalism used to implement the microkinetic models [70–73,89] as well as the conservation equations they are combined with are summarized in Chapter 9.

3.7 Raman Spectrometry

Raman spectroscopy, named after Sir C. V. Raman [120–122], is a spectroscopic technique studying rotational or vibrational states of molecules or phonons in a crystal lattice. The method relies on inelastic scattering of monochromatic light, usually provided by a laser source. The incident monochromatic, coherent laser light interacts with the sample species with most of it being transmitted or reflected. Just a small fraction of the incident light is scattered. The scattered light is emitted in all directions from the sample. If the

scattered light is dispersed in a spectrometer it turns out that most of it is elastically scattered light of the same wavelength as the incident light (Rayleigh scattering), but a small fraction of the scattered photons are shifted in their energy up or down. Raman bands with red-shifted photons are called Stokes bands, whereas blue-shifted Raman bands are referred to as Anti-Stokes bands. Typical intensity differences between incident laser light, Rayleigh scattered light, and Raman scattered light are three orders of magnitude each ($10^{-6}I_{\text{laser}} \approx 10^{-3}I_{\text{Rayleigh}} \approx I_{\text{Raman}}$).

In catalysis research Raman spectroscopy allows to investigate the changes of the catalyst material in-situ without the need of a special probe, an optical access to the catalyst is the only prerequisite. There are no general physical limitations such as temperature or pressure that constrict the method. In this work experiments using a fused silica fiber to irradiate the sample and to collect the scattered light (see Chapter 7), as well as experiments conducted in a reactor cell with a quartz window (see Chapter 8) under a confocal microscope are presented and illustrate the application of the spectroscopic technique. The method is bulk sensitive and the signal intensities are not directly interpretable with respect to the abundance of a species in an investigated sample.

The key step in practical Raman spectroscopy is the laser line rejection, e.g. the suppression of the intense Rayleigh scattered light. Two approaches are in use and both can be applied with the Raman spectrometer used in this work. First, laser line rejection by an optical filter. Here holographic notch or edge filter are used allowing measurements as close as $\approx 100 \text{ cm}^{-1}$ to the laser line. A disadvantage of this method is that a matching of the filter and the laser source needs to be done, because each filter is limited to a single excitation wavelength. The second method is the application of a so-called triple spectrometer. It consists of three spectrometers in a row. The first two spectrometers are used for laser line rejection allowing measurements as close as $\approx 10 \text{ cm}^{-1}$ to the laser. Additionally the triple spectrometer approach is not limited to a certain spectral line and allow access to UV laser excitation where suitable filters are missing. The price paid for the increased flexibility is low light throughput and the need for three spectrometers.

The spectrometer used in this work is a triple filter Raman spectrometer (S&I GmbH, TriVista 557) with two liquid nitrogen cooled CCD cameras (Princeton Instruments, Spec-10:100BR at first stage and Spec-10:2KBUV at third stage) as detectors. Each single spectrometer is build in Czerny-Turner geometry [123]. Optical access to the triple spectrometer is provided either by a confocal microscope (Olympus, BX51WI) or a fiber bundle spliced into a slit geometry at the spectrometer entrance port.

3.8 Thermogravimetry

Thermogravimetry analysis (TGA) is an analytic technique, which quantifies the weight change of a sample as a function of temperature in a controlled atmosphere. TGA is a typical coupled technique, which usually uses a MS or GC-MS for gas analysis. Simultaneous thermogravimetry/differential scanning calorimetry (TG/DSC) is another common combination, because the DSC extends the method to processes, which do not result in weight changes such as phase transformations. Moreover DSC gives information about the exo- or endothermicity of an event observed in the TGA.

In practice the sample is placed in an inert crucible that stands on a high-precision microbalance. Usually the sample is exposed to a constant temperature ramp of a few Kelvin per minute under an inert atmosphere, for example N_2 . Other important gases are O_2 in temperature programmed oxidation (TPO) or H_2 in temperature programmed reduction (TPR). The correlation of weight change, off gas analysis and temperature signal allows interpretation in terms of various material properties. Examples are moisture content, decomposition temperatures, phase transition temperatures, amount of solvent residuals, organic carbon content, et cetera.

TG/DSC measurements presented in this thesis were recorded on a Netzsch STA 449 C Jupiter thermogravimetric system with mass-spectrometric analysis of the decomposition products.

3.9 Ultraviolet-Visible-Near Infrared Spectrometry

Ultraviolet-visible-near infrared spectrometry (UV/vis-NIR) refers to absorption or reflectance spectrometry in the region of approximately $200 \text{ nm} \leq \lambda \leq 2500 \text{ nm}$. UV/vis spectrometry induces electronic transitions in the probed molecules.

The fundamentals of the method can be found in general textbooks [124, 125]⁷. In compliance with the molecular orbital theory, overlapping orbitals split into bonding and anti-bonding molecular orbitals. Usually all electrons are located in the bonding orbitals and the anti-bonding orbitals are empty. The adsorption experiment measures the transition from these populated ground state orbitals to the unpopulated excited

⁷The following paragraph is adapted from a script by L. Lehmann from Freie Universität Berlin [126].

state orbitals. The energy gap between bonding and anti-bonding orbitals increases with increasing orbital overlap, viz. σ -orbitals have larger energy gaps than π -orbitals. The absorption of a $\sigma \rightarrow \sigma^*$ transition is therefore located in the vacuum-UV, whereas a $\pi \rightarrow \pi^*$ transition absorbs in the “regular” UV/vis region. Electrons located in anti-bonding orbitals can be excited, too. A transition either in σ^* - or π^* -orbitals is possible. Again the $n \rightarrow \sigma^*$ transition is of higher energy compared to a $n \rightarrow \pi^*$ transition. The excited electron is after photon absorption in an anti-bonding orbital, which weakens the bonding in the molecule. A bond cleavage usually does not happen and the electron relaxes quickly back to its ground state. The direct relaxation into the ground state induces light emission of the exact same energy as was necessary for electron excitation. This process is complementary to the absorption and emission. There are other relaxation processes possible. Relaxation can happen alternatively by internal conversion, i.e. radiation free, from the excited state in a rotational or vibrational excited mode of the ground state, i.e. fluorescence, or via formation of a quantum mechanically “forbidden” intermediate state, i.e. via phosphorescence. This process demands a spin inversion to form the intermediate triplet state followed by a second spin inversion before relaxing into the ground state resulting in an extended lifetime of the metastable triplet state characteristic for phosphorescence phenomena.

The application of UV/vis-NIR spectroscopy is less routine in heterogeneous catalysis because difficulties with experimental artifacts and background corrections.

UV/vis spectra presented in this work have been measured using a Perkin-Elmer Lambda-25 spectrometer.

3.10 X-ray Diffraction

X-ray diffraction (XRD) is the routine method to characterize crystalline materials by means of qualitative and quantitative phase analysis.

The method originates on the fundamental work of Max von Laue [127–129], Sir William Henry Bragg [130, 131], and William Lawrence Bragg [130, 132, 133]. X-rays are elastically scattered on the electron shell of atoms in a crystalline solid. The crystallites behave as three-dimensional gratings for the incident X-ray photons and depending on the atom spacing constructive and destructive interference occurs. Bragg’s law describes the condition of constructive interference from stacked crystallographic planes of a crystal lattice, given by

$$n\lambda = 2d_{hkl} \sin \theta \quad (3.16)$$

where n is an integer determined by the given order, λ is the wavelength, θ is the angle between the incident X-ray and the scattering planes, and d is the distance between the lattice planes (h , k , and l , as given in Miller Notation). The intensity maxima detected by a CCD image sensor are referred to as Bragg peaks.

In catalysis research powder diffraction is a widespread method to identify solid specimens by means of the crystallographic structure. The polycrystalline powder is fixed on a sample holder. The randomly orientated crystals give diffraction rings around the beam axis, rather than the discrete Laue spots observed in single crystal diffraction. By rotating the sample holder, the rings are averaging and smoothed. The angle between the incident X-ray beam axis and the rings is called scattering angle and denoted as 2θ . By either moving the X-ray source or the detector or both simultaneously powder diffraction data are recorded. Usually these data are presented as diffractograms in which the diffracted intensity is plotted versus 2θ . The specimen identification is usually done by comparison of the apparent diffractograms against powder diffraction files (PDF) provided by a database maintained by the International Centre for Diffraction Data. XRD may also be used to characterize heterogeneous solid mixtures to determine the relative abundance of crystalline compounds. Accounting for instrument specific parameters, lattice constants and atom positions in the crystallites can be determined by Rietveld refinement [134], a full diffraction pattern refinement technique. It simultaneously refines all apparent reflexes. The peaks are described by a combination of Gaussian and Lorentzian shaped peaks. After phase assignment a scaling factor can be found for each phase, which allows for a quantitative phase analysis.

Additional information is included in the line broadening of the XRD reflexes. It can be used to characterize the crystallite size. Unfortunately a direct measure of the crystallite size is not possible. The measurable quantity is a so-called column height. The crystallite size is calculated by the peak broadening using the double-Voigt approach. Integral breadth-based volume weighted mean crystallite size (LVol-IB) of coherently diffracting domains were determined [135]. The estimate of crystallite size from LVol-IB depends on a particular crystallite shape and on the size distribution of the crystallites. It is assumed that all Pt particles are spherical, single domain, and of homogeneous size. Than the crystallite size is given by

$$d = \frac{4}{3} \text{LVol-IB} \quad (3.17)$$

In this work a STOE Stadi-P with autosampler and a Bruker D8 Advance theta/theta diffractometer were used for XRD.

3.11 X-ray Microtomography

The principle of radiography, e.g. imaging technique on the basis of X-ray transmission is as old as the discovery of the X-ray itself [136], the ability to reconstruct these images to a three-dimensional dataset is younger. In radiography, X-rays from a source (typically a tube) with an energy spectrum in the range of 20 – 120 keV pass through the sample object and are detected by a position sensitive detector. While the emitted photon passes through a sample, it undergoes different interactions with the matter, which contribute to their absorption such as the photoelectric effect, elastic scattering and the Compton effect. The observed contrast in the image, which is called “projection” of the sample, arises from the differential attenuation factors in the sample, which are given by the thickness, density and elemental composition of the sample. The attenuation of the intensity of the X-ray beam as it passes through the sample with thickness d is mathematically expressed in the well-known Lambert-Beer law

$$\frac{I}{I_0} = \exp(-\mu d) \quad (3.18)$$

where I_0 is the intensity of the incident X-ray beam, I the observed transmitted intensity and μ the linear attenuation coefficient of the sample in cm^{-1} , which is a constant over the sample thickness d [137, 138]. The method of X-ray computer-tomography was invented by Godfrey Hounsfield in 1972 [139], wherein he reconstructed the three-dimensional internal structure on an object using series of projections acquired at consecutive angles. As in the used experimental setup the source and detector are static, the sample is rotated in 360° , while every 0.28° a projection is acquired. While the method is optimized for a spatial resolution of $15 \mu\text{m}$, the number of acquired projections as well as the source-detector-distance and source-object-distance plays a major role in resolution and magnification. The reconstruction of the image is carried out by the Radon Transform [140], while the process itself is termed filtered backprojection [141].

In this work a custom made tomography station was used located at the Helmholtz-Zentrum Berlin. In addition to the setup described in [142, 143], a sample rotational stage was used for precise angular rotation.

Cumulative part
—
Results

Chapter 4

Microwave-Assisted Self-Propagating Combustion Synthesis for Uniform Deposition of Metal Nanoparticles on Ceramic Monoliths ¹

Abstract

A new microwave-assisted gel-combustion synthesis in self-propagating mode was developed for the deposition of adhesive metal nanoparticles on ceramic substrates. Pt particles with diameters less than 10 nm uniformly distributed on corundum foams were prepared by the fast and reliable combustion method with no additional calcination or reduction steps. The results are rationalized in terms of complexation of the Pt precursor by glycerol, reduction of the Pt precursor to colloidal Pt nanoparticles, followed by carburization of the organic ligands and rapid carbon burn off preserving the high dispersion and uniformity of the Pt nanoparticles on the foam support.

4.1 Introduction

Preparation of highly dispersed metal particles uniformly covering oxide supports plays a crucial role in many industrially important catalytic applications. This issue becomes particularly important for three-dimensional supports like monoliths, since, at the same surface area per unit volume, a ceramic monolith exhibits an order of magnitude smaller pressure drop than corresponding packed catalyst beds [144]. In addition to honeycomb monoliths with straight channels, reticulated ceramic foams have been recently suggested as "prestructured" supports because of their isotropic open cell structure and pore tortuosity [144–146]. These structural features provide significant advantages of foam-based catalysts for catalytic processes that are limited by mass or heat transfer.

It is well-known that metal deposition onto macroporous materials requires additional precautions to avoid maldistribution over the support body. Generally, changes in the spatial distribution occur during the drying step as a consequence of metal migration in the liquid phase, which is controlled by the convective flow of the solvent, molecular diffusion, and adsorption of the metal precursor [147]. This usually leads to the metal accumulation at the external surface and hence to so-called "egg-shell" concentration profiles across the porous support. There were many attempts to overcome this problem on monoliths by using ion exchange, homogeneous deposition/precipitation, and wet impregnation methods [148, 149]. However, even in the case of a strong propensity for anchoring of the metal precursor to a support, the metal maldistribution may still take place because of significant capillary and gravity forces during the drying of large monolithic supports. Therefore, various approaches for drying have been proposed in the literature such as rotation of the impregnated monolith [150], freeze-drying [151], microwave heating [152], and increasing the precursor viscosity [153].

In general, complete precursor decomposition and binding of metal particles on the oxide supports requires elevated temperatures. On the other hand, conventional long-term calcination at high temperatures may result in undesired sintering of the active phase. To fulfill these contradictory demands, one of the possible solutions is to control this process kinetically, whereby a high-temperature flash to completely decompose

¹Adapted from U. Zavyalova, F. Girgsdies, O. Korup, R. Horn, R. Schlögl *J. Phys. Chem. C* 113 (40) (2009) 17493-17501.

a precursor must be followed by a rapid cooling to prevent surface diffusion of metal species and hence their sintering. This approach can in principle be realized by nonequilibrium, highly exothermic combustion reactions.

Combustion synthesis has already been proven to be a quick and efficient preparation process suitable for producing a variety of oxide ceramic powders [154–156], noble metal doped CeO_2 [157, 158], and $\gamma\text{-Al}_2\text{O}_3$ [159, 160] powders, which reveal remarkable properties for various applications. In contrast to "volume" combustion methods, such as the solution combustion method [154–160] and self-propagating high-temperature synthesis (SHS) [161, 162], the "surface" combustion proceeds in a thin film of precursor, thus providing favorable conditions for both the formation and adhesion of the active phase to the substrate. Recent studies performed by different groups [163–166] have proven the combustion synthesis as a straightforward and energy-efficient route for the preparation of adhesive nanocrystalline oxide layers. However, only mixed oxide coatings based on lanthanum chromite perovskite [165] and Ce, Co, Cu, Cr, and Mn mixed oxides [164–166] were deposited on ceramic and metal monoliths by the single combustion synthesis step so far. Usually, the ignition of the exothermic combustion reactions is realized by heating in a conventional electric oven [157–160, 165] or by hot air ejected from a heat gun [166] at temperatures of about 500 – 600 °C.

In this paper, we report a new, microwave-assisted combustion synthesis (MACS) for fast and reliable preparation of uniformly distributed metal nanoparticles on ceramic monoliths without any additional calcination and reduction steps. The synthesis procedure can be realized using various organic fuels, such as urea [157–160], glycine [167–169], citric acid [162], oxalyldihydrazide [158, 160], or ammonium nitrate [170]. Glycerol was chosen in the present work as a chelating agent and combustion fuel, as it had shown good performance in the synthesis of various oxide materials before [168, 169]. Glycerol exhibits a high viscosity that favors more uniform metal distribution on monolith supports during the drying step. Moreover, taking into account environmental aspects, glycerol is a favorable fuel for the preparation due to the absence of toxic NO_x emissions during its combustion.

4.2 Experimental Methods

4.2.1 Materials

As support materials, reticulated $\alpha\text{-Al}_2\text{O}_3$ foams (Reticel Vesuvius Hi-Tech Ceramics) of 15 mm diameter and 10 or 20 mm height and either 45 or 80 ppi (pores per linear inch) were used. The BET surface area was typically around $S_{\text{BET}} = 0.7 \text{ m}^2 \text{ g}^{-1}$. For efficient binding of metal particles on the corundum support, the foam pellets were immersed in an acetone solution in an ultrasonic bath for 20 min, washed with water, and calcined at 800 °C for 6 h in air. A washcoat was not applied. All chemical reagents (analytical-grade purity) were purchased from Sigma-Aldrich and were used without any further purification.

4.2.2 Deposition of Metal Nanoparticles on Ceramic Foams

In a typical experiment procedure for the deposition of Pt nanoparticles on the ceramic foams, 1.4 g of $\text{C}_3\text{H}_8\text{O}_3$ was mixed with 10 ml of aqueous $\text{Pt}(\text{NH}_3)_4(\text{NO}_3)_2$ solution containing 10 g of Pt/l (molar ratio of $(\text{Pt}(\text{NH}_3)_4(\text{NO}_3)_2/\text{C}_3\text{H}_8\text{O}_3) = 1/30$). After the continuous stirring and heating of the glycerol-chelated Pt solution at 80 °C overnight, the foam cylinders were immersed into the obtained precursor solution at 80 °C for 2 h. Then, the excess solution was removed by blowing pressurized oil-free air through the foams. Drying and synthesis of metal nanoparticles were performed in a commercial microwave oven MWG 7017W (Diverse Electro) operating at 2.45 GHz at 700 W. Synthesis time was varied between 3 and 9 min. No further reduction steps were applied. The platinum loading in the final catalysts could be adjusted from 0.6 to $2.0 \pm 0.2 \text{ wt}\%$ by applying one to three impregnation steps, respectively. Several samples were prepared for each of the foam loading experiments in order to check for reproducibility of the deposition procedure. The temperature profile during the combustion synthesis in the microwave oven was measured by IR thermography (temperature range 60 – 370 °C) and IR pyrometry (temperature range 350 – 1000 °C). The self-propagating combustion front during the synthesis process was monitored by a digital camera.

In order to verify the adhesion of the catalytic layer to the support, the samples were stressed in an ultrasonic bath for 1h and weighed after drying [171].

To compare the new MACS method to conventional wet impregnation, Pt foam catalysts were also prepared by wet impregnation from the same Pt precursor without glycerin addition. The impregnated samples were dried at 110 °C overnight, calcined at 600 °C for 4 h in synthetic air [172], and reduced in a flowing 10 vol% H_2/He mixture at 600 °C.

²The BET surface was recently determined by Kr-BET and the surface area given in this paper needs to be corrected. The investigated corundum foam monoliths with 45 ppi exhibit a surface area of $S_{\text{BET}_{\text{Kr}}} = 0.09 \text{ m}^2 \text{ g}^{-1}$. Monoliths with 80 ppi exhibit a BET surface area of $S_{\text{BET}_{\text{Kr}}} = 0.16 \text{ m}^2 \text{ g}^{-1}$. The influence of coating the monoliths with 1 wt% Pt had no significant effect on the determined surface area.

4.2.3 Characterization

For the spatial surface-morphology characterization of the monoliths, the prepared foam catalysts were cut into about 2 mm thick slices and investigated by high-resolution scanning electron microscopy (HRSEM) with energy-dispersive X-ray (EDX) analysis. Images were recorded on a Hitachi-S4000 instrument equipped with a field emission gun (FEG) (cold) in secondary electrons mode. The electron accelerating voltage was 15 kV. Additionally, BSE (back scattered electrons) images were recorded for better material contrast and topography.

For determination of crystallite size and metal dispersion, the prepared metal foam catalysts were grinded in an agate mortar to obtain a fine powder. X-ray powder diffraction analysis (XRD) was performed in reflection mode on a D8 Advance theta/theta diffractometer (Bruker AXS) using Cu $K\alpha_{1+2}$ radiation ($\lambda = 1.54186 \text{ \AA}$). Real structure characterization was performed by whole powder pattern fitting using the Rietveld method. Nitrogen adsorption studies were carried out using a Quantachrome Autosorb-6 instrument at 77 K. Before adsorption, the samples were outgassed at 250 °C overnight. HRTEM studies were performed on a Philips CM200 transmission electron microscope (point resolution 0.19 nm, acceleration voltage 200 kV) with energy-dispersive X-ray spectroscopy (EDX). Samples for HRTEM analysis were prepared from suspensions of the powdered sample in chloroform. A drop of the chloroform slurry was placed into the holey-carbon film mounted on a copper grid. TG/DSC data were recorded on a Netzsch STA 449 C Jupiter thermogravimetric system with mass-spectrometric analysis of the decomposition products. All experiments were performed using alumina crucibles with sample amounts of approximately 20 mg at a heating rate of 2 °C min⁻¹ in dry synthetic air.

For investigation of the brownish film obtained as an intermediate stage during the MACS procedure, UV/vis spectra of the film material were taken on a Perkin-Elmer Lambda-25 spectrometer. TEM images and EDX spectra were obtained on a Philips CM200 FEG transmission electron microscope by dissolving a small amount of the brownish intermediate in ethanol and putting a droplet on a holey-carbon film mounted on a copper grid.

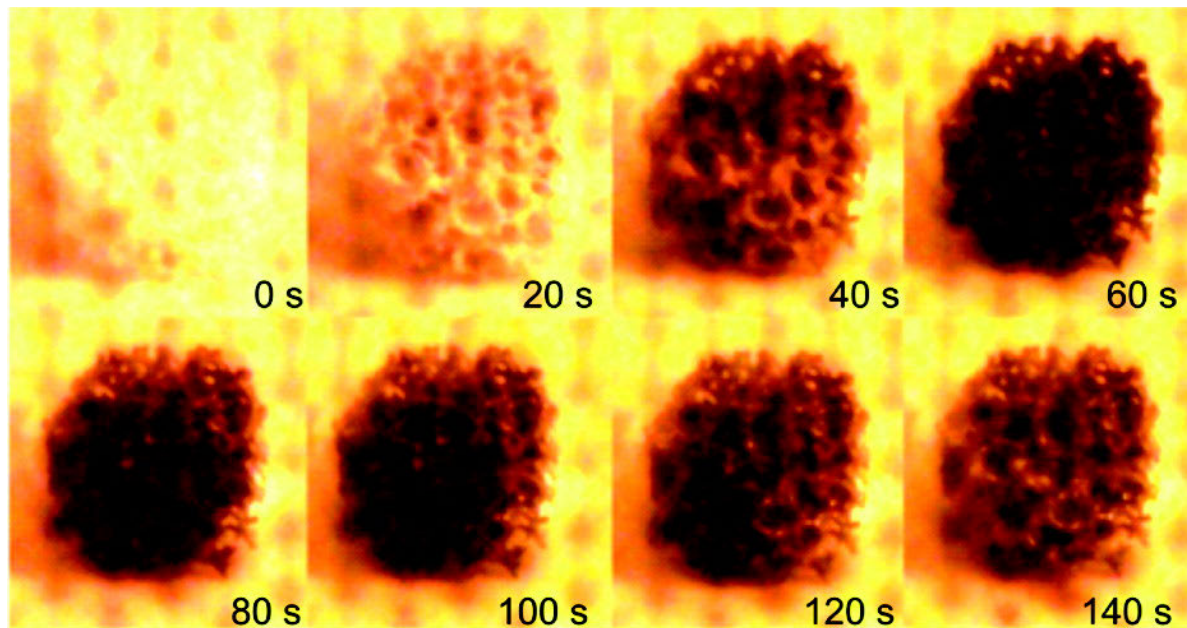
4.3 Results and Discussion

4.3.1 Ignition of Self-Propagating Combustion Synthesis by Microwave Irradiation

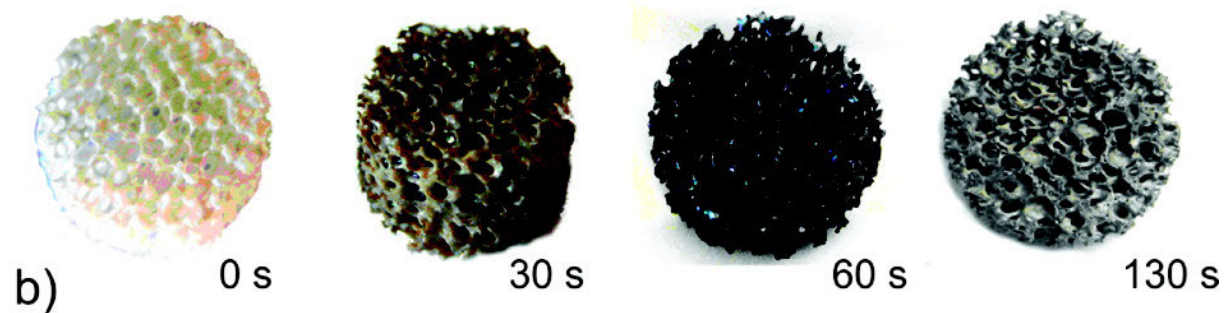
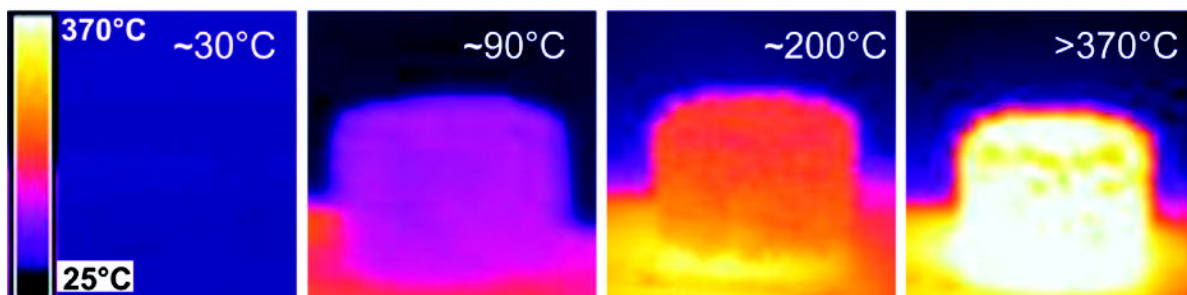
According to the blank tests, the corundum ceramic foams used as a support in this work are essentially microwave transparent and cannot contribute to microwave-assisted heating. Hence, microwave irradiation can provide rapid, selective, and noninertial heating of the glycerol-chelated metal precursor.

After preliminary investigations, the molar ratio of $\text{Pt}(\text{NH}_3)_4(\text{NO}_3)_2/\text{C}_3\text{H}_8\text{O}_3 = 1/30$ in the aqueous precursor solution was found to be sufficient for obtaining uniform Pt films on the ceramic foams by the single-step combustion process. As growing excess of organic fuel leads to sintering of combustion-synthesized nanoparticles and deposition of carbonaceous residues in the samples [170], higher glycerol content in the initial reactant mixture was not used.

Fig. 4.1 shows snapshots from the movie recorded during the MACS preparation process (see the Supporting Information). One can see the self-propagation of the combustion front with formation of metal coatings within less than 3 min. The thermographs recorded by IR thermography show that the temperature of the impregnated foam increases in the first 30 s to about 90 °C accompanied by evaporation of water, a good microwave absorber, and formation of a brownish gel-like film, as shown in Fig. 4.1b. After 60 s of microwave heating at 700 W, the temperature reaches 200 °C, leading to combustion of the gel film and formation of a carburized black coating. As can be seen in Fig. 4.1b, the combustion front starts from the bottom side of the foam which is in the focus of the microwave radiation and self-propagates through the entire foam. Apparently, Pt catalyzes the decomposition of the organic chelating agent, since the blank experiments showed no such effect in the absence of the Pt precursor. Further exposure to microwave heating (totally 130 – 160 s) supplemented by heat liberation from the combustion reaction increases the temperature rapidly above 370 °C, and the foam surface takes on the characteristic metal reflection, as shown in Fig. 4.1b. Foams prepared in this way are henceforth referred to as "as-prepared" catalysts. As the temperature range of the IR thermocamera was not high enough to determine the maximum synthesis temperature during the MACS process and to study the effect of loading on the combustion process, the microwave-assisted combustion synthesis was also followed by IR pyrometry using a fiber probe (temperature range 350 – 1000 °C). Three different foams were prepared by one, two, and three successive impregnation steps, respectively, and subjected to the microwave program. The results are shown in Fig. 4.2. Multiple impregnation steps of the monolith with increasing precursor thickness and metal concentration resulted in a drastic increase in the combustion temperature and synthesis velocity. If two or more impregnation steps were applied to the foam, the combustion front was even visible to the naked eye as a glowing layer traveling



a)



b)

Figure 4.1: Photos of the ceramic foams impregnated by glycerol-chelated Pt precursor: (a) snapshots recorded in time intervals of 20 s during microwave-assisted combustion synthesis; (b) thermographs recorded by an IR thermocamera (temperature range 25 – 370 °C) during the synthesis in a microwave oven operated at 700 W. (0 s) foam impregnated by the precursor solution, (30 s) foam coated by brownish gel-like film, (60 s) in situ carburized intermediate, and (130 s) Pt-coated ceramic foam.

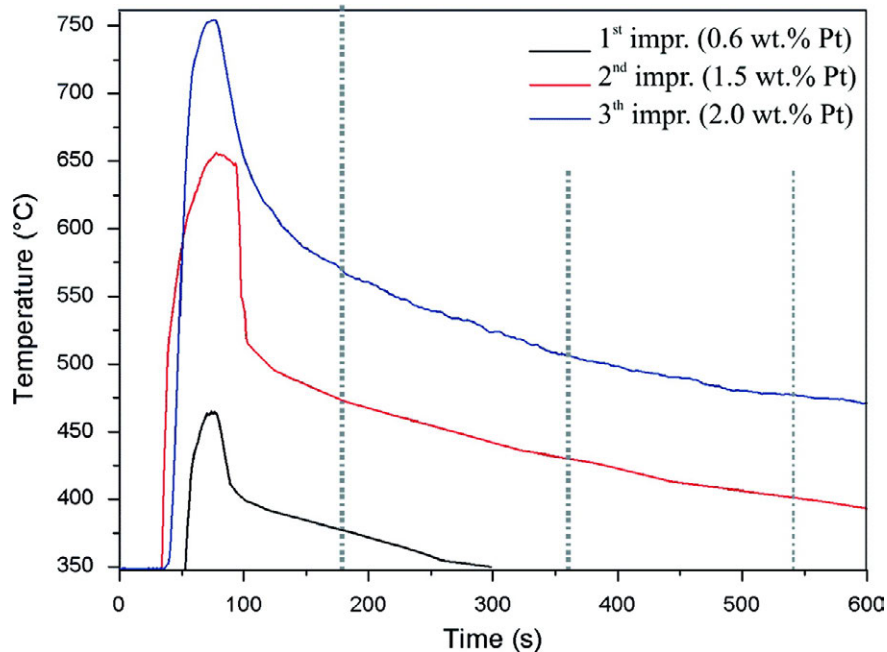


Figure 4.2: Temperature profiles recorded by IR pyrometry (temperature range 350 – 1000 °C, fiber probe) during MACS after (a) one impregnation step with 0.6 wt% Pt loading, (b) two impregnation steps with 1.5 wt% Pt loading, and (c) three impregnation steps with 2.0 wt% Pt loading.

Table 4.1: Characterization of Pt Deposited on 80 ppi Corundum Foams by the Conventional Method (CM) and MACS Preparation with Various Synthesis Times and Pt Loadings.

Nr	Pt loading, wt%	preparation method	synthesis time in MO, min	mean particle size (EM), nm	mean crystallite size (XRD), nm	Pt spec. surf. area ^a , m ² g ⁻¹	dispersion %
1	0.6	CM		50	30	7	3
2	0.6	MACS	3	5		42	20
3	0.6	MACS	6	20	15	14	7
4	0.6	MACS	9	30	20	11	5
5	1.5	MACS	6	30	19	11	5
6	2.0	MACS	6	30	21	10	5

^aPt fcc structure with $a = 3.92 \times 10^{-10}$ m and a density of $\rho = 21.45$ g cm⁻³.

through the foam from bottom to top ($T_{\max} = 650 - 750$ °C, see the Supporting Information). One can see from the obtained thermograms that, similar to conventional self-propagating high-temperature synthesis (SHS), microwave-assisted combustion synthesis proceeds in steps including (i) warming up (0 – 50 s), (ii) ignition and combustion reaction (50 – 100 s), and (iii) cooling and secondary physicochemical transformations (100 – 800 s). To investigate the influence of the synthesis time in the microwave on the physicochemical properties of the catalysts (Tab. 4.1), the process was stopped after 3, 6, and 9 min, respectively (dashed lines). We have also examined the effect of pore density, that ranges from 45 ppi (pores per linear inch) to 80 ppi and geometrical size (diam × height) (15 × 10 vs 15 × 20 mm) of foams on the MACS parameters. The data showed that the synthesis velocity (synthesis time per foam volume) increases with decreasing pore density and is not influenced much by the catalyst volume, which can be explained by the fact of homogeneous heating provided by MW radiation with enhanced diffusion rates [173]. As the MW absorption increases with increasing temperature caused by exothermic energy released during the combustion reaction, microwave energy and combustion synthesis assist each other in sustaining the reaction [174]. Hence, ignition of the combustion reactions by MW radiation makes it possible to heat also large monoliths very rapidly and uniformly.

4.4 Synthesis Mechanism

Obviously, the MACS process is rather complex and may involve not only metal precursor decomposition, and the combustion of organic fuel, but also complexation and redox reactions between the fuel and the metal precursor and also reactions between decomposition products. To rationalize the observed effects, we

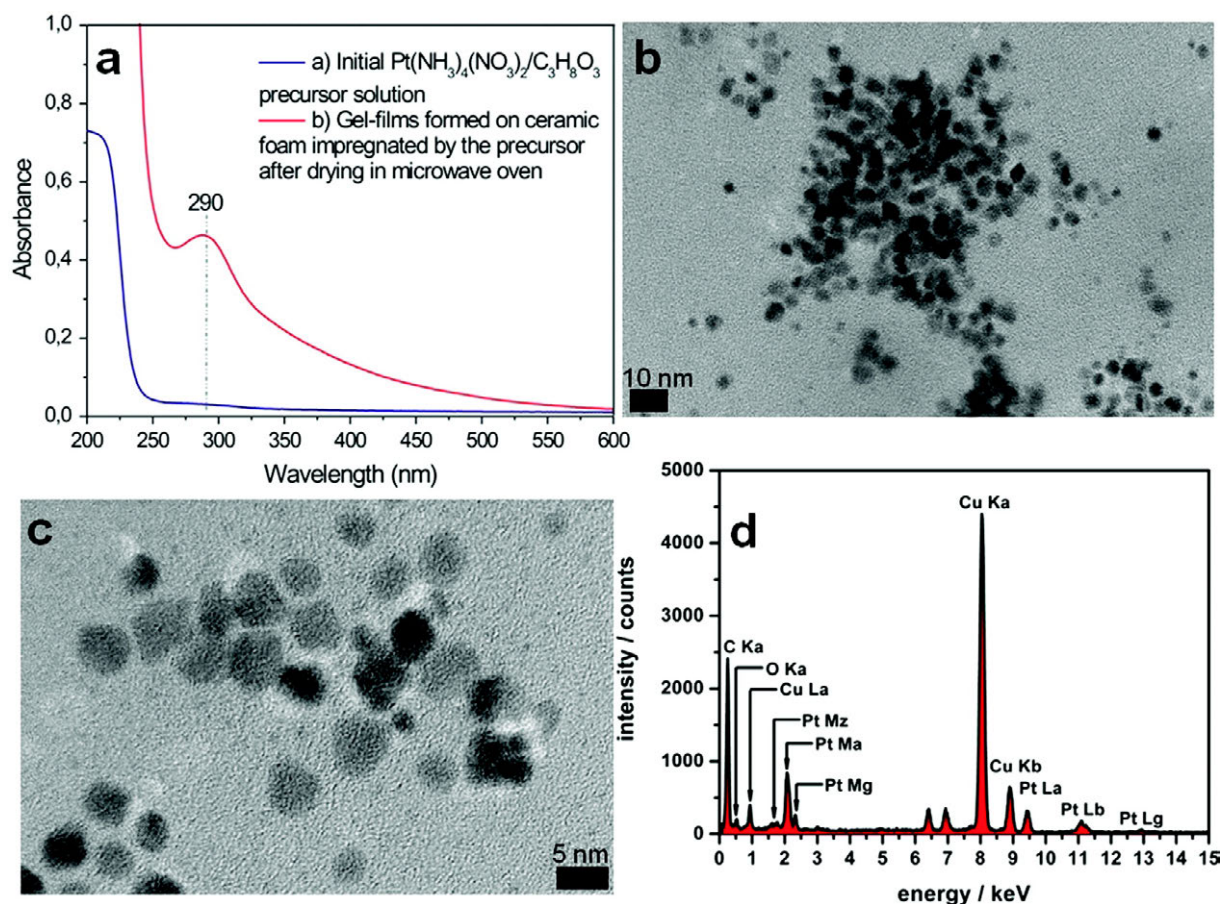


Figure 4.3: (a) UV/vis spectra of (a) initial transparent $\text{Pt}(\text{NH}_3)_4(\text{NO}_3)_2/\text{C}_3\text{H}_8\text{O}_3$ precursor solution and (b) brownish gel-like films formed on corundum foam impregnated by the precursor after drying in a microwave oven at 700 W for 30 s. (b, c) TEM images of Pt nanoparticles in the brownish intermediate formed during the MACS process. (d) EDX spectrum of the nanoparticles identifying them clearly as Pt (Cu peaks stem from the TEM grid).

tried to trace the "elementary" steps and the "intermediate" products during the preparation.

As mentioned above, using glycerol as fuel favors the formation of brownish gel-like films on the $\alpha\text{-Al}_2\text{O}_3$ support at temperatures of about 90 °C (see Fig. 4.1b (30 s)). To investigate the nature of the brownish intermediate, the synthesis in the microwave oven was interrupted after 30 s of heating at 700 W and a UV/vis spectrum of the brownish film was taken. The brownish material was further investigated by TEM and EDX. The combined results are shown in Fig. 4.3. Fig. 4.3a shows a comparison between the UV/vis spectrum of the initial $\text{Pt}(\text{NH}_3)_4(\text{NO}_3)_2/\text{C}_3\text{H}_8\text{O}_3$ precursor solution and the brownish film. The results show that after rapid water evaporation and selective heating of the supported precursor in the microwave a broad UV/vis absorption background results, which begins at around 600 nm and increases steeply with decreasing wavelength. Such a background is very typical for light scattering by colloidal Pt nanoparticles [175]. The absorption band centered at 290 nm can be assigned to a ligand to metal charge transfer (LMCT) transition of glycerol-chelated Pt cations. The process in the microwave begins probably with a complexation of the Pt ions by glycerol followed by reduction of the Pt ions to colloidal platinum nanoparticles. To verify the assumption of colloidal Pt nanoparticles, the brownish intermediate was investigated by TEM and EDX (Fig. 4.3b-d). In agreement with the UV/vis data, the brownish material consists indeed of colloidal Pt nanoparticles with a very narrow size distribution around 5 nm. The Pt peaks are clearly visible in the EDX spectrum (the Cu peaks in Fig. 4.3d stem from the TEM grid used). Further microwave heating of the colloidal film results in a carbonaceous overlayer seen as a black coating on the corundum foam (see Fig. 4.1b (60 s)). SEM/EDX analysis of the carburized intermediate obtained during the microwave synthesis for 1 min showed a significant amount of amorphous carbon in this sample, which uniformly covers the foam surface, as shown in Fig. 4.4. The TG plots in synthetic air for the as-prepared 2 % Pt/ $\alpha\text{-Al}_2\text{O}_3$ foam catalyst and the corresponding carburized intermediate after 1 min in the microwave oven are shown in Fig. 4.5. According to the TG-MS analysis, the carbon film burns completely off below 350 °C with evolution of water and CO_2 corresponding to a weight loss of about 2.5 wt%. Except CO_2 and H_2O , also traces of CO ($m/e = 28$) and H_2 ($m/e = 2$) were observed at the decomposition of the carburized intermediate in synthetic air in the

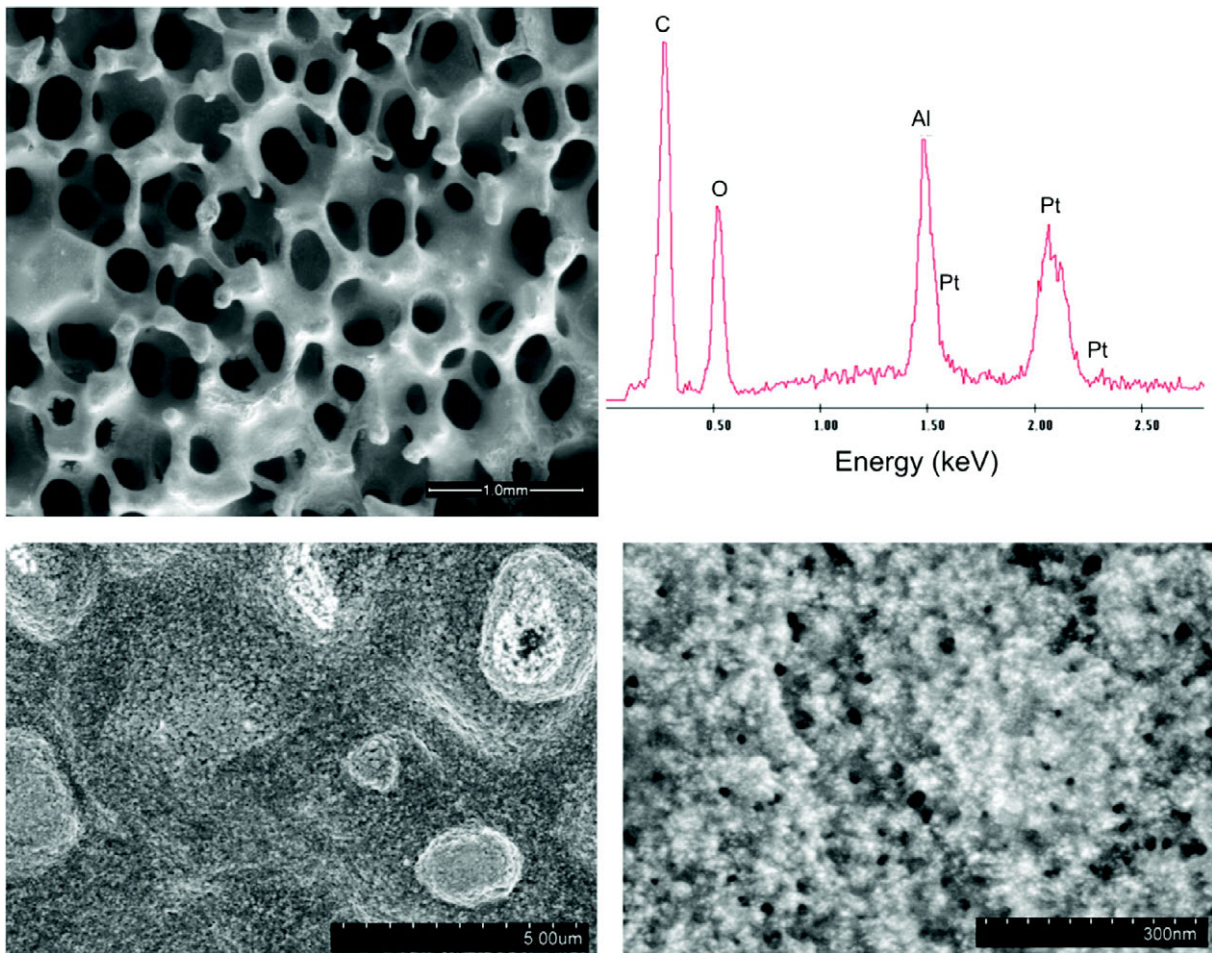


Figure 4.4: Low- and high-magnification SEM images of the carburized intermediate product obtained during the combustion synthesis by microwave heating for 1 min. The sample shows the formation of a uniform carbonaceous layer on Pt as revealed by the overview EDX spectra.

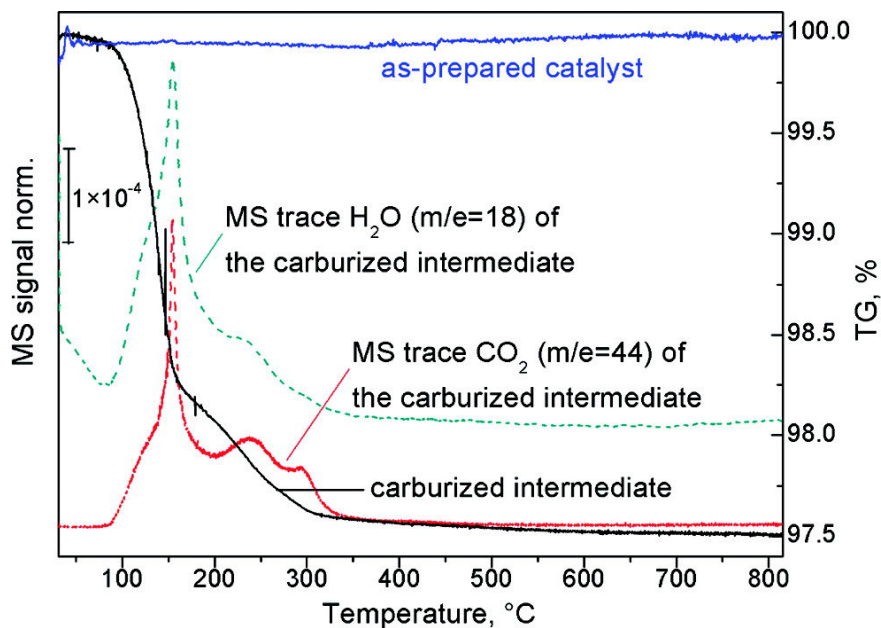


Figure 4.5: TG plots (in synthetic air) of as-prepared 2 % Pt/ α -Al₂O₃ catalyst (top curve) and the carburized intermediate (bottom curve) during the microwave synthesis for 1 min. The heating rate is 2 °C min⁻¹. MS spectra (dashed lines) show evolved water ($m/e = 18$) and CO₂ ($m/e = 44$) during the decomposition of the carburized intermediate.

temperature range 140 – 190 °C. These gases are probably formed by pyrolysis of glycerol [176]. One has to recall that amorphous carbon is a good microwave absorber in the 2.45 GHz region which can be easily heated up to 1200 °C [174]. Therefore, microwave heating promotes the catalytic effect of this dielectric solid, which is at a much higher temperature than the surrounding gases. Hence, microwave heating can favor heterogeneous catalytic reactions of the volatile compounds formed by glycerol pyrolysis [176].

Note that microwave heating gives rise to hot spots inside the dielectric solid, where the temperature is locally much higher than the average temperature of the bed, as measured by the optical pyrometer. Therefore, the carbonaceous overlayer may provide local overheating which in turn leads to further structural transformations, ultimately resulting in burning off the carbon. The carbon could also serve as a reducing agent for the metal oxide phase, if the latter had been formed in the previous precursor combustion stages. The carbon burn off is accompanied by a reaction front propagating through the monolith body, as visually observed by changes in color from black to metallic.

The as-prepared sample has shown no considerable weight loss in the temperature range 30 – 1000 °C. This means that the carbon overlayer is completely burned off upon further exposure to the MW radiation. Temperature-programmed reduction with hydrogen at a heating rate of 2 °C min has shown no reduction of the as-prepared 2 % Pt/ α -Al₂O₃ catalyst in the temperature range from 60 to 1000 °C.

Summarizing the above presented results, the preparation process can be visualized in the scheme shown in the Fig. 4.6. After water evaporation, the glycerol-chelated metal precursor forms a brownish gel-like film on the foam support under MW radiation. As evidenced by UV/vis spectroscopy, TEM, and EDX, this brownish film consists of colloidal Pt nanoparticles and glycerol-chelated Pt ions. Further MW radiation leads to a transformation of this brownish film into a carbon overlayer which might prevent agglomeration of the metal nanoparticles [177]. The carbon overlayer acts as a microwave absorber, providing rapid, selective, and noninertial heating until the carbon burns off, leaving the metal nanoparticles highly dispersed behind.

4.4.1 Characterization of the Prepared Pt-Coated Foam Catalysts

As the specific surface area of the α -Al₂O₃ foam support was only 0.7 m² g⁻¹ and no high-surface-area washcoat was applied, the surface area measured by nitrogen adsorption after metal deposition did not change significantly and remained low at about 1 m² g⁻¹ ³.

Fig. 4.7a-c shows images of the uncoated ceramic foam support (80 ppi), which consists of large α -Al₂O₃ crystallites of about 0.5 – 1.0 μ m. The foam support structure (space group 167: trigonal) can be clearly seen on the HRTEM images (see Fig. 4.8). Uniformity of the Pt particle distribution across the monolith body was investigated by SEM/EDX analysis of the monoliths cut into 2 mm thick slices. Fig. 4.7g-j shows

³The statement is generally correct but the determined surface area was recently determined by Kr-BET and has to be revised, see section 4.2.1.

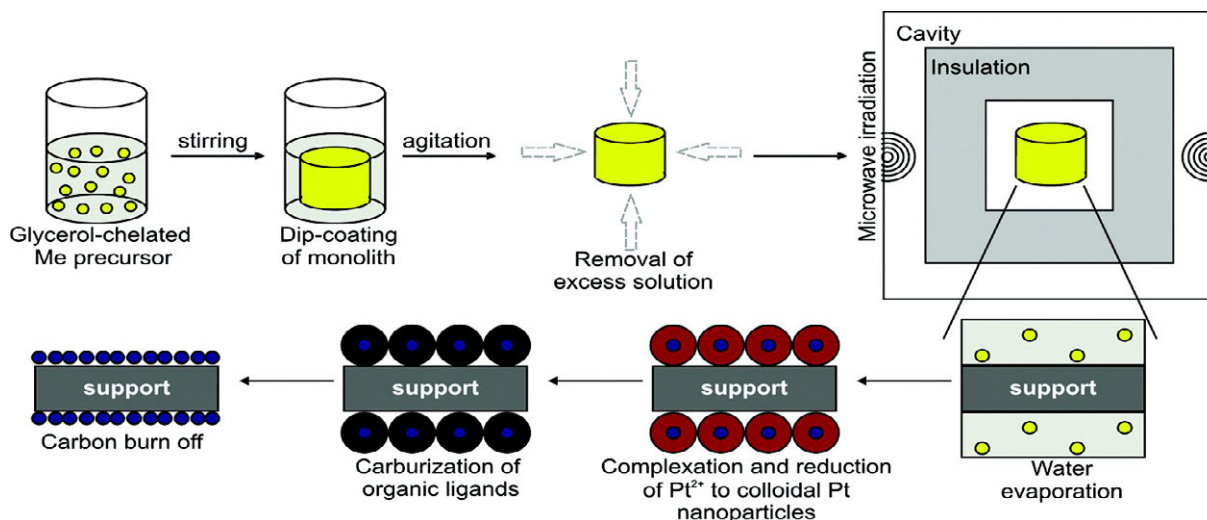


Figure 4.6: Schematic representation of the sequence of events during MACS catalyst synthesis.

representative images from the various parts of the 0.6 % Pt/ α -Al₂O₃ catalyst prepared by the MACS method during 3 min. The results show that the preparation technique leads to uniform deposition of the metal nanoparticles throughout the whole foam body. For comparison, Pt foam catalysts were also prepared by conventional incipient wetness impregnation using the same Pt precursor without glycerol addition followed by calcination and reduction at 600 °C in 10 vol% H₂/He flow [172]. Apparently, the combustion reactions on the support surface with a high-temperature flash followed by rapid cooling favor the formation of well-dispersed metal nanoparticles and prevent their sintering even on the low surface area of the α -Al₂O₃ support. As evidenced by the high-resolution SEM and TEM micrographs shown in Fig. 4.7j and Fig. 4.8, low-index surface terminated Pt nanocrystallites with an average particle size from 3 to 6 nm (see Fig. 4.7l) were formed by the MACS preparation. The EDX analysis of the as-prepared catalysts showed only Pt and alumina but no carbon or other contaminations.

The structure of all prepared Pt-coated foam monoliths was characterized by whole powder pattern fitting using the Rietveld method. For instance, XRD patterns with Rietveld fitting of 0.6 % Pt/ α -Al₂O₃ foam catalysts prepared from a Pt(NH₃)₄(NO₃)₂ precursor by conventional thermal treatment [172] and by the MACS technique are shown in Fig. 4.9. The integral breadth-based volume weighted mean crystallite size (LVol-IB) of Pt, according to the line-broadening analysis, and an average Pt particle size observed by electron microscopy for the prepared samples are summarized in Tab. 4.1. Taking into account Eq. 4.1 for the particle diameter (d) and assuming that all Pt particles are spherical, single domain, and of homogeneous size, the Pt specific surface area and metal dispersion on the ceramic foams were calculated and are given in Tab. 4.1.

$$d = 4/3 \text{ LVol-IB} \quad (4.1)$$

The results show that the LVol-IB of Pt measured by XRD in the catalyst prepared by the conventional method is about 30 nm, whereas, for the MACS-prepared sample, the Pt mean crystallite size is about 15 nm (see Fig. 4.9). For the sample Nr. 2 obtained by the MACS method during 3 min, Pt peaks are hardly detected by XRD, and the mean Pt particle size was evaluated on the basis of HRSEM and HRTEM images of the sample (see Figs. 4.7j and 4.8). The results show that the average Pt particle size increases significantly with increasing synthesis time in the microwave oven. Hence, rapid cooling may allow preventing the growth of the metal particles, and the synthesis time can be optimized in each case on the basis of the synthesis thermograms, as shown in Fig 4.2.

Despite the fact that the multiple impregnation steps with increasing metal concentration result in a drastically increasing combustion temperature (see Fig. 4.2), it does not influence the Pt mean particle size and the metal dispersion significantly. Apparently, not the temperature in the combustion wave but the kinetics of the secondary physicochemical transformations after ignition and combustion determines the metal dispersion.

The adhesion tests proved that the adherence between the deposited metal catalyst at various Pt loadings and the ceramic support is excellent. The catalyst is strongly bonded to the support, and not even vibrations of high intensity and duration can damage the system. Particularly, after treatments of different duration (15 – 60 min) are carried out in an ultrasonic bath, the average weight losses were always negligible (less than 0.1 wt% of the deposited catalyst weight in every case). Therefore, MACS has the advantage of allowing both the simultaneous formation of the nanocrystalline metal catalysts and its adhesion to the ceramic

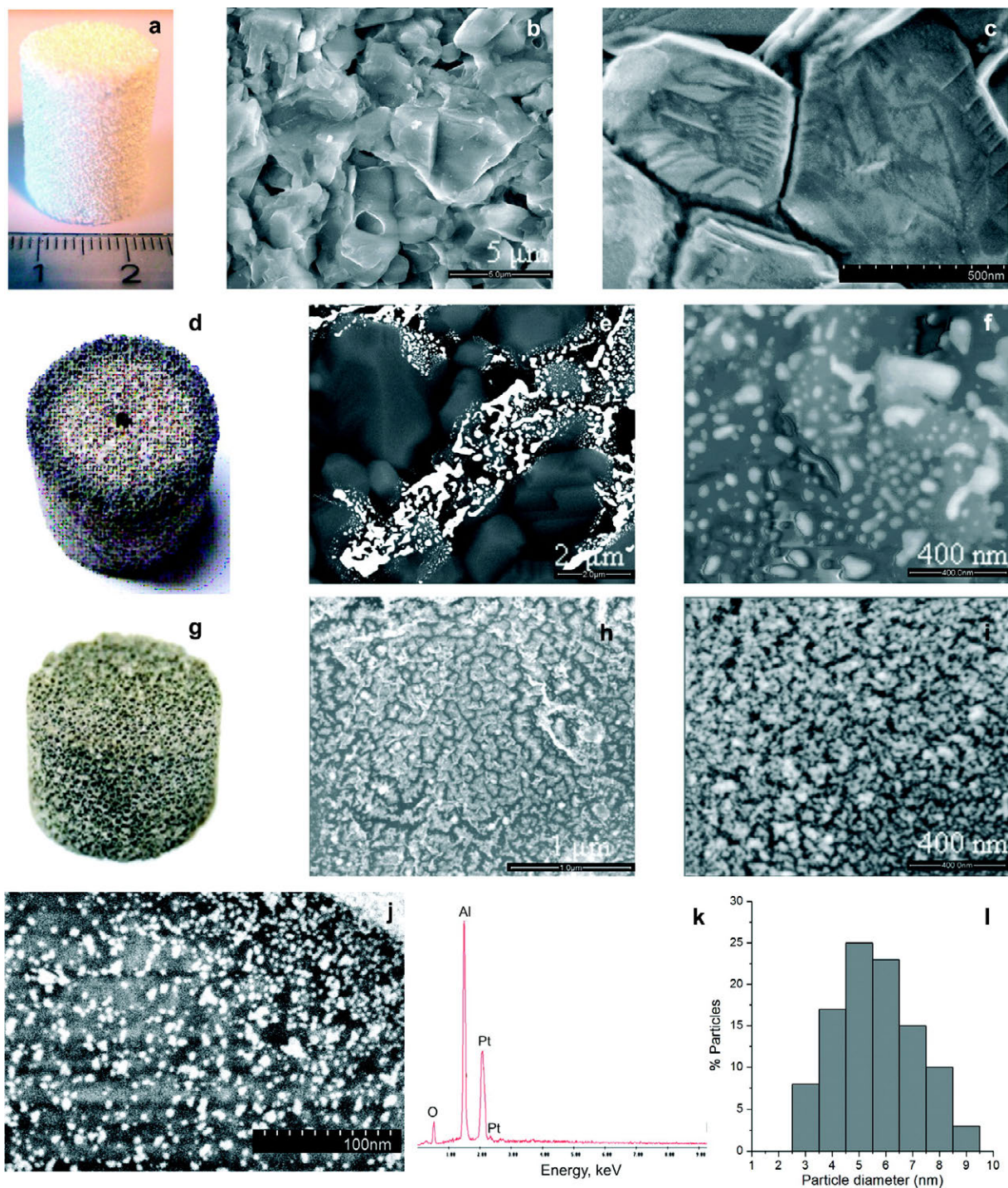


Figure 4.7: Representative pictures of (a-c) uncoated ceramic foams (Retitel Hi-Tech Ceramics), (d-f) 0.6 % Pt/ α -Al₂O₃-coated foam prepared by conventional wet impregnation [172]; (g-j) 0.6 % Pt/ α -Al₂O₃ foam catalyst prepared by the MACS method during 3 min. (e, h) BSE images: Pt-bright, Al₂O₃-gray. (k) Overview EDX spectra and (l) particle size distribution histogram of the corresponding catalyst prepared by the MACS method.

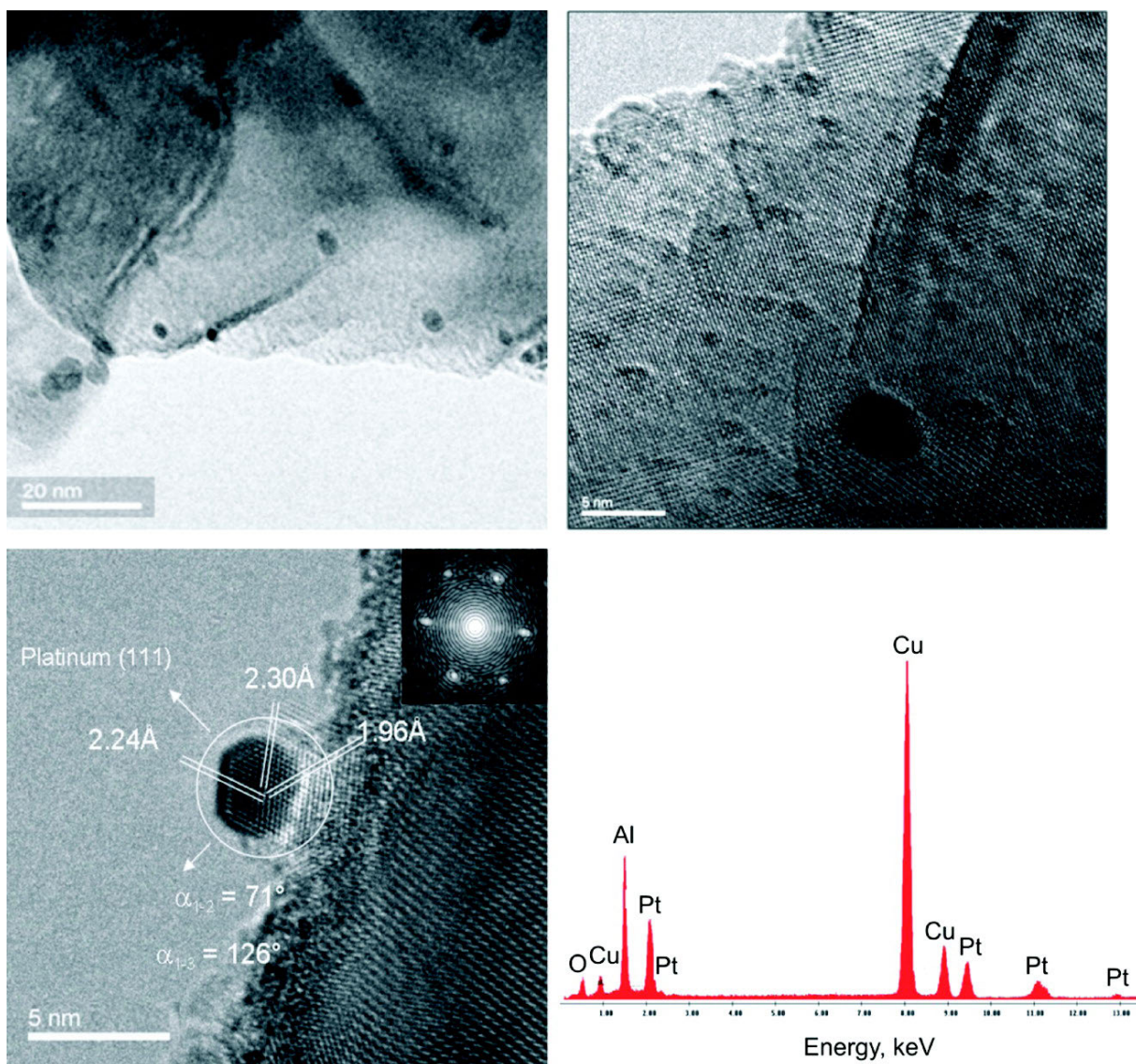


Figure 4.8: HRTEM micrographs and EDX spectrum (powder preparation) of the 0.6 % Pt/ α -Al₂O₃ foam catalyst prepared by the MACS method during 3 min. The copper peaks in the EDX spectrum stem from the TEM grid used.

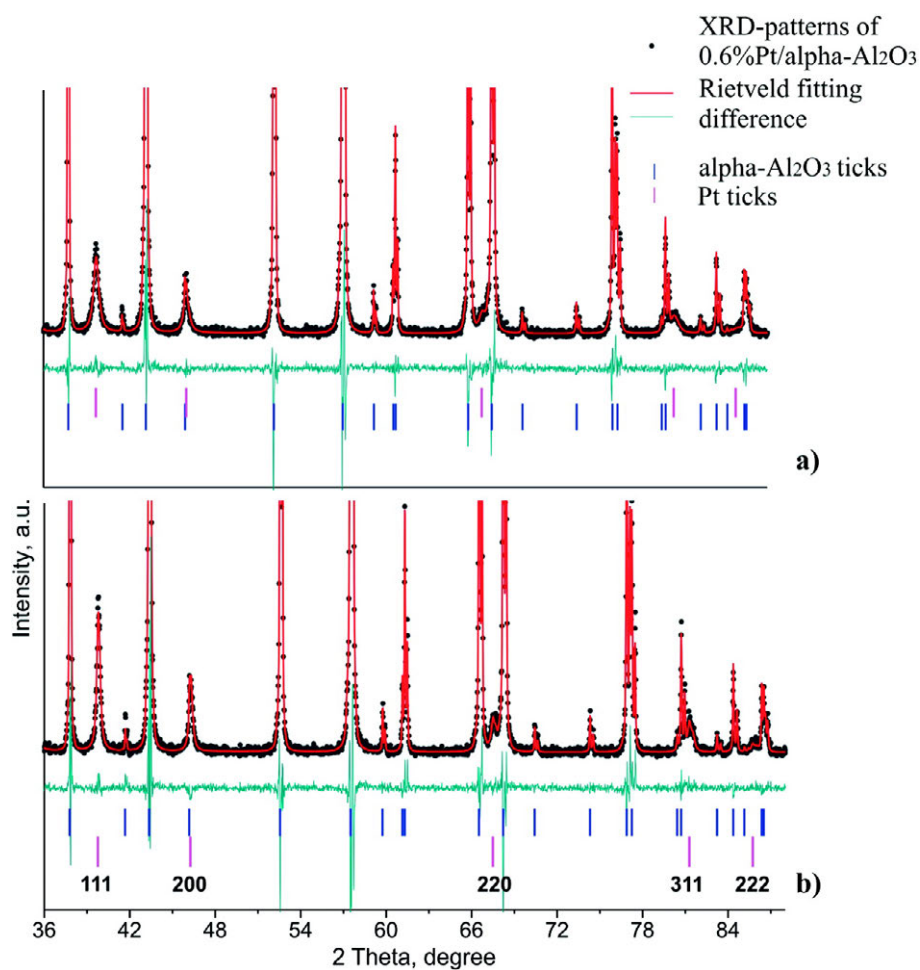


Figure 4.9: Comparison of XRD patterns with Rietveld fitting of 0.6 % Pt/ α -Al₂O₃ foam catalysts prepared by (a) the MACS method during 6 min and (b) wet impregnation from Pt(NH₃)₄(NO₃)₂ followed by drying, conventional calcination, and reduction at 600 °C [172].

support.

4.5 Conclusion

In summary, we have demonstrated that homogeneous, thermally stable, and strongly adherent nanocrystalline metal films on ceramic monoliths can be achieved by the microwave-assisted self-propagating combustion of glycerol-chelated metal precursors. This simple and energy-efficient technique does not require additional calcination or reduction steps and allows obtaining uniform catalyst deposition across the large monolith supports even at low metal loading. Therefore, we believe that this method is promising for producing large monolith catalysts for the automotive industry, selective catalytic reductions, or catalytic gas-phase oxidations.

Acknowledgement

We are gratefully acknowledging Gisela Weinberg, Wiebke Frandsen, and Norbert Pfaender for their assistance with SEM and TEM measurements. This work was supported by the German Research Foundation within the framework of the Emmy-Noether-Program and the German Federal Ministry of Education and Research within the framework of the Excellence Cluster "Unifying Concepts in Catalysis".

Supporting Information

Two movies recorded during the MACS preparation of the Pt-coated corundum foams with different Pt loadings. In the first case (file "jp905692g_si_001.avi", 11 MB) with 0.6 % Pt on a 45 ppi ceramic foam, the formation of a brownish gel-like film, carburized black coating, and then rapid self-propagating combustion resulting in the final product with characteristic metal reflection can be seen. In the second case (file "jp905692g_si_002.avi", 15 MB) with 2.0 % Pt on an 80 ppi ceramic foam support, more violent combustion as a glowing layer traveling through the monolith can be observed. This material is available free of charge via the Internet at <http://pubs.acs.org>.

Chapter 5

Reactor for In-Situ Measurements of Spatially Resolved Kinetic Data in Heterogeneous Catalysis¹

Abstract

The present work describes a reactor that allows in-situ measurements of spatially resolved kinetic data in heterogeneous catalysis. The reactor design allows measurements up to temperatures of 1300 °C and 45 bar pressure, i.e. conditions of industrial relevance. The reactor involves reactants flowing through a solid catalyst bed containing a sampling capillary with a side sampling orifice through which a small fraction of the reacting fluid (gas or liquid) is transferred into an analytical device (e.g. MS, GC, HPLC) for quantitative analysis. The sampling capillary can be moved with μm resolution in or against flow direction to measure species profiles through the catalyst bed. Rotation of the sampling capillary allows averaging over several scan lines. The position of the sampling orifice is such that the capillary channel through the catalyst bed remains always occupied by the capillary preventing flow disturbance and fluid bypassing. The second function of the sampling capillary is to provide a well which can accommodate temperature probes such as a thermocouple or a pyrometer fiber. If a thermocouple is inserted in the sampling capillary and aligned with the sampling orifice fluid temperature profiles can be measured. A pyrometer fiber can be used to measure the temperature profile of the solid catalyst bed. Spatial profile measurements are demonstrated for methane oxidation on Pt and methane oxidative coupling on Li/MgO, both catalysts supported on reticulated $\alpha\text{-Al}_2\text{O}_3$ foam supports.

5.1 Introduction

Reactor measurements are central to heterogeneous catalysis research and sophisticated reactor designs have been developed, e.g. for kinetic measurements [178] and high throughput screening [179]. However, apart from reactors which feature a number of discrete sampling points (typically less than ten), most reactor designs have in common that reaction products are analyzed in the reactor effluent stream be it gaseous or liquid. The reaction pathway, i.e. how the reactants are transformed into the products remains hidden and only a single kinetic data point is obtained for a set of reaction variables. Furthermore, heterogeneous catalysts are dynamic systems that adapt to the chemical potential of the surrounding fluid phase, which in turn is determined by the composition of the fluid phase, its temperature and pressure. Consequently, if a heterogeneous catalytic reaction is studied under temperature and pressure conditions conveniently manageable in a laboratory reactor it is always questionable whether the obtained data and any derived kinetic model can be extrapolated to industrially relevant conditions.

The reactor described in this work allows simultaneous measurements of spatially resolved species and temperature profiles at temperatures up to about 1300 °C and pressures up to 45 bar. If mass transport limitations can be excluded, differential reaction rates can be directly calculated from the species profiles and correlated to composition and temperature values at the respective point in the catalyst bed. If transport limitations are inevitably connected to the reaction conditions, numerical simulations can be used to validate microkinetic models by means of spatial species data [2]. Errors introduced by an incorrect heat balance can be avoided by using the measured temperature profile as input.

In contrast to early reactor designs by Horn et al. [5–7] for atmospheric pressure measurements, the novel

¹Adapted from R. Horn, O. Korup, M. Geske, U. Zavyalova, I. Oprea, R. Schlögl *Rev. Sci. Instrum.* 81 (6) (2010) 064102.

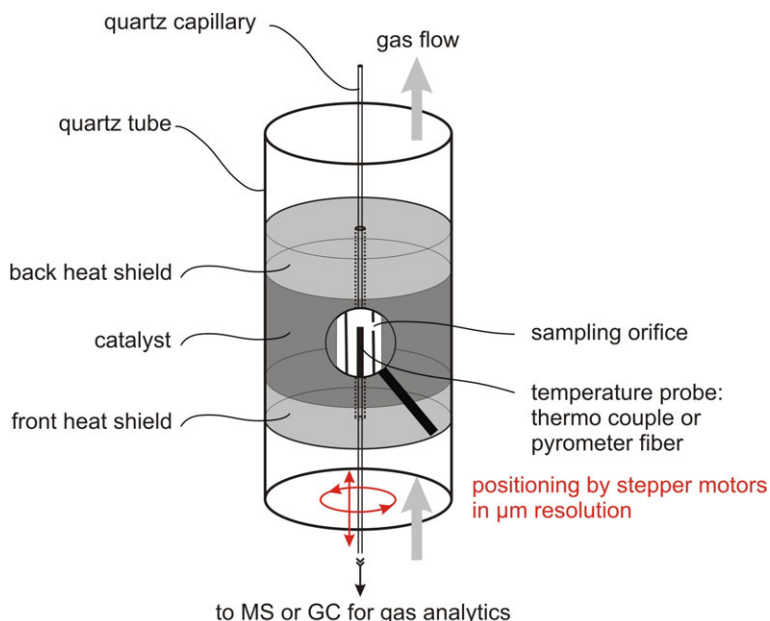


Figure 5.1: Principle of spatially resolved measurement of i) kinetic data, ii) gas temperature and iii) solid temperature.

reactor presented in this work can be safely operated up to 45 bar pressure and is much more flexible in terms of scan range and exchangeability of the catalyst bed. However, the measurement principle as depicted in Fig. 5.1 is the same as in the earlier works [5–7].

The catalytic reaction is conducted in a flow reactor containing the catalyst bed sandwiched between two inert packings to check in each experiment for activity of the support as well as pre- and post-catalytic chemistry. The inert packings also limit heat losses by radiation and are therefore called heat shields. As the gas flow is typically arranged from bottom to top, the stack sequence in flow direction is front heat shield, catalyst, back heat shield (cp. Fig. 5.1). Profiles of reactants, intermediates and products are measured by moving a thin sampling capillary with μm resolution through the centerline of the catalyst bed. Sampling occurs via a side sampling orifice drilled at such a distance from the closed capillary tip that no open channel results from moving the capillary up and down. The catalyst bed can be of various shape. Reticulated foams, sphere beds and catalyst coated channels have been measured successfully up to a total length of 120 mm. In addition to species sampling the capillary can accommodate a thermocouple to measure the gas temperature or a pyrometer fiber to measure the temperature of the catalyst. The application examples presented in this work stem from the field of high temperature gas phase oxidation catalysis. After a detailed description of the reactor design in Section 5.2, spatially resolved measurements for methane oxidation on Pt and Li/MgO coated reticulated foam supports are presented and briefly discussed.

5.2 Reactor Design

5.2.1 Reactor Body

An annotated three dimensional drawing of the reactor is shown in Fig. 5.2. The quartz reactor tube is 200 mm long, has an inner diameter of 18 mm and an outer diameter of 38 mm (wall thickness 10 mm). Both ends of the reactor tube containing the catalyst bed are conically shaped. For pressure sealing of the reactor tube, the cone faces are greased with laboratory silicone grease and form fit tightly into a lower and an upper water cooled copper clamp. The lower copper clamp is mounted to a stainless steel flange which in turn is mounted to a fixed aluminum baseplate. The upper copper clamp is mounted to a movable cover plate also made of aluminum. As high axial but no lateral force must be applied to the quartz tube, a precise vertical movement of the upper mounting clamp is required. This is accomplished by four linear bearings mounted between cover and base plate allowing for precise vertical movements of up to 110 mm. For exchange of the reactor tube, the upper cover plate can be lifted and lowered easily by means of a hydraulic jack. If the reactor is closed and pressurized, springs (not shown in Fig. 5.2) hinged on hooks between base and cover plate keep the quartz tube pressure sealed. The entire reactor stands on four legs with bases.

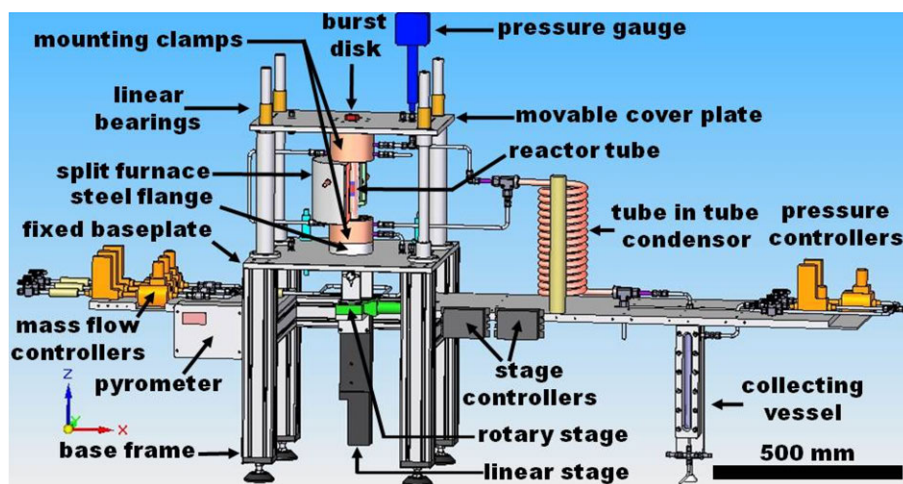


Figure 5.2: Annotated 3D reactor drawing.

5.2.2 Gas Flow Control, Pressure Control, Heater and Safety

The gas flow through the reactor setup is arranged from left to right and through the reactor tube from bottom to top. At the inlet side, three gas pipes are connected to mass flow controllers. In oxidation catalysis the feed gas is typically composed of an oxidant O_2 , N_2O , ..., a hydrocarbon (CH_4 , C_2H_6 , C_3H_8 , ...) and an inert standard (Ar , He , N_2 , ...). Therefore three gases can be mixed using this gas supply. The feed gas mixture enters the reactor tube from the bottom, flows through the catalyst bed and leaves at the top. After leaving at the top, the reactor effluent gases pass through a tube in tube heat exchanger to remove all condensable species which are collected in a reservoir. The reservoir can be emptied under operation without pressure loss by means of a needle valve. The dry reactor effluent passes through pressure controllers which expand it to atmospheric pressure. Three exit lines can be chosen, one for operation at atmospheric pressure, the second for operation at pressures between 1 bar and 7 bar and the third for pressures between 7 bar and 45 bar. For precise pressure measurement in the reactor, a digital pressure gauge is connected close to the reactor tube outlet.

To heat the catalyst, the quartz reactor tube is surrounded by a split furnace (450 W, maximum element temperature 1150 °C) connected to a power supply and a temperature controller. The heat transfer between heater and catalyst bed occurs primarily via radiation resulting in a maximum temperature of about 1000 °C inside the reactor tube without accounting for any heat of reaction. Taking into account that many catalytic oxidation reactions liberate significant amounts of heat, temperatures above 1000 °C can result. For methane oxidation on Pt, the reactor has been successfully operated at temperatures up to 1300 °C.

As reacting gas mixtures containing fuel and oxidant under pressure can explode, a number of safety measures have been taken in designing and operating the reactor. In the first place, feeding of potentially explosive mixtures to the reactor can be avoided by providing upper and lower limits to the mass flow controllers which are outside the flammability limits of the gas mixture. Secondly, the reactor is equipped with a 1/2 inch burst disk rated to a burst pressure of 45 bar being therefore the highest possible reactor pressure. In case of an explosion, the burst disk breaks and releases the pressure instantaneously. In addition to the burst disk, the reactor itself functions like a pressure relief valve, as number and strength of the springs between base and cover plate determine the leak pressure of the system. Depending on the application and the target pressure the spring load can be adjusted to a value slightly higher than the target pressure. To protect the operator in case of a bursting reactor tube, the ceramic split furnace surrounding the reactor tube is enclosed in a metal housing. Additionally, the entire reactor is shielded by a safety screen (not shown in Fig. 5.2).

5.2.3 Measurement of Gas Species Profiles

For measurement of high resolution gas species profiles a thin quartz capillary (OD = 700 μm , ID = 530 μm) runs through the center of the quartz tube and the catalyst bed. The latter can be of various shape. The sampling capillary possesses a small side sampling orifice with a diameter of about 50 μm located at such a distance from the upper, closed end of the capillary that no open channel is left behind if the sampling orifice is moved to the lowest sampling point in the catalyst bed. Keeping the channel filled by the capillary is mandatory to avoid gas bypassing. The lower open end of the sampling capillary is connected to a micro-volume stainless steel cross which in turn is connected to a stainless steel holder. The stainless steel holder is mounted to a rotary stage and the rotary stage is mounted to a linear stage. With this arrangement it is possible to move the sampling capillary with μm resolution up and down and to rotate it. Rotating

the capillary is important because some catalyst geometries (e.g. reticulated foams) can have irregular flow patterns and high quality spatial profile measurements will require averaging at different scan lines. To seal the capillary against the outside but still allow movement with minimum force, the capillary runs through a grease pit located between two stainless steel liners which have a slightly larger diameter than the capillary. When the capillary is inserted into these liners its outer surface picks up a thin grease layer. The annular gap between the capillary and the steel liners is narrow enough that even maximum reactor operation pressure (45 bar) is not sufficient to squeeze the high viscous grease through this annular gap. On the other hand, the grease allows slow movement of the capillary with minimum force as the pressure difference exerts only small forces.

Gas species sampling is accomplished by means of a transfer capillary connecting the micro-volume stainless steel cross with a mass spectrometer. The transfer capillary is evacuated by means of a membrane pump to allow for rapid gas transport and avoid blocking by condensation of condensable species (e.g. water). Typically a flow of around $5 \text{ cm}^3 \text{ min}^{-1}$ is sampled through the sampling orifice.

5.2.4 Measurement of Gas and Surface Temperature Profiles

To measure spatially resolved gas and surface temperature profiles, a thermocouple or a pyrometer fiber can be inserted in the sampling capillary respectively. If the fiber tip or the thermocouple tip are aligned with the orifice position, the measured temperature can be assigned to the respective species composition measured at a certain point in the catalyst bed. This lifts the requirement of isothermicity in kinetic measurements, as the differential reaction rate measured at a particular point in the catalyst bed can be assigned to the catalyst temperature at this point. If a thermocouple is used, thermal contact exists between the sampled gases and the thermocouple tip but not between the thermocouple tip and the catalyst bed. Therefore, the thermocouple measurement is strongly biased to the real gas temperature as was shown in Ref. [2]. If a pyrometer fiber is used, thermal radiation emitted from the catalyst surface can be collected and transformed into a surface temperature using a pyrometer. A two wavelength pyrometer should be used as the surface emissivity might change along the scan line.

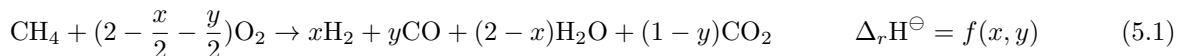
Different temperature profiles measured by thermocouple and pyrometer fiber indicate heat transport limitations which are in most cases also indicative for external mass transport limitations due to similar transport mechanisms. Heat and mass transport limitations do often occur in high temperature catalytic reactions as chemical reactions at the catalyst surface are very fast. For example, in methane catalytic partial oxidation on Rh coated foam catalysts, temperature gradients of several hundred degree centigrade have been measured at the entrance of the foam catalyst and both, experimental data [7] and numerical simulations [2] indicate strong oxygen transport limitation at the catalyst entrance.

5.3 Application Examples

5.3.1 Methane Oxidation on Pt Coated α -Al₂O₃ Foam Catalysts from 1.4 bar to 15 bar

The reactor described in Section 5.2 was used to study methane oxidation on autothermally operated Pt coated α -Al₂O₃ foam catalysts at pressures from 1.4 to 15 bar. The pressure was varied to investigate whether gas phase reactions proceed in parallel to catalytic reactions and whether transport limitations occur. For this application the catalyst bed was formed by two 10 mm long α -Al₂O₃ foam catalysts (45 pores per linear inch) coated by 0.6 wt% Pt using the microwave assisted combustion synthesis method [87] and sandwiched between two uncoated 10 mm long 45 ppi foams which served as heat shields. The 1 mm channels for the sampling capillary were drilled before coating with Pt. The feed gas mixture consisted of CH₄/O₂/Ar (911/228/858 ml min⁻¹ at STP). To assign a catalyst temperature to each gas species composition, the surface temperature was measured by means of a pyrometer fiber inserted in the capillary as described in Section 5.2.4. Spatial reactor profiles were measured for total pressures of 1.4 bar, 5.1 bar, 10 bar and 15 bar. All data are summarized in Fig. 5.3.

Even though a detailed discussion of the experimental results is beyond the scope of this paper which focusses on the description of the reactor, the profiles reveal immediately interesting details of the methane oxidation mechanism. It can be seen that there exists a short zone behind the catalyst entrance where CH₄ and O₂ are rapidly converted. The chemistry in this entrance zone which extends from 0 – 2400 μm can be described by Eq. 5.1 with x taking values between $0 \leq x \leq 2$ and y taking values between $0 \leq y \leq 1$.



Non-catalytic methane total oxidation occurs for pressures $p \geq 10$ bar as can be seen from Fig. 5.3 (10 and 15 bar measurements) where a slight conversion of O₂ is already observed in the front heat shield accompanied

by liberation of heat due to the high combustion enthalpy of methane ($\Delta_r H^\ominus = -803 \text{ kJ mol}^{-1}$). This explains why at 10 and 15 bar the temperature in the front heat shield is higher than in the catalyst section. Upon complete O_2 conversion, secondary reactions like steam reforming (Eq. 5.2) and watergas shift (Eq. 5.3) are taking place until the mixture leaves the catalyst (2400 – 20460 μm).



As shown in Fig. 5.4 the O_2 profiles fall on top of each other in the catalytic zone and are highly linear. As can be deduced from an O_2 mass balance, the strict linearity observed in the oxidation zone between 0 and 2000 μm is in disagreement with O_2 film transport limitation as this should lead to an exponentially decreasing O_2 flow rate in this section as outlined in Eq. 5.4.

$$\rho \cdot u \cdot \frac{dY_{\text{O}_2}^{\text{bulk}}}{dz} = \frac{S}{V} \cdot k_{\text{O}_2}^m \cdot \rho \cdot (Y_{\text{O}_2}^{\text{surface}} - Y_{\text{O}_2}^{\text{bulk}}) \Rightarrow F_{\text{O}_2}^z = F_{\text{O}_2}^0 \cdot \exp\left(-\frac{S}{V} \frac{k_{\text{O}_2}^m}{u} \cdot z\right) \quad (5.4)$$

In Eq. 5.4, ρ denotes the gas density in kg m^{-3} , u the linear gas velocity in m s^{-1} (which can be considered constant in this short section), $Y_{\text{O}_2}^{\text{bulk}}$ and $Y_{\text{O}_2}^{\text{surface}}$ the O_2 mass fraction in the bulk and at the Pt surface respectively ($Y_{\text{O}_2}^{\text{surface}} = 0$ in case of full transport limitation), S/V the catalyst surface to free gas volume ratio in m^{-1} , $k_{\text{O}_2}^m$ the O_2 film mass transport coefficient in m s^{-1} and $F_{\text{O}_2}^z$ the O_2 molar flow rate in mol min^{-1} at position z , the quantity that is actually measured in Fig. 5.4.

The observed strict linearity is rather in agreement with a constant O_2 consumption rate r in $\text{mol m}^{-2} \text{ s}^{-1}$ at the Pt surface as can be derived from the corresponding O_2 mass balance (Eq. 5.5):

$$\rho \cdot u \cdot \frac{dY_{\text{O}_2}}{dz} = -r \cdot \frac{S}{V} \cdot M_{\text{O}_2} \Rightarrow F_{\text{O}_2}^z = F_{\text{O}_2}^0 - r \cdot \frac{S}{V} \cdot \frac{F_{\text{total}}^0 \cdot \bar{M}^0}{\rho \cdot u} \cdot z \quad (5.5)$$

Eq. 5.5, in which M_{O_2} and \bar{M}^0 denote the molar mass of oxygen and the mean molar mass of the gas mixture at the position $z = 0$, is in qualitative agreement with the measured linear decrease in $F_{\text{O}_2}^z$ between 0 and 2000 μm independent of reactor pressure. The chemical interpretation of the observed zeroth order kinetics could be a blockage of most active Pt sites by one dominant surface species. In situ Raman measurements which will be discussed in a forthcoming paper indicate, that the Pt surface is under above mentioned reaction conditions nearly entirely covered by carbon deposits.

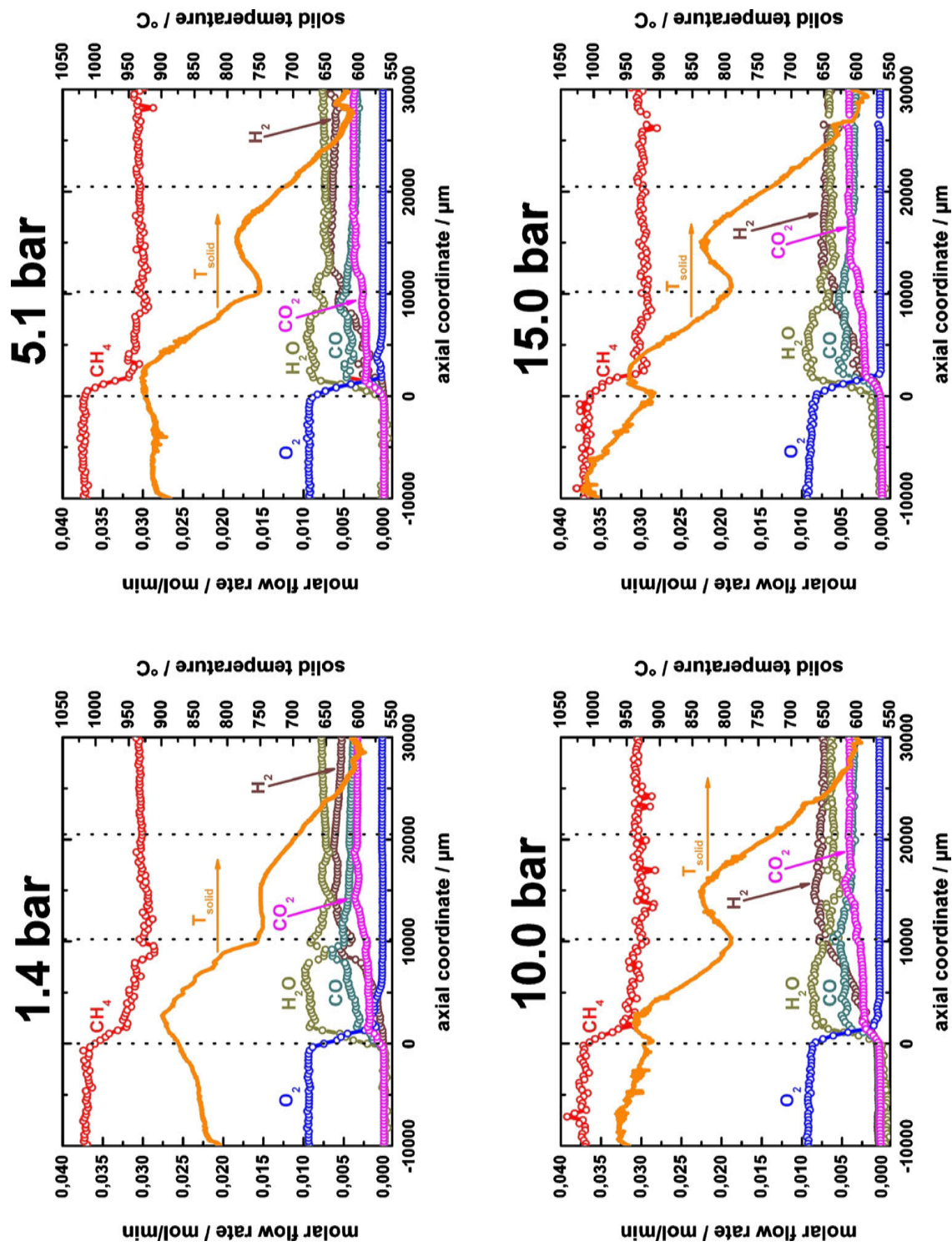


Figure 5.3: Spatial profile measurements for methane oxidation on 0.6 wt% Pt coated 45 ppi α -Al₂O₃ foam catalysts. Gas flow: 911 ml min⁻¹ CH₄, 228 ml min⁻¹ O₂, 858 ml min⁻¹ Ar. C/O = 2.0. Autothermal operation. Front heat shield -10000 μ m \rightarrow 0 μ m, catalyst section 0 μ m \rightarrow 10240 μ m (Pt foam 1) and 10240 μ m \rightarrow 20460 μ m (Pt foam 2), back heat shield 20460 μ m \rightarrow 30000 μ m.

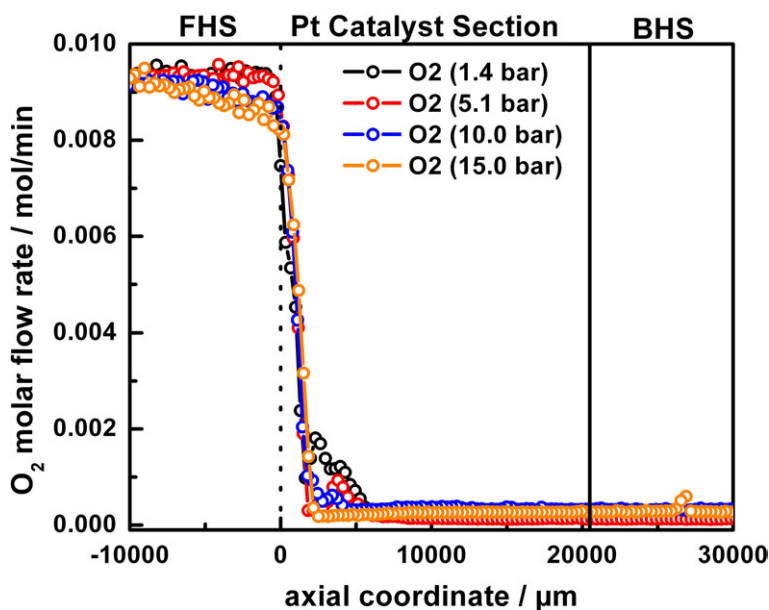


Figure 5.4: Oxygen profiles from Fig. 5.3 superimposed. Linearity and pressure independence indicate zeroth order kinetics in the oxidation zone.

5.3.2 Methane Oxidative Coupling on Li/MgO Coated α -Al₂O₃ Foam Catalysts at Atmospheric Pressure

The oxidative coupling of methane (OCM, Eq. 5.6) to C2 hydrocarbons (C₂H₆, C₂H₄ and C₂H₂) on Li doped MgO was chosen as second example to demonstrate how important mechanistic insight can be obtained from spatial reactor profile measurements.



The OCM reaction is debated in the literature in terms of a so called 'heterogeneous - homogeneous mechanism' meaning that the Li/MgO catalyst produces CH₃· radicals which desorb into the gas phase and couple there to CH₃-CH₃ which is further dehydrogenated to CH₂=CH₂ [180]. Methane oxidative coupling, even though highly attractive from an industrial point of view, is still at the research stage as one-pass yields higher than about 25 % could not yet been achieved. The reason for this virtual bound is still unclear.

Profile measurements were conducted in an analogous manner as described in Section 5.3.1 with the only differences that two 10 mm long 0.8 wt% Li/MgO coated 45 ppi α -Al₂O₃ foams served as catalyst section, much lower flow rates were used (CH₄/O₂/Ar = 25.6/6.4/8.0 ml min⁻¹ at STP) and that the reactor was heated to about 780 °C. Very low total flow rates had to be used as methane oxidation on Li/MgO is much slower than on Pt and external heating was necessary as the reaction, due to its low rate, does not produce sufficient heat for autothermal operation. The spatial profiles are depicted in Fig. 5.5. Again, the pyrometer fiber was used as temperature probe to measure the catalyst temperature.

The pyrometer temperature profile shows that the reactor is very isothermal in the catalytic section (788 ± 2 °C). The increase of the temperature curve towards the ends of both heat shields is a measurement artifact as radiation from the much hotter heating coils of the oven is reflected by the mounting clamps into the heat shields. Longer heat shields could eliminate this problem. The species profiles reveal a number of interesting details. It can be seen that methane is lost with constant rate by total oxidation to CO₂ and H₂O. This total oxidation occurs either in the gas phase as it is not restricted to the catalyst section or at the α -Al₂O₃ support. C2 coupling products (at 780 °C only C₂H₆ + C₂H₄) are not formed before the reactants enter the catalyst section indicating that pre-catalytic C2 formation does not occur. Even though only small amounts of C2 are formed the profile shows clearly that C2 species are formed with a constant rate and that the formation continues behind the catalyst section in the back heat shield. This could be due to loose catalyst material that has been transported by the gas flow to the back heat shield. However, as the gas flow is extremely slow and directed against gravity this explanation is not very likely. The post-catalytic C2 production could also indicate formation of C2 products in the gas phase triggered by the catalyst in line with a 'heterogeneous - homogeneous' mechanism. CO seems to be a secondary product as its formation starts quite late in the catalyst section. Virtually no hydrogen is formed at all.

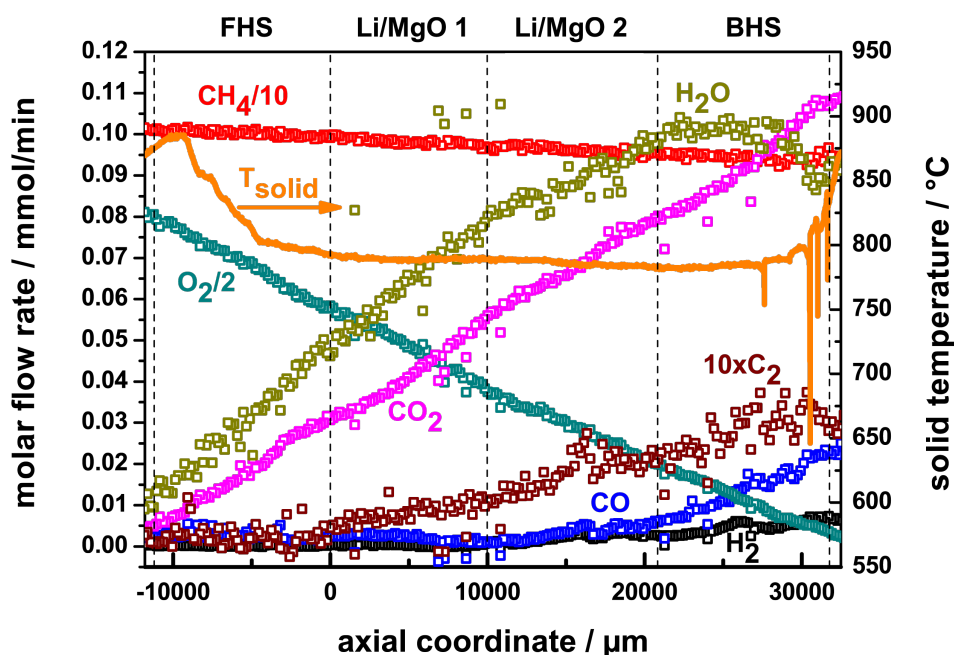


Figure 5.5: Spatial profile measurements for methane oxidative coupling on Li/MgO. Catalyst section formed by two 0.8 wt% Li/MgO coated α -Al₂O₃ foams. Gas flow CH₄/O₂/Ar = 25.6/6.4/8.0 ml min⁻¹. Reactor temperature by external heating 780 °C.

5.4 Summary and Conclusions

A novel reactor allowing simultaneous measurements of spatially resolved species and temperature profiles in heterogeneous catalytic reactions under industrially relevant conditions is presented. The principle of spatial profile measurements is based on a movable sampling capillary for species analysis which houses either a thermocouple for gas temperature measurements or a pyrometer fiber for catalyst temperature measurements. The maximum operation pressure and the maximum operation temperature of the reactor are 45 bar and 1300 °C respectively. For operation under pressure, the reactor tube is sealed by form fitting into mounting clamps which are pressed together using a variable number of springs. The spring load can be adjusted to match the target pressure allowing the reactor to open and release pressure if the target pressure is exceeded. In case of an explosion, a rupture disk ensures instantaneous pressure release. Application examples are given for high temperature methane oxidation on Pt coated foam catalysts and methane oxidative coupling on Li/MgO coated foam catalysts. Reaction pathways and kinetic implications are briefly discussed.

Acknowledgement

The authors thank the German Research Foundation for funding the Emmy-Noether-Junior-Research-Group 'High Temperature Catalysis'. Further support was provided by the German Federal Ministry of Education and Research within the framework of the Excellence Cluster 'Unifying Concepts in Catalysis'.

Chapter 6

Catalytic Partial Oxidation of Methane on Autothermally Operated Pt Catalysts: Reaction Pathways, Zoning Effects, and Impact of Mass and Heat Transport¹

6.1 Introduction

Heterogeneously catalyzed gas phase oxidation reactions are often characterized by reaction temperatures of several hundred degrees centigrade. In particular for the oxidation of small alkanes, high temperatures are common either to activate the alkane or as a result from rapid heat production after reaction light-off. An example is the catalytic partial oxidation (CPO) of methane to synthesis gas on platinum at temperatures above 800 °C. Characteristic for high temperature oxidation catalysis is the strong influence of mass and heat transport as well as gas phase reactions above the catalyst surface. Because the number of intermolecular collisions increases with pressure, gas phase chemistry becomes generally more important at elevated pressures. Consequently, product yields and selectivities in high temperature oxidation catalysis are often the result of a complex network of reactions at the catalyst surface and in the surrounding gas phase which are coupled in a non-linear way by heat transport, mass transport and exchange of reactive intermediates [181]. In a conventional catalytic reactor measurement inlet and outlet streams to and from the reactor are analyzed respectively. The reactor itself is usually treated as a black box and the pathways via which reactants are transformed into products remain hidden. Spatially resolved species, gas and surface temperature profiles measured through a catalyst bed under in-situ high temperature/high pressure conditions reveal details about the reaction pathways, e.g. zoning in the catalyst bed, the impact of transport limitations and the influence of gas phase chemistry, especially at elevated pressure.

6.2 Experimental

Three different catalyst systems have been investigated using methane rich syngas relevant reactant mixtures. (A) Platinum nanoparticles supported on reticulated α -alumina foams, (B) platinum nanoparticles supported on α - or γ -alumina spheres, and (C) a polycrystalline platinum tube. The supported catalysts are prepared by using a microwave assisted combustion synthesis [87] or classically by wet impregnation with aqueous chloroplatinic acid followed by reduction in hydrogen. The platinum tube of 100 mm length, ID = 4.4 mm, OD = 5 mm, and a purity of 99.95 % was delivered by ÖGUSSA, Vienna, Austria. Spatial profiles of species and temperatures were measured in a reactor setup based on a capillary sampling method developed earlier by one of the authors [5]. Fig. 6.1 illustrates the principle of the measurement. Briefly, species profiles are measured by sliding a thin quartz capillary (700 μm) with a side sampling orifice (50 μm) centerline through the catalyst bed, e.g. Pt nanoparticles on alumina spheres or foams. The active catalyst is placed between two heat shields, which minimize heat losses by radiation. The platinum tube was fit in special endcaps to assure, that gas flows only inside the tube. Gases sampled through the orifice are quantified by mass

¹Adapted from O. Korup, M. Geske, S. Mavlyankariev, R. Schlögl, R. Horn *Prepr. Pap. - Am. Chem. Soc., Div. Fuel Chem.* 55 (2) (2010) 149-150.

spectrometry. Temperature profiles are measured by inserting either a thermocouple or a pyrometer fiber into the gas sampling capillary so that the tip of the temperature sensor is aligned with the gas sampling orifice. The profiles measured with pyrometer and thermocouple reflect surface or gas phase temperatures respectively. A linear stepper motors is attached to the capillary-temperature probe assembly so that it can be moved with μm resolution up and down along a scan line through the stack. A second stepper motor allows rotating the probe to average over several scan lines, smoothing irregularities in the bed structure.

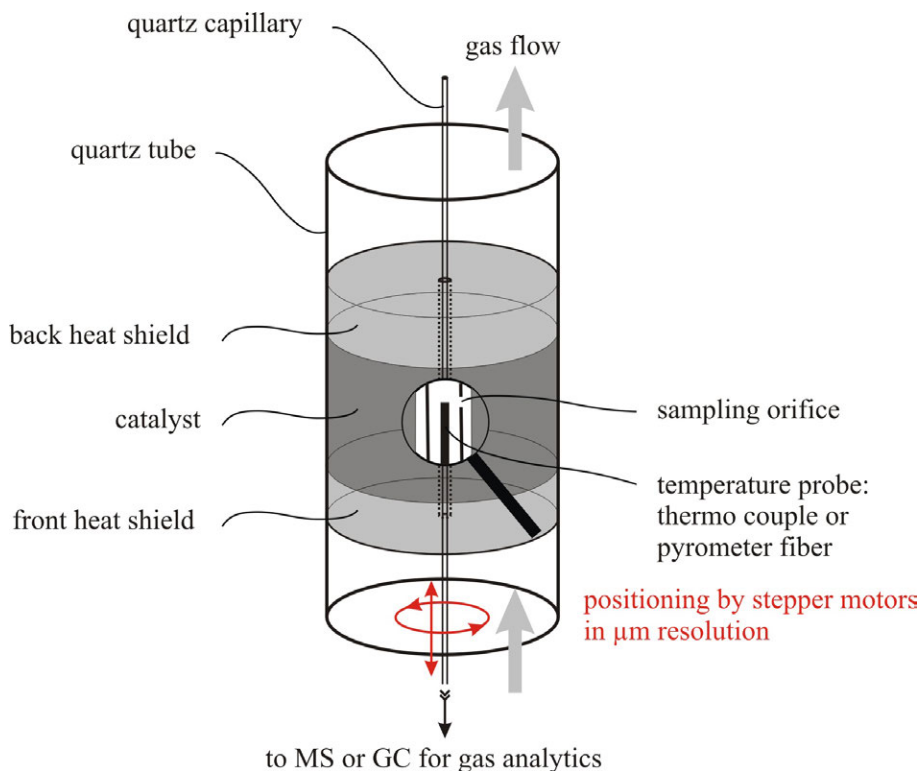


Figure 6.1: Schematic of spatial profile measurements.

6.3 Results and Discussion

In Fig. 6.2 displays a reactant/product and surface temperature profile through sphere bed, 30 mm long and 18 mm in diameter. The γ -alumina spheres of 2.5 mm diameter were loaded with 1 wt% Pt and had a BET surface area of $199 \text{ m}^2 \text{ g}^{-1}$. This profile was measured autothermal at atmospheric pressure and a gas feed of $\text{CH}_4/\text{O}_2/\text{Ar} = 2010/628/2362 \text{ ml min}^{-1}$, respectively a total flow of 5000 ml min^{-1} and $\text{C/O} = 1.6$. The profiles show no reactant conversion prior the catalyst section between -5000 and $0 \mu\text{m}$ axial position documenting the inert nature of the catalyst support. At the catalyst entrance an oxidation zone between 0 and $8000 \mu\text{m}$ axial position is found, where O_2 and CH_4 are rapidly consumed until O_2 is fully converted. The predominant oxidation products are CO_2 and H_2O . CO is formed only in small amounts in the oxidation zone. In the oxidation zone reactant conversion and product formation occur with constant rate indicating zeroth order kinetics possibly due to blockage of nearly all available catalytic sites. In-situ Raman experiments on a polycrystalline platinum foil indicate, that the foils surface has regions free of any detectable species and other regions with large amounts of defective carbon on top. These regions are separated sharply at the grain boundaries of the differently orientated crystallites of the platinum foil. After O_2 is completely consumed, methane conversion diminishes and H_2O and CO_2 become co-reactants. In this second zone steam reforming and CO_2 reforming occur. H_2 and CO are the only products formed in the steam reforming zone. The slopes of H_2 and CO in the reforming zone clearly reflect the H_2/CO molar ratio of 3/1. The temperature profile shown in Figure 2 reflects the heat production by the strongly exothermic oxidation reactions in the oxidation zone. Here the surface temperature is highest. Heat conduction to the front heat shield leads to a flat plateau. Adjacent, in the reforming zone the surface temperature decreases by heat consumption, because of the strongly endothermic reforming reactions. The selectivity to synthesis gas is high. In Fig. 6.3 an example of a high pressure test is shown. The examined catalyst was a stack of two 10 mm long, $\text{OD} = 16.5 \mu\text{m}$, α -alumina foams coated with 0.6 wt% Pt. The foams had 80 pores per linear

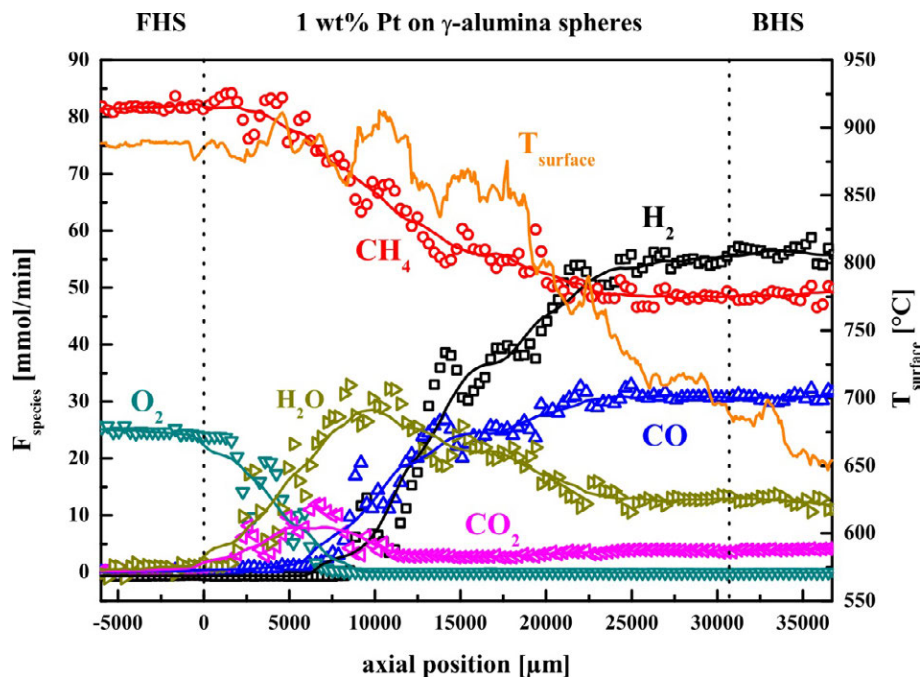


Figure 6.2: Surface temperature and species profiles through a catalyst bed of 1 wt% Pt-coated γ -alumina spheres (sphere diameter: 2.5 mm; gas feed: $\text{CH}_4/\text{O}_2/\text{Ar} = 2010/628/2362 \text{ mln min}^{-1}$; $\text{C}/\text{O} = 1.6$; reactor pressure of 1 bar).

inch, a mean pore diameter of $175 - 225 \mu\text{m}$, and a low BET surface area of $0.7 \text{ m}^2 \text{ g}^{-1}$. The profile was measured autothermal at 15 bar reactor pressure and a gas feed of $\text{CH}_4/\text{O}_2/\text{Ar} = 600/300/100 \text{ mln min}^{-1}$, respectively a total flow of $1000 \text{ mln min}^{-1}$ and $\text{C}/\text{O} = 2.0$. Again a distinct zoning can be observed, including oxidation (0 to $2250 \mu\text{m}$ axial coordinate) and adjacent reforming zone. In a series of experiments with different pressures at constant gas feed (not shown here) the influence of pressure (1-15 bar) on surface chemistry was apart from an increasing H_2 production rate with pressure (residence time effect) negligible. Pre-catalytic gas phase combustion of $\text{CH}_4 + \text{O}_2$ and formation of H_2O , CO , and CO_2 started to contribute (-10000 to $0 \mu\text{m}$ axial position) at 15 bar reactor pressure but the effect was still minor. Fig. 6.4 shows a profile measured through a platinum tube which can be considered a catalytic wall reactor. The profile was measured autothermally at atmospheric pressure and a gas feed of $\text{CH}_4/\text{O}_2/\text{Ar} = 600/300/100 \text{ mln min}^{-1}$, respectively equal to $1000 \text{ mln min}^{-1}$ total flow and a $\text{C}/\text{O} = 2.0$. The profile differs significantly from the two supported catalysts. The tube shows just one long reaction zone, which produces all observed products in parallel. The zeroth order kinetic in this oxidation zone can just be observed for the first $750 \mu\text{m}$ from the catalyst entrance and is subsequently overlapped with an exponential decay due to diffusive mass transport limitation. Steam reforming reactions are absent on the polycrystalline platinum tube. The selectivity to synthesis gas on the tube wall is low.

6.4 Conclusions

The results presented in this contribution show that spatially resolved reactor profiles are a powerful tool to get in-situ insight in mechanistic details in catalytic partial oxidation of methane on Pt. The method provides profiles of gas species, gas temperature and surface temperature which can be analyzed in terms of reaction pathways, mass and heat transport limitation. The latter could be shown in profile measurements through a polycrystalline platinum tube, which shows one reaction zone with strong mass transport limitation and low syngas selectivity. The Pt nanoparticle coated sphere bed shows high syngas selectivities illustrating the particle size dependence of CPO on Pt. Generally the reaction is divided in two zones. First a zeroth order methane combustion and heat production followed by a consecutive endothermic steam reforming with H_2 and CO formation. Increasing the pressure up to 15 bar at constant inlet mass flow rate has only a minor effect on the surface reactions, but pre-catalytic gas phase combustion becomes noticeable.

²The BET surface was recently determined by Kr-BET and the surface area given in this paper needs to be corrected. The investigated corundum foam monoliths with 45 ppi exhibit a surface area of $S_{\text{BETKr}} = 0.09 \text{ m}^2 \text{ g}^{-1}$. Monoliths with 80 ppi exhibit a BET surface area of $S_{\text{BETKr}} = 0.16 \text{ m}^2 \text{ g}^{-1}$. The influence of coating the monoliths with 1 wt% Pt had no significant effect on the determined surface area.

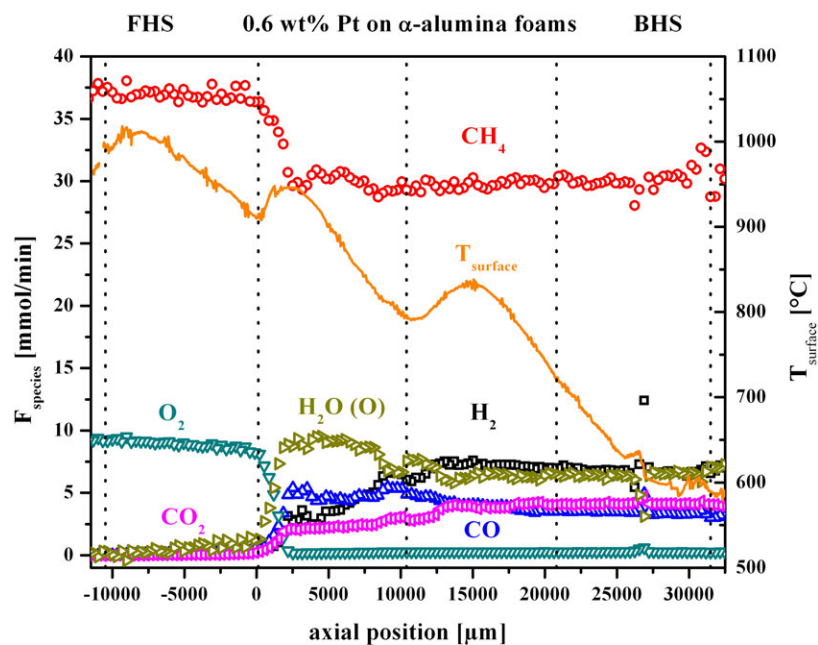


Figure 6.3: Surface temperature and species profiles through a catalyst stack of two 0.6 wt% Pt-coated α -alumina foams (80 ppi, each 10 mm length, OD = 16.5 mm diameter; gas feed: $\text{CH}_4/\text{O}_2/\text{Ar} = 911/228/858 \text{ mln min}^{-1}$; C/O = 2.0; reactor pressure of 15 bar).

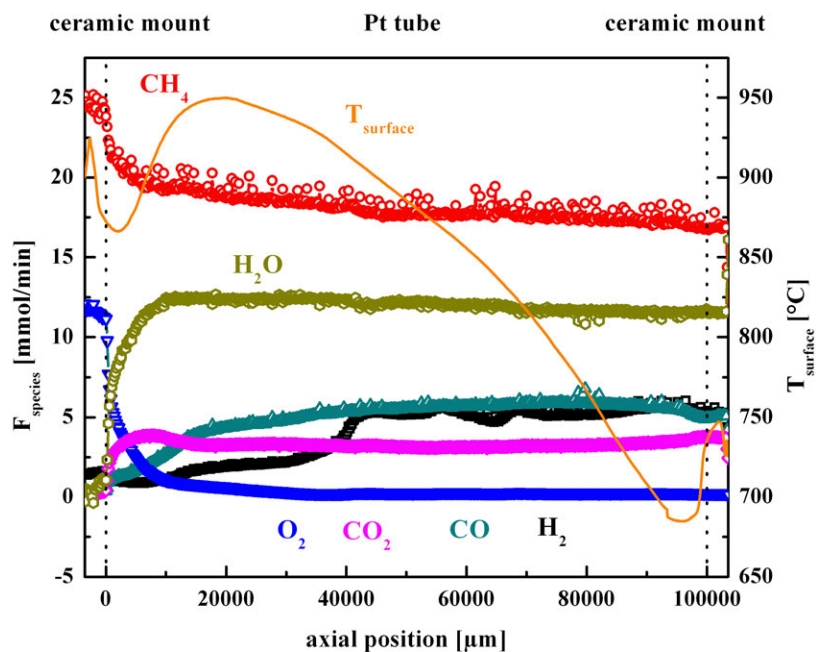


Figure 6.4: Surface temperature and species profiles through a polycrystalline Pt tube of 100 mm length, ID = 4.4 mm, OD = 5 mm (gas feed: $\text{CH}_4/\text{O}_2/\text{Ar} = 600/300/100 \text{ mln min}^{-1}$; C/O = 2.0; reactor pressure of 1 bar).

Acknowledgement

All authors thank the German Research Foundation for funding the Emmy-Noether-Junior-Research-Group 'High Temperature Catalysis'. Further support was provided by the German Federal Ministry of Education and Research within the framework of the Excellence Cluster 'Unifying Concepts in Catalysis'.

Chapter 7

Measurement and Analysis of Spatial Reactor Profiles in High Temperature Catalysis Research¹

Abstract

Spatial reactor profile measurements are a novel tool in chemical reaction engineering research. In this technique species concentrations or molar flow rates, phase temperatures and spectroscopic information are measured as function of the axial coordinate in a continuous flow tubular reactor. The obtained spatial gradients can be analyzed in terms of kinetic and mechanistic information about the reaction under study. The advantage of the spatial profile technique is that transient data are obtained at steady state and that it can be applied at temperature and pressure conditions relevant for industrial application. After a detailed description of the method various application examples are discussed such as methane catalytic partial oxidation on rhodium and platinum coated foam catalysts, methane oxidative coupling in the gas phase and oxidative dehydrogenation of ethane to ethylene on a supported molybdenum oxide catalyst. It is demonstrated how information about film transport limitation and reaction pathways can be extracted. The importance of spatial reactor profiles for validation of microkinetic models is highlighted for gas phase methane oxidative coupling at elevated pressure. Finally the idea of spatially resolved Raman spectroscopy using an optical fiber sensor is demonstrated and key parameters such as spatial resolution and position accuracy are determined.

Keywords

Reactor profiles, Methane, Ethane, Platinum, Rhodium, Molybdenum oxide, Partial oxidation, Transport limitation, Oxidative coupling, Oxidative dehydrogenation, Raman spectroscopy, Kinetic modeling

7.1 Introduction

Laboratory reactor measurements are central to research in chemical reaction engineering, answering questions such as:

1. What reaction conditions must be chosen to achieve a certain reactant conversion?
2. If consecutive or parallel reactions occur, what is the maximum yield of the target product?
3. Under which conditions is the reaction influenced by pore and/or film transport limitations?
4. Which kinetics does the reaction follow? What are the kinetic parameters?
5. What is the reaction mechanism?

Among the various reactor types used in the lab, continuous flow tubular reactors are particularly flexible. They can be designed and operated to study homogeneous gas phase reactions, homogeneous liquid phase

¹Adapted from O. Korup, S. Mavlyankariev, M. Geske, C. F. Goldsmith, R. Horn *Chem. Eng. Process.* 50 (10) (2011) 998-1009.

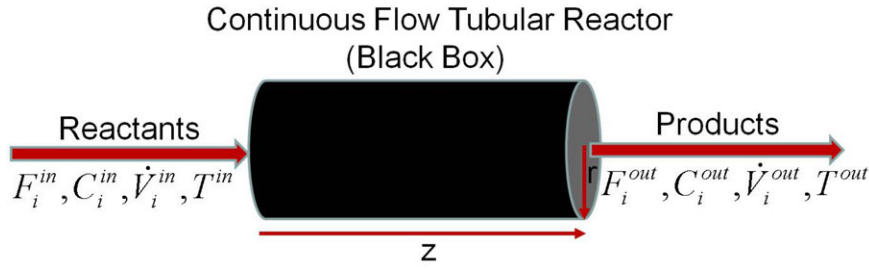


Figure 7.1: Conventional 'in-out' measurements in a continuous flow tubular reactor.

reactions, heterogeneously catalyzed reactions of gases and liquids or even three-phase reactions in a trickle bed.

Fig. 7.1 shows a schematic of conventional laboratory measurements in a continuous tubular flow reactor. Precisely measured reactant streams are well mixed and fed to the reactor ($F_i^{\text{in}}, C_i^{\text{in}}, \dot{V}^{\text{in}} = \sum \dot{V}_i^{\text{in}}$) in which all chemical transformations occur followed by product analysis of the effluent stream ($F_i^{\text{out}}, C_i^{\text{out}}, \dot{V}^{\text{out}} = \sum \dot{V}_i^{\text{out}}$) using one or several analytical methods. Typically isothermicity is assumed ($T \neq f(z), T_{\text{in}} = T_{\text{out}}$). Integral quantities such as species consumption and production rates \tilde{R}_i , reaction rates \tilde{r}_j , reactant conversions \tilde{X}_i , product selectivities \tilde{S}_i and yields \tilde{Y}_i can then be calculated from the difference between inlet and outlet values as shown exemplarily for a heterogeneous catalytic reaction in Eqs. 7.1-7.5 (A_{cat} = catalyst surface area).

$$\tilde{R}_i = \frac{\dot{V}^{\text{out}} C_i^{\text{out}} - \dot{V}^{\text{in}} C_i^{\text{in}}}{A_{\text{cat}}} = \frac{F_i^{\text{out}} - F_i^{\text{in}}}{A_{\text{cat}}} \quad (7.1)$$

$$\tilde{R}_i = \sum_j \nu_{ij} \tilde{r}_j \quad (7.2)$$

$$\tilde{X}_i = \frac{F_i^{\text{in}} - F_i^{\text{out}}}{F_i^{\text{in}}} \quad (7.3)$$

$$\tilde{S}_{k,i} = \frac{F_k^{\text{in}} - F_k^{\text{out}}}{F_i^{\text{in}} - F_i^{\text{out}}} \nu_i \quad (7.4)$$

$$\tilde{Y}_{k,i} = \tilde{X}_i \cdot \tilde{S}_{k,i} \quad (7.5)$$

However, the reactor itself is treated as black box in this conventional approach. No information can be extracted at steady state from the 'in-out' quantities calculated by Eqs. 7.1-7.5 in terms of how reactants are transformed into products, whether parallel or consecutive reaction channels exist, which reaction intermediates occur, what the state of the catalyst is along the varying chemical potential in flow direction and what temperature profile the different phases inside the reactor have. Transient experiments such as SSITKA [182] or TAP [183,184] can address some of these questions, however they are either rather costly due to use of isotopes as in SSITKA or require reactor operation (vacuum) far from industrially relevant conditions. Unrealistic reactor conditions are particularly critical as catalysts are known to be dynamic systems adapting to the reaction atmosphere inside the reactor with the consequence that the studied kinetics might not be representative for an industrial reactor.

In a flow reactor, transient processes are translated into spatial gradients in axial and radial direction. If radial gradients are minimized experimentally axial gradients can be measured and can provide kinetic and mechanistic information that is conveniently obtained at steady state without requiring expensive isotopes. Another advantage is that reactor profiles can be measured under virtually any temperature and pressure of relevance. With respect to Fig. 7.1, measurement of spatial reactor profiles implies the measurement of all reactor variables as a function of position, such as the concentrations or molar flow rates of fluid species ($C_i(z), F_i(z)$), the temperature of the fluid be it gaseous or liquid ($T_g(z), T_l(z)$), the catalyst (solid) temperature ($T_s(z)$), and if possible spatially resolved spectroscopic information ($I(\lambda, z)$) characterizing the bulk and surface state of the catalyst.

In some laboratories, flow reactors have been built with a few discrete fluid sampling and temperature measurement points, so that species and temperature profiles inside the reactor can be obtained at those positions. However, in this approach typically fewer than 10 positions are sampled, and the gradients between the sampling points are often insufficiently resolved [185].

Species profiles with significantly higher resolution are obtained by continuous translation of one or more thin sampling capillaries along the flow direction of a reactor, thereby continuously transferring species into an analytical device. This method was developed independently by Partridge et al. at Oak Ridge National Lab USA [77,79], Bosco and Vogel at the Paul Scherrer Institute in Switzerland [80] and Horn and Degenstein

at the University of Minnesota USA in the group of Schmidt [6]. Since their development all three reactor designs have been further developed with different foci and applied to various scientific problems. The spatially resolved capillary-inlet mass spectrometry system (SpaciMS) developed at Oak Ridge National Lab was designed to measure spatially resolved maps of species and temperatures in straight channel monoliths which are used for example in emission control catalysts for stationary and mobile applications [79]. Besides providing spatial resolution the SpaciMS was also optimized to provide superior temporal resolution for the study of transient processes which are regularly encountered in such catalysts during start up, shut down or load changes of the combustion engine. The SpaciMS design has been developed into a commercial product and is now distributed by Hiden Analytical UK. A comprehensive review of the development of the SpaciMS system and its various applications has been recently published [79].

Also the optically accessible channel reactor developed at the Paul Scherrer Institute has found further application for example for a spatially resolved kinetic study of CO methanation [186]. In a recent study by Schuurman et al. [187] a design quite similar to that developed at the Paul Scherrer Institute was used for spatially resolved DRIFTS in CO oxidation over Pt catalysts, even though the capillary sampling technique was not yet used in this work.

In the present paper the further development and application of the spatial profile technique by Horn et al. will be outlined. In contrast to the designs developed at Oak Ridge National Lab and at the Paul Scherrer Institute which use an open end capillary the design by Horn et al. uses a closed capillary with a side sampling orifice such that the capillary channel remains always filled during sampling avoiding flow disturbance and bypassing induced by an open end capillary. A closed capillary design with side sampling orifice is not restricted to open channels and allows sampling along the centerline of packed beds taking advantage of the axial symmetry there. This opens up a wide application area in heterogeneous catalysis research and also offers the possibility for spatially resolved fiber spectroscopy in packed beds. A third-generation spatial-profile reactor has been developed in the High Temperature Catalysis Group at the Fritz Haber Institute of the Max Planck Society in Berlin, Germany [82]. The latest developments described in this paper concern spatial profile measurements at high reactor pressures, spatial profile measurements in packed beds, and spatially resolved laser spectroscopy using fiber probes. Current research topics – such as methane partial oxidation on Pt catalysts, gas phase methane oxidative coupling, and ethane oxidative dehydrogenation to ethylene on molybdenum catalysts – will serve as examples.

7.2 Measurement of Species, Fluid and Solid Temperature Profiles, and the Principle of Spatially Resolved Fiber Spectroscopy

The principle of spatial reactor profile measurements is shown in Fig. 7.2. In reference to Fig. 7.2, it will be outlined below how species, temperature and spectroscopic profiles are obtained. For details of the latest profile reactor operated at the Fritz Haber Institute in Berlin, the reader is referred to [82].

7.2.1 Species Profiles

For species in a flow reactor, sub-mm profiles can be obtained by continuous movement of a thin sampling capillary along the flow direction of the reactor, which continuously withdraws small samples into an analytical device such as a mass spectrometer or a gas chromatograph. Even though all published work so far is in the field of heterogeneous gas phase catalysis, application to liquid phase reactions should be straightforward using an HPLC for species analysis. In the first spatial profile reactor developed by Horn et al. [6], a thin fused silica capillary (OD = 0.65 mm) open at one end was used, as silica can be considered rather inert in terms of chemical surface reactivity. Even though open-end capillaries are still in use in the SpaciMS approach of Partridge et al. [79] and in the channel reactor described by Bosco and Vogel [80], Horn and Degenstein abandoned this solution in later experiments, because turbulence and backmixing that were introduced at the open end of the capillary lead to distorted profiles, as seen in [6, 80], which falsely suggested that reactant conversion and product formation began prior to contact with the catalyst. Furthermore, if irregular catalyst beds such as sphere beds or reticulated foams are investigated, an open capillary would break upon pushing back. Therefore, current measurements employ sealed capillaries with a side-sampling orifice that is located at such a distance from the closed tip that the capillary channel remains filled at any sampling position (Fig. 7.2), thereby substantially improving the quality of the profiles [7, 82]. In terms of the orifice diameter a compromise must be made between spatial resolution, sampling flow rate withdrawn from the reactor, and transfer time to the analytical device. Whereas the first orifices were scored by hand and had diameters of several hundred microns [5–7], laser drilled orifices of 10–50 μm are currently in use (Fig. 7.3) giving a resolution of roughly 200 – 1000 sampling points per centimeter reactor length. For profile measurements the sampling capillary is moved continuously in or against flow direction using a stepper motor. Scan rates are chosen according to the gradients to be resolved. Typical values range from 1 $\mu\text{m s}^{-1}$ to

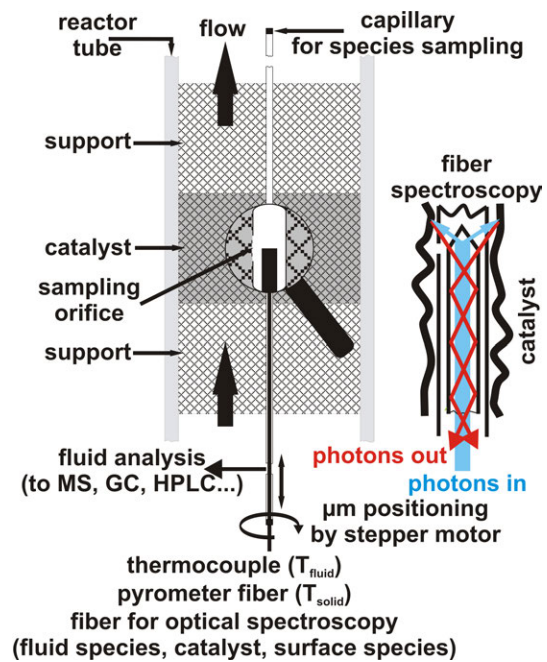


Figure 7.2: Principle of species, temperature and spectroscopic profile measurements in a continuous flow tubular reactor.

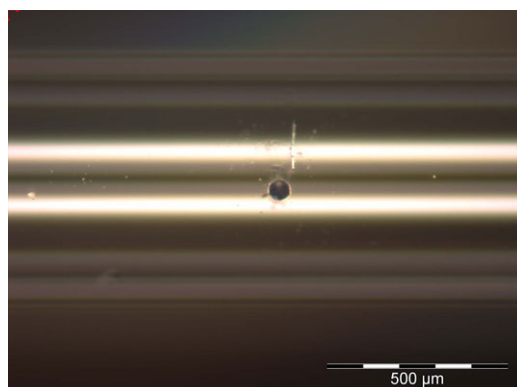


Figure 7.3: Laser drilled side sampling orifice in 700 μm fused silica capillary.

$100 \mu\text{m s}^{-1}$. Profile measurements in packed beds require rotating the capillary back and forth as it would otherwise break upon axial movement due to shearing by the particles. Rotation is accomplished by a rotary stage fitted to the translation stage [82].

7.2.2 High Pressure Measurements

The advantage of measuring spatial reactor profiles is that this technique can be applied to high-temperature, high-pressure conditions as frequently encountered in industry. High-pressure measurements require moving the fragile capillary with minimum force while simultaneously maintaining the reactor gas tight. In the SpaciMS design by Partridge et al. [79] flexible bellows are used to allow movement of the capillary. However, at elevated pressure the forces on these bellows become enormous, limiting this design to atmospheric or subatmospheric pressures. Bosco and Vogel used a high-temperature septum port for their capillary movement, allowing for up to 4 bar reactor pressure [80]. An alternative solution suitable for even higher reactor pressures was developed by Horn et al. [7]. Here the capillary is guided through two closely fitting liners and a grease pit in between them. Upon insertion the capillary picks up some grease, which provides both smooth movement through the liners and pressure sealing at the same time. With the first reactor employing this design, profile measurements up to 11 bar reactor pressure were demonstrated [10]. The current reactor operated at the Fritz Haber Institute employs a grease seal of the capillary port [82], and spatial profiles up to 40 bar pressure can be measured.

7.2.3 Temperature Profiles

Reactor temperature profiles are obtained by inserting a temperature sensor into the sampling capillary so that its tip is aligned with the sampling orifice (Fig. 7.2). For catalytic applications accurate measurement of the catalyst temperature is crucial. This measurement is accomplished by inserting a beveled fused silica fiber in the sampling capillary (Fig. 7.2, low OH silica for transmittance in NIR range) which collects thermal radiation from the solid catalyst and guides it to a pyrometer for temperature measurement. Because the emissivity of the solid material might change along the scan line, a two color pyrometer must be used.

If a thermocouple is inserted in the sampling capillary, its tip is in direct contact with the sampled gases but not with the solid catalyst. For this reason thermocouple profiles are strongly biased towards the gas temperature, as shown by numerical simulations of methane oxidation in Rh coated foam-catalysts using a 1D model that included mass and heat transfer resistances between the bulk gas phase and the solid catalyst [2]. In case of heat transfer resistance, surface and gas phase temperature profiles will deviate substantially [2,3].

7.2.4 Spatially Resolved Spectroscopy

As reviewed by Urakawa and Baiker [188], the measurement of spatially resolved spectroscopic data in catalytic reactors has recently gained a lot of attention, as catalysts are dynamic systems that continuously adapt to the local chemical potential in the reactor. Measuring spectroscopic profiles along the centerline of a catalytic flow reactor would be particularly informative, as no thermal gradients are induced by radiation losses which can be the case in many commercial or self-designed spectroscopic cells equipped with a window for optical access. Since an optical fiber can be used to guide light from the catalyst to a pyrometer for measurement of spatial temperature profiles, it is obvious that optical fibers could be used for spatially resolved spectroscopy inside the profile reactor. Even though the authors are currently focussing on Raman spectroscopy, other optical techniques such UV/vis or fluorescence spectroscopy should be compatible with the fiber approach. The most simple way of spatially resolved Raman spectroscopy using a single beveled fused silica fiber is shown in Fig. 7.2. Here the same fiber is used to guide the laser light to the catalyst surface, collect the scattered light, and transmit it to a spectrometer. The conical shape of the fiber tip assures illumination and acceptance of scattered light nearly perpendicular to the fiber axis (Fig. 7.4). A demonstration experiment will be described in Section 7.4.

7.3 Application Examples

7.3.1 Catalytic Partial Oxidation (CPO) of Methane on Rh and Pt Foam Catalysts

The scientific motivation that originally lead to the development of the spatial profile technique in the group of Schmidt in Minneapolis was to clarify whether methane catalytic partial oxidation to syngas followed a direct or an indirect reaction scheme [6]. The pioneering work of Hickman and Schmidt showed that methane can be oxidized to syngas in excellent yields using Rh or Pt coated foam monoliths in millisecond contact

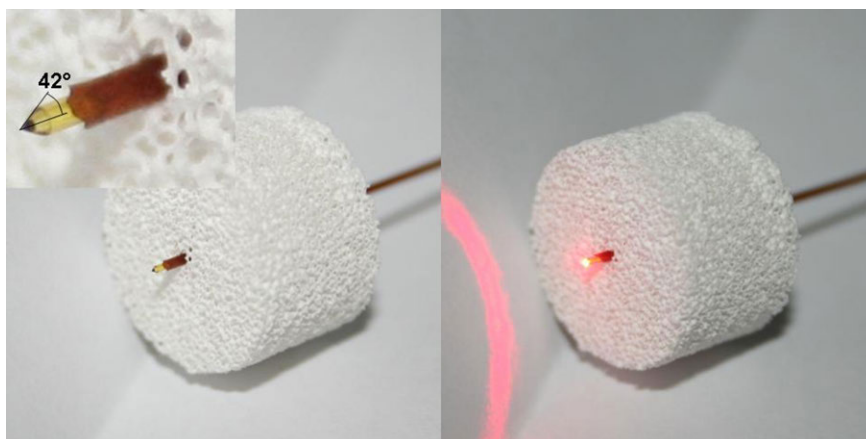
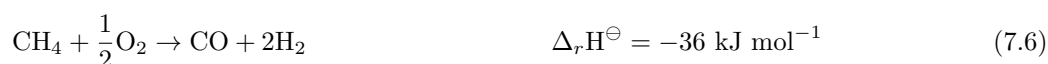


Figure 7.4: Illumination and angular acceptance of a properly beveled optical fiber for spatially resolved Raman spectroscopy.

time [1]. Since then it has been heavily debated in the literature whether CO and H₂ are directly formed in the presence of gas-phase oxygen (direct scheme, Eq. 7.6) or whether there is a combustion zone at the entrance of the foam in which CH₄ is combusted to CO₂ and H₂O (Eq. 7.7) followed by steam (Eq. 7.8) and dry (Eq. 7.9) reforming, eventually producing synthesis gas (indirect scheme).



7.3.2 Spatial Profiles on Rh and Mechanistic Discussion

Fig. 7.5 shows temperature and species profiles measured for methane CPO on a 5 wt% Rh coated foam catalyst (experimental conditions in figure caption). From a qualitative inspection of these profiles and others measured for different conditions [6, 7], it could be concluded that two reaction zones exist in a Rh coated foam, namely a short oxidation zone at the entrance of the foam (0 → 1.5 mm), followed by a longer second zone (1.5 → 9.6 mm) that is dominated by steam reforming and to a minor extent water-gas shift (Eq. 7.10). Qualitatively similar results are also found for Pt [7].



Syngas is formed in both zones, viz. in presence of gas-phase oxidation and after complete O₂ consumption by steam reforming. However, CO₂ reforming (Eq. 7.9) as suggested in the indirect scheme was never observed experimentally. Therefore, from the point of view of a formal kinetic description, methane CPO on both Rh and Pt can be described by Eqs. 7.6-7.8, and 7.10.

At first glance it is surprising that H₂ and O₂ can co-exist in the gas phase over a Rh surface at temperatures around 1000 °C. To rationalize this finding, the profiles in Fig. 7.5 and similar profiles measured for other conditions on Rh were modeled in several follow up publications using different elementary step reaction mechanisms [2–4]. Both these model studies as well as other independent experimental studies measuring spatial profiles at varying pressure [10] revealed that methane CPO on Rh foams is nearly completely film transport limited for the stoichiometrically limiting component O₂. In consequence the actual concentration of O₂ in immediate vicinity of the Rh surface is essentially zero and the surface coverage of oxygen at the Rh surface negligible [2]. Taking these results on Rhodium into account it has been argued by some groups [4] that the co-existence of H₂ and O₂ revealed by the spatial profiles [6, 7] is solely due to the vanishing O₂ concentration at the Rh surface. Therefore it is an interesting question to study H₂ formation by CPO on a catalytic system where transport limitations are much less pronounced than on Rhodium, and it will be shown in the following that this is the case on Platinum.

7.3.3 Recent Work on Pt

In comparison to Rh where irreducible mass transport limitations prevail under all experimental conditions [7], Pt is, at least from a scientific point of view, a much more interesting CPO catalyst, because early

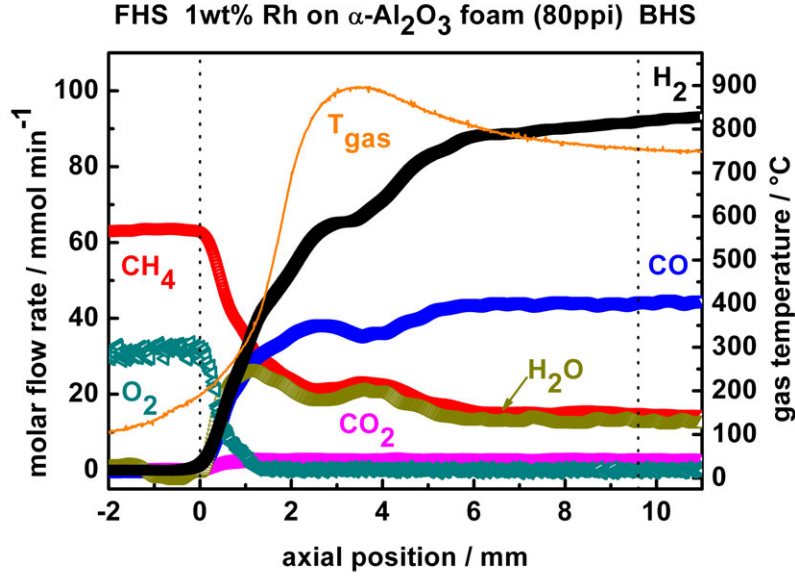


Figure 7.5: Species and gas temperature profiles for methane CPO on a 5 wt% Rh coated 80 ppi foam catalyst ($\alpha\text{-Al}_2\text{O}_3$). Total inlet gas stream $\dot{V}_{\text{CH}_4} + \dot{V}_{\text{O}_2} + \dot{V}_{\text{Ar}} = 4700 \text{ mln min}^{-1}$ at 273 K. Inlet stoichiometry $\text{C/O} = \dot{V}_{\text{CH}_4} / (2 \cdot \dot{V}_{\text{O}_2}) = 1.0$ and $\dot{V}_{\text{Ar}} / \dot{V}_{\text{O}_2} = 3.76$ (80 ppi, $L_f = 9.6 \text{ mm}$, $d_f = 17 \text{ mm}$, porosity $\varepsilon = 0.7$). Catalyst foam between dotted lines.

experimental studies indicate that methane CPO on Pt coated foams is much slower and kinetically controlled [7,10]. This can be rationalized by simple experiments and a 1D mole balance on O_2 which can be applied as the product of Reynolds number based on the hydraulic diameter of the ppi foam and the Schmidt number of O_2 $\text{Re}_{d_h} \cdot \text{Sc}_{\text{O}_2} \approx 0.7$ is much bigger than $d_h / l_{\text{foam}} \approx 0.01$ but much smaller than $l_{\text{foam}} / d_h \approx 100$ [189]. Spatial profile measurements at constant inlet flow rate and increasing pressure on Rh remain unchanged [10]. This pressure invariance is consistent with a reaction that is complete controlled by film transport. Fig. 7.6 shows a similar experiment on a Pt foam catalyst, in which the pressure is raised from 1 bar to 15 bar at constant inlet gas flow. To stay outside the explosive limits, a C/O ratio of 2 was chosen. All other conditions are given in the caption. It is clearly visible that the absolute values of the slopes of all species increase with increasing pressure. The temperature maximum in the front heat shield must be a measurement artifact because the reactor is operated autothermally (without external heating) and no exothermic chemistry is observed in the front heat shield. This behavior is reproducibly observed in methane CPO profiles measured at elevated pressures. A potential explanation, which however still lacks experimental verification, is that methane, which has a strong absorption band at 6096.4 cm^{-1} , absorbs selectively NIR radiation detected by the two color pyrometer at the longer measurement wavelength $\lambda_2 = 1.64 \mu\text{m}$ or $\tilde{\nu}_2 = 6097.6 \text{ cm}^{-1}$ but not at the shorter measurement wavelength $\lambda_1 = 1.52 \mu\text{m}$ or $\tilde{\nu}_1 = 6578.9 \text{ cm}^{-1}$. As the temperature value is calculated from the intensity ratio $I(\lambda_1) / I(\lambda_2)$ erroneously high temperatures are measured if NIR absorption by methane becomes pronounced. This is in particular the case at high pressures and in the front heat shield where the methane density is highest due to low gas temperatures. A quantitative correction for such a gas induced absorption of thermal radiation might be possible based on the known gas composition but has not yet been established.

Both the pressure invariance of the Rh profiles as described by Bitsch-Larsen et al. in an earlier paper [10] and the shortening of the Pt profiles in Fig. 7.6 are easily understood in terms of a simple 1D mole balance (Eq. 7.11) on the stoichiometrically limiting component O_2 , in which R_{O_2} denotes the consumption rate of O_2 in $\text{mol m}^2 \text{ s}^{-1}$ at the catalyst surface (negative), a_c the specific surface area of the foam catalyst per unit volume in m^{-1} and A_c the cross sectional area of the foam in m^2 .

$$\frac{dF_{\text{O}_2}}{dz} = R_{\text{O}_2} a_c A_c \quad (7.11)$$

If R_{O_2} is fully determined by transport limitation, then $C_{\text{O}_2}^{\text{surface}} \approx 0$, and R_{O_2} will be given by

$$R_{\text{O}_2} = -k_c \cdot (C_{\text{O}_2}^{\text{bulk}} - C_{\text{O}_2}^{\text{surface}}) \approx -k_c \cdot C_{\text{O}_2}^{\text{bulk}} \quad (7.12)$$

with k_c being the O_2 mass transfer coefficient in m s^{-1} and $C_{\text{O}_2}^{\text{bulk}}$ the O_2 concentration in the bulk gas phase. Taking into account that $C_{\text{O}_2}^{\text{bulk}} \propto p$ and $k_c \propto p^{-1}$ [10] mass transport does not speed up with increasing pressure which is why the Rh profiles in [10] are pressure invariant.

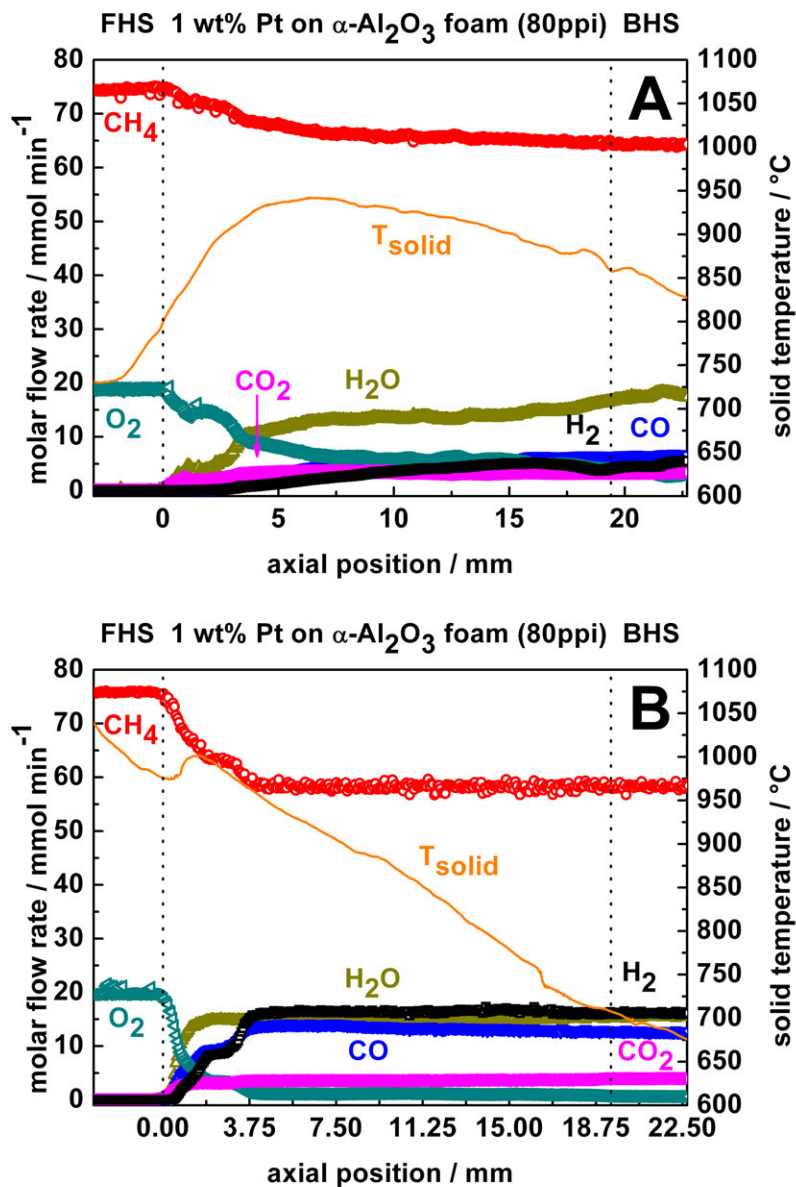


Figure 7.6: Spatial surface temperature profiles and species evolution through an α -Al₂O₃ foam monolith coated with 1 wt% Pt (80 ppi, $L_f = 19.4$ mm, $d_f = 15.5$ mm, porosity $\varepsilon = 0.7$). Effect of reactor pressure. A: 1 bar, B: 15 bar. Gas feed of $\dot{V}_{\text{Ar/CH}_4/\text{O}_2} = 1718/1826/456$ mln min⁻¹, respectively a total gas feed of $\dot{V}_{\text{total}} = 4000$ mln min⁻¹.

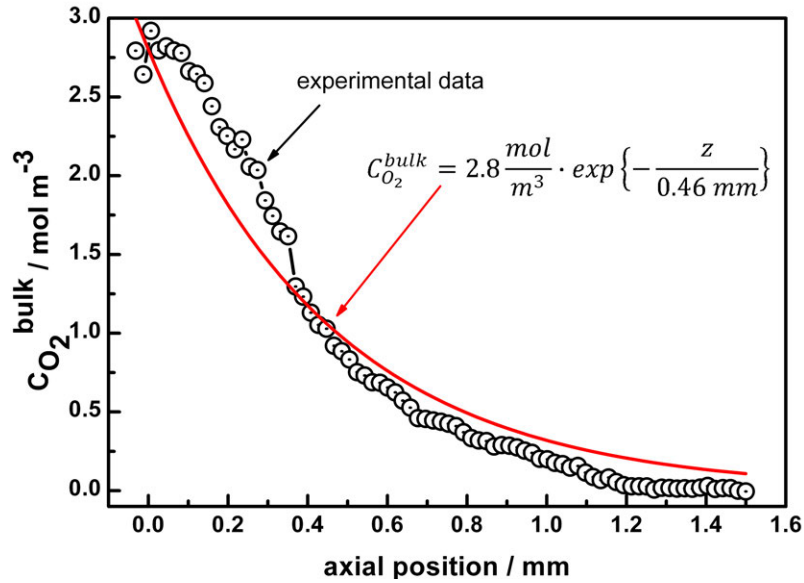


Figure 7.7: Determination of $k_c \cdot a_c$ by fitting Eq. 7.14 to the experimental data in Fig. 7.5.

If kinetics dominate, R_{O_2} in Eq. 7.11 will be given by Eq. 7.2. Since the various reaction rates r_j increase with increasing reactant concentrations ($C_i^{bulk} \approx C_i^{surface} \propto p$), R_{O_2} will increase (become more negative), and all profiles become steeper exactly as observed in Fig. 7.6.

The relative impact of film transport to surface kinetics can be estimated by calculating the highest possible slope of an O_2 profile that can be achieved for a certain foam catalyst and flow conditions. Even though various transport correlations have been published for mass transfer in reticulated foam catalysts, they have usually been optimized for low cell density foams and comparably high Reynolds numbers (e.g. 10-45 ppi and $7 < Re < 1100$ [190] or 5.9-15.3 ppi and $15 < Re < 200$ [191]). In the present work 80 ppi foams with small pores ($d_p \approx 500 \mu\text{m}$) were used leading to very low Reynolds numbers ($Re \approx 1$) based on a hydraulic diameter [144, 192] of $d_h = 4 \cdot \epsilon / S_v = 4 \cdot 0.73 / 160 \times 10^4 \mu\text{m} = 182 \mu\text{m}$ (ϵ = porosity, S_v = specific surface area [192]) and flow field parameters extracted from the spatial profiles (e.g. Figs. 7.5 and 7.6). Because there is no doubt from experiments and simulations that the O_2 profile in Fig. 7.5 is nearly fully film transport controlled, it is safer to extract the pseudo first-order rate constant $k_c \cdot a_c$ from an exponential fit of the O_2 profile in Fig. 7.5 than to extrapolate a transport correlation beyond its validity range. Reformulating Eqs. 7.11 and 7.12 in terms of the limiting slope of the O_2 profile in presence of full film transport yields

$$\left(\frac{dF_{O_2}}{dz}\right)_{\text{limit}} = -k_c \cdot a_c \cdot A_c \cdot C_{O_2}^{bulk} \Rightarrow \left(\frac{dC_{O_2}^{bulk}}{dz}\right)_{\text{limit}} = -\frac{k_c \cdot a_c}{u} \cdot C_{O_2}^{bulk}. \quad (7.13)$$

Integrating Eq. 7.13 in which u is the superficial flow velocity in m s^{-1} yields

$$C_{O_2}^{bulk, z} = C_{O_2}^{bulk, 0} \cdot \exp\left(-\frac{k_c \cdot a_c}{u} \cdot z\right). \quad (7.14)$$

By fitting the experimental $C_{O_2}^{bulk, z}$ profiles (data from Fig. 7.5) to the exponential function derived in Eq. 7.14, the pseudo first-order rate constant $k_c \cdot a_c$ can be determined, as shown in Fig. 7.7 and Eq. 7.15. The value for the superficial velocity in the oxidation zone u was calculated from the data in Fig. 7.5 to $u \approx 1.7 \text{ m s}^{-1}$.

$$0.46 \times 10^{-3} \text{ m} = \frac{1.7 \text{ m s}^{-1}}{k_c \cdot a_c} \Rightarrow k_c \cdot a_c \approx 3700 \text{ s}^{-1}. \quad (7.15)$$

From the $k_c \cdot a_c$ value it is now possible to calculate the limiting slope $(dF_{O_2}/dz)_{\text{limit}}$ in an 80 ppi foam for the Pt experiments that would be obtained if full film transport limitation existed.

$$\left(\frac{dF_{O_2}}{dz}\right)_{\text{limit}} = -k_c \cdot a_c \cdot A_c \cdot \bar{x}_{O_2} \cdot C_{\text{total}} \quad (7.16)$$

To compare to other experiments on 80 ppi foams, the dependence of k_c on the inlet volumetric flow rate and on pressure has to be accounted for. This can be done by means of Eq. 7.17 [10, 191]. The mean O_2 mole

fraction \bar{x}_{O_2} is taken as average value over the region from which the slope is determined. The temperature dependence of k_c is weak ($T^{1.3}$ [10]) and can be neglected as their relative variation is small (cp. Tab. 7.2).

$$k_c(\dot{V}_2, p_2) = k_c(\dot{V}_1, p_1) \cdot \left(\frac{\dot{V}_2}{\dot{V}_1} \right)^{0.43} \left(\frac{p_1}{p_2} \right)^{0.93} \quad (7.17)$$

If Eq. 7.16 is applied to the Rh foam profiles shown in Fig. 7.5 and the Pt foam profiles shown in Figs. 7.6A, B, and 7.8 A, B (experimental conditions in the figure captions) the values in Tab. 7.1 are obtained.

It can be clearly seen in the first row of Tab. 7.1 that within experimental error methane CPO on Rh coated foams is nearly fully mass transport limited. The deviation results from the imperfect fit in Fig. 7.7 because the data reflect to some extent the pore structure of the foam. The experimentally observed slope of the O_2 profile (Fig. 7.6) of $-53 \text{ mmol mm}^{-1} \text{ min}^{-1}$ comes close to the calculated limiting value of $-83 \text{ mmol mm}^{-1} \text{ min}^{-1}$.

The situation for Pt is quite different. Here the ratios between the calculated limiting slopes and the experimentally observed slopes of the O_2 profiles vary between 26, indicating basically no impact of film transport ($\text{C/O} = 2.0$, 1 bar, 4000 ml min^{-1}), and roughly 3 indicating moderate impact of film transport ($\text{C/O} = 2.0$, 15 bar, 4000 ml min^{-1}). Pt foam catalysts operate therefore in a regime largely determined by surface kinetics, which implies that the O_2 concentration at the Pt surface is not much lower than in the bulk gas phase. The influence of this surface oxygen on the hydrogen selectivity is summarized in Tab. 7.2. Firstly, a comparison of the H_2 selectivities measured on Rh and on Pt at the same reactant stoichiometry $\text{C/O} = 1.0$ shows clearly that a pronounced film transport limitation as present on Rh has indeed a strong positive effect (50 % vs. 28 % and 30 %) but it also makes clear that even in full kinetic control as on Pt, H_2 can be formed in significant selectivities. Therefore, attributing the co-existence of H_2 and O_2 in the oxidation zone solely to film transport limitations is not correct. Secondly it is an interesting and new result, in particular with respect to an industrial CPO process, that S_{H_2} is not negatively influenced by pressure (8 % at 1 bar vs. 11 % at 15 bar). Therefore it would be very interesting to study CPO under pressure also at more favorable C/O ratios if a proper reactor design would prevent explosions.

Table 7.1: Estimation of the relative impact of O₂ film transport limitation on methane CPO in Rh and Pt foam catalysts.

Profile	Cat	\dot{V} (mlh min ⁻¹)	p (bar)	$k_c \cdot a_c$ (s ⁻¹)	C_{total} (mol m ³)	\bar{x}_{O_2}	$\left(\frac{dF_{\text{O}_2}}{dz}\right)_{\text{limit}}$ (mmol min ⁻¹ mm ⁻¹)	$\left(\frac{dF_{\text{O}_2}}{dz}\right)_{\text{exp}}$ (mmol min ⁻¹ mm ⁻¹)
Fig. 7.5	Rh	4700	1	3700	15	0.11	-83	-53
Fig. 7.6A	Pt	4000	1	3450	15	0.088	-52	-2.0
Fig. 7.6B	Pt	4000	15	280	216	0.078	-53	-17
Fig. 7.8A	Pt	2000	1	2560	15	0.13	-56	-2.7
Fig. 7.8B	Pt	4000	1	3450	15	0.09	-53	-4.4

Table 7.2: H₂ selectivity at 50 % O₂ conversion determined from the spatial reactor profiles.

Profile	Cat	C/O	$F_{\text{O}_2}^0$ (mmol min ⁻¹)	$z \left(\frac{F_{\text{O}_2}^0}{2}\right) = z_{1/2}$ (μm)	$T_{\text{cat}}^{z_{1/2}}$ (K)	$F_{\text{CH}_4}^0$ (mmol min ⁻¹)	$F_{\text{CH}_4}^{z_{1/2}}$ (mmol min ⁻¹)	$F_{\text{H}_2}^0$ (mmol min ⁻¹)	$S_{\text{H}_2}^{z_{1/2}}$ (%)
Fig. 7.5	Rh	1.0	31	400	1273 [2]	63.5	52.4	11	50
Fig. 7.6A	Pt	2.0	18.8	4032	1183	74	69	0.8	8
Fig. 7.6B	Pt	2.0	19.6	1053	1267	75.8	70.3	1.2	11
Fig. 7.8A	Pt	1.0	12.6	2009	1250	24.1	20.2	2.2	28
Fig. 7.8B	Pt	1.0	25	3426	1340	48.6	39.5	5.6	30

7.3.4 Possible Origin of Reduced CPO Reactivity of Pt Compared to Rh

After discussing phenomenologically the difference between Rh and Pt as CPO catalysts in terms of transport limitations, the question remains why the surface reactivity of Pt is so much lower than that of Rh even though both metals behave quite similarly in terms of dispersion on the support and are both excellent oxidation catalyst. This question cannot be answered in this work with certainty and will require much further research. However, an important experimental finding shall be mentioned here that might be related to the observed difference in reactivity. For Rh Dalle Nogare et al. [2] have shown numerically that the Rh surface is basically empty in the oxidation zone. This prediction still lacks experimental confirmation but it is basically what is to be expected for a catalyst surface under strict transport control.

On a Pt foil in-situ Raman experiments have revealed that the Pt surface is clean before ignition of CPO but is covered with carbon deposits immediately afterwards (cp. Fig. 7.9).

As will be outlined in a forthcoming article, these carbon deposits are initially rather amorphous and defect rich but become with time on stream rather graphitic and resistant to oxidation by gas-phase oxygen or steam. Similar carbon deposits have recently been reported on Pt/Al₂O₃ catalysts [193] indicating that the observations on the Pt foil can be transferred to supported Pt catalysts. Therefore an obvious explanation of the reduced surface reactivity of Pt compared to Rh could be that these oxidation resistant carbon deposits block a majority of active sites making them inaccessible for catalysis. This argument can be substantiated by taking into account that Pt is an excellent hydrogenation and hence also a dehydrogenation catalyst which at high temperature obviously leads to formation of surface carbon. If this is true then current state-of-the-art micro kinetic models have to be rewritten as none of them include such non-reactive carbon species, making it highly unlikely that they could predict spatial profiles on Pt foams correctly [70, 72].

7.3.5 Gas Phase Methane Oxidative Coupling

In Section 7.3.1 it was illustrated for methane oxidation on Rh and Pt coated foam catalysts, how spatial profiles can be analyzed in a semi quantitative way, for example to study the influence of film transport on catalytic reactions. Another interesting aspect of spatial reactor profiles is that they have a high information density and are hence ideal datasets for comparison to microkinetic numerical simulations. For methane CPO on Rh foam catalysts this was already demonstrated in several publications [2–4]. Because catalyst and gas temperature can be measured at any point in the reactor it is even possible to use the experimental temperature profiles as input, thereby avoiding large errors that result from solving the energy balance in cases in which heat flow from or to the reactor cannot be accurately modeled. However, it should be kept in mind that also the experimental temperature profiles of the gas phase or the solid phase measured by a thermocouple or a pyrometer fiber in the sampling capillary respectively might be biased by experimental artifacts such as thermal radiation from the oven coils or absorption of thermal radiation by gas constituents. Therefore experimental temperature profiles should only be used as input for kinetic simulations if their bias by such artifacts is small.

Oxidative coupling of methane to ethylene (OCM) is a reaction closely related to methane partial oxidation and is currently studied by the authors, using the combined approach of spatial reactor profile measurements and microkinetic numerical simulations. This high-temperature reaction ($T_r \approx 800$ °C) is a promising one-step reaction pathway to transform methane into ethylene, which is a valuable intermediate for the chemical industry [19]. Unfortunately all research efforts have failed so far to design this reaction into a competitive technical OCM process. Interestingly there seems to be a virtual upper bound of about 25-30 % per reactor pass [19] with respect to combined C₂ yield (C₂H₄ + C₂H₆), and the kinetic reason for this upper bound is unknown. Since the pioneering work of Keller and Bhasin [194] more than 2700 research articles and reviews and about 140 patents have been published on OCM, demonstrating that hundreds of chemically different materials catalyze OCM, yet there is no convincing explanation as to why all catalytic data fall roughly on or below a conversion-selectivity trajectory given by $X + S \leq 100$ [195]. The most likely explanation for this indifference of OCM towards the nature of the catalytic material is that at a certain temperature methane oxidation in the gas phase dominates over catalytic oxidation steps, so that product selectivities and yields are not longer determined by the nature of the catalyst.

Spatial reactor profiles could be valuable datasets to develop a quantitative gas-phase and surface microkinetic model of OCM because they can be measured at high-temperature, high-pressure conditions, and they can provide mechanistic information on how methane and oxygen are transformed into C₂H₆ and C₂H₄ and the unwanted by-products CO and CO₂. Validation of microkinetic models, in particular gas-phase models, requires experimental data of high information content, such as spatial profiles, since detailed kinetic mechanisms may contain hundreds of reactions, even for comparatively simple systems such as gas-phase oxidation of methane [70, 196].

To illustrate the concept Fig. 7.10 shows species and temperature profiles measured in the empty quartz tube of the profile reactor described in [82]. This experiment was performed at 8 bar reactor pressure, a typical

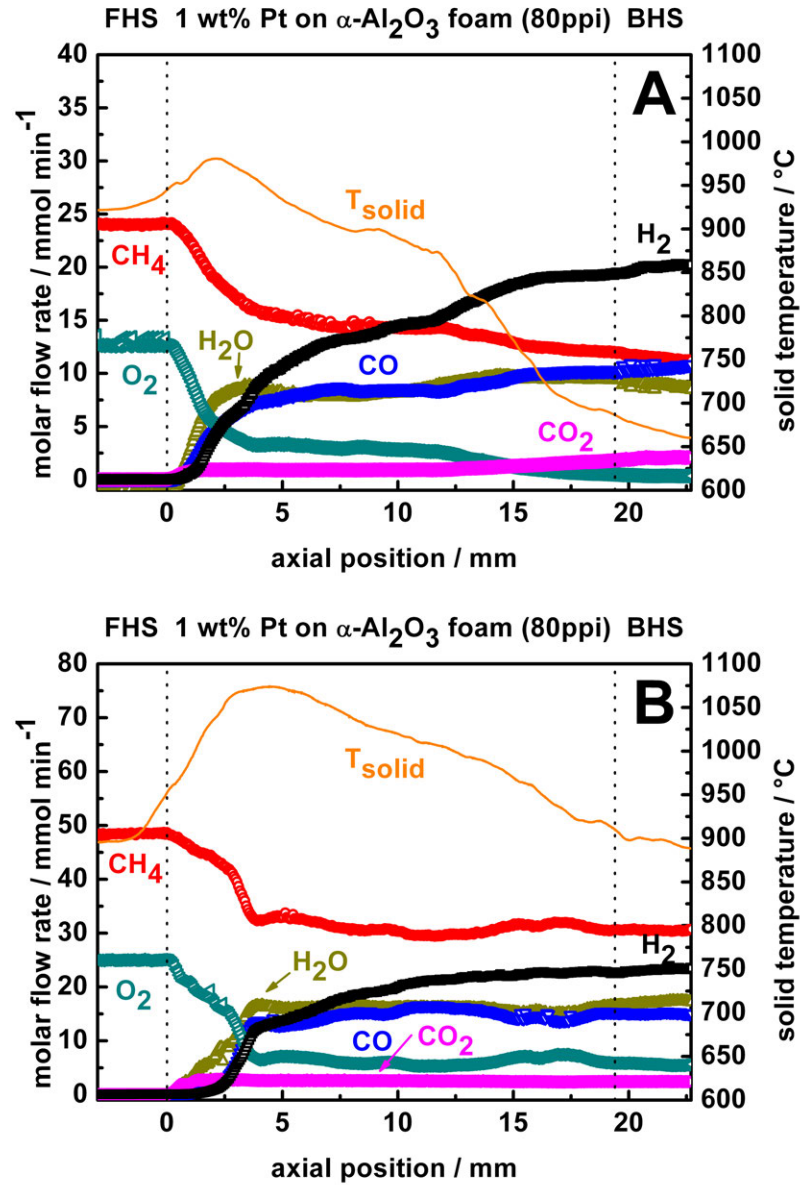


Figure 7.8: Spatial surface temperature profiles and species evolution through a 1 wt% Pt coated α - Al_2O_3 foam monolith at constant reactor pressure of $p = 1$ bar. Effect of flow rate. Gas feeds: A: $\dot{V}_{\text{Ar}/\text{CH}_4/\text{O}_2} = 1112/592/296 \text{ mln min}^{-1}$, i.e. total gas feed of $\dot{V}_A = 2000 \text{ mln min}^{-1}$; B: $\dot{V}_{\text{Ar}/\text{CH}_4/\text{O}_2} = 2224/1184/592 \text{ mln min}^{-1}$, i.e. total gas feed of $\dot{V}_B = 4000 \text{ mln min}^{-1}$. The shape of the temperature profile in (A) is probably somewhat distorted by irregularities in the pore structure along the scan line.

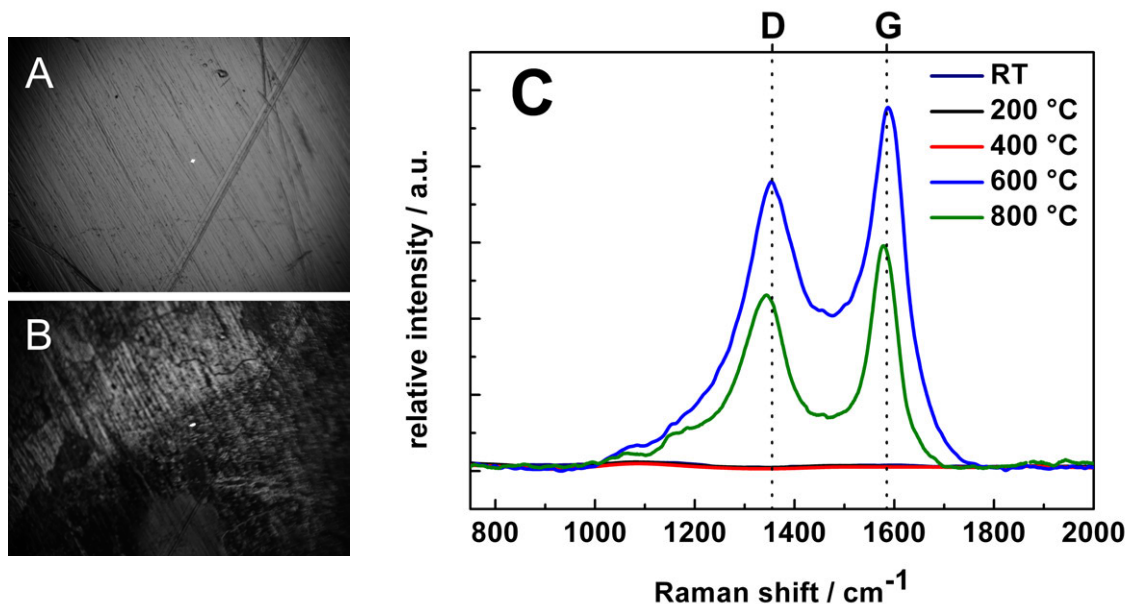


Figure 7.9: Microscopic picture of Pt foil section prior reaction light-off (A) and after reaction light-off (B). C: In-situ Raman spectra of D and G band of carbonaceous surface deposits formed after reaction light-off.

OCM gas stoichiometry of $C/O = 4.0$ and a total flow rate of $4000 \text{ mln min}^{-1}$ ($\dot{V}_{\text{CH}_4} = 3200 \text{ mln min}^{-1}$, $\dot{V}_{\text{O}_2} = 400 \text{ mln min}^{-1}$, $\dot{V}_{\text{Ar}} = 400 \text{ mln min}^{-1}$). Blank 80 ppi $\alpha\text{-Al}_2\text{O}_3$ foam supports were used to guide the capillary and to provide a uniform flow pattern at the entrance to the free gas phase, which begins at 0 mm. A uniform inlet flow is important for selecting proper inlet boundary conditions for the flow in the tube, which was modeled using the Boundary Layer code implemented in ChemKin Pro [197].

As the boundary layer model requires solving the energy balance, a separate experiment was conducted to measure the oven temperature profile. For that the reactor tube was filled with a 150 mm long stack of graphite cylinders serving as black body for an accurate pyrometric temperature measurement. All cylinders were equipped with a central bore hole through which the pyrometer fiber could be vertically translated. After setting the oven to a certain heating power and waiting for three hours for thermal equilibration the temperature profile through the graphite cylinders was measured reflecting the oven temperature profile closely. This procedure was repeated for five different electrical heating powers. The experimental oven temperature profiles were then fitted by a third order polynomial both in position and electrical heating power. The obtained function was finally used to calculate the oven temperature profile for the heating power of 440 W applied in the gas phase OCM measurement shown in Fig. 7.10 and served as wall temperature boundary condition in the boundary layer simulation. The dashed lines in Fig. 7.10 represent predictions by a dedicated OCM gas-phase kinetic model, developed by Zanthoff and Baerns for gas-phase OCM at elevated pressures [198] comprising 33 species and 192 elementary reactions.

From the experimental profiles it can be seen that CO is the major carbon containing product in gas-phase methane oxidative coupling. C_2H_6 and C_2H_4 are formed in much smaller amounts, and it can be clearly discerned that C_2H_6 is the primary and C_2H_4 the secondary product. Interesting to note, in particular in view of the predictions by the microkinetic model, is the crossing of the C_2H_4 and C_2H_6 profile (here at 35 mm) which is reproducibly observed also for other experimental conditions. The negative molar fraction of the ethylene trace between 16 mm and 26 mm is an experimental artifact from the mass spectrometric species analysis, which is due to an isobaric interference on $m/z = 30$ amu by C_2H_6 , CH_3OH and CH_2O . As 30 amu is used to correct the ethylene peak at 27 amu for ethane fragmentation at this mass, negative peak areas are always obtained when the signal at 30 amu is caused by CH_3OH and CH_2O , which are formed in trace amounts at low temperatures. There is basically no CO_2 formation by gas-phase methane oxidation in contrast to catalytic OCM where CO_2 is the dominant product (not shown). It can be further seen that there is an ignition-delay zone (0 – 16 mm) at the beginning of the free gas phase where no noticeable chemistry occurs. This ignition delay is a combined effect of the increasing temperature and the build-up of a radical pool. Experimental reactant conversion and product formation begin at about 16 mm axial position and continue until the end of the free gas phase. C_2H_4 reaches maximum concentration at around 57 mm and is then consumed by steam reforming.

The kinetic model [198] captures the final gas composition at the reactor outlet sufficiently well, but it does not reproduce the species development inside the reactor. Sufficient reproduction of reactor exit concentra-

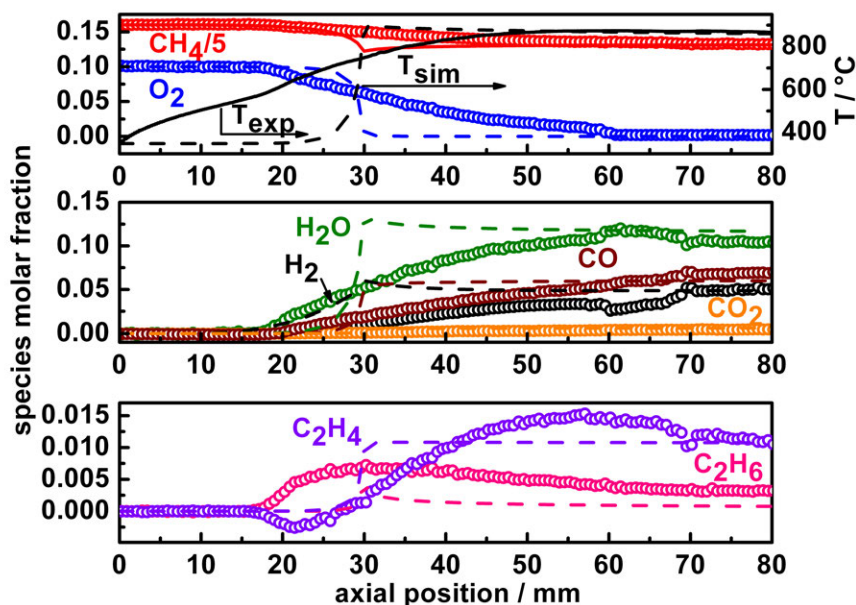


Figure 7.10: Experimental reactor profiles (scatter) and boundary layer numerical simulations (dashed lines) of gas phase methane oxidative coupling. Reactor pressure $p = 8$ bar, reactant stoichiometric $C/O = 4.0$, $\dot{V}_{CH_4} = 3200$ mln min^{-1} , $\dot{V}_{O_2} = 400$ mln min^{-1} , $\dot{V}_{Ar} = 400$ mln min^{-1} , $\dot{V}_{total} = 4000$ mln min^{-1} .

tions has been observed not only for the kinetic model used in this work [198] but also for other models tested, probably because these models have been optimized to fit OCM reactor outlet data well.

The species development in Fig. 7.10 as predicted by the model is basically confined to a narrow region between 20 and 30 mm whereas the experimental profiles develop over a much longer length between 16 and 81 mm. Consequently the numerically predicted gradients are too steep and not in quantitative agreement with the experimental data. Also important qualitative features of the experimental profiles such as the crossing of the C_2H_6 and the C_2H_4 profiles are not reproduced by the model indicating severe deficiencies in terms of the included reaction steps and/or the kinetic parameters.

Even though the used boundary layer model is an appropriate description for the flow in the empty reactor tube one notes the disagreement between the simulated centerline gas temperature T_{sim} and the temperature measured by the thermocouple in the sampling capillary T_{exp} . Between 0 and 25 mm where the experimental temperature increases rapidly the centerline gas temperature in the boundary layer simulation increases only slowly. However, this could be realistic as the linear flow velocity of the gas is rather high starting from 6.8 cm s^{-1} at the inlet and increasing up to 13 cm s^{-1} at the end of the free gas phase section. Furthermore because the thermocouple is not only in contact with the sampled gases but sees also radiation from the oven coils it could be argued that the thermocouple temperature is biased to values which are too high and that the simulated temperature is more realistic. How strongly the thermocouple temperature profiles deviates from the true gas temperature profile will be investigated in the future using CFD simulations combined with appropriate heat transport by conduction, convection and radiation.

In summary it was shown for the example of methane oxidative coupling in the gas phase how spatial reactor profiles can be used to validate even substantial microkinetic reaction models comprising several dozens species and up to several hundred reactions. It could be demonstrated that even in cases where reactor outlet data are described sufficiently well by the model the species development in the reactor can still be falsely predicted. If spatial reactor data are used for validation it will be possible to optimize model parameters in such a way that the model also captures the development of the various species correctly, provided that all parameters stay within physically reasonable bounds.

7.3.6 Oxidative Dehydrogenation of Ethane to Ethylene on Molybdenumoxide Catalysts

For the final example of spatial reactor profiles in this work a transition metal oxide catalyzed reaction has been chosen, namely oxidative dehydrogenation of ethane to ethylene (ODH) on a molybdenum oxide catalyst. Transition metal oxide catalysts are interesting to study by spatial profiles, as they can change their oxidation state and can adjust to the changing chemical potential of the gas. Similar to OCM, ODH is an industrially interesting production route of ethylene and has therefore received considerable scientific attention [199, 200].

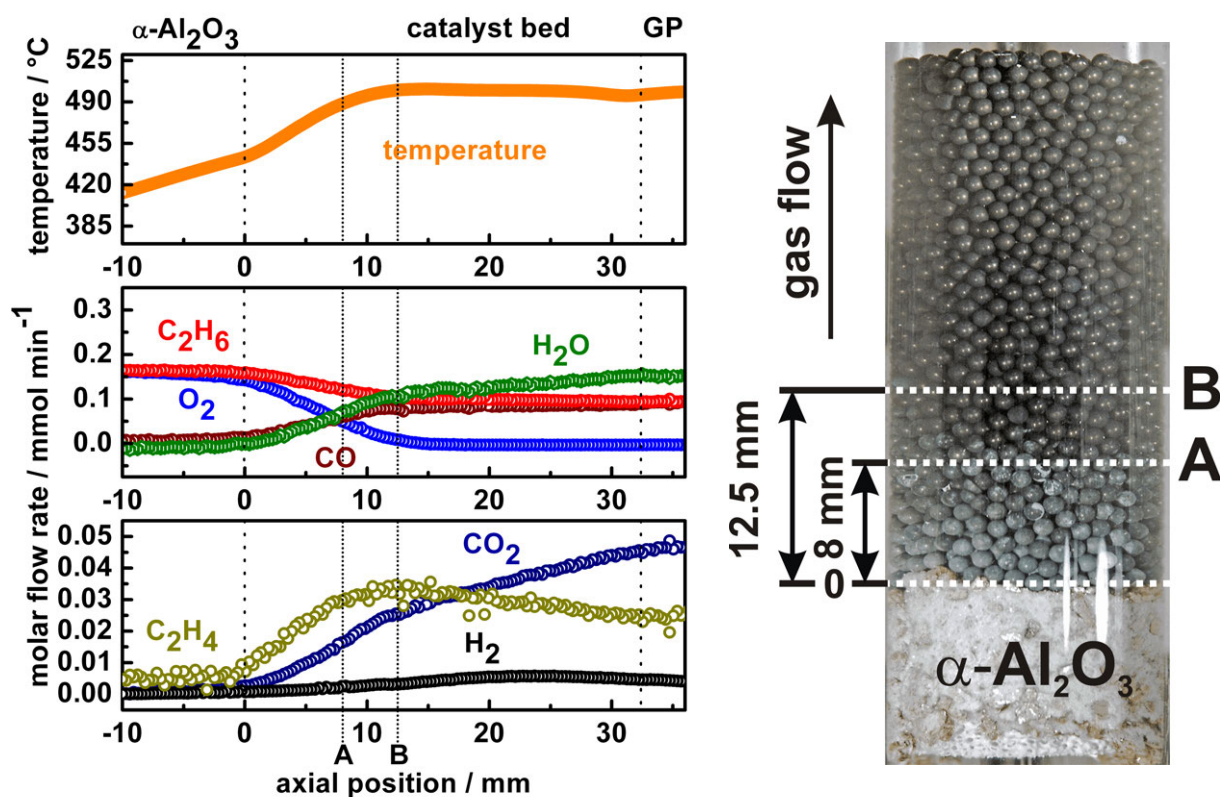


Figure 7.11: Left: Species and catalyst temperature profiles for ethane ODH on MoO_x coated α -Al₂O₃ spheres. Feed gas: $V_{\text{C}_2\text{H}_6} = 4 \text{ mln min}^{-1}$, $V_{\text{O}_2} = 4 \text{ mln min}^{-1}$, $V_{\text{Ar}} = 58 \text{ mln min}^{-1}$. Reactor pressure $p = 1 \text{ bar}$. Right: Photograph of the sphere bed after 3 h time on stream.

Various chemically different catalysts are active for ODH, among them noble metals such as Pt, oxides of group IA and IIA metals e.g. Li/MgO, and transition metal oxides e.g. VO_x, MoO_x. We applied the spatial profile technique to ethane ODH on MoO_x supported on γ -Al₂O₃ spheres to resolve how gas composition and temperature influence the redox state of the catalyst, which was analyzed ex-situ after quenching. For this purpose we adjusted the feed rate such that complete O₂ conversion was reached in the bed in contrast to regular partial oxidation catalysis where full O₂ conversion has to be avoided.

A 3 cm high bed of catalyst spheres ($d_s = 1 \text{ mm}$) was placed inside the profile reactor held in place by an 80 ppi α -Al₂O₃ support foam. The catalyst spheres were prepared by incipient wetness impregnation of γ -Al₂O₃ spheres (Sasol, 157 m² g⁻¹) using an aqueous solution of (NH₄)₆Mo₇O₂₄ · 4H₂O such that a 30 wt% MoO₃ loading was achieved. After drying at 120 °C the spheres were calcined at 540 °C for 6 h.

For profile measurements a gas mixture consisting of 4 mln min⁻¹ C₂H₆, 4 mln min⁻¹ O₂ and 58 mln min⁻¹ Ar was fed to the reactor. The maximum reactor temperature was adjusted to stay below 520 °C to avoid sublimation of MoO₃. The species and temperature profiles as well as a photograph of the sphere bed quenched after 3 h time on stream are shown in Fig. 7.11. Oxygen is consumed after passing about 12.5 mm of the catalyst bed (point B). Oxidation products are C₂H₄, CO, CO₂ and H₂O. H₂ formation is negligible in the entire bed. As can be seen on the photograph of the sphere bed, the MoO_x catalyst reacts sensitively to the gradually declining O₂ concentration in the gas phase by changing its color from gray to dark-violet. The color transition occurs after about 8 mm where 70 % of the initial O₂ has been converted ($T^{8 \text{ mm}} = 757 \text{ K}$, $C^{8 \text{ mm}} = 0.3 \text{ mol m}^{-3}$, $p^{8 \text{ mm}} = 1850 \text{ Pa}$). Ex-situ XRD analysis (not shown) revealed that the gray spheres in the oxidation zone consist mainly of Al₂(MoO₄)₃ and trace amounts of MoO₂. The presence of MoO₄ tetrahedrons both in polymeric and monomeric form was also confirmed by ex-situ Raman spectroscopy. The dark-violet spheres showed a characteristic Raman signature of phase pure MoO₂ which was also confirmed by XRD. Therefore it can be concluded that the bulk phase of the catalyst consists of molybdenum in +VI oxidation state as long as the O₂ gas phase pressure is higher than about 1850 Pa and at lower values it is produced to +IV as in MoO₂.

From the CO₂ production after full consumption of gas-phase O₂ it can be seen that the reduction of the catalyst bed has not been finished in this experiment, due to the high amount of catalyst compared to the small feed rate of hydrocarbons. Very interestingly lattice oxygen seems to oxidize preferentially the

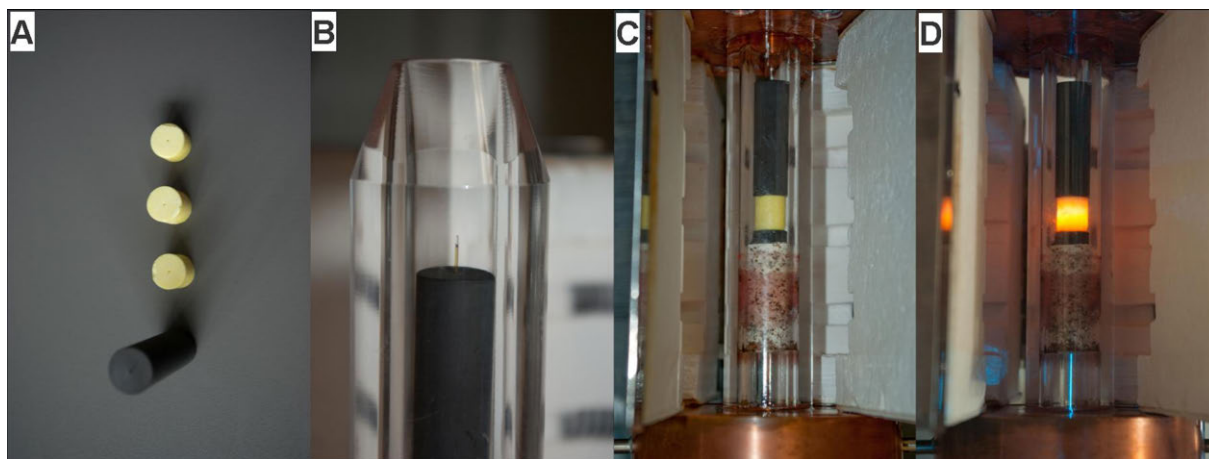


Figure 7.12: A: Graphite and sulfur cylinders for demonstrating the principle of spatially resolved Raman spectroscopy. B: Optical fiber sticking out of the sampling capillary which was inserted in the graphite - sulfur stack. C: Assembly mounted in the profile reactor. D: Spatially resolved Raman in operation - fiber tip in the center of the sulfur cylinder.

target product C_2H_4 to CO_2 and H_2O whereas C_2H_6 is obviously preferentially oxidized by gas phase O_2 (Fig. 7.11).

In summary spatial reactor profile measurements can also bring new insight in transition metal oxide catalysis as it becomes possible to correlate measured kinetic data to information about the chemical state of the catalyst. Current developments of the spatial profile technique in the authors lab aim to extend the spatial profile technique to spatially resolved optical spectroscopy as will be described in forthcoming papers. Simultaneous measurement of species, temperature and spectroscopic profiles would provide in-situ information about the catalyst without that quenching and ex-situ characterization will be necessary. With this technique at hand, spatially resolved transients, isotope labeling and other interesting in-situ experiments will become feasible. A proof of principle experiment for spatially resolved Raman spectroscopy is described in the following section. For first catalytic applications, the reader is referred to forthcoming articles.

7.4 Spatially Resolved Fiber Spectroscopy

To demonstrate the principle of spatially resolved optical spectroscopy with a fiber probe inside the species sampling capillary, Raman spectroscopy was chosen as the initial method. An Ar^+ laser (300 mW, 488 nm) was coupled into a bare fluorine doped fused silica fiber (OD = 440 μm). The fiber tip was beveled (cone angle 42 $^\circ$, Fig. 7.4 left) such that the acceptance angle of the fiber was nearly perpendicular to the fiber axis (Fig. 7.4 right). Scattered light was collected by the same fiber and transferred into a fiber bundle consisting of 19 fluorine doped fused silica fibers (OD = 110 μm) arranged in a circular closed package at the reactor side and on top of each other in form of a line (height 2 mm) at the spectrometer side. The scattered light was analyzed by means of a triple filter Raman spectrometer (TriVista S&I GmbH) with a CCD camera as detector operated in subtractive mode.

To study the spatial resolution of this arrangement and the influence of the surrounding sampling capillary a stack of sulfur/graphite cylinders (OD = 15 mm) was prepared so that a sharp transition from a good Raman scatterer (sulfur) to a very poor highly absorbing Raman scatterer (graphite) was created (Fig. 7.12). All cylinders had a central channel fitting the sampling capillary tightly. As shown in Fig. 7.13 the actual measured spectra are a linear superposition of the Raman spectrum of the fiber material (fused silica) and the Raman spectrum of the sample at the place of analysis. To remove the fused silica background blank spectra were measured with high accuracy outside of the graphite/sulfur stack and subtracted after normalization from all spectra measured inside the stack. The difference spectra are plotted as function of position in the right panel of Fig. 7.13. Position accuracy and spatial resolution of the method were determined as shown in Fig. 7.14. One intense sulfur Raman peak at 480 cm^{-1} and one weak sulfur Raman peak at 446 cm^{-1} were integrated and plotted against position (upper panels). This was done both for the data measured when the fiber tip was outside of the sampling capillary (left panels in Fig. 7.14) and when the fiber tip was inside the sampling capillary (right panels in Fig. 7.14). As the step like functions obtained (Fig. 7.14 upper panels) are a convolution between a nearly perfect step function (sulfur – graphite interface) and the spread function of the optical arrangement (fiber + spectrometer), the latter can be obtained by calculating the first derivative of the spatial data around the sulfur – graphite transition (Fig. 7.14 lower panels). The analysis shows that the position accuracy is excellent as only a small offset of about 350 – 370 μm exists.

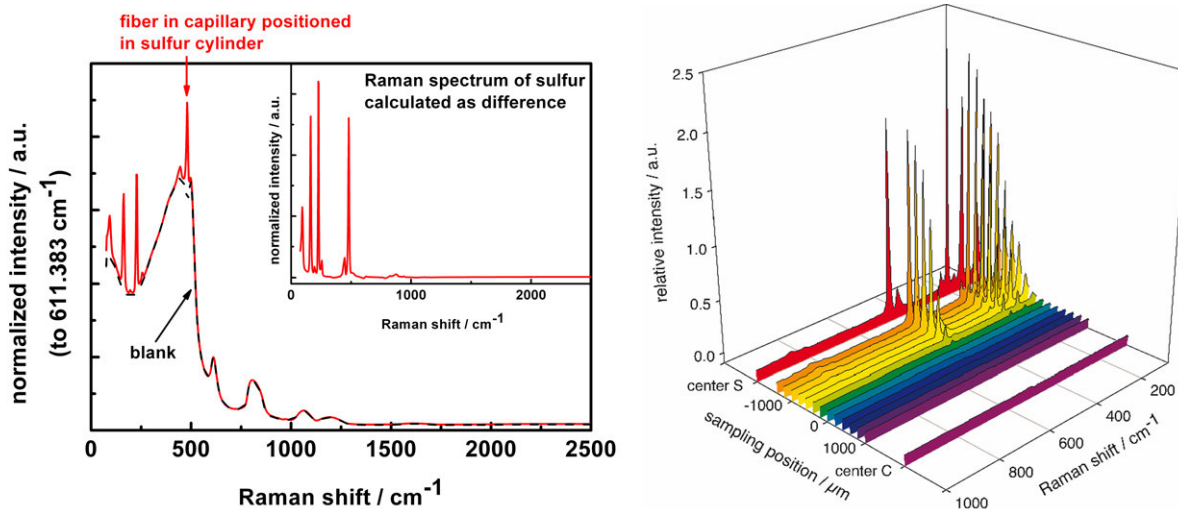


Figure 7.13: Left: Single Raman spectra of the fiber tip in air (blank measurement, dotted line). Raman spectrum with fiber tip positioned in the sulfur cylinder (solid line). Raman spectrum of sulfur calculated as difference (inset). Right: Background corrected Raman spectra measured around the graphite – sulfur transition.

This small offset is due to the fact that the acceptance angle of the fiber is somewhat less than 90 °. The spread function of the optical system can be well fitted by a Gaussian function (solid lines in the lower panels of Fig. 7.14). If the Full Width at Half Maximum (FWHM) of the Gaussian is taken as a measure for the spatial resolution of the method then a spatial resolution of 620 – 650 μm can be achieved, which is more than sufficient for catalysis applications, since most catalytic variations occur over many millimeters if or even centimeters (Section 7.3.1-7.3.6).

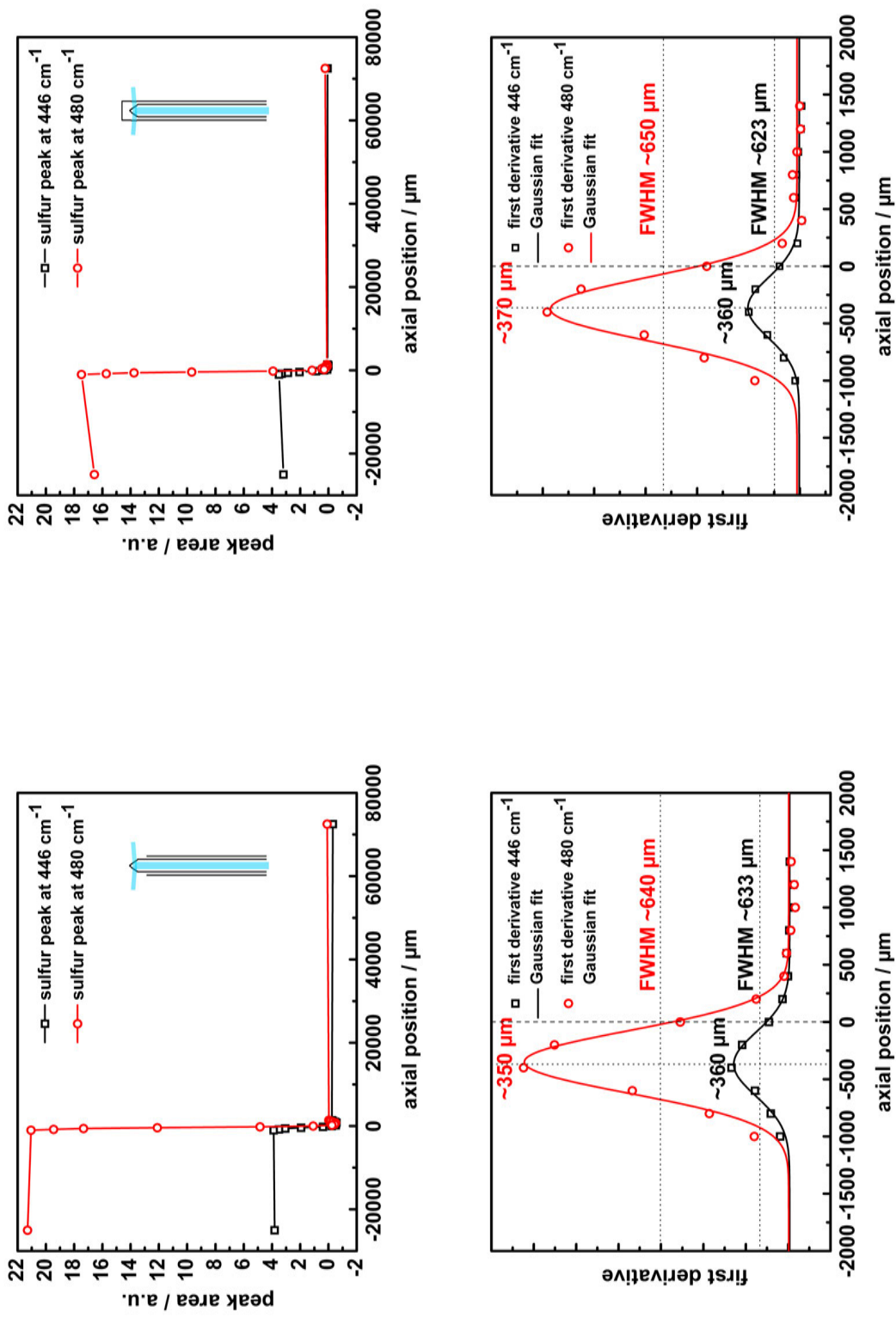


Figure 7.14: Determination of position accuracy and resolution of spatially resolved Raman measurements. Upper Panels: Peak areas of Raman peaks at 446 cm^{-1} and 480 cm^{-1} plotted against tip position with the fiber tip outside of the sampling capillary (left) and inside of the sampling capillary (right). Lower panels: First derivatives (points) fitted by a Gaussian function (solid line).

7.5 Conclusions

In this work the principles and applications of spatial profile measurements in a flow reactor have been demonstrated. This rather new method provides detailed measurements of species concentrations, flow rates, phase temperatures and spectroscopic information as a function of position in a chemical reactor with or without a catalyst. After a detailed description of the method and a brief review of its development, application data are presented and analyzed. By means of demonstration experiments on catalytic partial oxidation of methane on Rh and Pt foam catalysts, methane oxidative coupling in the gas phase and ethane oxidative dehydrogenation on molybdenum oxide catalysts, it is outlined how spatial reactor profiles can be analyzed to extract mechanistic information about the investigated reaction, e.g. whether parallel or consecutive reactions occur, whether a reaction is influenced by transport processes or not and how the catalyst changes due to the changing chemical potential along the flow coordinate. The use of spatial reactor profiles for validation of microkinetic models is also outlined. Because spatial reactor profiles can be measured at temperature and pressure conditions relevant for industrial reactors, the authors believe that this technique is a valuable extension of the currently available experimental toolbox in chemical reaction engineering research and will find more widespread application in the future.

Acknowledgements

Our first and foremost thanks go to Prof. Robert Schlögl for hosting the Emmy Noether Junior Research Group 'High Temperature Catalysis' in his Department of Inorganic Chemistry at the Fritz Haber Institute of the Max Planck Society. We are grateful for his continuous support both with scientific input and funds. We would also like to thank Achim Klein-Hoffmann for shaping our pyrometer and Raman fiber probes. The authors thank the German Research Foundation for funding the High Temperature Catalysis Group within the Emmy Noether Program and the German Federal Ministry of Education and Research for providing further funds within the framework of the Excellence Cluster 'Unifying Concepts in Catalysis'. CFG gratefully acknowledges support from the Alexander von Humboldt Foundation.

Chapter 8

Carbon formation in catalytic partial oxidation of methane on platinum: Model studies on a polycrystalline Pt foil¹

Abstract

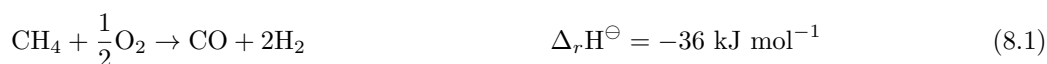
A polycrystalline Pt foil has been investigated as model catalyst in methane catalytic partial oxidation to synthesis gas. It is demonstrated that a substantial amount of carbonaceous deposits forms on the Pt foil upon reaction light-off blocking a large fraction of Pt surface atoms. By using in situ Raman spectroscopy and quantitative spectral analysis the evolution and spatial distribution of these carbonaceous compounds with reaction temperature and reaction time have been characterized. The chemical composition of the carbon material changes from highly reactive and strongly disordered directly after reaction light-off to highly ordered, oxidation and steam reforming resistant after several hours time on stream at 800 °C reaction temperature. Remarkably the carbon distribution at the Pt surface was found to be inhomogeneous and related to the nature of the microcrystals forming the polycrystalline foil in a yet unknown manner.

Keywords

Catalytic partial oxidation, Methane, Synthesis gas, Platinum, Carbon, Raman spectroscopy

8.1 Introduction

The catalytic partial oxidation (CPO) of methane (Eq. 8.1) is a potential technology for decentralized conversion of natural gas, consisting mainly of methane, into synthesis gas or hydrogen. In comparison to industrial synthesis gas production by highly endothermic steam reforming (Eq. 8.2) carried out in large and cost-intensive tube furnaces, methane CPO is exothermic and can produce synthesis gas yields close to thermodynamic equilibrium in millisecond contact times if proper catalysts are chosen. Due to the high rate and exothermicity, technical CPO reactors could be much smaller than steam reformers and could operate adiabatically as the reaction is self sustained and high temperatures favor synthesis gas production over total oxidation (Eq. 8.3).



Hickman and Schmidt [1,57–59] showed that Pt and Rh supported on highly porous α -alumina foam monoliths (porosity > 80 %) make excellent CPO catalysts due to their low pressure drop at outstanding transport

¹Adapted from O. Korup, R. Schlögl, R. Horn *Catal. Today* 181 (1) (2012) 177-183.

characteristics.

By means of spatial reactor profiles it was later shown by Horn et al. [7] that on both Rh and Pt coated foam catalysts syngas formation can be formally described by a combined oxidation (Eq. 8.4) and steam reforming (Eq. 8.2) mechanism. Dry (CO₂) reforming, as sometimes reported in the literature, is not observed [52].

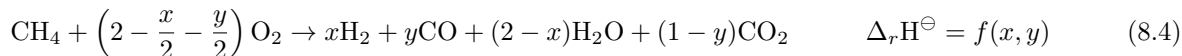


Fig. 8.1 shows a comparison of spatial profiles measured in Rh and Pt foam catalysts for a stoichiometric CH₄/O₂ ratio according to Eq. 8.1 reproduced from [7] with permission by Elsevier. These profiles were measured at exactly equal conditions (equal metal loading, equal reactant stoichiometry, equal flow rate, equal support) reflecting the difference in the catalytic performance of Rh and Pt. It can be seen that even though species and temperature develop similarly in both foam catalysts quantitative differences exist leading to an overall lower methane conversion and lower syngas selectivity at the end of the Pt foam catalyst compared to the Rh foam catalyst ($X_{\text{CH}_4}^{\text{Rh}} = 76\%$, $X_{\text{CH}_4}^{\text{Pt}} = 62\%$, $S_{\text{H}_2}^{\text{Rh}} = 96\%$, $S_{\text{H}_2}^{\text{Pt}} = 65\%$, $S_{\text{CO}}^{\text{Rh}} = 92\%$, $S_{\text{CO}}^{\text{Pt}} = 73\%$).

While it was demonstrated experimentally [10] and numerically [2–4] for Rh foam catalysts that methane CPO is film transport limited under basically all investigated conditions, it was found that methane CPO on Pt foam catalysts is largely kinetically controlled [7, 10]. Indeed it is clearly seen in Fig. 8.1 that reactant conversion and product formation is much slower on the Pt foam catalyst than on the Rh foam catalyst and the question arises why this is the case.

Giving an answer to this question is of considerable interest not only from a fundamental but also from a practical point of view because it could be that the superior catalytic performance of the Rh foam catalyst in terms of methane conversion and synthesis gas selectivity is solely due to the higher reaction rate leading to pronounced film transport limitation and a very low O₂ concentration at the Rh surface as it was numerically predicted by Dalle Nogare et al. [2]. In this case all surface reactions would proceed at the highest physically possible rate, viz. the rate of species transport to the Rh surface, leading to high methane conversion in the oxidation and steam reforming zone (Fig. 8.1). In terms of syngas selectivity a low O₂ concentration at the Rh surface leads to high selectivity to partial oxidation products already at the end of the oxidation zone which is then further improved by rapid steam reforming in the steam reforming zone.

This more physical explanation shines a new light onto the selectivity discussion given in the landmark paper by Hickman and Schmidt [1] where the poorer performance of Pt compared to Rh was attributed solely to a difference in the activation barrier for the surface reaction $\text{H}^* + \text{O}^* \rightarrow \text{OH}^*$ of $E_a^{\text{Pt}} = 20 \text{ kcal mol}^{-1}$ vs. $E_a^{\text{Rh}} = 2.5 \text{ kcal mol}^{-1}$, respectively. It is in fact rather unlikely that such differences in activation barriers have a pronounced influence at temperatures close to 1000 °C and in presence of pronounced film transport limitations such as on Rh.

In the present paper we demonstrate that oxidation and steam reforming resistant carbon deposits form on a Pt surface upon ignition of methane oxidation blocking a large fraction of Pt surface atoms. This observation, even though obtained on a polycrystalline Pt foil as a model system and not yet reproduced for a Pt coated foam catalyst, could be a tentative explanation why methane oxidation and methane steam reforming is significantly slower on Pt compared to Rh with all the catalytic consequences outlined above.

8.2 Experimental

All experiments were conducted in a temperature controlled in situ reactor cell (Linkam Scientific Instruments, type CCR1000) located under a confocal Raman microscope. The reactor was operated at 1atm pressure and could be heated up to 1000 °C using a pre-defined temperature program monitored by a thermocouple in direct thermal contact with the reactor sample holder.

A high purity platinum foil was used as model catalyst (Goodfellow Cambridge Limited, 99.99+ % purity, polycrystalline ~ 4 mm x 4 mm x 0.125 mm) mounted on the inner rim of the reactors virtually unreactive ceramic crucible. The platinum foil was cleaned prior to the experiments by repeated rinsing in diluted nitric acid. After placing the foil in the reactor cell it was further cleaned by oxidation at 800 °C (30 min, 20 vol.% O₂ in Ar, 50 mln min⁻¹) followed by reduction at the same temperature (30 min, 20 vol.% H₂ in Ar, 50 mln min⁻¹) and cooling down to room temperature.

Online gas analytics was accomplished by a calibrated mass spectrometer (Pfeiffer Vacuum) in analog scan mode using the Ar peak at $m/z = 40$ as internal standard.

Raman spectra were recorded by a triple filter Raman spectrometer (TriVista S&I GmbH) with a CCD camera (Princeton Instruments) as detector attached to a confocal microscope (Olympus, 10x long-working distance objective), using an Ar⁺ laser with $\lambda_0 = 488 \text{ nm}$ excitation wavelength (3 mW on the sample). The spectrometer was operated in triple subtractive mode and each spectrum was integrated for 10 min.

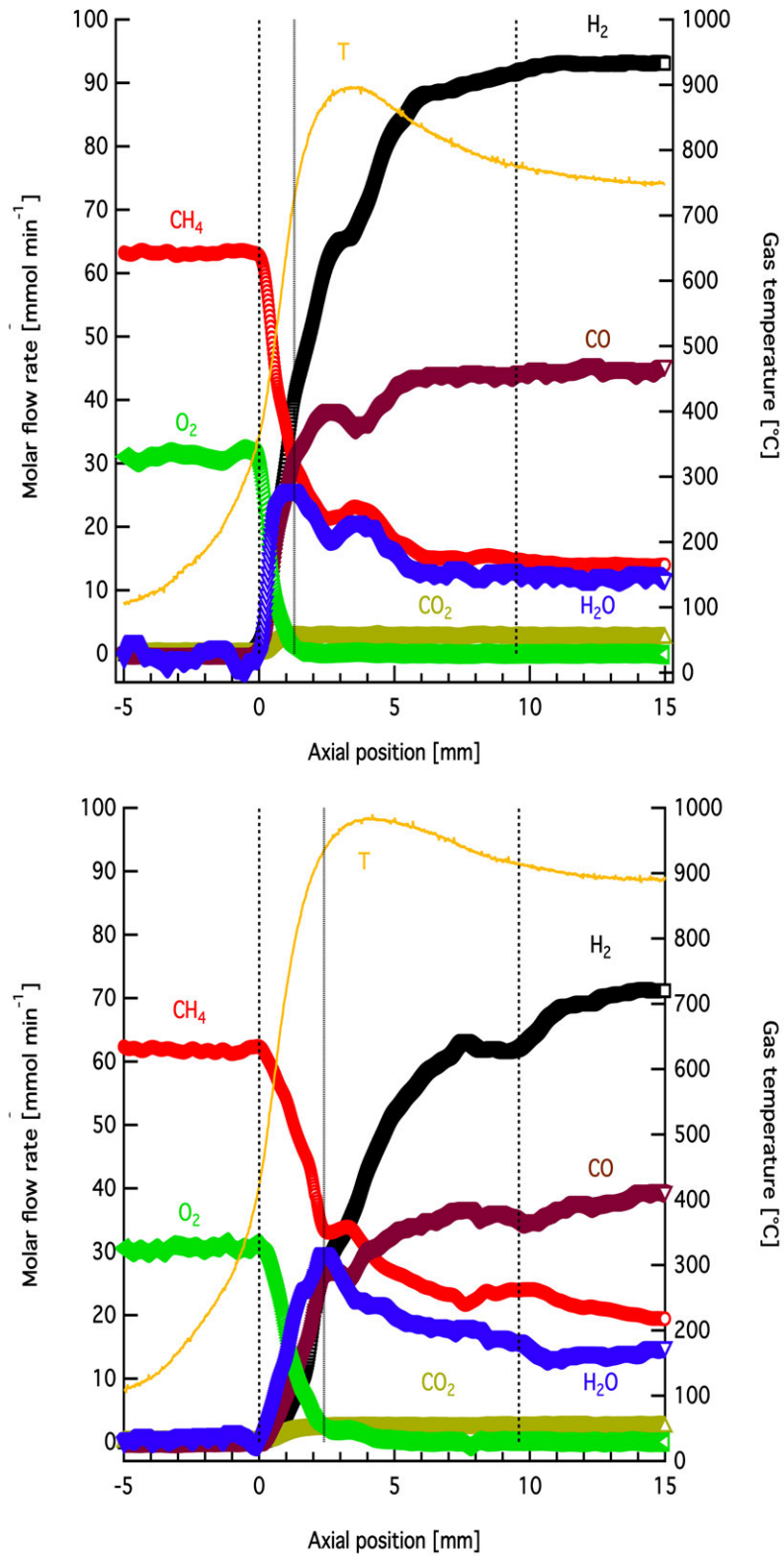


Figure 8.1: Comparison of two spatially resolved species and gas phase temperature profiles for methane CPO on rhodium and platinum. Top: 5 wt% Rh supported on an 80 ppi α -alumina foam monolith of about ~ 10 mm length. Bottom: 5 wt% Pt supported on an analog foam monolith. Total inlet gas feed in both cases $\dot{V}_{\text{CH}_4} + \dot{V}_{\text{O}_2} + \dot{V}_{\text{Ar}} = 4700 \text{ mln min}^{-1}$ at 273 K. Inlet stoichiometry $\text{C/O} = \dot{V}_{\text{CH}_4}/(2 \cdot \dot{V}_{\text{O}_2}) = 1.0$ and $\dot{V}_{\text{Ar}}/\dot{V}_{\text{O}_2} = 3.76$. Catalyst foam between first and last dotted line. Length of oxidation zone indicated by second dotted line. Data reproduced from [7] with permission by Elsevier.

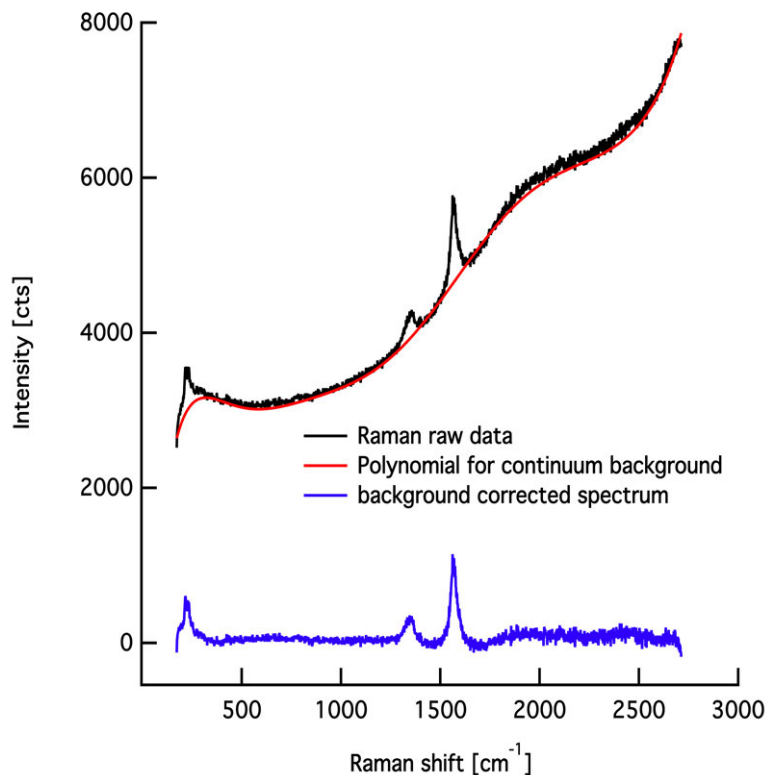


Figure 8.2: Background correction of in-situ Raman spectra of carbonaceous deposits on a platinum foil during CPO of methane recorded at 800 °C reactor temperature. Black: Raman raw data, Red: estimated polynomial for continuum background by black body radiation from the sample adapted from Gornushkin et al. [201] and Blue: background corrected Raman spectrum.

A two point wavelength calibration was used (laser wavelength and first-order Stokes phonon band of Si at 520 cm^{-1}).

At the applied laser wavelength of 488 nm an intense continuum background occurs at temperatures above 600 °C due to black body radiation from the sample. To overcome this problem an algorithm developed by Gornushkin et al. [201] was adapted to automatically eliminate the continuum background without significantly compromising the spectral integrity in the region of interest². An exemplary spectrum of untreated raw data (black trace), estimated black body background (red trace) and corrected spectrum (blue trace) is depicted in Fig. 8.2. For better comparability the baseline corrected spectra were normalized to the G band intensity and fitted depending on the general peak shape. Two cases can be discriminated as shown in Fig.8.3. Baseline separated peaks are fitted by two Lorentzian-shaped bands with maxima at about $\sim 1350 \text{ cm}^{-1}$ (D band) and $\sim 1580 \text{ cm}^{-1}$ (G band) (Fig. 8.3, top panel). If two broad and overlapping Raman bands occur they are fitted by the five peak method proposed by Sadezky et al. [90]. These authors suggest a combination of four Lorentzian-shaped bands labeled D4, D1, G, and D2 centered around 1200, 1350, 1580, and 1620 cm^{-1} respectively, and one Gaussian-shaped D3 band centered around 1500 cm^{-1} . For spectral analysis the Stokes shift band position, full width at half maximum (FWHM), and integrated band intensity were determined from the spectra.

8.3 Results and Discussion

8.3.1 Raman Spectra of Defective Carbon

The first-order Raman spectra of disordered and amorphous carbonaceous materials such as coke or soot are characterized by two broad and usually overlapping peaks with maxima at around $\sim 1350 \text{ cm}^{-1}$ (D peak) and $\sim 1580 \text{ cm}^{-1}$ (G peak). The G or ‘graphite’ peak is attributed to the vibrational mode of in-plane bond stretching motion of sp^2 -hybridized carbon atoms with E_{2g} symmetry in an ideal graphitic lattice [202]. The D or ‘defect’ bands are characteristic for disordered graphite. Their intensity relative to the G peak increases with increasing degree of disorder [203]. The D bands are attributed in literature as follows: The intense D1 band, which is located at about $\sim 1350 \text{ cm}^{-1}$ is associated with the A_{1g} breathing mode of

²The correction was accomplished in two steps by a MATLAB script, which is exemplified in appendix D.

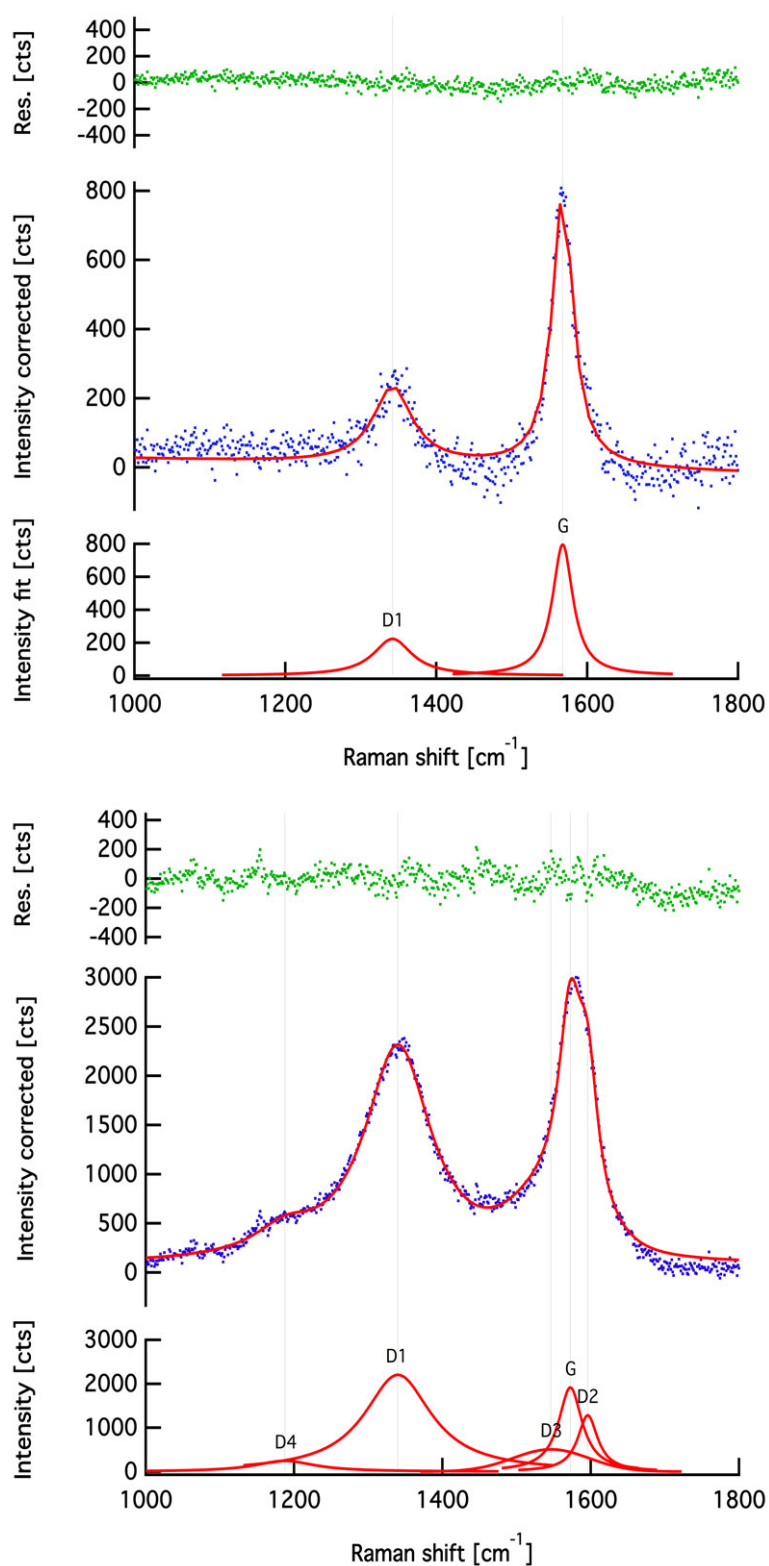


Figure 8.3: Top: Fit of two baseline separated carbon peaks by two Lorentzian-shaped bands [202]. Bottom: Fit of two broad overlapping peaks by combination of four Lorentzian-shaped and one Gaussian-shaped bands after Sadezky et al. [90].

a graphitic lattice. It is assigned to carbon atoms adjacent to lattice disturbance such as graphene layer edges [90,203–205] or a hetero atom in the case of doped graphite [90,205]. The D1 FWHM exhibits a nearly linear negative correlation with the amount of apparent elemental carbon in carbonaceous materials [206,207]. The shoulder of the D1 band at about $\sim 1200\text{ cm}^{-1}$, usually referred to as D4, is assigned to $\text{sp}^2\text{-sp}^3$ bonds or C–C or C=C stretching vibrations of polyene-like structures with A_{1g} symmetry [90,208,209]. The signal intensity between the two main features of the carbon signal is assigned to an additional band D3 located at about $\sim 1500\text{ cm}^{-1}$. The D3 band originates from amorphous carbon species, viz. organic molecules, fragments, and functional groups, on interstitial places in the disturbed graphitic lattice of soot [90,208–211]. For soot and related carbonaceous materials it has been shown that the D3 band intensity together with the D1 band FWHM allow to derive information about the relative abundance and structural order of graphite-like and molecular carbon [90,207]. These spectroscopic parameters give most information on amorphisation/graphitization of a certain carbon material. Finally the G band around $\sim 1580\text{ cm}^{-1}$ is also suggested to be a superposition of two bands in which the additional band at $\sim 1620\text{ cm}^{-1}$ is referred to as D2 band. The D2 band was assigned to a lattice vibration analogous to the G band but involving vibrations of surface graphene layers [90,205].

8.3.2 In-situ Raman Spectra During Temperature Programmed Reaction

A temperature programmed experiment with nine temperature steps from room temperature to $800\text{ }^\circ\text{C}$ reactor temperature was performed to investigate the existence and nature of carbon deposits forming on platinum during methane CPO. The Raman sampling position was chosen arbitrarily close to position 24 in a region with less scratch marks from cut and handling as indicated in Fig. 8.4. At a constant gas feed rate of composition $\dot{V}_{Ar}/\dot{V}_{CH_4}/\dot{V}_{O_2} = 8.94/5.81/2.41\text{ mln min}^{-1}$ respectively ($\text{C/O} = 1.2$), the reactor cell was stepwise heated (heating rate 50 K min^{-1}) starting from room temperature. After the target temperature was reached the temperature was hold for 10 min until the Raman spectrum was taken. Subsequently the next temperature set point was addressed. Fig. 8.5 shows the molar flow rates of the reactants and the products as followed by online mass spectrometry. The reactor temperature set points are indicated by dotted vertical lines and the corresponding Raman spectra were recorded at the dashed line positions. A plot of the G-band normalized Raman spectra is shown in Fig. 8.6.

At ambient temperature up to $300\text{ }^\circ\text{C}$ no reaction was observed as indicated by the constant reactant molar flow rates. No product species were detected. The recorded Raman spectra in this temperature range showed no significant differences in comparison to the clean platinum foil after oxidative and reductive treatment. At a reactor temperature of $400\text{ }^\circ\text{C}$ the oxygen molar flow rate decreased barely visible indicating a beginning of reaction. Water and carbon dioxide are the exclusive reaction products at $400\text{ }^\circ\text{C}$. The minor reactivity detected by the mass spectrometer did not lead to any changes in the Raman spectrum at this temperature, it was still the same as for the clean platinum foil.

Reaction light-off occurred during heating to $500\text{ }^\circ\text{C}$. The methane molar flow rate decreased in a step-like manner under total consumption of oxygen. The reaction products at $500\text{ }^\circ\text{C}$ were that of methane combustion CO_2 and H_2O with only traces of CO being formed. Hydrogen was not yet detected at this temperature. From the catalytic data (Fig. 8.5) it can be seen that the reactant and product molar flow rates stayed approximately constant after the first 10 min upon reaching the next temperature level. In the Raman spectrum the carbon region changed dramatically after reaction light-off, now showing the typical broad and strongly overlapping carbon peaks as described in detail in Section 8.3.1. As outlined in the introduction this carbon formation could block/passivate parts of the active Pt centers in methane CPO explaining why methane CPO on α -alumina supported platinum catalysts is slower than on the corresponding Rh catalysts operating in film transport regime. However this is a hypothesis at the moment as the experimental confirmation on α -alumina supported platinum foam catalysts is still due.

If the temperature was further increased to $600\text{ }^\circ\text{C}$ carbon monoxide and hydrogen were formed in larger amounts. The reactivity plot in Fig. 8.5 shows a significant induction behavior of the methane CPO under this conditions. Immediately after the heating step to $600\text{ }^\circ\text{C}$ the reactivity of the platinum foil is highest as indicated by the step-like increase in methane conversion and carbon monoxide and hydrogen formation. At the same time the molar flow rates of carbon dioxide and water show a mirror like decrease. This initial activity decays then asymptotically to the new steady state activity. For the temperature step to $700\text{ }^\circ\text{C}$ the same response is observed. Immediately after the temperature increase, methane conversion and synthesis gas selectivities are highest but decrease towards a new steady state. Upon switching to $800\text{ }^\circ\text{C}$ the induction period is lost and the new steady state is almost immediately reached.

Fig. 8.6 shows the corresponding Raman spectra recorded at each temperature set point and Table 8.1 summarizes the fitting parameters according to Sadezky et al. [90]. As discussed in Section 8.3.1 the D1 FWHM together with the D3 band intensity can be used as indicators for the chemical nature of carbonaceous materials allowing discrimination between different defective carbon species. Fig. 8.6 shows clearly that the carbon species formed on the platinum surface change their structure significantly as a function of reaction

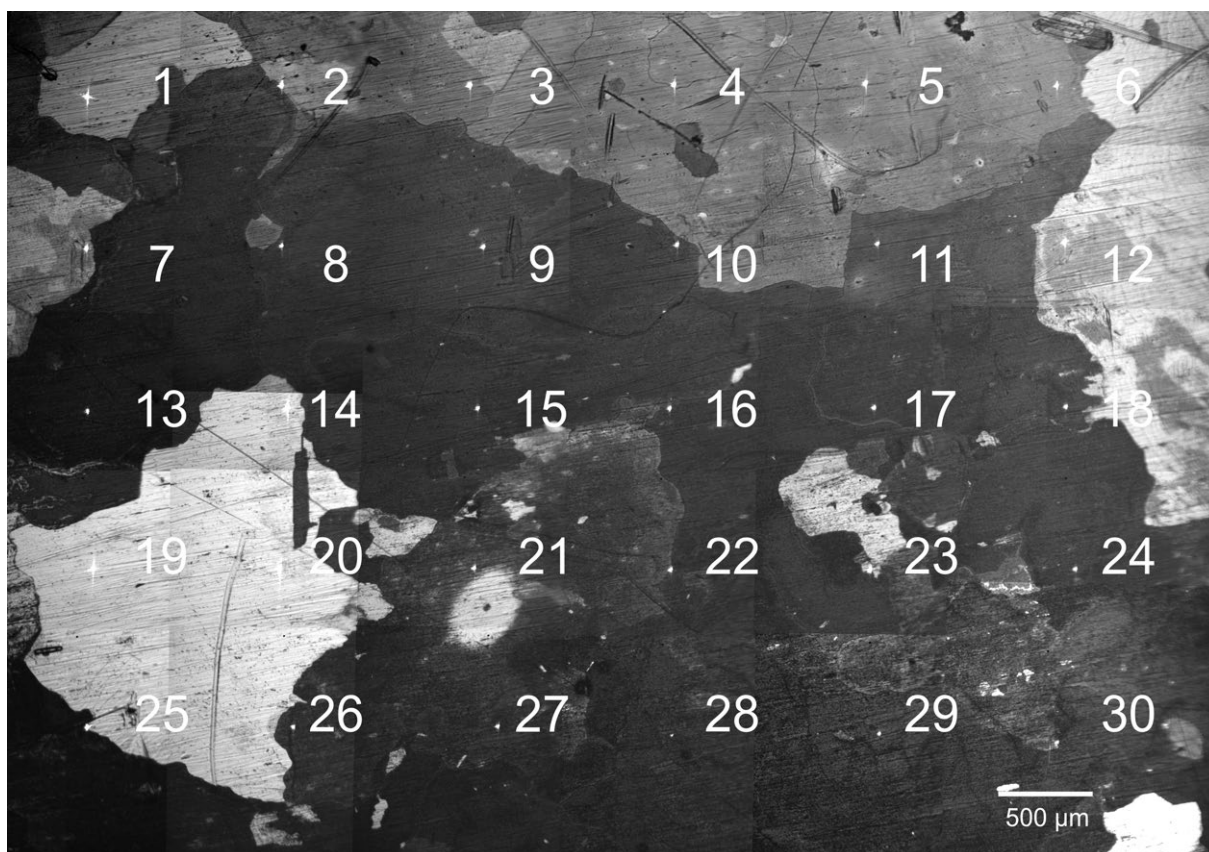
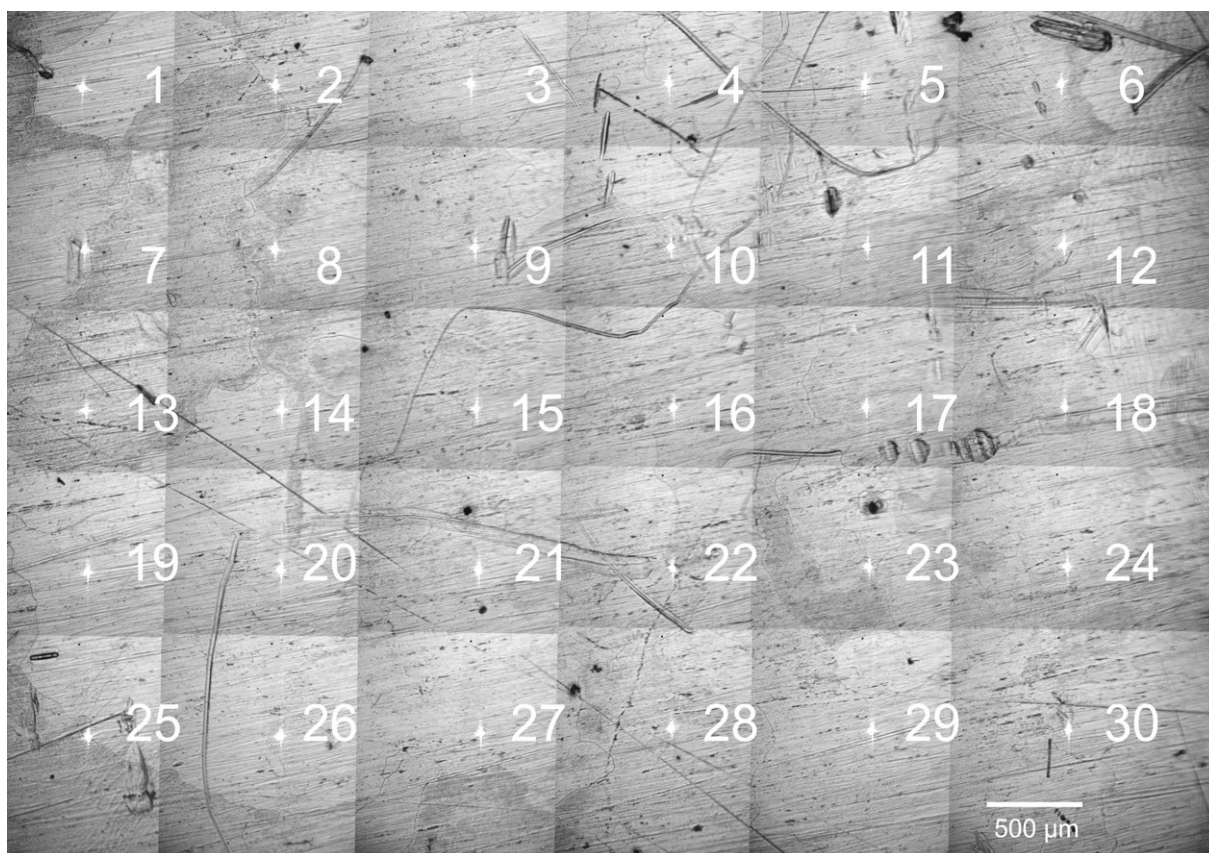


Figure 8.4: Light-optical micrograph of the polycrystalline platinum foil serving as model catalyst in methane CPO. The bright laser spots indicate the Raman sampling positions. Top: Platinum foil after oxidative and reductive cleaning as described in Section 8.2. Bottom: Platinum foil under CPO conditions at $T = 800\text{ }^{\circ}\text{C}$ reactor cell temperature.

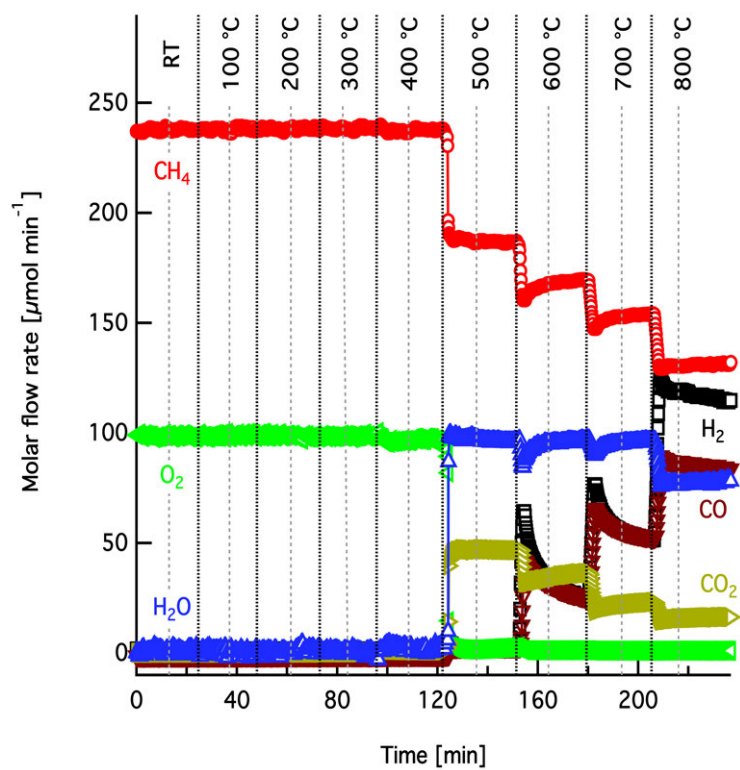


Figure 8.5: Molar flow rates of reactants and products during temperature programmed methane CPO. Dotted lines indicate reactor temperature set points. Dashed lines indicate time coordinates where a corresponding Raman spectra was recorded.

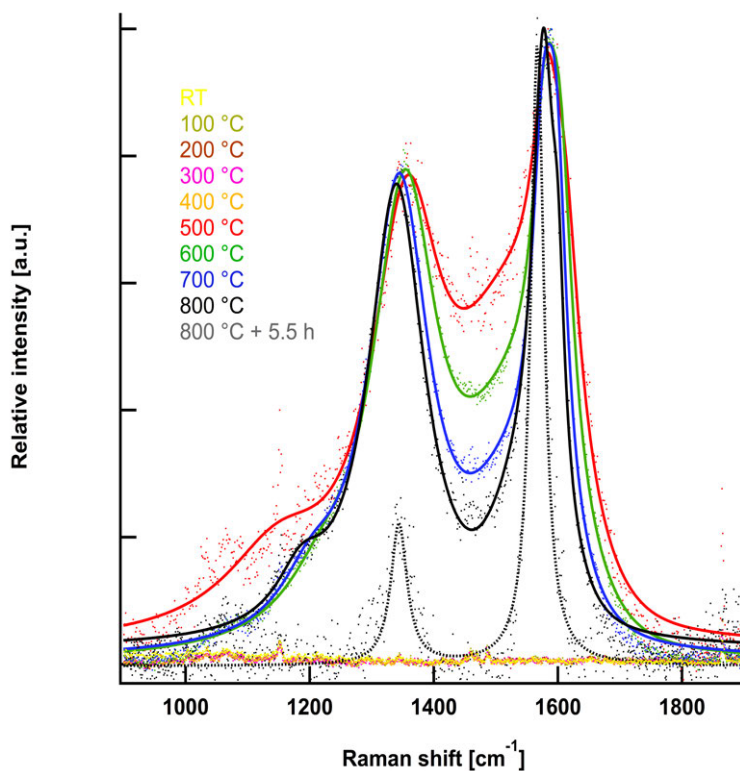


Figure 8.6: Evolution of carbon Raman bands as function of reactor cell temperature. Dots: normalized measured Raman intensity, lines: fit according to Sadezky et al. [90].

temperature. The D3 band intensity decreased by one fourth of its initial value by increasing the temperature from 500 to 800 °C. Simultaneously the D1 FWHM is reduced by more than 20 %. This is a direct evidence for a steady loss in the amorphous molecular carbon fraction and increasing structural order of the initially amorphous coke deposits with increasing temperature. Furthermore the carbon Raman spectra show a pronounced change with time on stream. The dotted spectrum in Fig. 8.6 shows the state of the surface carbon after keeping the reactor temperature at 800 °C for additional 5.5 h under reaction conditions. The spectrum turns into an almost perfect graphite spectrum with two narrow bands at about ~ 1344 and $\sim 1567 \text{ cm}^{-1}$. Obviously, under the investigated conditions the highly reactive molecular carbon species are gasified either by oxidation or by methanation with time on stream from the Pt surface. Due to the totally defect controlled reactivity of carbon materials only unreactive, highly ordered carbon is left behind.

Table 8.1: Fitting parameters for quantitative spectral analysis of carbon Raman bands formed during temperature programmed methane CPO on a platinum foil according to the five band fitting procedure proposed by Sadezky et al. [90].

T [°C]	D4 pos. [cm ⁻¹]	D4 FWHM [cm ⁻¹]	D4 area [a.u.]	D1 pos. [cm ⁻¹]	D1 FWHM [cm ⁻¹]	D1 area [a.u.]	D3 pos. [cm ⁻¹]	D3 FWHM [cm ⁻¹]
RT-400	—	—	—	—	—	—	—	—
500	1149	211.5	41.4	1356	142.5	149.9	1528	187.5
600	1221	144.8	16.0	1354	129.8	149.9	1536	179.6
700	1203	119.0	14.9	1345	120.0	140.2	1536	154.7
800	1187	96.7	12.1	1340	111.1	125.5	1550	116.2
800	—	—	—	1344	31.6	11.1	—	—

T [°C]	D3 area [a.u.]	G pos. [cm ⁻¹]	G FWHM [cm ⁻¹]	G area [a.u.]	D2 pos. [cm ⁻¹]	D2 FWHM [cm ⁻¹]	D2 area [a.u.]
RT-400	—	—	—	—	—	—	—
500	80.5	1581	57.3	34.6	1612	60.9	30.7
600	57.7	1579	50.7	35.4	1605	48.0	31.9
700	33.4	1576	44.5	34.1	1598	41.1	31.8
800	21.6	1577	42.5	48.7	1600	25.0	10.6
800	—	1567	26.0	40.0	—	—	—

8.4 In-situ Raman x,y-Mapping of Platinum Foil During Methane CPO

To confirm the observations described above and obtain a more generalized picture of the platinum foil, a 6 x 5 grid of sampling points was selected to cover the entire Pt foil uniformly. Fig. 8.4 enumerates the sampling positions indicated by the bright laser dots in the displayed composite light-optical micrographs. The clean platinum foil was heated to 800 °C reactor temperature with 50 K min⁻¹ under a constant gas feed of $\dot{V}_{Ar}/\dot{V}_{CH_4}/\dot{V}_{O_2} = 11.73/11.42/2.84$ mln min⁻¹ respectively corresponding to a C/O ratio of 2.0. After about ~ 16 min the final reactor cell temperature was reached where the Pt foil was hold for another 30 min time on stream before the first Raman spectrum was measured at sampling position 1. After the first spectrum was taken all other positions were addressed successively by computer controlled movement of the reactor cell mounted on the x, y, z microscope table under the fixed laser focus. Fig. 8.7 shows the molar flow rates of reactant and products measured by online mass spectrometry during the mapping experiment. After reaction light-off oxygen is fully consumed but the initial high methane conversion decreased quickly within the first ~ 10 min accompanied by a decrease in all product flow rates. With further time on stream the flow rates of H₂, CO increase slightly before they reach steady state at about ~ 3 h time on stream. The first Raman spectrum (position 1) was recorded after the strong initial reactivity changes had leveled off. Prior measuring of the Raman spectra a light-optical micrograph was recorded at each sampling position. The right panel of Fig. 8.4 depicts a superposition of all sampling positions during the mapping experiment together with a panoramic view of the entire foil. Already from the light-optical micrograph the coke deposits covering the platinum foil can be identified. Remarkably, the surface is not evenly covered by carbon deposits but rather distinct zones of higher and lower gray contrast can be discriminated, which are separated by sharp boundaries. By their size and shape these zones can be assigned to the randomly oriented crystallites forming the foil microstructure. Generally, highly graphitized carbon species can be identified. Most of the sampling positions resemble each other and exhibit two sharp carbon bands, located at about ~ 1344 (D1) and ~ 1567 cm⁻¹ (G). The blue trace in Fig. 8.8, left panel, recorded at sampling position 15 represents this most common peak shape. The right graph in Fig. 8.8 shows the relative D band intensity ((D1 area)/(G area) or (D4+D1 area)/(G+D2 area)) as a function of the gray level in the light-optical micrographs from Fig. 8.4 and allows discrimination between sampling positions with different spectral information. The majority of sampling points concentrate at a relative D intensity around 0.5 or smaller and medium to dark gray level. Deviations from the average spectral shape and therefore position in Fig. 8.8 will be highlighted in the following.

Position one and two are apparently covered by the defect richest carbon which is in line with the results discussed earlier showing that amorphous and inhomogeneous carbon species are formed after reaction light-off. The black trace in Fig. 8.8 shows the Raman spectrum recorded at position one. The peak shape is broader than all other spectra and D and G band are strongly overlapping. The G band maximum is significantly shifted to higher wavenumbers compared to all other spectra due to a rather high D2 band intensity. In the Raman spectrum measured at position two a shoulder to the G band can still be discerned but much less pronounced than at position one. With longer time on stream the rather reactive amorphous carbon is being removed from the surface or converted into an oxidation resistant highly ordered planar carbon. For all spectra measured later than position two the five band fitting procedure suggested by Sadezky and coworkers [90] does no longer lead to converging results due to the graphite-like nature of the carbon surface species. It can therefore be estimated that the structural changes of the initial carbon species are largely finished within 1 h after reaction light-off.

Positions 7, 14, and 25 gave Raman spectra of significantly lower signal intensity as can be seen in Fig. 8.8 on the lower signal to noise ratio, represented by the green trace in Fig. 8.8 (left panel). Even though the intensity of a Raman band cannot be easily correlated with the surface concentration of a particular species, it can be assumed the the amount of surface carbon is less than for the other sampling positions in agreement with the gray contrast observed in the light-optical micrograph (Fig. 8.4, right panel).

Position 19 and 20 attract particular attention (represented by red trace in Fig. 8.8, left panel), because they do not exhibit any detectable carbon bands. Also the crystallite that is probed at these positions looks rather metallic in the light-optical micrograph. This is an remarkable finding which has important consequences for the microkinetic modeling of such reactions in which all catalytic sites are always treated alike which is called the ‘mean field approach’ [2, 4].

The origin of this interesting phenomenon can not be explained so far and needs further investigation. But the fact that some foil domains coke strong and some do not or weaker suggests that the reaction is structure sensitive. It is well known from surface science literature that the activity for breaking H–H, C–H, and C–C bonds is controlled by surface irregularities, steps, and kinks. Their abundance and accessibility direct the selectivity and activity in hydrocarbon conversion. Dehydrogenation reactions on Pt are controlled by the step density of a Pt single crystal surface [91]. The step density is determined by the angle and orientation

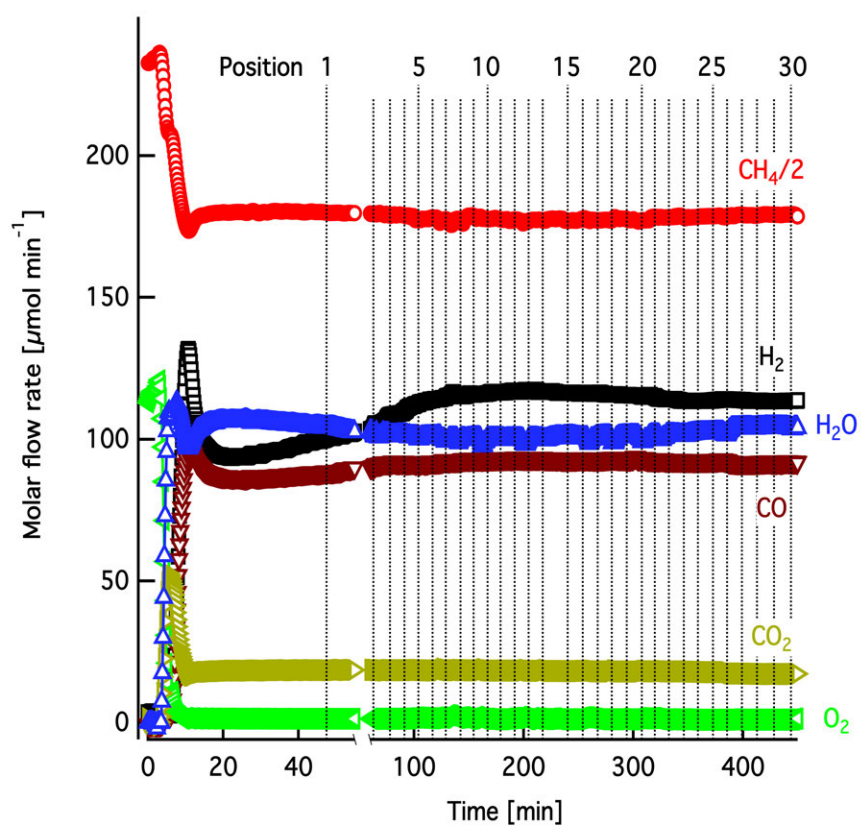


Figure 8.7: Reactant and product molar flow rates measured during the in-situ Raman mapping experiment under methane CPO conditions. Dotted vertical lines indicate the time coordinate where Raman spectra were recorded. Positions correlate with Fig. 8.4.

of the crystal phase. For this reason the observed inhomogeneous carbon distribution could reflect domains with higher and lower step density, respectively reactivity. Furthermore surface additives are influencing the working catalyst. These additives are deposited reversibly or irreversibly by the catalyst pretreatment, by the reaction mixture under the conditions of reaction, by addition of a promotor, or by migration of bulk impurities to the surface. A contamination from the reactor cell itself can cause surface additives, too. These add species may also cause structural reconstruction or subsurface chemistry.

8.5 Conclusions

The results presented in this paper give evidence for a substantial formation of surface carbon in methane CPO over a polycrystalline platinum foil. Using in-situ Raman spectroscopy and spectral analysis by curve fitting with five first-order Raman bands (G, D1, D2, D3, D4) according to [90], formation, evolution and nature of surface carbon could be characterized. Highly defective and inhomogeneous carbonaceous compounds are directly formed after reaction light-off and transformed into ordered graphite-like species. This transformation occurs on a timescale of several ten minutes up to approximately one hour. The carbon distribution at the Pt surface was found to be inhomogeneous and somehow related to the nature of the micro-crystals making up the polycrystalline Pt foil. The exact origin of this unisotropy is not yet understood and needs further systematic investigation. The blockage of Pt surface sites by oxidation resistant graphitic carbon could be the reason why methane CPO on Pt proceeds much slower and with poorer synthesis gas selectivity compared to Rh which operates reportedly in a film transport limited regime at low surface coverage. With respect to literature published on microkinetic modeling of methane CPO on Pt (e.g. [70,72]) it can be concluded that these models have to be revised as they predict an empty Pt surface under methane CPO conditions and do neither consider multilayer carbon formation on the Pt surface nor the inhomogeneities observed in the present study.

Acknowledgements

All authors thank the German Research Foundation for funding the Emmy-Noether-Junior-Research-Group "High Temperature Catalysis". Further support was provided by the German Federal Ministry of Education and Research within the framework of the Excellence Cluster "Unifying Concepts in Catalysis".

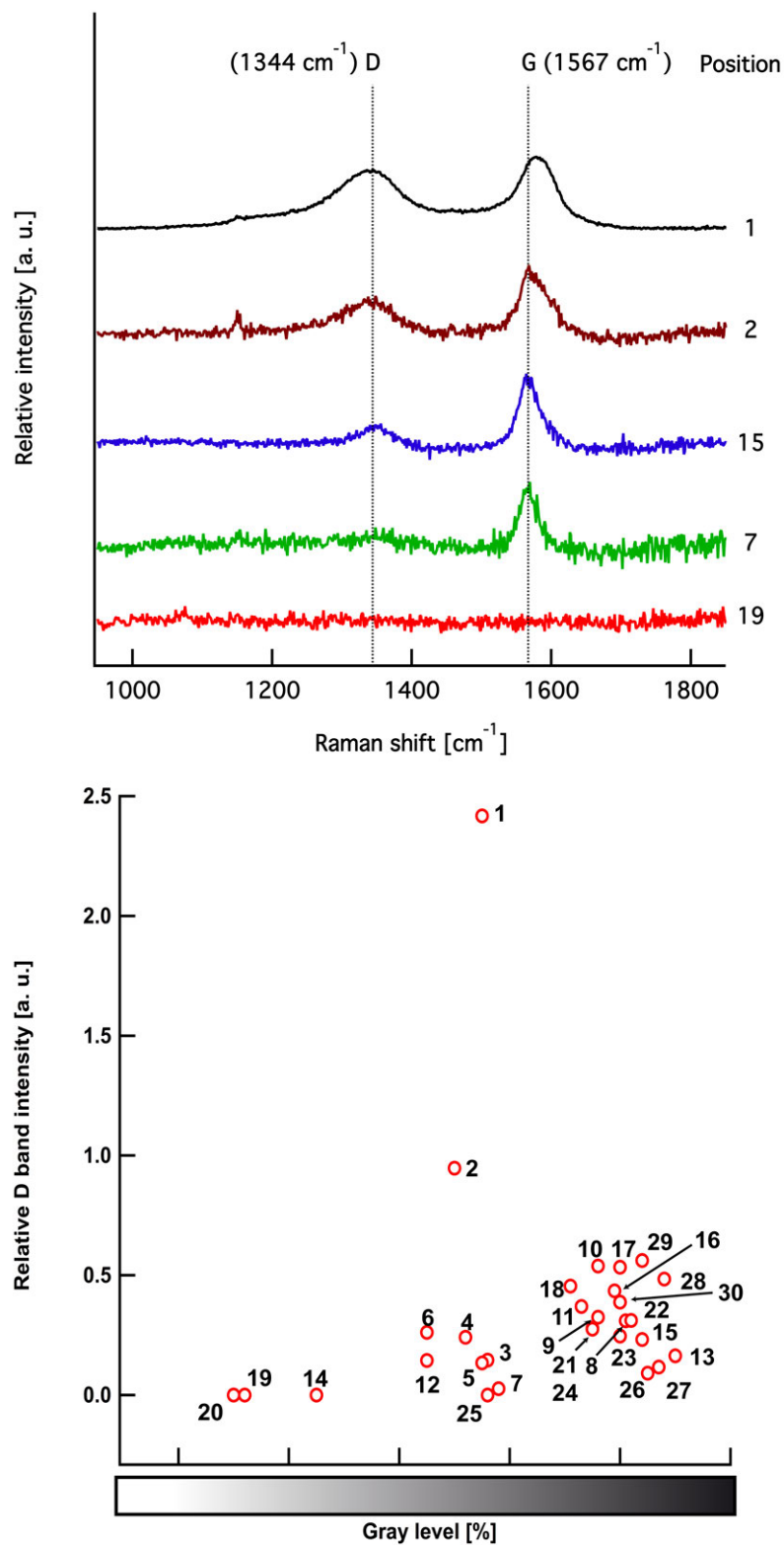


Figure 8.8: Top: Selected in-situ Raman spectra recorded during methane CPO on a polycrystalline platinum foil. Spectra are normalized to the G band maximum for better comparability. Bottom: Cloud plot of relative D band intensity as a function of observed gray level in the light-optical micrographs of Fig. 8.4 right. Positions correlate with Fig. 8.4.

Chapter 9

Catalytic Partial Oxidation of Methane on Platinum Investigated by Spatial Reactor Profiles, Spatially Resolved Spectroscopy, and Microkinetic Modeling¹

Abstract

Spatially resolved profile measurements, Raman spectroscopy, electron microscopy, and microkinetic modeling have been used to study the catalytic partial oxidation of methane on Pt. The measured species profiles through Pt coated foam catalysts exhibit a two-zone structure: an abrupt change in reaction rates separates the fast exothermic oxidation chemistry at the entrance of the reactor from the slow endothermic reforming chemistry. Spatially resolved Raman spectroscopy and electron microscopy confirm that the position of the mechanistic change could be correlated with Pt transportation and formation of carbonaceous deposits blocking the majority of active Pt sites in the reforming zone. The species profiles were simulated using a pseudo-2D heterogeneous model, which includes heat and mass transport limitations, and two state-of-the-art chemical kinetic mechanisms. Although both mechanisms are in quantitative agreement with the oxygen profiles, the two mechanisms differ substantially in their predictions of the branching ratio between partial and complete oxidation, as well as surface site coverages. The experimentally observed change in reaction rates is attributed to carbon formation, which the mechanisms are unable to reproduce, since they do not include carbon-carbon coupling reactions.

Keywords

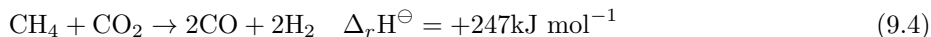
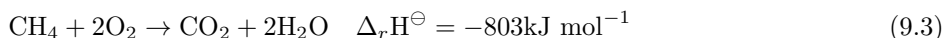
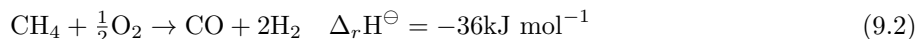
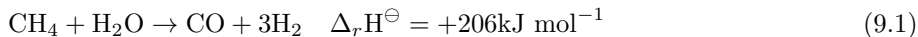
Catalytic partial oxidation, Methane, Synthesis gas, Platinum, Microkinetic modeling, Carbon formation, Raman spectroscopy, Electron microscopy

9.1 Introduction

Methane steam reforming (Eq. 9.1) is currently the dominant technology for synthesis gas production [39]. The process is highly endothermic, and industrial production requires large and capital-intensive operations. Catalytic partial oxidation (CPO) of methane (Eq. 9.2) is an attractive alternative, since it is slightly exothermic and considerably faster, with nearly equilibrium yields in synthesis gas within millisecond contact

¹Submitted to Journal of Catalysis. Authors: O. Korup, C. F. Goldsmith, G. Weinberg, M. Geske, T. Kandemir, R. Schlögl, R. Horn

times [1, 57–59], possibly in autothermal operation.



The global mechanism by which methane is oxidized to synthesis gas on noble metal catalysts is frequently debated in the literature. One school of thought suggests that the mechanism must be a two-step process that consists of initially highly exothermic methane complete oxidation (Eq. 9.3) followed by endothermic reforming reactions, i.e. steam (Eq. 9.1) and dry reforming (Eq. 9.4). The main argument is a commonly observed steep temperature gradient over the catalyst bed [36, 53]. Investigations of product selectivities demonstrated that the CO_2 and H_2O selectivity increased with simultaneous synthesis gas loss by either increasing the space velocity or increasing the O_2/CH_4 ratio [36, 54, 55]. Additionally, transient experiments did not indicate a direct reaction pathway [64–66]. In contrast, authors proposed a single step process. Experiments on Pt and Pt/10 % Rh meshes and millisecond contact time suggest a direct reaction pathway, as the increasing synthesis gas selectivity with decreasing contact time cannot be explained by the two step mechanism [56, 59, 62, 63].

Due to the exothermicity and rapidness of catalytic methane oxidation, differential reactant conversion cannot be achieved; furthermore, irreducible transport limitations exist under these conditions. Consequently, classical kinetic studies by contact time variations are nearly impossible, since changing flow rates leads to unclear transport characteristics and hot spot formation. Furthermore, discussions that rely on global mechanism descriptions can be misleading, since in reality the catalytic partial oxidation of methane is neither a single-step nor two-step process, but a mechanism involving dozens of elementary reactions. Which product channels are favored at a given position is a complex function of the reaction rates, which in turn are influenced by the chemical potential of the gases in contact with the surface. Microkinetic modeling – using a chemical kinetic mechanism composed of reactive intermediates and elementary reactions, coupled with a description of the flow field including heat- and mass-transport limitations – is a valuable tool in resolving the debate over CPO. A properly validated microkinetic model can be used not only to answer questions regarding the underlying mechanism, but it can also be used to predict product yields under new reactor conditions, potentially saving time and money.

High-resolution reactor profiles can be measured via the capillary sampling technique developed by Horn et al. [5], providing profiles of species and temperature with sub-millimeter resolution. The reactant conversion and product formation can be followed as a function of position, and the obtained reactor profiles can be used for testing of kinetic models.

The previous work on methane CPO on Rh and Pt supported on ceramic foam monoliths [2, 5, 7, 10] gave clear evidence that both partial and complete methane oxidation proceeds in parallel in a narrow oxidation zone at the entrance of the catalyst foam. This oxidation zone is followed by a longer endothermic steam reforming zone, and at sufficiently low catalyst temperatures, water gas shift is also observed. Dry reforming does not have a significant impact. The studies found Rh superior in synthesis gas selectivity over Pt [7, 10], and no catalyst deactivation was observed over the investigated time period. The high synthesis gas selectivity on the Rh catalyst was investigated by microkinetic modeling with consideration of transport phenomena [2, 3]. A strong transport limitation within the oxidation zone was found. It was concluded that the coexistence of H_2 and CO in the oxidation zone in presence of O_2 and at the high local temperatures is due to a strong O_2 deficit at the Rh surface. For Pt such a detailed analysis is missing so far.

Recently it was suggested that the transport limitations for a Pt-coated foam monolith are less pronounced than on a Rh-coated foam monolith under similar conditions [83]. Nonetheless, a significant selectivity to synthesis gas can be achieved with the Pt catalyst in the presence of gas phase oxygen.

In this paper methane CPO on Pt coated foam monoliths is investigated. A pseudo-2D heterogeneous reactor model accounting for mass and heat transport has been developed and is combined with two state-of-the-art microkinetic models. The microkinetic models are tested against high resolution spatial reactor profiles. Peculiar features in the species profiles have been investigated by spatially resolved Raman spectroscopy and electron microscopy providing new impulses for model improvements.

9.2 Experimental

9.2.1 Catalyst Preparation

The catalysts used in this study are Pt coated, cylindrical $\alpha\text{-Al}_2\text{O}_3$ foam monoliths with a pore density of 80 ppi (pores per linear inch). The monoliths (length = 20 mm and diameter = 16.2 mm) were prepared by

incipient wetness impregnation with aqueous H_2PtCl_6 as precursor. Prior to impregnation the foam support was cut to the desired length and a centerline channel of 1 mm diameter was drilled through the foam. The foams were washed in acetone in order to remove any residuals from the cooling fluid, then boiled in nitric acid to remove possible metal contaminations from the drilling and confectioning step. Next the support was dried and calcined at 800 °C in static air. The impregnation was done in a multi-step approach, in which the foams were soaked in the precursor solution by dropwise addition of liquid on the foams. The precursor solution consisted of 7 ml deionized water (Millipore) and the equivalent amount of $\text{H}_2\text{PtCl}_6 \cdot 6 \text{H}_2\text{O}$ (Alfa Aesar, 99.95 % purity, 37-40 % Pt content) corresponding to a nominal Pt loading of 1 wt%. The freshly impregnated foams were then vacuum dried at room temperature over night, and the procedure was repeated until the entire precursor solution had been applied. After the last drying step the foams were reduced in a tubular furnace in 7 vol% H_2 in Ar ($\dot{V}_{\text{total}} = 3000 \text{ mln min}^{-1}$) at a monolith core temperature of 500 °C for 5 h. After reduction the Pt loading was determined by gravimetry. An average loading of 1 wt% Pt was found.

9.2.2 Catalytic Testing

The capillary sampling technique used in the present work has been described in detail previously [5], and only a brief summary will be provided here. The reactor uses a fused silica capillary with side orifice to sample a small gas volume from the centerline symmetry axis of the catalyst bed and to transfer it to the gas analytic devices. Here, online gas analytics were accomplished by a calibrated mass spectrometer (Pfeiffer Vacuum) operated in analog scan mode and applying the Ar peak at $m/z = 40$ as internal standard. The sampling capillary additionally accommodates an optical fused silica fiber with conical shaped tip connected to a two-color ratio pyrometer. The sampling capillary/pyrometer tip probe allows for simultaneous species analysis with surface temperature measurements through the catalyst bed. The catalysts were operated under auto-thermal operation conditions.

In the present work two distinct catalyst foams were investigated: One foam was left intact, whereas a second foam was sliced in half lengthwise prior to impregnation (see Section 9.4.2 for details). Both monoliths were tested in the same way. The catalyst foam monoliths were sandwiched in between two clean 80 ppi foam monoliths of 10 mm length serving as heat shields to reduce radiative heat losses. Fig. 9.1 depicts the catalyst stack made up by two half monoliths prior to installation in the reactor. The catalyst stack was wrapped in a ceramic mate (3M Interam) and gas tightly fit in the center of the reactor tube. Next, the stack was heated in reaction atmosphere until reaction light-off. Subsequently, the reactor furnace was switched off and profiles were measured after the furnace temperature reached a steady state in autothermal reactor operation.

9.2.3 Catalyst Characterization

After catalytic testing, the foam monoliths were characterized by means of geometric, BET and Pt surface area, as well as by metal dispersion and Pt crystallite size.

To determine the fluid-dynamically relevant foam surface area, i.e. geometric surface area of the struts, lab X-ray micro-computer-tomography (μ -CT) was applied. The μ -CT apparatus [142, 143] used to characterize the foam monolith consisted of a micro-focus 150 kV X-ray source with a tungsten target and a flat $120 \times 120 \text{ mm}^2$ panel detector, both from Hamamatsu. Source and detector are static in this setup and the foam monolith was rotated by 360° , while every 0.28° a projection was acquired. Using the Octopus V8.5 software [212] the foam volume was reconstructed. The corresponding voxel size of the reconstructed volume is $15 \mu\text{m}$. The geometric surface area was determined using VGStudio MAX V2.1 [213].

Because the struts of the ceramic foam are not ideally flat, but contain a certain amount of surface roughness, cracks, and fractures, the effective surface area differs by approximately one to two orders of magnitude from the geometric surface area by μ -CT [190, 214] and needs to be determined by a complementary technique. The effective surface area was therefore determined by isothermal adsorption of krypton at 77 K by the static-volumetric method (Quantachrom Autosorb-1).

The accessible Pt surface area and metal dispersion were measured on coarsely crushed samples after the reaction tests by determining the hydrogen monolayer coverage capacity by chemisorption at 40 °C in a Quantachrom Autosorb-1 apparatus. How the different surface areas are utilized in microkinetic modeling is specified in Section 9.3.

Raman spectra presented in this work were recorded by a triple filter Raman spectrometer (TriVista S&I GmbH) with a liquid nitrogen cooled CCD camera (Princeton Instruments) as detector. The spectrometer was attached to a confocal microscope (Olympus, 10 \times long-working distance objective), using an Ar^+ laser with $\lambda = 488 \text{ nm}$ excitation wavelength (2.2 mW on the sample). The microscope is equipped with a motorized optical table that allows reproducible positioning with μm resolution. The spectrometer was operated in triple subtractive mode and each spectrum was integrated for 10 min. A two point wavelength calibration

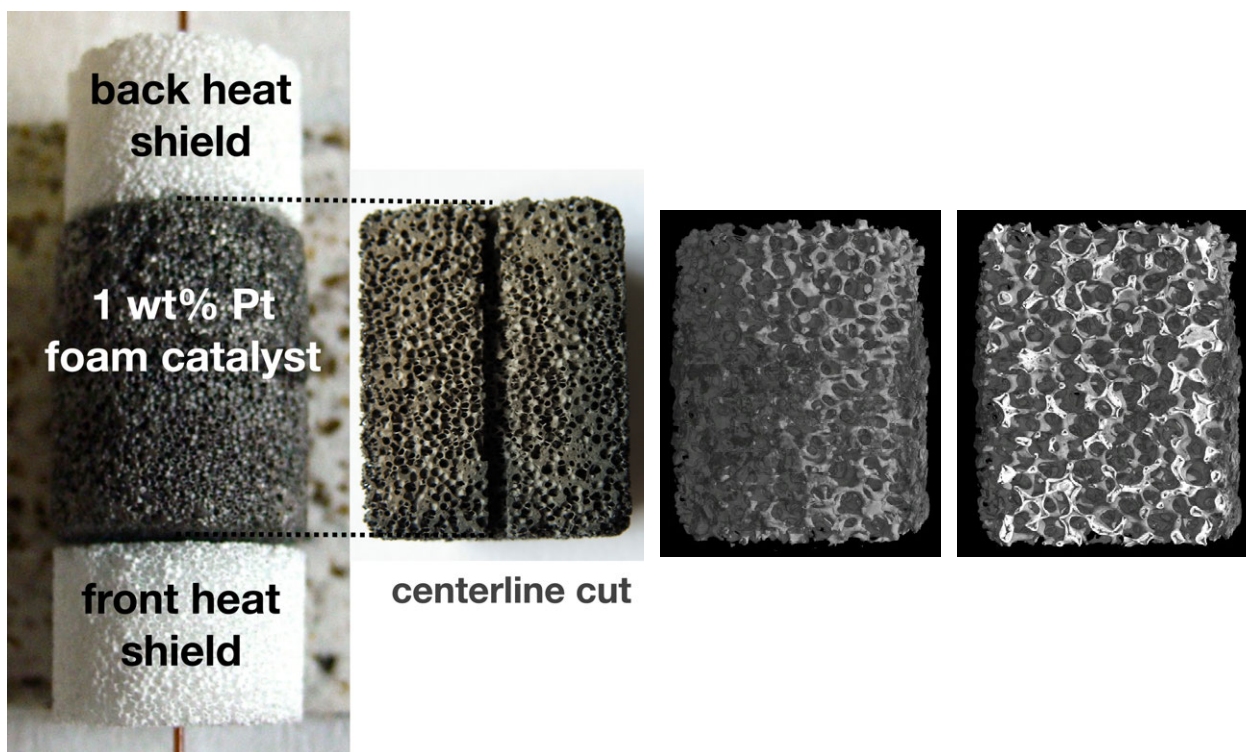


Figure 9.1: Left: Photograph of catalyst stack before reaction test, with one half foam monolith showing the centerline channel. Right: Foam structure visualization of the reconstruction of an intact foam monolith from X-ray μ -CT (overview and intermediate cut). For better visualization μ -CTs from a 45 ppi foam are shown.

was used (laser wavelength and first-order Stokes phonon band of Si at 520 cm^{-1}). The Raman spectra included a broad continuum like background, which was subtracted applying the method of Gornushkin et al. [201].

To add additional topographical and morphological information of the catalyst and support, scanning electron microscopy was applied to the half monolith sample, prior to and after reaction test. A Hitachi S-4800 FEG (cold) SEM was used. Due to interference by charging of the mostly insulating catalyst foams a FEI Quanta 200 FEG (hot) ESEM was used to address these perturbations, if necessary. A low vacuum with 60 Pa water pressure was applied. Both SEMs are equipped with an EDAX Genesis 4000 System (Vers. 6.1) and an energy dispersive X-ray detector.

The Pt particle size was determined after reaction tests and powdering the foam monolith by full powder XRD pattern fitting using the Rietveld method. The integral breadth-based volume weighted mean crystallite size (L Vol-IB) of Pt was determined assuming that all Pt particles are spherical and single domain. The particle diameter d is given by

$$d = 4/3 \text{ LVol-IB} \quad (9.5)$$

Powder XRD was measured on a Bruker D8 Advance theta/ theta diffractometer.

9.3 Numerical Modeling

9.3.1 Model Equations

To model the detailed chemistry for methane partial oxidation inside a Pt-coated α -alumina foam monolith, a pseudo-2D heterogeneous reactor model including transport phenomena is used. The system consists of three phases: a bulk gas phase, a boundary layer gas phase, and a chemically reactive surface. The coupling between chemistry and transport is modeled using a simplified system of Navier-Stokes equations for the conservation of mass, momentum, and energy, including conservation equations for N_{gas} gas-phase species in the gas bulk and in the gas boundary layer and $N_{surface}$ surface species on the surface. Gas-phase reactions are neglected, because they are not significant at atmospheric pressure [2, 3, 215]. In the following, the bulk gas phase is denoted with no subscript; the surface is denoted with a subscript s ; and boundary layer variables are denoted with a subscript bl . Fig. 9.2 depicts schematically the modeling domains. In this work the following simplifying assumptions have been made:

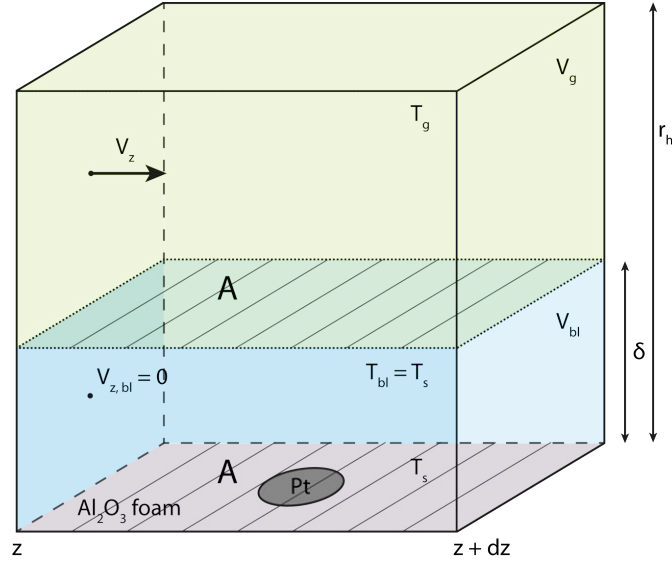


Figure 9.2: Sketch of volume element illustrating the modeling domains. δ strongly exaggerated for illustration purpose ($\delta \ll r_h$).

1. The gases are ideal.
2. Given the high flow rates of the gas, the radial symmetry, the small pore diameter, and the high heat-transfer rates of the foam, we assume that there are no spatial gradients in the r and ϕ direction: $\nabla x = \frac{\partial x_z}{\partial z} \vec{e}_z$.
3. There is convective transport in the bulk gas phase, but no convective transport in the boundary layer: $v = v_z, v_{z,bl} = 0$.
4. The boundary layer is assumed to be thin enough that the surface area of the boundary layer is equal to the surface area of the foam: $A_{bl} = A_s = A$.
5. The small cracks and pores within the surface are assumed to be inaccessible during operation. Consequently, the relevant surface-area-to-volume ratio, S_v , is assumed to be the geometric surface-area-to-volume ratio determined from the μ -CT study.
6. The percentage of the surface area that is catalytically active, f_{active} , is taken to be the ratio of the surface areas from the H_2 chemisorption and Kr adsorption measurements.
7. Species are transported between the bulk gas phase and the boundary layer gas phase. The mass flow rate is assumed to be proportional to the surface area times the difference in mass density across the boundary: $\sim AK_k (\rho_i - \rho_{i,bl})$.
8. The mass and heat transport coefficients K_k and K_T across the boundary layer are estimated from the Sherwood number and the Nusselt number, respectively.
9. Only the boundary-layer gases are coupled with the surface.
10. The pressure is constant, and pressure drop along the length of the reactor is negligible.
11. The boundary layer volume is constant: $dV = -dV_{bl} = 0$.
12. The boundary layer temperature is equal to the surface temperature, which is assumed to be equal to the pyrometer reading: $T_{bl} = T_s = T_{pyrometer}$.

All equations are written on a void volume basis, and symbols are explained in the Nomenclature at the end of the document:

Equation of state:

$$\rho = \frac{p\bar{W}}{RT} \quad (9.6)$$

Conservation of mass:

$$\frac{\partial \rho}{\partial t} = -\frac{\partial \rho v_z}{\partial z} - \frac{S_v}{\gamma} \sum_k^{N_{gas}} K_k (\rho y_k - \rho_{bl} y_{k,bl}) \quad (9.7)$$

$$\frac{\partial \rho_{bl}}{\partial t} = \frac{S_v}{1-\gamma} \sum_k^{N_{gas}} K_k (\rho y_k - \rho_{bl} y_{k,bl}) + \frac{f_{active} S_v}{1-\gamma} \sum_k^{N_{gas}} \dot{s}_{k,bl} W_k \quad (9.8)$$

Conservation of momentum:

$$\frac{\partial v_z}{\partial t} = -\frac{v_z}{\rho} \left(\frac{\partial \rho}{\partial t} + \frac{\partial \rho v_z}{\partial z} \right) - v_z \frac{\partial v_z}{\partial z} + \frac{\epsilon}{\tau} \frac{\partial}{\partial z} \left(\mu \frac{\partial v_z}{\partial z} \right) \quad (9.9)$$

Conservation of species in the bulk gas:

$$\frac{\partial y_k}{\partial t} = -v_z \frac{\partial y_k}{\partial z} - \frac{1}{\rho} \frac{\partial j_{k,z}}{\partial z} - \frac{y_k}{\rho} \left(\frac{\partial \rho}{\partial t} + \frac{\partial \rho v_z}{\partial z} \right) + \frac{1}{\rho} \dot{w}_k W_k - \frac{1}{\rho} \frac{S_v}{\gamma} K_k (\rho y_k - \rho_{bl} y_{k,bl}) \quad (9.10)$$

$$y_{\text{bath gas}} = 1 - \sum_{k \neq \text{bath gas}}^{N_{gas}} y_k$$

Conservation of species in the boundary layer:

$$\begin{aligned} \frac{\partial y_{k,bl}}{\partial t} = & -\frac{1}{\rho_{bl}} \frac{\partial j_{k,z,bl}}{\partial z} - \frac{y_{k,bl}}{\rho_{bl}} \frac{\partial \rho_{k,bl}}{\partial t} + \frac{1}{\rho_{bl}} \dot{w}_{k,bl} W_k + \frac{1}{\rho_{bl}} \frac{f_{active} S_v}{1-\gamma} \dot{s}_{k,bl} W_k \\ & + \frac{1}{\rho_{bl}} \frac{S_v}{1-\gamma} K_k (\rho y_k - \rho_{bl} y_{k,bl}) \end{aligned} \quad (9.11)$$

$$y_{\text{bath gas,bl}} = 1 - \sum_{k \neq \text{bath gas}}^{N_{gas}} y_{k,bl}$$

Conservation of species on the surface:

$$\begin{aligned} \frac{d\theta_k}{dt} &= \frac{\dot{s}_k \sigma_k}{\Gamma} \\ \theta_{\text{Pt}} &= 1 - \sum_{k \neq \text{Pt}}^{N_{\text{surf}}} \theta_k \end{aligned} \quad (9.12)$$

Conservation of energy in the bulk gas phase:

$$\begin{aligned} \rho c_p \frac{\partial T}{\partial t} = & -\frac{\partial T}{\partial z} \left(\sum_k j_{k,z} c_{p,k} + \rho v_z c_p \right) + \frac{\epsilon}{\tau} \frac{\partial}{\partial z} \left(\lambda \frac{\partial T}{\partial z} \right) - \sum_k h_k \dot{w}_k W_k \\ & + \frac{S_v}{\gamma} \sum_k h_k K_k (\rho y_k - \rho_{bl} y_{k,bl}) - \frac{S_v}{\gamma} K_T (T - T_{bl}) \end{aligned} \quad (9.13)$$

Conservation of energy in the boundary layer:

$$\begin{aligned} \rho_{bl} c_{p,bl} \frac{\partial T_{bl}}{\partial t} = & -\frac{\partial T_{bl}}{\partial z} \sum_k j_{k,z,bl} c_{p,k,bl} + \frac{\epsilon}{\tau} \frac{\partial}{\partial z} \left(\lambda_{bl} \frac{\partial T_{bl}}{\partial z} \right) - \sum_k h_k \dot{w}_{k,bl} W_k \\ & - \frac{f_{active} S_v}{1-\gamma} \sum_k h_k \dot{s}_{k,bl} W_k - \frac{S_v}{1-\gamma} \sum_k h_k K_k (\rho y_k - \rho_{bl} y_{k,bl}) \\ & + \frac{S_v}{1-\gamma} K_T (T - T_{bl}) - \frac{S_v}{1-\gamma} K_T (T_{bl} - T_s) \end{aligned} \quad (9.14)$$

Conservation of energy in the surface:

$$\begin{aligned} \rho_s c_{p,s} \frac{\partial T_s}{\partial t} = & \frac{\partial}{\partial z} \left(\lambda_s \frac{\partial T_s}{\partial z} \right) - \frac{\epsilon f_{active} S_v}{1-\epsilon} \sum_k^{N_{\text{surf}}} h_k \dot{s}_k W_k + \frac{\epsilon S_v}{1-\epsilon} K_T (T_{bl} - T_s) \\ & - \frac{\epsilon S_v}{1-\epsilon} \sigma \left(T_s^4 - \frac{\kappa}{2} \int_{-\infty}^{\infty} T_s^4 [z + z^*] e^{-\kappa |z^*|} dz^* \right) \end{aligned} \quad (9.15)$$

Table 9.1: Catalyst characterization.

support material	$\alpha - \text{Al}_2\text{O}_3$
pore density (manufacturer)	80 ppi
monolith dimensions (diameter/length)	16.2/20 mm
catalyst mass ($\text{Al}_2\text{O}_3 + \text{Pt}$)	3.90 g
Pt loading	1.09 wt%
geometric surface area (from μ -CT)	$4650 \text{ m}^2 \text{ m}^3$
Kr-BET surface area	$0.159 \text{ m}^2 \text{ g}^{-1}$
Pt surface area	$0.015 \text{ m}^2 \text{ g}^{-1}$
Pt dispersion	0.6 %
Solid foam volume (from μ -CT)	$1.00 \cdot 10^{-6} \text{ m}^3$
Gas void volume (bulk + b.l., from μ -CT)	$3.03 \cdot 10^{-6} \text{ m}^3$
porosity (from μ -CT)	0.7
tortuosity (from Ref. [2])	1.7

The energy balances of the surface and the boundary layer are given for completeness, but not solved during profile simulation. As mentioned above, the temperature of the gas in the boundary layer is assumed to be equilibrated with the surface temperature, and both temperatures are given by the pyrometer measurement. Finally, the estimation of the boundary layer thickness and volume fraction are defined:

$$\delta = \frac{D_{\text{O}_2} m}{K_{\text{O}_2}} \quad (9.16)$$

$$r_h = \frac{1}{2} \frac{4\epsilon}{S_v} \quad (9.17)$$

$$\gamma = 1 - \frac{\delta}{r_h} \quad (9.18)$$

The simulations were performed using a FORTRAN code developed in house, which utilizes the API libraries of CHEMKIN [197]. A detailed description of the derivation of the reactor model, the numerical procedures used to solve the system of equations, and model validation against high-resolution spatial reactor profiles in catalytic carbon monoxide oxidation on Pt is subject of an upcoming paper by the authors. In this work the focus is on visualizing the capabilities of state-of-the-art microkinetic models considering transport phenomena against the recently available reactor profiles in Pt foam catalysts.

9.3.2 Microkinetic Models

Two state-of-the-art microkinetic models for CH_4 oxidation on Pt are used in conjunction with the reactor model outlined above. The first reaction mechanism was adapted from Deutschmann and coworkers; this mechanism was developed for modeling methane CPO on a Pt gauze [70], and some of the rate parameters were subsequently updated to model the conversion of automotive exhaust gases on alumina-supported Pt [71]. Since the reactant mixture in this study does not contain nitrogen, reactions involving NO_x were removed from the reaction mechanism, as were reactions regarding the decomposition of heavier molecular weight reactants that were not used in the present work. The resulting simplified mechanism consists of 23 reversible elementary reactions among 12 surface and 7 gas-phase species. The reaction mechanism is given in Tab. 9.4 in the Appendix and will be referred to in the following as Mechanism 1.

The second reaction mechanism was adapted from work of Vlachos and coworkers on methane partial oxidation, combustion, and reforming. The original rate coefficient parameters were taken from [72]; the reactions specific to synthesis gas formation were recently updated, [73], and these updates were included. Reactions involving oxygenates, such as methanol and formaldehyde, were removed from the mechanism. Preliminary calculations revealed that inclusion of these species was unnecessary, as the corresponding rates of production were negligible under partial oxidation conditions. Including these oxygenates also adversely affected the numerical stability of the simulations. The resulting simplified mechanism consists of 32 reversible elementary reactions amongst 13 surface and 7 gas-phase species. The reaction mechanism can be found in Tab. 9.5 in the Appendix and will be referred to as Mechanism 2. For both mechanisms, the desorption of radicals from the surface into the gas phase was neglected, and homogeneous chemistry in the gas phase was not included.

Additional catalyst key parameters for the reactor models are summarized in Tab. 9.1.

Table 9.2: Product selectivities of experimental and simulated reactor performance at catalyst bed end (axial position of 20 mm).

Conversion X [%] or selectivity S [%]	Experiment	Mechanism 1	Mechanism 2
$X_{\text{CH}_4}^{\text{@}2000 \text{ mln min}^{-1}}$	63	33	51
$X_{\text{CH}_4}^{\text{@}4000 \text{ mln min}^{-1}}$	59	41	56
$X_{\text{O}_2}^{\text{@}2000 \text{ mln min}^{-1}}$	> 99	99	99
$X_{\text{O}_2}^{\text{@}4000 \text{ mln min}^{-1}}$	> 97	98	97
$S_{\text{H}_2}^{\text{@}2000 \text{ mln min}^{-1}}$	70	28	41
$S_{\text{H}_2}^{\text{@}4000 \text{ mln min}^{-1}}$	67	39	52
$S_{\text{CO}}^{\text{@}2000 \text{ mln min}^{-1}}$	83	24	≈ 99
$S_{\text{CO}}^{\text{@}4000 \text{ mln min}^{-1}}$	90	55	≈ 99
$S_{\text{H}_2\text{O}}^{\text{@}2000 \text{ mln min}^{-1}}$	30	72	59
$S_{\text{H}_2\text{O}}^{\text{@}4000 \text{ mln min}^{-1}}$	33	61	48
$S_{\text{CO}_2}^{\text{@}2000 \text{ mln min}^{-1}}$	17	76	≈ 1
$S_{\text{CO}_2}^{\text{@}4000 \text{ mln min}^{-1}}$	10	45	≈ 1

9.4 Results and Discussion

9.4.1 Microkinetic Modeling Results Compared with Experimental Reactor Profiles

With the aim of gaining mechanistic insight in the methane CPO, two chemical kinetic mechanisms have been used and are compared to the measured reactor profiles. Figs. 9.3 and 9.4 depict experimental and simulated reactor profiles measured at 2000 and 4000 mln min⁻¹ gas feed at a C/O ratio of 1.0. The exact gas feed composition is given in the figure captions. Figs. 9.5 and 9.6 give the corresponding predicted surface mole fractions.

The experimental profiles are divided in two reaction zones. The first zone is characterized by rapid methane and oxygen conversion and is accompanied by heat production. The second zone is characterized by much slower methane and oxygen conversion and steam reforming. At 2000 mln min⁻¹ flow rate CH₄ steam reforming and water gas shift are coupled, yielding a flat CO profile. At 4000 mln min⁻¹, when the catalyst temperature is higher, exothermic water gas shift is less pronounced. Both kinetic models show significant deviations in the predicted exit gas composition compared with the experimental reactor profiles. Only the O₂ profile is, apart from the sudden change in slope, predicted by both mechanisms with quantitative accuracy. Methane conversion by Mechanism 1 and Mechanism 2 are predicted to be 33 % and 51 %, respectively, whereas the experimentally observed conversion is 63 %. The main difference between the measured and predicted profiles concerns the extent of total oxidation. Mechanism 1 overpredicts the branching fraction towards total oxidation, indicated by the high predicted selectivity to CO₂ at the expense of low selectivity to CO. Mechanism 2, in contrast, predicts the CO profile with quantitative accuracy. The H₂ selectivity however is under-predicted by both mechanisms, and the selectivity to CO₂ in Mechanism 2 amounts to almost zero. Mechanism 1 predicts water gas shift (i.e. CO + H₂O \rightleftharpoons CO₂ + H₂), whereas Mechanism 2 shows no water gas shift. Generally speaking, Mechanism 2 does a better job of predicting the measured profiles under most conditions. However, under certain conditions – particularly high-pressure, fuel-rich experiments – Mechanism 1 was in better agreement with the experimental data.

Tab. 9.2 summarizes the product selectivities at the end of the catalyst section, i.e. at 20 mm axial position. At a gas feed rate of $\dot{V}_{\text{total}} = 4000 \text{ mln min}^{-1}$ the oxidation zone is stretched over the length of the entire catalyst bed. For the first ≈ 6 mm, the profiles of CH₄ and O₂ are linear. After 6 mm, the net rate of reactant conversion decreases abruptly, which is exhibited as a kink in the species profiles (see Fig. 9.3). The H₂ and CO profiles diverge after this position, with higher H₂ formation rate compared to CO. The total oxidation products, H₂O and CO₂, form a plateau. The linearity of the initial oxidation zone has been observed on Pt catalysts before [82, 88]. Neither the linearity in the first oxidation zone suggesting an apparent zeroth order kinetic nor the kink in the species profiles can be reproduced by the mechanisms.

It has been speculated that this apparent zeroth-order reaction kinetics could be attributed to a low active-site density due to blockage of the active sites by carbonaceous deposits [88]. The existence and impact of the carbonaceous deposits will be discussed in greater detail in Sections 9.4.2 and 9.4.3. With respect to the microkinetic models, neither Mechanism 1 nor Mechanism 2 includes reactions that would lead to the growth in heavier molecular weight carbonaceous species. Consequently, it should come as no surprise that neither mechanism is capable of reproducing features that might be attributable to more complex heterogeneous surface effects. Both mechanisms predict vacant Pt sites as the largest site fraction in the initial

oxidation zone, which is to be expected, given the high temperatures in this region. The two mechanisms differ dramatically, however, with respect to the surface coverages of other adsorbed species (see Fig. 9.6). Mechanism 1 predicts that chemisorbed CO(s) is the next most abundant surface intermediate, and that the surface concentration of non-oxygenated carbon intermediates – CH₃(s), CH₂(s), CH(s), and C(s) – are orders of magnitude lower. Mechanism 2, in contrast, predicts that both CH(s) and C(s) will be present in large amounts, with CO(s) roughly one-to-two orders of magnitude lower. Perhaps significantly, Mechanism 2 predicts that methylidyne, CH(s), will become the most abundant surface intermediate (MASI) \approx 3 mm prior to the kink. Given the large uncertainty in the rate parameters, the fact that the model predicts CH(s) as the MASI so close to the experimentally observed kink is quite encouraging. If one were to posit a sequence of nucleation and agglomeration reactions that involve the coupling of CH(s), C(s), and heavier molecular weight carbonaceous species, then it is conceivable that such a mechanism would be able to reproduce a kink or some similar discontinuity in the reaction rates due to carbon growth and site blockage. Development of such a mechanism, however, was beyond the scope of the paper.

As will be discussed in Section 9.4.3, the dispersion of Pt along the reactor length is no longer uniform. Consequently, the fraction of the surface area that is catalytically active will change with position: $f_{active} = f(z)$. The exact change in this coverage, however, was difficult to quantify, and so a constant value was assumed for the simulations. Were it possible to include both carbon growth and spatial gradients in the catalyst load, then we would expect the models to perform significantly better.

9.4.2 Spatially Resolved Raman spectroscopy

The hypothesis that the change in the shape of the O₂ profiles was correlated with surface carbon blockage was inferred from experiments on a polycrystalline Pt foil that showed significant carbon deposition during methane CPO at 800 °C [11]. However the stagnation flow geometry of the applied reactor cell in that study cannot exclude transport limitation over the Pt foil. Therefore a low oxygen partial pressure above the surface and a correspondingly oxygen-deficient catalyst surface could be a reason for the observed formation of surface carbonaceous deposits. As mass transport is much more efficient in the Pt foam catalysts applied in this study [83] the foam catalyst was spectroscopically characterized in more detail to verify if the observation on the Pt foil can be transferred to the foam monolith catalysts. A catalyst stack was prepared, consisting of two half monoliths, both with a half centerline channel. The stack was catalytically tested analogous to the regular shaped catalyst foams. After 18 h under autothermal operation at a gas feed of CH₄/O₂/Ar = 592/296/1112 mln min⁻¹ (C/O = 1.0) the reaction was shut down quickly by sudden replacing of the reactive gas feed by pure Ar of 4000 mln min⁻¹ feed rate.

Fig. 9.7 depicts a reactor profile measured through the half shell monoliths. Qualitatively, the species profiles exhibit the same features as observed with the intact full foam monoliths. Similar zoning is observed with a zone of fast CH₄ and O₂ conversion and formation of H₂, CO, and H₂O. CO₂ is again produced with low selectivity. The species profiles seem to be displaced by about 1-2 mm, and a rounded profile shape is observed both in the first millimeters and at the kink position. This spatial offset is probably due to a slight increase in the linear velocity through the foam due to the void created by the slice. Mixing between the local gas and the bypass gas could then explain the rounding of the profiles. The kink position was determined by linear fitting of the species profiles prior and after the kink position. The intercept (see Fig. 9.7) of the fitting lines is located around 5-6 mm axial position, which is in agreement with the kink position in the reactor profiles of the regular shaped foam monolith.

The catalyst stack was separated after the reaction test, and Raman spectra were recorded along the centerline channel of both half monoliths. The obtained Raman spectra were normalized to the most intense Raman band of the corundum support, 420 cm⁻¹. Fig. 9.8 shows the collected Raman spectra as a function of the axial position in the foam half channel of one half monolith. Within the first 5 mm of the catalyst the Raman spectra are dominated by a noisy background signal and the weak Raman peaks of the corundum support located at 382, 420, 578, 649, and 754 cm⁻¹ [216,217].

At \approx 5 mm axial position, which coincides with the sudden change in slope of all species profiles, two new bands at \approx 1350 and \approx 1580 cm⁻¹ appear. As the position increases, these two peaks dominate the background signal. These two bands are characteristic for defective carbon materials such as coke or soot. The maxima are referred to as D band and G band. The G band or ‘graphite peak’ is assigned to the vibrational mode of in-plane bond stretching motion of sp²-hybridized carbon atoms with E_{2g} symmetry. It is characteristic for an ideal graphitic lattice [202]. The D band or ‘defect peak’ is a superposition of up to four peaks characteristic for disordered graphite [90]. The relative intensity and broadening of the D band compared to the G peak intensity is a measure of the structural disorder of the carbon material. If the carbon bands are broadened and overlapping the D band can be separated, following the method of Sadezky et al. [90]. The so-called D1 peak, i.e. the major peak in the D band, is associated with the A_{1g} breathing mode of a graphitic lattice and is assigned to carbon atoms located adjacent to lattice disturbances such as graphene layer edges [90, 203–205]. The D1 full width at half maximum has a nearly linear negative correlation with

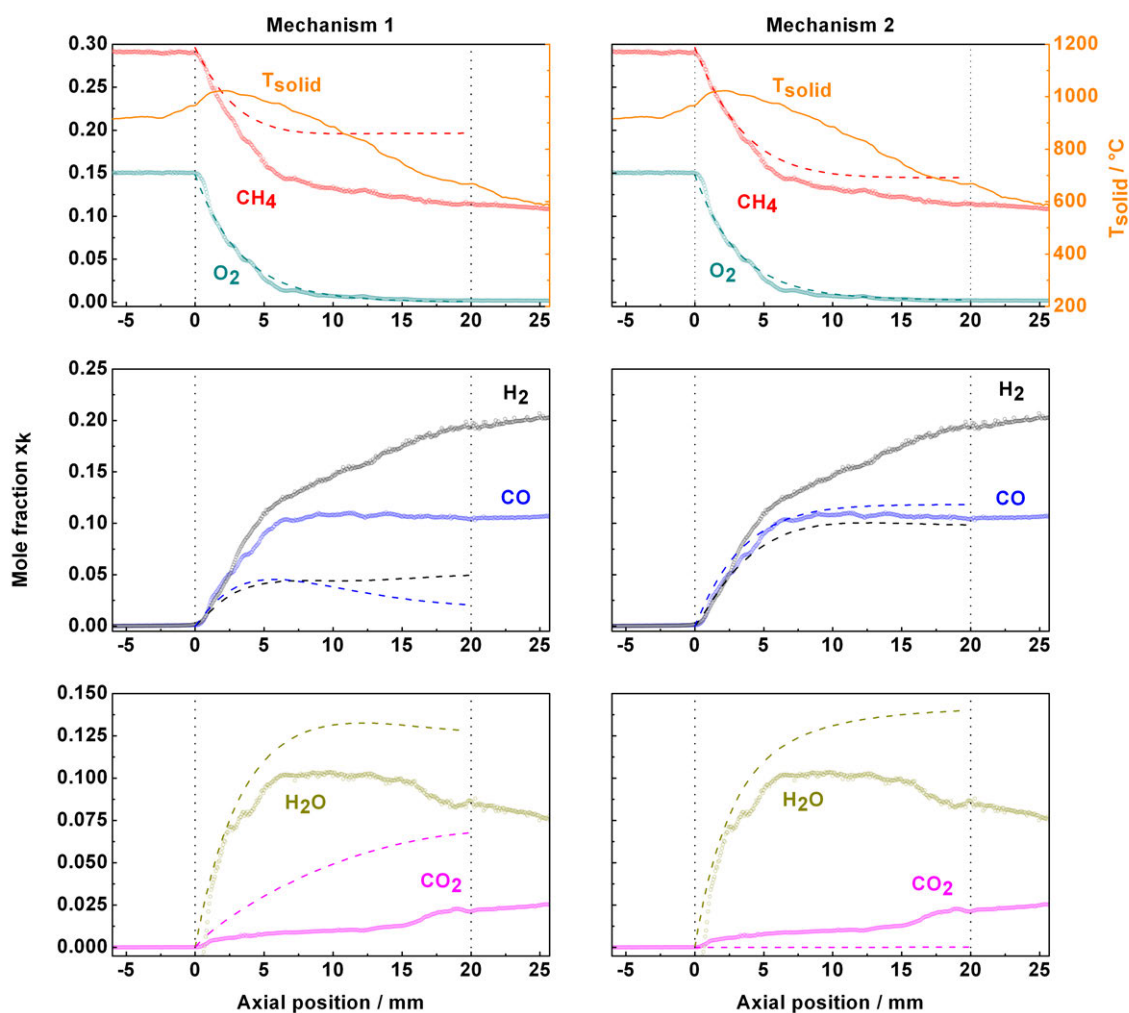


Figure 9.3: Mole fractions of CH₄ and O₂ with catalyst surface temperatures (top panels), mole fractions of H₂ and CO (center panels), and mole fractions of H₂O and CO₂ (bottom panels) comparing prediction of the microkinetic models (dashed lines) of Mechanism 1 [70, 71, 89] (left panels) and Mechanism 2 [72, 73] (right panels) with experimental reactor profiles (symbols). Reactor in autothermal operation with a gas feed of CH₄/O₂/Ar = 592/296/1112 mln min⁻¹ (C/O = 1.0).

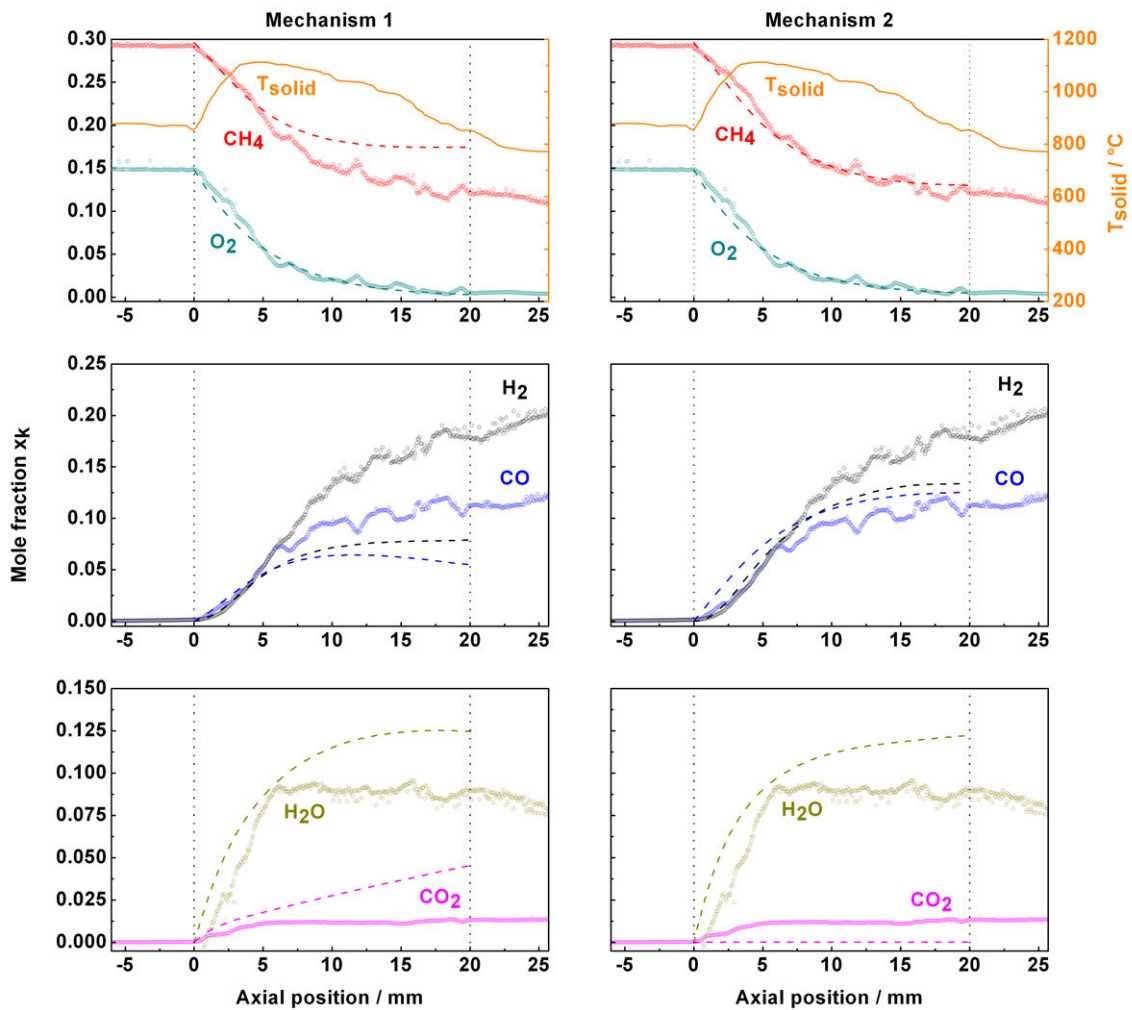


Figure 9.4: Mole fractions of CH_4 and O_2 with catalyst surface temperatures (top panels), mole fractions of H_2 and CO (center panels), and mole fractions of H_2O and CO_2 (bottom panels) comparing prediction of the microkinetic models (dashed lines) of Mechanism 1 [70, 71, 89] (left panels) and Mechanism 2 [72, 73] (right panels) with experimental reactor profiles (symbols). Reactor in autothermal operation with a gas feed of $\text{CH}_4/\text{O}_2/\text{Ar} = 1184/592/2224 \text{ mln min}^{-1}$ ($\text{C/O} = 1.0$).

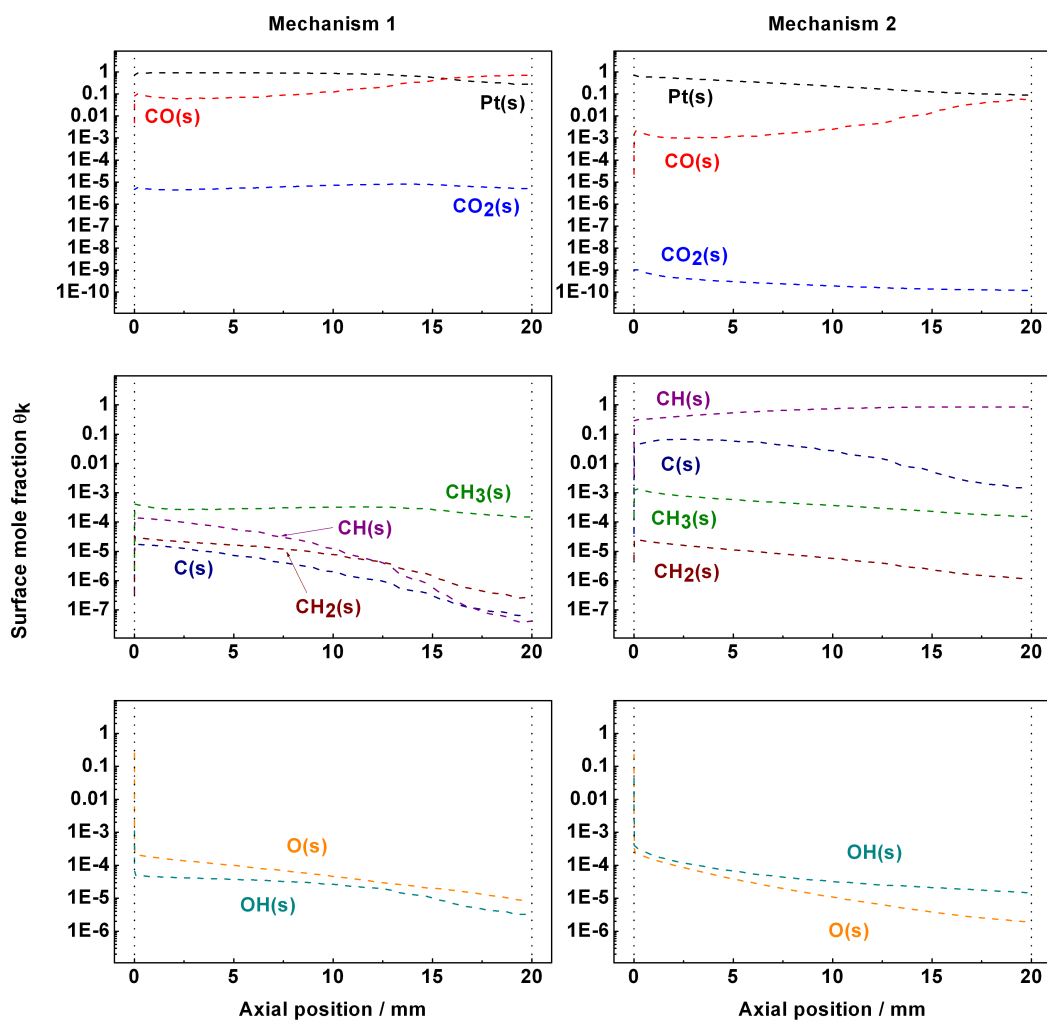


Figure 9.5: Surface mole fractions of Pt(s), CO(s), and CO₂(s) (top panels), surface mole fractions of C(s), CH(s), CH₂(s), and CH₃ (center panels), and surface mole fractions of O(s) and OH(s) (bottom panel) comparing the predictions of the microkinetic models (dashed lines) of Mechanism 1 [70, 71, 89] (left panels) and Mechanism 2 [72, 73]. Corresponding gas phase species and reaction conditions in Fig. 9.3.

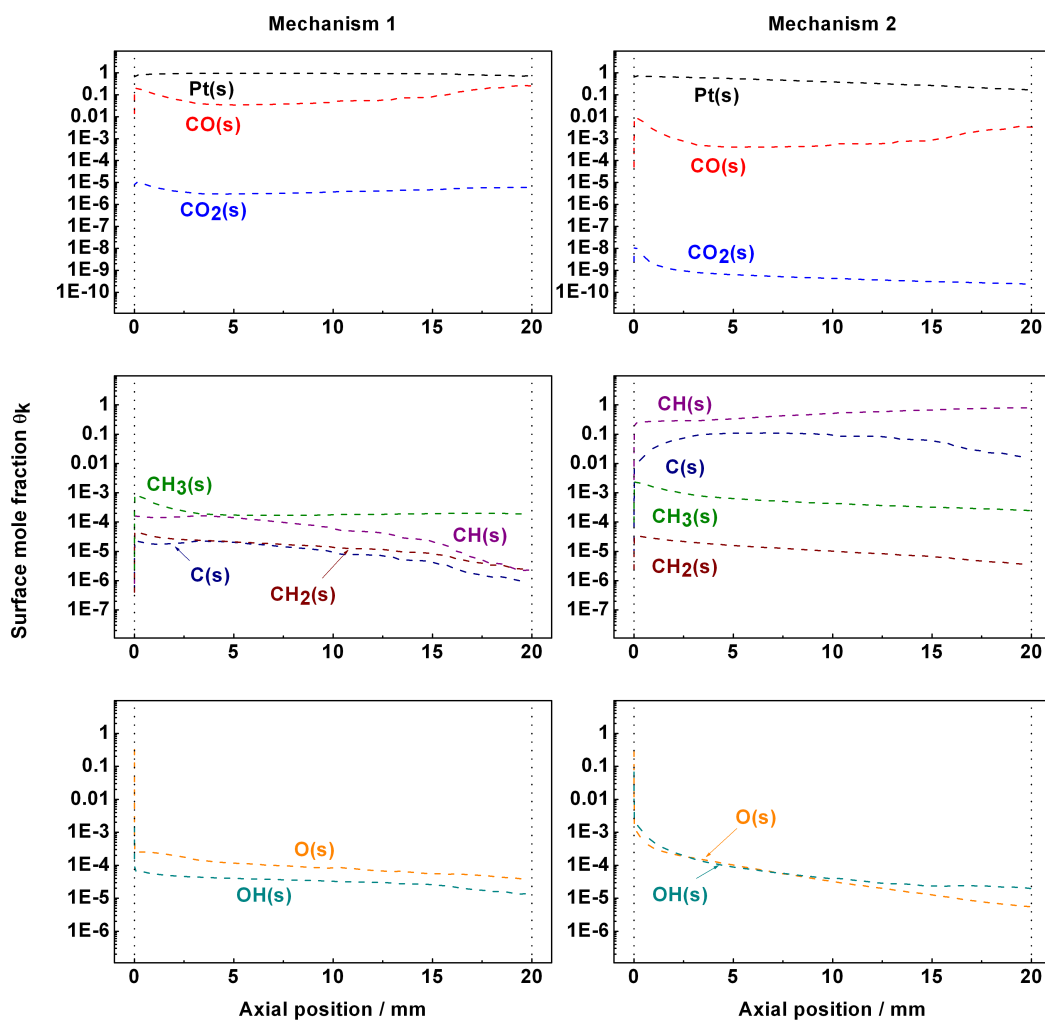


Figure 9.6: Surface mole fractions of Pt(s), CO(s), and CO₂(s) (top panels), surface mole fractions of C(s), CH(s), CH₂(s), and CH₃ (center panels), and surface mole fractions of O(s) and OH(s) (bottom panel) comparing the predictions of the microkinetic models (dashed lines) of Mechanism 1 [70, 71, 89] (left panels) and Mechanism 2 [72, 73]. Corresponding gas phase species and reaction conditions in Fig. 9.4.

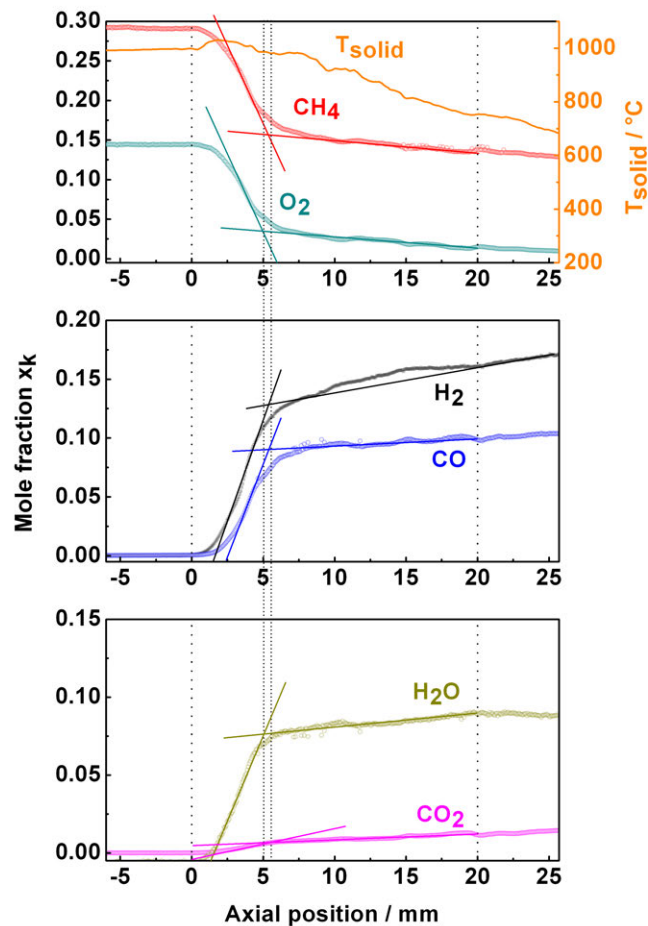


Figure 9.7: Mole fractions of CH_4 and O_2 with catalyst surface temperatures (top panel), mole fractions of H_2 and CO (center panel), and mole fractions of H_2O and CO_2 (bottom panel). Reactor in autothermal operation with a gas feed of $\text{CH}_4/\text{O}_2/\text{Ar} = 592/296/1112 \text{ mln min}^{-1}$ ($\text{C}/\text{O} = 1.0$).

the abundance of elemental carbon in a carbonaceous material [206,207]. Three other peaks are described to contribute to the D band shape and intensity. The D3 located at $\approx 1500 \text{ cm}^{-1}$ originates from amorphous, molecular carbon species [90,208–210]. The D4 peak located at $\approx 1200 \text{ cm}^{-1}$ is assigned to $\text{sp}^2\text{-sp}^3$ bonds or C–C or C=C stretching vibrations of polyene-like structures with A_{1g} symmetry [90,208,209]. The D2 peak also exhibits a shoulder at $\approx 1620 \text{ cm}^{-1}$. It is assigned to a lattice vibration analogous to the G band but involving vibrations of surface graphene layers [90,205].

The carbon bands observed in this study are non-overlapping, which is consistent with a structured carbon material. The D3 band intensity, which is a good measure for the amorphization of a carbon material is absent in the apparent dataset. The G band shows a shoulder centered at 1617 cm^{-1} indicating a fraction of graphene-like fragments on the catalyst. In summary, although a quantitative interpretation of the Raman intensities is difficult, it can be concluded that carbonaceous deposits are formed in the reaction zone following the kink position, and that their relative abundance increases towards the end of the catalyst. Additionally, the absence of gas-phase oxygen favors the formation of carbonaceous deposits. In agreement with our earlier study on a polycrystalline Pt foil [11], the carbon species exhibit a graphitic nature that is resistant to steam reforming.

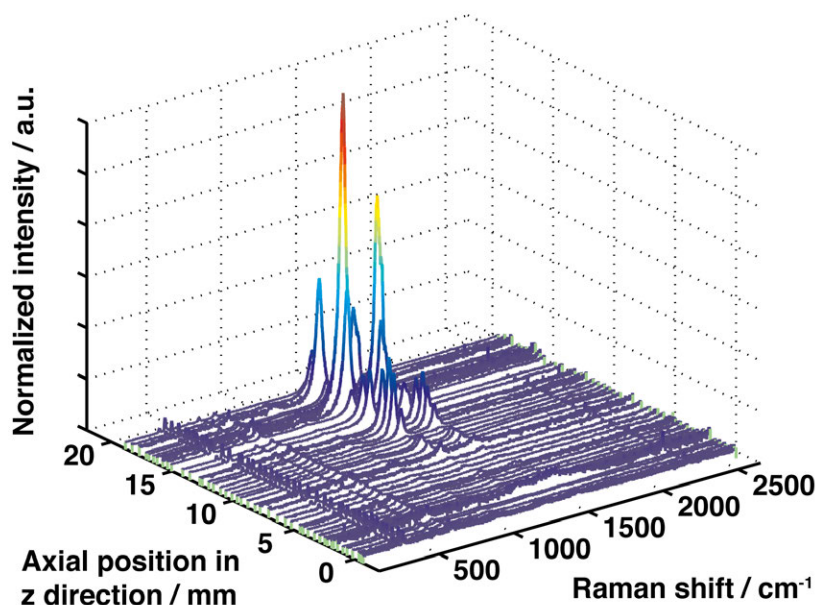


Figure 9.8: Detection of carbonaceous deposits by Raman microscopy after reaction test of two half monoliths. Axial position z along the capillary channel centerline.

9.4.3 Spatially Resolved SEM

The foam half monoliths were additionally investigated using electron microscopy to characterize the catalyst surface morphology. The SEM study was done prior to and after the reaction to compare between the as-prepared catalyst with the used catalyst.

The first noteworthy observation is a strong redistribution/dispersion of the metal particles after the reaction test. Fig. 9.9A and 9.9B represent typical Pt agglomerates as they were present over the whole half monolith after preparation. The preparation method resulted in a rather inhomogeneous metal distribution, with patches of high metal particle density next to bare positions. After the reaction test the Pt agglomerates disappeared, and roughened corundum crystallites (Fig. 9.9C) remained. Higher magnification, as depicted in Fig. 9.9D, shows that although some Pt is still present at the original position, the particle size has decreased considerably and a lot of Pt is transported away. Reviewing the literature, it is speculated that the loss of Pt metal is due either to transport as volatile PtO_2 in the presence of oxygen [62, 218–220], or by catalytic restructuring proceeded by the formation and decomposition of short-lived radical species that interact with the Pt particles [62, 221]. Three different sections could be identified in the used half monolith, which are represented by the electron micrographs of Fig. 9.11. Fig. 9.11A presents a composite image of the entire half monolith; note that the reactor inlet, corresponding to $z = 0$, is at the bottom of the image. Electron micrographs were recorded along the centerline channel. After the reaction test no large agglomerates of Pt could be found. Up to an axial position of ≈ 5 mm the catalyst material was found to be clean, with only small Pt particles covering the corundum crystallites (Fig. 9.11H, 9.11I, and 9.11J). Filament-like carbon species are found throughout the intermediate zone, corresponding to the kink position at ≈ 6 mm and continuing up to ≈ 15 mm (Fig. 9.11E). Increased magnification reveals that the carbon filaments are directly attached to Pt particles (indicated by arrows in Fig. 9.11F). The final section corresponds to the last ≈ 5 mm of the catalyst monolith. Within this section, the carbonaceous deposits have agglomerated into roundish particles that cover the entire support surface. The sharp edges of the corundum crystallites as observed in the oxygen rich catalyst section are blurry and are barely visible due to the carbon encapsulation on top. The carbon spheres exhibit an eggshell structure enclosing Pt particles (Fig. 9.11C arrows).

Another interesting finding regards the Pt particle size. The overall integral breadth-based volume weighted mean Pt crystallite size was determined on a series of seven powdered catalyst monoliths coated with a nominal Pt loading of 1 wt% and amounts to 46 ± 8 nm (see Tab. 9.3). The particle size distributions for the BSE images in Fig. 9.11D, 9.11G, and 9.11J are given in Fig. 9.10. In all three images the most abundant Pt particle diameter is roughly 45 nm independent of the axial position. A closer inspection, however, yields some interesting differences. First, the number of particles smaller than 35 nm increases along the length of the reactor. Second the number of particles greater than 150 nm is largest at the end of the reactor. Taken

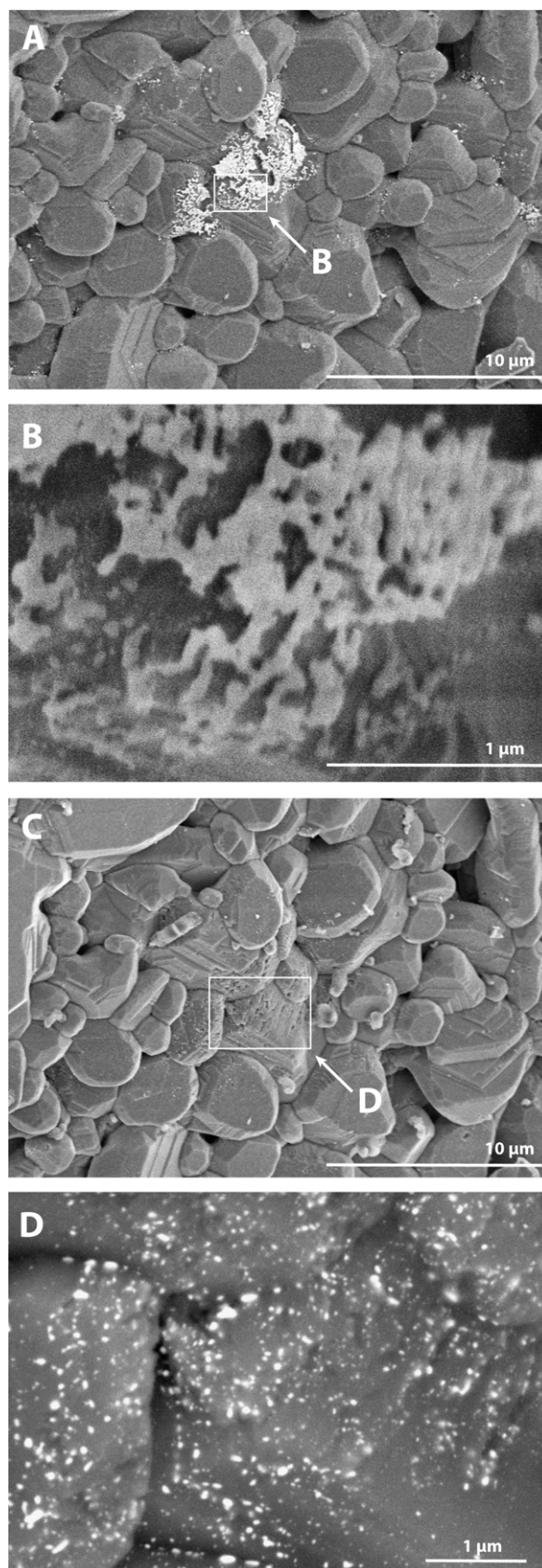


Figure 9.9: Electron micrographs comparing the as prepared Pt coated foam monolith with the monolith after reaction test at an axial position of about 4 mm. A: SE image (HV, 5 kV) as prepared. B: SE image (HV, 1 kV) as prepared. C: SE image (HV, 5 kV) after reaction test. D: BSE image (Low vacuum (60 Pa H₂O), 15 kV) after reaction test.

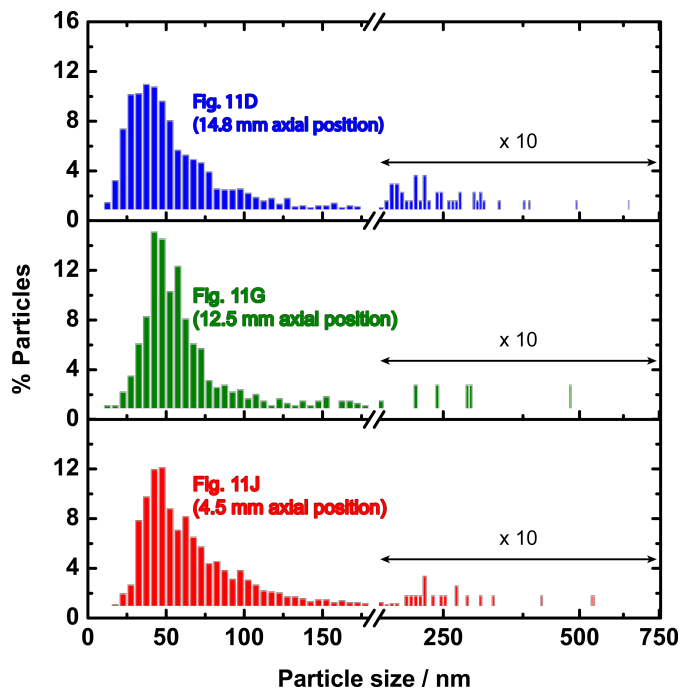


Figure 9.10: Plot of particle size distributions for Fig. 9.11D, 9.11G, and 9.11J with a bin width of 5 nm.

Table 9.3: Integral breadth-based volume weighted mean Pt crystallite size of powdered foam monoliths with a nominal Pt loading of 1 wt%. XRD analysis after reaction tests.

ID	a [\AA]	L Vol-IB [nm]	W_{Pt} [%]
#10253	3.92455(9)	42(2)	1.1
#10254	3.92731(8)	50(3)	1.1
#12357	3.92558(7)	60(4)	1.0
#12358	3.92618(8)	46(10)	1.1
#12359	3.92483(14)	30(2)	1.1
#12360	3.92760(9)	49(3)	1.1
#10774	3.92700(10)	44(3)	0.9

together, the SEM and XRD results confirm that both the particle size distribution and the total Pt loading have been changed by the reaction, and both properties are now functions of position, as seen in Figs. 9.11D, 9.11G, and 9.11J. Although neither the mechanism nor the rate of the catalyst transport can be determined at this time, it is clear nonetheless, that the Pt particles are redistributed prior to and/or during operation. Pt is transported from the front of the foam support – where the temperatures are highest – to the cooler, post-oxidation zone at the rear of the foam.

9.5 Conclusion

Spatially resolved high-resolution reactor profiles of species concentrations and catalyst surface temperature in autothermal methane CPO on Pt are presented. The measured profiles exhibit a two-zone structure. In the first zone, the rate of reactant conversion is fast and linear. In the second zone, the reaction rates are considerably slower, and the sharp decrease in net rates results in a kink in the species profiles. Post-reaction characterization of the catalyst by Raman spectroscopy and electron microscopy revealed that the Pt distribution changed when compared to the freshly prepared monolith. Characterization of the foam prior to reaction revealed islands of Pt particle agglomerates, but after several hours on stream, these Pt islands were re-dispersed. In the front of the foam where oxidation rates are highest, the large Pt agglomerates have disappeared, and only small Pt particles remain. In the post-oxidation zone where O_2 partial pressure is lowest, the catalyst surface is enriched by larger spherical Pt particles covered with carbon deposits. These results clearly demonstrate that Pt is transported during operation from the hot catalyst front to the catalyst back. The kink position is correlated with the formation of carbonaceous deposits. The morphology of the carbon material changes from filament-like to a mixture of thickened filaments and large roundish agglomerates. Towards the end of the reactor, the Pt particles are embedded in the carbon material. The measured profiles are compared with predicted profiles from a pseudo-2D heterogeneous reactor model

that couples heat and mass transport limitations with detailed chemical kinetics. Two state-of-the-art microkinetic models taken from the literature are used: Mechanism 1 (developed by Deutschmann and coworkers [70, 71, 89]) and Mechanism 2 (developed by Vlachos and coworkers [72, 73]). Although the model profiles are correct with respect to O_2 , the product profiles differ considerably. Mechanism 1 underpredicts methane conversion and overpredicts the branching fraction towards total oxidation. Mechanism 2 is in better agreement with the measured profiles, but it consistently underpredicts the rate of water gas shift. Although both models predict a high concentration of vacant sites in the initial oxidation zone, the two models differ significantly in their prediction of the surface coverages. Mechanism 1 predicts that $CO(s)$ is the next most abundant surface species, whereas Mechanism 2 predicts high coverages of $CH(s)$ and, to a lesser extent, $C(s)$. Since neither mechanism includes a submechanism for carbon growth, it is not surprising that the simulations fail to predict the kink in the measured profiles. Nonetheless, the transition from a largely vacant surface to a surface covered with $CH(s)$ predicted by Mechanism 2 coincides remarkably well with the kink position and formation of carbonaceous deposits. The disparities between the measured and predicted profiles indicate the need for further work in chemical kinetic mechanism development. The reactions that lead to the formation and agglomeration of carbonaceous species in low- O_2 environments is critical.

9.6 Acknowledgements

All authors thank the German Research Foundation for funding the Emmy-Noether-Junior-Research-Group "High Temperature Catalysis". Further support was provided by the German Federal Ministry of Education and Research within the framework of the Excellence Cluster "Unifying Concepts in Catalysis". CFG gratefully acknowledges the financial support from the Alexander von Humboldt foundation.

The authors explicitly thank A. Fischer from Technische Universität Berlin for krypton BET measurements, I. Manke and A. Hilger from Helmholtz-Zentrum Berlin for the μ -CT measurements, and S. Wrabetz and F. Girgsdies from the Fritz Haber Institute of the Max Planck Society for validating the H_2 chemisorption measurements by CO chemisorption in a microcalorimetric experiment and for determining the Pt crystallite size by XRD respectively.

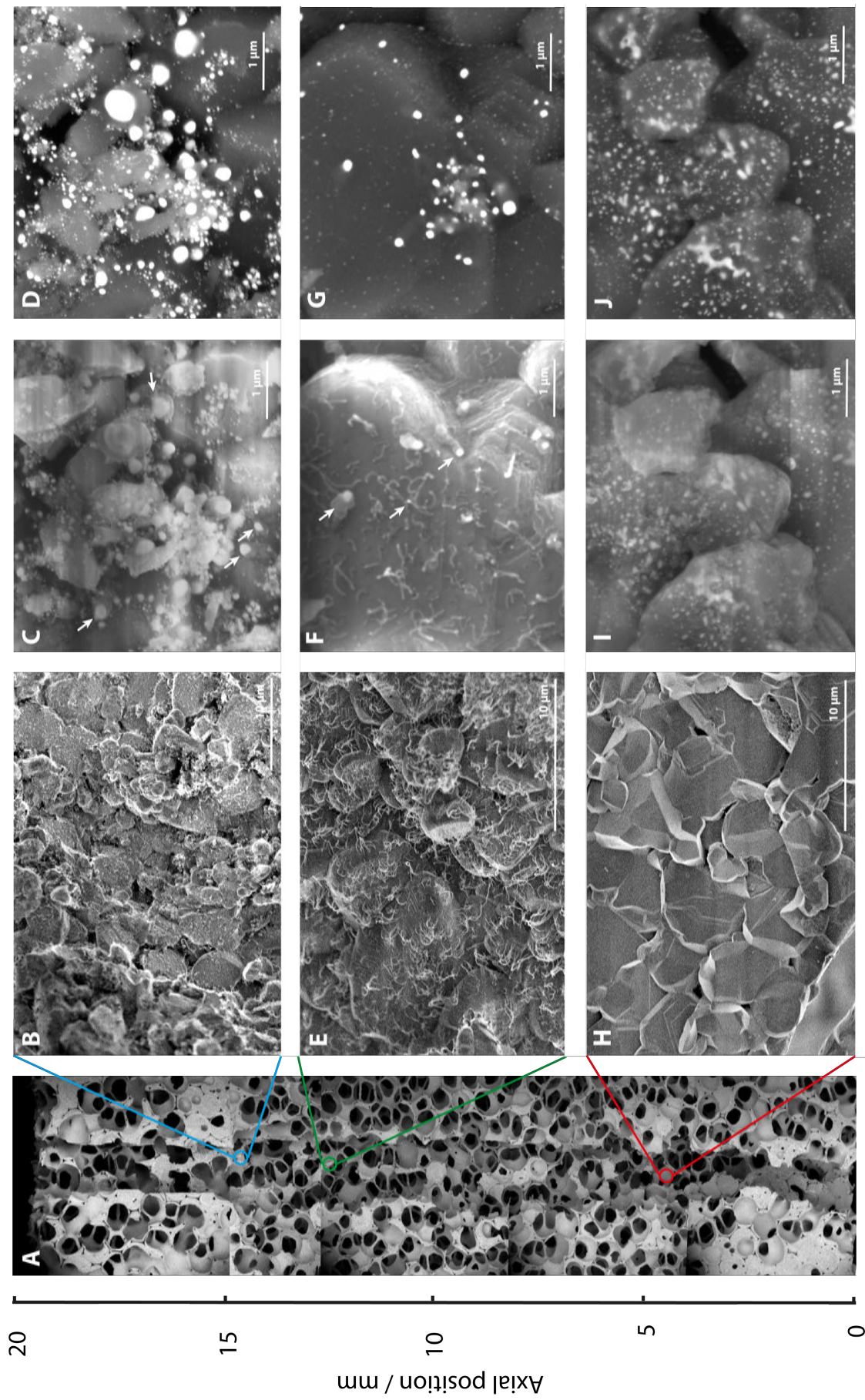


Figure 9.11: Selected electron micrographs from the centerline channel of a half monolith. A: Overview composite picture of the centerline channel with axial position (BSE image, Low vacuum (60 Pa H₂O), 15 kV). B: SE image (HV, 1.5 kV) of the end section of the catalyst foam. Filament-like and agglomerated carbonaceous deposits covering the catalyst surface. C, D: Magnified SE/BSE image (Low vacuum (60 Pa H₂O), 15 kV) of some of the agglomerated carbon deposits. E: SE image (HV, 1.5 kV) of the middle section of the catalyst bed. Filament-like structured carbon covering the catalyst surface. F, G: Magnified SE/BSE image (Low vacuum (60 Pa H₂O), 15 kV) of some of the filament-like carbon deposits. H: SE image (HV, 1.5 kV) of the front section of the catalyst foam, prior to the kink position. I, J: Magnified SE/BSE image (Low vacuum (60 Pa H₂O), 15 kV) of clean catalyst surface. No carbon species visible.

9.7 Appendix: Reaction Mechanisms

Table 9.4: Deutschmann surface reaction mechanism of C1 oxidation on Pt adopted from [70,71,89], changed.

reaction step	reaction	pre-exponential factor ^a	temperature exponent, β	activation energy (cal mol ⁻¹)
Adsorption-desorption reactions				
R'1	$\text{CH}_4 + 2 \text{Pt(s)} \rightarrow \text{CH}_3\text{(s)} + \text{H(s)}$	0.010	0.0	0.0
R'2	$\text{CH}_3\text{(s)} + \text{H(s)} \rightarrow \text{CH}_4 + 2 \text{Pt(s)}$	3.300×10^{21}	0.0	$11942 - 669\theta_{\text{H(s)}}$
R'3 ^d	$\text{O}_2 + 2 \text{Pt(s)} \rightarrow 2 \text{O(s)}$	0.070	0.0	0.0
R'4	$2 \text{O(s)} \rightarrow \text{O}_2 + 2 \text{Pt(s)}$	3.218×10^{21}	0.0	$53671 - 28662\theta_{\text{O(s)}}$
R'5	$\text{H}_2 + 2 \text{Pt(s)} \rightarrow 2 \text{H(s)}$	0.046	0.0	0.0
R'6	$2 \text{H(s)} \rightarrow \text{H}_2 + 2 \text{Pt(s)}$	2.121×10^{21}	0.0	$16507 - 1433\theta_{\text{H(s)}}$
R'7	$\text{H}_2\text{O} + \text{Pt(s)} \rightarrow \text{H}_2\text{O(s)}$	7.500×10^{-1}	0.0	0.0
R'8	$\text{H}_2\text{O(s)} \rightarrow \text{H}_2\text{O} + \text{Pt(s)}$	5.013×10^{12}	0.0	11742
R'9	$\text{CO} + \text{Pt(s)} \rightarrow \text{CO(s)}$	8.400×10^{-1}	0.0	0.0
R'10	$\text{CO(s)} \rightarrow \text{CO} + \text{Pt(s)}$	2.126×10^{13}	0.0	$32528 - 7882\theta_{\text{CO(s)}}$
R'11	$\text{CO}_2 + \text{Pt(s)} \rightarrow \text{CO}_2\text{(s)}$	5.000×10^{-3}	0.0	0.0
R'12	$\text{CO}_2\text{(s)} \rightarrow \text{CO}_2 + \text{Pt(s)}$	3.565×10^{10}	0.0	5651
R'13	$\text{CH}_4 + \text{O(s)} + \text{Pt(s)} \rightarrow \text{CH}_3\text{(s)} + \text{OH(s)}$	5.000×10^{18}	0.7	$10032 + 1911\theta_{\text{O(s)}}$
R'14	$\text{CH}_3\text{(s)} + \text{OH(s)} \rightarrow \text{CH}_4 + \text{O(s)} + \text{Pt(s)}$	3.700×10^{21}	0.0	20995
R'15	$\text{CH}_4 + \text{OH(s)} + \text{Pt(s)} \rightarrow \text{CH}_3\text{(s)} + \text{H}_2\text{O(s)}$	1.000	0.0	2388
R'16	$\text{CH}_3\text{(s)} + \text{H}_2\text{O(s)} \rightarrow \text{CH}_4 + \text{OH(s)} + \text{Pt(s)}$	3.700×10^{21}	0.0	26416
Surface reactions				
R'17	$\text{CH}_3\text{(s)} + \text{Pt(s)} \rightarrow \text{CH}_2\text{(s)} + \text{H(s)}$	1.262×10^{22}	0.0	16815
R'18	$\text{CH}_2\text{(s)} + \text{H(s)} \rightarrow \text{CH}_3\text{(s)} + \text{Pt(s)}$	2.943×10^{22}	0.0	$98 - 669\theta_{\text{H(s)}}^b$
R'19	$\text{CH}_2\text{(s)} + \text{Pt(s)} \rightarrow \text{CH(s)} + \text{H(s)}$	7.000×10^{22}	0.0	$14140 + 11942\theta_{\text{C(s)}}^b$
R'20	$\text{CH(s)} + \text{H(s)} \rightarrow \text{CH}_2\text{(s)} + \text{Pt(s)}$	8.110×10^{21}	0.0	$170 - 669\theta_{\text{H(s)}}^b$
(R'21 \equiv R27) ^c	$\text{CH(s)} + \text{Pt(s)} \rightarrow \text{C(s)} + \text{H(s)}$	3.460×10^{18}	0.398	31300
(R'22 \equiv R28) ^c	$\text{C(s)} + \text{H(s)} \rightarrow \text{CH(s)} + \text{Pt(s)}$	3.910×10^{20}	-0.398	13200
R'23	$\text{CH}_3\text{(s)} + \text{O(s)} \rightarrow \text{OH(s)} + \text{CH}_2\text{(s)}$	3.700^{21}	0.0	8741
R'24	$\text{OH(s)} + \text{CH}_2\text{(s)} \rightarrow \text{CH}_3\text{(s)} + \text{O(s)}$	2.342×10^{22}	0.0	6205
R'25	$\text{CH}_2\text{(s)} + \text{O(s)} \rightarrow \text{OH(s)} + \text{CH(s)}$	3.700×10^{21}	0.0	5995
R'26	$\text{OH(s)} + \text{CH(s)} \rightarrow \text{CH}_2\text{(s)} + \text{O(s)}$	1.163×10^{21}	0.0	6401
R'27	$\text{CH(s)} + \text{O(s)} \rightarrow \text{OH(s)} + \text{C(s)}$	3.700×10^{21}	0.0	5995
R'28	$\text{OH(s)} + \text{C(s)} \rightarrow \text{CH(s)} + \text{O(s)}$	1.882×10^{21}	0.0	51151
CO oxidation on Pt				
R'29	$\text{CO(s)} + \text{O(s)} \rightarrow \text{CO}_2\text{(s)} + \text{Pt(s)}$	3.700×10^{20}	0.0	$25795 - 7882\theta_{\text{CO(s)}}$
R'30	$\text{CO}_2\text{(s)} + \text{Pt(s)} \rightarrow \text{CO(s)} + \text{O(s)}$	3.94×10^{21}	0.0	$39551 + 14331\theta_{\text{O(s)}}$
R'31	$\text{C(s)} + \text{O(s)} \rightarrow \text{CO(s)} + \text{Pt(s)}$	3.700×10^{21}	0.0	$0.0 - 7882\theta_{\text{CO(s)}}$
R'32	$\text{CO(s)} + \text{Pt(s)} \rightarrow \text{C(s)} + \text{O(s)}$	1.664×10^{21}	0.0	$49064 + 14331\theta_{\text{O(s)}}$
Hydroxyl reactions on Pt				
R'33	$\text{H(s)} + \text{O(s)} \rightarrow \text{OH(s)} + \text{Pt(s)}$	3.700×10^{20}	0.0	16839
R'34	$\text{OH(s)} + \text{Pt(s)} \rightarrow \text{H(s)} + \text{O(s)}$	1.004×10^{21}	0.0	$31215 - 17488\theta_{\text{O(s)}}^b$
R'35	$\text{H(s)} + \text{OH(s)} \rightarrow \text{H}_2\text{O(s)} + \text{Pt(s)}$	3.700×10^{21}	0.0	4156
R'36	$\text{H}_2\text{O(s)} + \text{Pt(s)} \rightarrow \text{H(s)} + \text{OH(s)}$	6.824×10^{20}	0.0	$16136 + 39973\theta_{\text{O(s)}}^b$
R'37	$2 \text{OH(s)} \rightarrow \text{H}_2\text{O(s)} + \text{O(s)}$	3.700×10^{21}	0.0	11512
R'38	$\text{H}_2\text{O(s)} + \text{O(s)} \rightarrow 2 \text{OH(s)}$	2.515×10^{20}	0.0	$9117 + 57462\theta_{\text{O(s)}}^b$
R'39	$\text{CO(s)} + \text{OH(s)} \rightarrow \text{HCOO(s)} + \text{Pt(s)}$	3.700×10^{21}	0.0	22499
R'40	$\text{HCOO(s)} + \text{Pt(s)} \rightarrow \text{CO(s)} + \text{OH(s)}$	1.333×10^{21}	0.0	208
R'41	$\text{HCOO(s)} + \text{O(s)} \rightarrow \text{OH(s)} + \text{CO}_2\text{(s)}$	3.700×10^{21}	0.0	0.0
R'42	$\text{OH(s)} + \text{CO}_2\text{(s)} \rightarrow \text{HCOO(s)} + \text{O(s)}$	2.787×10^{21}	0.0	36078
R'43	$\text{HCOO(s)} + \text{Pt(s)} \rightarrow \text{H(s)} + \text{CO}_2\text{(s)}$	3.700×10^{21}	0.0	0.0
R'44	$\text{H(s)} + \text{CO}_2\text{(s)} \rightarrow \text{HCOO(s)} + \text{Pt(s)}$	2.787×10^{21}	0.0	21508
R'45	$\text{CO(s)} + \text{OH(s)} \rightarrow \text{CO}_2\text{(s)} + \text{H(s)}$	1.000×10^{19}	0.0	$9243 - 7165\theta_{\text{CO(s)}}$
R'46	$\text{CO}_2\text{(s)} + \text{H(s)} \rightarrow \text{CO(s)} + \text{OH(s)}$	1.000×10^{19}	0.0	2006

^aSticking coefficient [dimensionless]; pre-exponential factor for unimolecular reaction [s^{-1}]; pre-exponential factor for bimolecular reaction [$\text{cm}^2 \text{mol}^{-1} \text{s}^{-1}$]

^bThe coverage dependency of this species is not used. Preliminary calculations demonstrated that the surface coverage was too low to matter, and that including it led to significant numerical instabilities.

^cHere the parameters from the Vlachos mechanism are used, because the original Deutschmann reaction rate from [71] is suspiciously high and led to numerical instabilities.

^dThe desorption rate constant as written leads to numerical instability. To obtain a converging solution, the rate constant for desorption was obtained directly from the equilibrium constant, as detailed in [222].

Table 9.5: Vlachos surface reaction mechanism of C1 oxidation on Pt adopted from [72, 73], changed.

reaction step	reaction	pre-exponential factor ^a	temperature exponent, β	activation energy (cal mol ⁻¹)
Oxygen adsorption-desorption steps				
R1	$O_2 + 2 Pt(s) \rightarrow 2 O(s)$	6.86×10^{-4}	0.766	0.0
R2	$2 O(s) \rightarrow O_2 + Pt(s)$	1.54×10^{19}	0.930	$50396.5 - 32005.4\theta_{O(s)}$
CO oxydation on Pt				
R3	$CO + Pt(s) \rightarrow CO(s)$	1.00×10^{10}	0.000	0.0
R4	$CO(s) \rightarrow CO + Pt(s)$	6.12×10^{14}	0.390	$41320.4 - 15047.3\theta_{CO(s)}$
R5	$CO_2 + Pt(s) \rightarrow CO_2(s)$	4.69×10^{-2}	0.250	0.0
R6	$CO_2(s) \rightarrow CO_2 + Pt(s)$	1.51×10^{13}	-0.250	2866.2
R7	$CO_2(s) + Pt(s) \rightarrow CO(s) + O(s)$	5.14×10^{19}	-0.280	$29855.8 + 7643.1\theta_{O(s)} + 11464.6\theta_{CO(s)}$
R8	$CO(s) + O(s) \rightarrow CO_2(s) + Pt(s)$	4.32×10^{18}	0.460	$25795.4 - 8359.6\theta_{O(s)} - 3582.7\theta_{CO(s)}$
H ₂ oxidation on Pt				
R9	$H_2 + 2 Pt(s) \rightarrow 2 H(s)$	9.67×10^{-4}	0.858	0.0
R10	$2 H(s) \rightarrow H_2 + 2 Pt(s)$	5.43×10^{16}	1.910	$19346.5 - 5971.2\theta_{H(s)}$
R11	$OH(s) + Pt(s) \rightarrow H(s) + O(s)$	3.64×10^{17}	1.330	$26989.6 - 10031.5\theta_{O(s)} + 955.4\theta_{H(s)}$ $+12420.0\theta_{H_2O(s)}^b$
R12	$H(s) + O(s) \rightarrow OH(s) + Pt(s)$	4.92×10^{18}	1.080	$8598.5 + 6926.5\theta_{O(s)} - 1910.8\theta_{H(s)}$ $-12420.0\theta_{H_2O(s)}^b$
R13	$H_2O(s) + Pt(s) \rightarrow H(s) + OH(s)$	3.18×10^{22}	-0.390	$17674.6 + 11225.8\theta_{O(s)}^b + 1194.2\theta_{H(s)}$ $+12420.0\theta_{OH(s)} - 10986.0\theta_{H_2O}$
R14	$H(s) + OH(s) \rightarrow H_2O(s) + Pt(s)$	3.03×10^{22}	-0.370	$13375.4 - 21735.0\theta_{O(s)}^b - 1910.8\theta_{H(s)}$ $-12420.0\theta_{OH(s)} + 16480.4\theta_{H_2O}$
R15	$H_2O(s) + O(s) \rightarrow 2 OH(s)$	2.42×10^{18}	0.330	$8598.5 + 16719.2\theta_{O(s)} + 12420.0\theta_{OH(s)}$
R16	$2 OH(s) \rightarrow H_2O(s) + O(s)$	3.04×10^{17}	0.530	$22690.4 - 33199.6\theta_{O(s)} - 12420.0\theta_{OH(s)}$ $+32483.1\theta_{H_2O(s)}$
R17	$H_2O + Pt(s) \rightarrow H_2O(s)$	1.45×10^{-4}	1.160	0.0
R18	$H_2O(s) \rightarrow H_2O + Pt(s)$	1.38×10^6	2.490	$9553.8 + 25078.8\theta_{OH(s)}^b - 2388.5\theta_{H_2O(s)}$
Coupling between CO and H ₂ chemistry on Pt				
R19	$CO_2(s) + H(s) \rightarrow CO(s) + OH(s)$	1.94×10^{18}	-0.330	$9553.8 + 12897.7\theta_{O(s)}^b - 1433.1\theta_{H(s)}$ $-10748.1\theta_{H_2O(s)}^b + 4299.2\theta_{CO(s)}$
R20 ^d	$CO(s) + OH(s) \rightarrow CO_2(s) + H(s)$	4.28×10^{15}	0.820	$23884.6 - 20063.1\theta_{O(s)}^b + 1433.1\theta_{H(s)}$ $+14091.9\theta_{H_2O(s)}^b - 10509.2\theta_{CO(s)}$
CH ₄ oxidation and reforming on Pt				
R21	$CH_4 + 2 Pt(s) \rightarrow CH_3(s) + H(s)$	4.82×10^{-2}	0.154	9000
R22	$CH_3(s) + H(s) \rightarrow CH_4 + 2 Pt(s)$	5.42×10^{19}	-0154	11300
R23	$CH_3(s) + Pt(s) \rightarrow CH_2(s) + H(s)$	3.74×10^{17}	0.419	15800
R24	$CH_2(s) + H(s) \rightarrow CH_3(s) + Pt(s)$	3.61×10^{19}	-0419	13300
R25	$CH_2(s) + Pt(s) \rightarrow CH(s) + H(s)$	5.41×10^{18}	0.222	9000
R26	$CH(s) + H(s) \rightarrow CH_2(s) + Pt(s)$	2.50×10^{20}	-0.222	35400
R27	$CH(s) + Pt(s) \rightarrow C(s) + H(s)$	3.46×10^{18}	0.398	31300
R28	$C(s) + H(s) \rightarrow CH(s) + Pt(s)$	3.91×10^{20}	-0.398	13200
R29	$CH_3(s) + O(s) \rightarrow CH_2(s) + OH(s)$	2.69×10^{20}	-0.230	10800
R30	$CH_2(s) + OH(s) \rightarrow CH_3(s) + O(s)$	5.03×10^{18}	0.230	26600
R31	$CH_2(s) + O(s) \rightarrow CH(s) + OH(s)$	3.55×10^{20}	-0.414	0.0
R32	$CH(s) + OH(s) \rightarrow CH_2(s) + O(s)$	3.81×10^{18}	0.414	44700
R33	$CH(s) + O(s) \rightarrow C(s) + OH(s)$	2.08×10^{20}	-0.225	27500
R34	$C(s) + OH(s) \rightarrow CH(s) + O(s)$	6.49×10^{18}	0.225	27700
R35	$CH_2(s) + H_2O(s) \rightarrow CH_3(s) + OH(s)$	1.71×10^{19}	0.099	14100
R36	$CH_3(s) + OH(s) \rightarrow CH_2(s) + H_2O(s)$	7.89×10^{19}	-0.099	12300
R37	$CH(s) + H_2O(s) \rightarrow CH_2(s) + OH(s)$	1.43×10^{19}	0.269	34000
R38	$CH_2(s) + OH(s) \rightarrow CH(s) + H_2O(s)$	9.43×10^{19}	-0.269	3300
R39	$C(s) + H_2O(s) \rightarrow CH(s) + OH(s)$	2.29×10^{19}	0.090	15600
R40	$CH(s) + OH(s) \rightarrow C(s) + H_2O(s)$	5.90×10^{19}	-0.090	29300
R41	$CO(s) + Pt(s) \rightarrow C(s) + O(s)$	7.26×10^{18}	0.468	76800
R42	$C(s) + O(s) \rightarrow CO(s) + Pt(s)$	1.86×10^{20}	-0.468	22300
R43	$CO(s) + H(s) \rightarrow CH(s) + O(s)$	7.56×10^{18}	0.073	45800
R44	$CH(s) + O(s) \rightarrow CO(s) + H(s)$	1.79×10^{18}	-0.073	9300
R45	$CO(s) + H(s) \rightarrow C(s) + OH(s)$	1.91×10^{20}	-0.168	40700
R46	$C(s) + OH(s) \rightarrow CO(s) + H(s)$	1.14×10^{18}	0.168	4400
R47	$2 CO(s) \rightarrow C(s) + CO_2(s)$	2.32×10^{20}	0.393	48800
R48	$C(s) + CO_2(s) \rightarrow 2 CO(s)$	5.81×10^{20}	-0.393	0.0
Reactions of COOH on Pt				
R49	$COOH(s) + Pt(s) \rightarrow CO(s) + OH(s)$	2.61×10^{17}	0.030	$8837.3 + 12897.7\theta_{O(s)}^b - 10748.1\theta_{H_2O(s)}^b$ $+4299.2\theta_{CO(s)}$
R50 ^d	$CO(s) + OH(s) \rightarrow COOH(s) + Pt(s)$	3.00×10^{17}	0.470	$23884.2 - 19824.2\theta_{O(s)}^b + 14091.9\theta_{H_2O(s)}^b$ $-10509.2\theta_{CO(s)}$
R51	$COOH(s) + Pt(s) \rightarrow CO_2(s) + H(s)$	1.43×10^{18}	0.580	$955.4 + 1433.1\theta_{H(s)}$
R52	$CO_2(s) + H(s) \rightarrow COOH(s) + Pt(s)$	6.51×10^{19}	-0.110	$1671.9 - 1433.1\theta_{H(s)}$
R53	$CO(s) + H_2O(s) \rightarrow COOH(s) + H(s)$	2.47×10^{18}	0.490	$24362.3 + 1194.2\theta_{H(s)} + 12420.0\theta_{OH(s)}\theta_{CO(s)}$ $-1194.2\theta_{H_2O(s)} - 7404.2\theta_{CO(s)}$
R54	$COOH(s) + H(s) \rightarrow CO(s) + H_2O(s)$	3.96×10^{19}	-0.030	$4776.9 - 1910.8\theta_{H(s)} - 12420.0\theta_{OH(s)}\theta_{CO(s)}$ $+1194.2\theta_{H_2O(s)} + 7404.2\theta_{CO(s)}$
R55	$CO_2(s) + OH(s) \rightarrow COOH(s) + O(s)$	1.48×10^{19}	0.050	$26273.1 - 9792.7\theta_{O(s)}^b + 12420.0\theta_{H_2O(s)}^b$
R56	$COOH(s) + O(s) \rightarrow CO_2(s) + OH(s)$	5.28×10^{18}	0.450	$7165.4 + 7165.4\theta_{O(s)}^b - 12420.0\theta_{H_2O(s)}^b$
R57	$CO_2(s) + H_2O(s) \rightarrow COOH(s) + OH(s)$	4.22×10^{19}	-0.050	$17196.9 + 11703.5\theta_{O(s)}^b + 12420.0\theta_{OH(s)}^b$ $-11464.6\theta_{H_2O(s)}^b$
R58	$COOH(s) + OH(s) \rightarrow CO_2(s) + H_2O(s)$	1.75×10^{18}	0.560	$11942.3 - 21257.5\theta_{O(s)}^b - 12420.0\theta_{OH(s)}^b$ $+16002.7\theta_{H_2O(s)}^b$
Reactions of HCOO on Pt				
R59	$CO_2(s) + H(s) \rightarrow HCOO(s)$	6.50×10^{19}	-0.08	$17913.5 - 3105.0\theta_{H(s)}^b$
R60	$HCOO(s) \rightarrow CO_2(s) + H(s)$	8.16×10^9	0.420	0.0
R61	$CO_2(s) + OH(s) + Pt(s) \rightarrow HCOO(s,s) + O(s)$	5.80×10^{28}	-0.340	$36304.6 - 16958.1\theta_{O(s)}^b + 25078.8\theta_{H_2O(s)}^b$
R62	$HCOO(s,s) + O(s) \rightarrow CO_2(s) + OH(s) + Pt(s)$	1.48×10^{20}	-0.160	0.0
R63	$CO_2(s) + H_2O(s) + Pt(s) \rightarrow HCOO(s,s) + OH(s)$	1.07×10^{29}	-0.360	$25556.5 + 11942.3\theta_{O(s)}^b + 12420.0\theta_{OH(s)}^b$ $-11464.6\theta_{H_2O(s)}^b$
R64	$HCOO(s,s) + OH(s) \rightarrow CO_2(s) + H_2O(s) + Pt(s)$	2.41×10^{19}	0.070	$3105.0 - 21018.4\theta_{O(s)}^b - 12420.0\theta_{OH(s)}^b$ $+16002.7\theta_{H_2O(s)}^b$

Nomenclature

ρ	Mass density, kg m^{-3}
p	pressure, Pa
R	Ideal gas constant, $8.3144621 \text{ J K}^{-1} \text{ mol}^{-1}$
T	Temperature, K
$\bar{W} \equiv \sum_k x_k W_k$	Average molecular weight, kg kmol^{-1}
y_k	Mass fraction for species k , $\text{kg}_k \text{ kg}_{tot}^{-1}$
$x_k = \frac{1}{\sum_j \frac{y_j}{W_j}} \frac{y_k}{W_k}$	Mole fraction for species k , $\text{mol}_k \text{ mol}_{tot}^{-1}$
D_{km}	Mixture-average diffusion coefficient for species k , $\text{m}^2 \text{ s}^{-1}$
v_z	Velocity, m s^{-1}
μ	Average dynamic viscosity, $\text{kg m}^{-1} \text{ s}^{-1}$
$j_k = -\rho D_{km} \frac{\epsilon}{\tau} \frac{W_k}{\bar{W}} \frac{\partial x_k}{\partial z}$	Flux of species k due to molecular diffusion, $\text{kg m}^{-2} \text{ s}^{-1}$
W_k	Molecular mass of species k , kg kmol^{-1}
\dot{w}_k	Molar rate of production per unit volume of species k by homogeneous chemistry, $\text{mol m}^{-3} \text{ s}^{-1}$
\dot{s}_k	Molar rate of production per unit area for species k due to surface chemistry, $\text{mol m}^{-2} \text{ s}^{-1}$
τ	Tortuosity of the foam, m m^{-1}
θ_k	Site fraction of species k on Pt surface, mol mol^{-1}
Γ	Surface site density, mol m^{-2}
σ_k	Number of sites occupied by k , mol mol^{-1}
h_k	Specific enthalpy, J kg^{-1}
c_p	Average heat capacity, $\text{J K}^{-1} \text{ kg}^{-1}$
λ	Average thermal conductivity, $\text{W m}^{-1} \text{ K}^{-1}$
$K_k = S_h l^{-1} D_{km}$	Mass transfer coefficient, m s^{-1}
$K_T = N_u l^{-1} \lambda$	Heat transfer coefficient, $\text{W m}^{-2} \text{ K}^{-1}$
z	Axial coordinate, m
S_v (from μ -CT)	Geometric foam surface area to total gas-phase volume, m^{-1}
A (from μ -CT)	Geometric surface area of catalyst foam, m^2
$l = \frac{4\epsilon}{S_v}$	Characteristic length, m
$\delta = \frac{D_{O_2 m}}{K_{O_2}}$	Boundary layer thickness, m
$\gamma = \frac{V_{void} - V_{bl}}{V_{void}}$	Volume fraction of bulk gas, $\text{m}^3 \text{ m}^{-3}$
$\epsilon \equiv \frac{V_{void}}{V_{total}}$	Foam porosity, with $V_{total} = V_{void} + V_{solid}$
t	Time, s
$\text{C/O ratio} = \frac{\dot{V}_{CH_4}}{2\dot{V}_{O_2}}$	Ratio between atomic carbon and oxygen in gas feed
κ	Extinction coefficient, 2550 m^{-1} [2]
\vec{e}_z	Unit vector
f_{active}	Ratio of active metal surface area (from H_2 chemisorption) and support surface area (from Kr-BET), $\text{m}^2 \text{ m}^{-2}$
\dot{V}_k	Volumetric flow rate of species k , ml min^{-1}

Dimensionless numbers

$$\begin{aligned}
 Re &= \frac{\rho v_z l}{\mu} \\
 Sc &= \frac{\mu}{\rho D_{km}} \\
 Pr &= \frac{\mu c_p}{\lambda}
 \end{aligned}$$

Transport correlations

$$\begin{aligned}
 S_h &= 0.045 Re^{1/2} Sc^{1/3} \\
 N_u &= 0.045 Re^{1/2} Pr^{1/3}
 \end{aligned}$$

Appendix

Appendix A

IR Thermography - Pyrometer calibration

As was described above in section 3.4 it is recommended to calibrate a two-color ratio pyrometer against a reference. Therefore the setup depicted in Fig. A.1 was used. A cylindrical graphite monolith of 50 mm length and 16 mm diameter was placed in the isothermal zone of a horizontal tube furnace (Carbolite, model MTF 12/38/250). The graphite cylinder had a centerline drilling of 1 mm diameter to accommodate a type K thermocouple (Thermocoax 2ABI034) and the pyrometer optic, as it was used later in the profile measurements. The pyrometer optic consists of a fused silica capillary with 700 μm outer diameter and 530 μm inner diameter surrounding a 450 μm outer diameter low -OH silica fiber (Polymicro Technologies), with conical shaped tip. Thermocouple and pyrometer tip have been placed in the graphite monolith center, face to face.

The calibration was done by setting the furnace to a given temperature and recording the thermocouple and pyrometer temperature reading, after thermal equilibrium was reached. The correction factor $k = \epsilon_1/\epsilon_2$ was varied in the range of $0.8 \leq k \leq 1.2$ resulting in the top diagram of Fig. A.2. Additionally the k value was determined, which gave unity between thermocouple and pyrometer temperature. Fig. A.2 illustrates how strong a given k influences the temperature reading of the pyrometer, but how narrow on the other hand the optimal k value windows is. The optimal correction factor was found to $k = 1.027$, yielding to ≤ 5 K deviation from the thermocouple temperature, in a temperature range of $400 \leq T \leq 1100$ °C.

The independence of temperature measurements from the emissivity of a probed body was experimentally verified. Therefore two graphite monoliths were stacked around an Al_2O_3 monolith and the assembly was positioned in the exact center of the reactor furnace as depicted in Fig. A.3. Both materials exhibit significantly different spectral emissivities. The spectral emissivity of alumina is tabulated in a range of 0.22 – 0.4 [18], whereas the spectral emissivity of graphitic carbon is in the range of 0.7 – 0.8 [18]. The edge marked in Fig. A.3 (top panel) by a red dashed line corresponds to an axial position of zero in the measured temperature profile (Fig. A.3 bottom panel). Although the spectral emissivities of the probed monoliths deviate strongly a temperature step of just 3°C is observed at the monolith intersection.

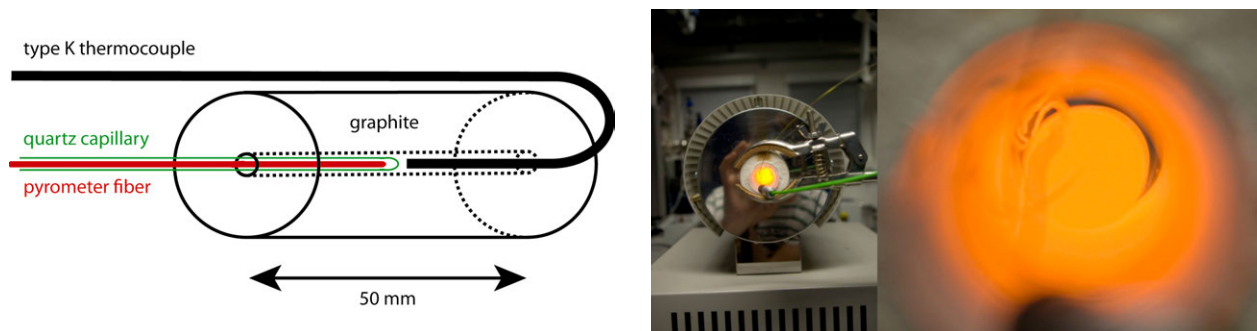


Figure A.1: Setup for pyrometer calibration to thermocouple in a graphite monolith inside the isothermal zone of a tube furnace.

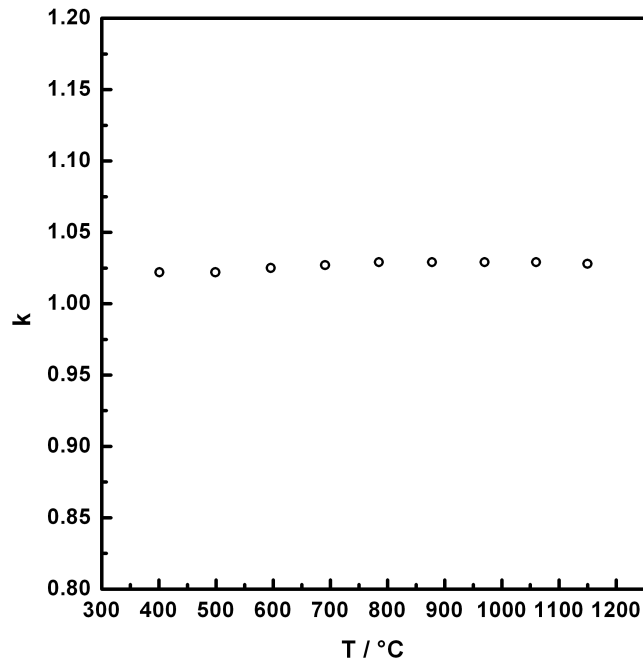
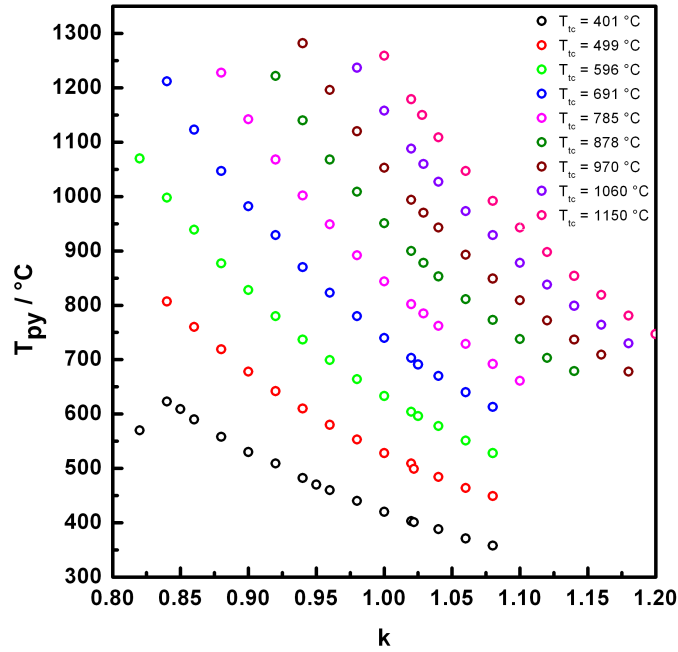


Figure A.2: Top: Temperature reading of the pyrometer T_{py} by variation of k at a given graphite monolith temperature measured by a type K thermocouple T_{tc} . Bottom: k optimal in the temperature range of $400 \leq T \leq 1100$ °C.

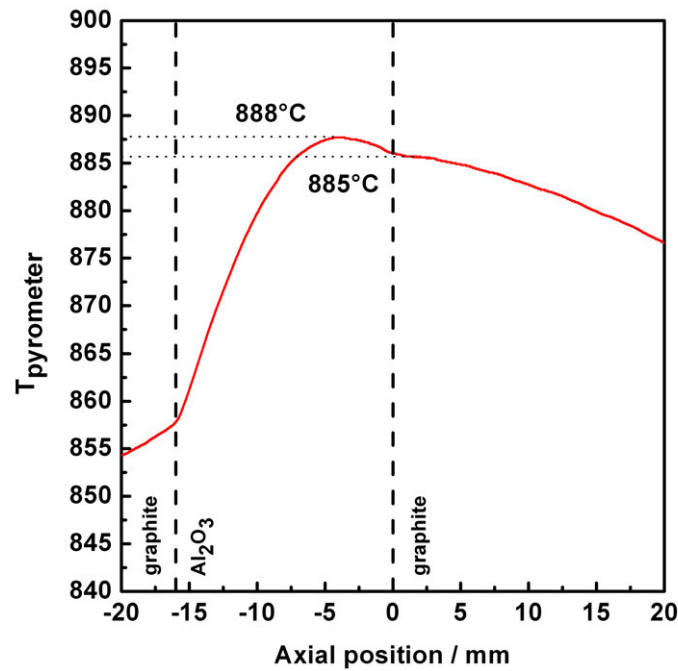
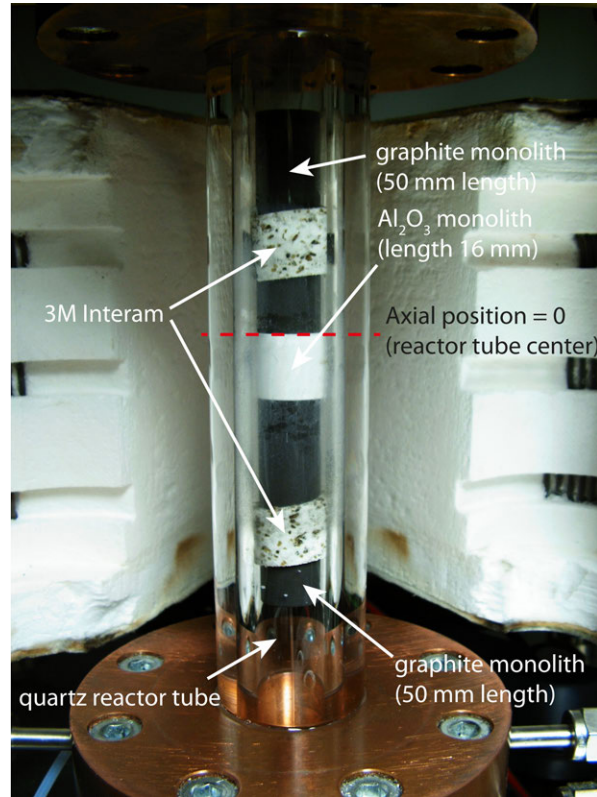


Figure A.3: Top: Photograph of test stack assembly to verify independence of the pyrometer from spectral emissivity after calibration. Upper and lower monolith made from graphite. Center monolith made from alumina. Bottom: Temperature profile along the monolith intersection from alumina to graphite in the furnace center zone. Furnace power set 450 W.

Appendix B

Quantitative Mass Spectrometry: MS Calibration

Quantitative mass spectrometry is done in this work by applying the internal standard method. The quantification is possible because all reactants and products can be separated clearly under the investigated reaction conditions by MS. The reason for this special situation is, that the investigated reaction (i.e. methane combustion) was done using an argon-methane-oxygen-mixture. The oxygen-argon-ratio was chosen equivalent to the nitrogen-oxygen-ratio in air. This avoids the interference of nitrogen at $m/z = 28$ with the reaction product carbon monoxide and has additionally the advantage, that no nitrogen oxides can be formed under the high temperature and high pressure conditions. Secondly argon is inert and does not change its amount during reaction.

As was mentioned above (section 3.5) the sensitivity of the used SEM detector is a function of the detected ions mass, charge, energy, and electronic configuration. Therefore all reactants and products have been calibrated in binary mixtures with argon over a broad concentration range. The calibration was done in the profile reactor using an empty reactor tube. The sampling capillary was hold by clean and dry corundum foam monoliths. The gas sampling was done in exactly the same configuration as in the reaction tests but at room temperature and ambient pressure. The gas mixtures where dosed by freshly calibrated mass flow controllers and premixed by traveling through the gas inlet system of the profile reactor and streaming through an 80 ppi corundum foam of 20 mm length (FHS). The different mixtures were measured in random order. The MS was operated in analog scan mode recoding complete mass spectra up to $m/z = 50$. The faster MID mode of the MS measuring just at selected m/z values was not applied, because it was less accurate and gave larger signal noise. The data evaluation was done by integration of the peak area by the trapezoidal rule, followed by linear regression of the analyte to argon ratios. Peak areas of the following nominal m/z ratios where chosen for species identification: H_2 (2), CH_4 (15), CO (28), O_2 (32), Ar (40), and CO_2 (44). Water could not be measured by the MS and was calculated from the oxygen mass balance, because condensation free transfer to the MS could not be assured. The contribution of fragments to $m/z = 28$ originating from carbon dioxide are considered, but usually of minor influence because of the high CO selectivities compared to CO_2 . Fig. B.1 to B.3 depict the fitting results. Each datapoint represents the mean peak area of a series of 20 mass spectra.

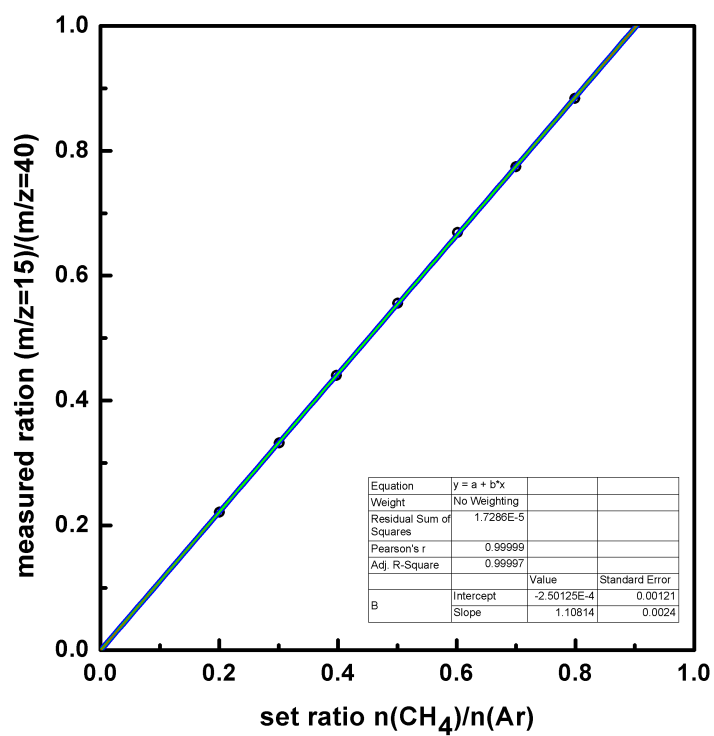


Figure B.1: MS calibration line for CH₄. Black symbols: Measured ratio between methane and argon peak area (($m/z = 15$)/($m/z = 40$)), red line: linear regression of measured data, green lines: confidence band (95 %), blue lines: prediction band (95 %).

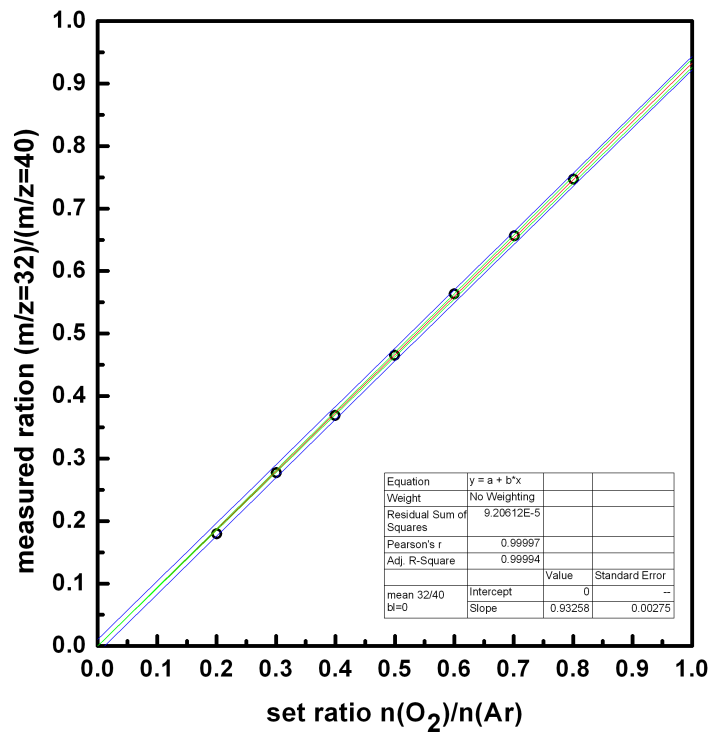
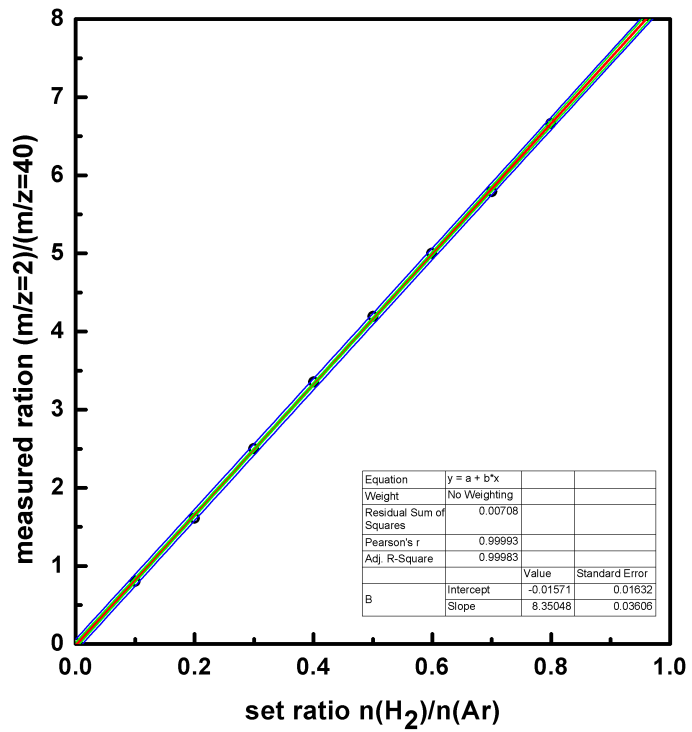


Figure B.2: MS calibration line for H₂ (top) and O₂ (bottom). Black symbols: Measured ratio between analyte and argon peak area (m/z values see at ordinate), red line: linear regression of measured data, green lines: confidence band (95 %), blue lines: prediction band (95 %).

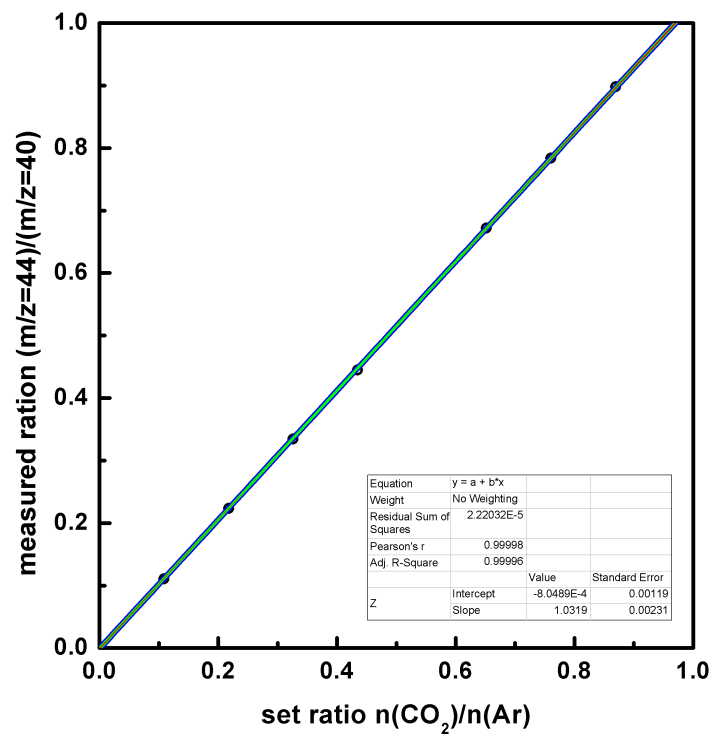
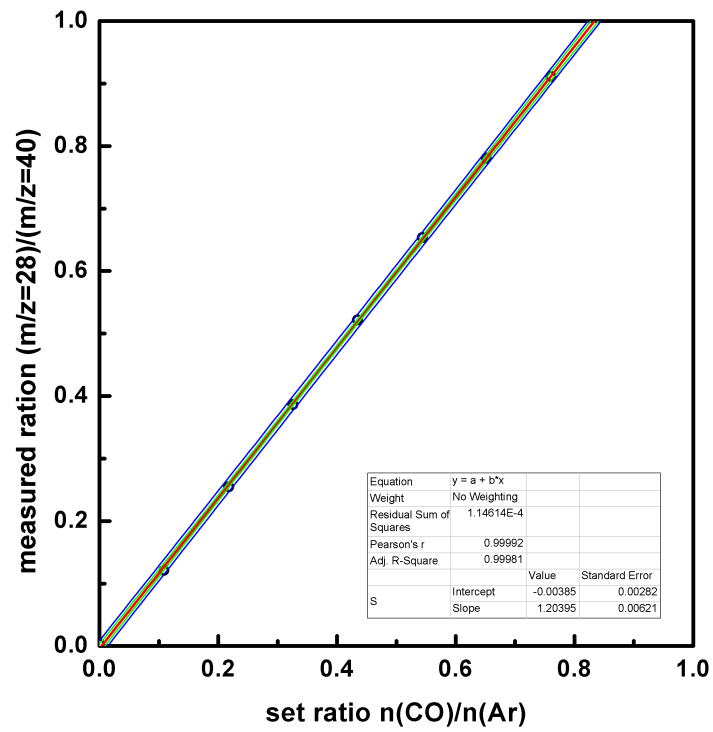


Figure B.3: MS calibration line for CO (top) and CO₂ (bottom). Black symbols: Measured ratio between analyte and argon peak area (m/z values see at ordinate), red line: linear regression of measured data, green lines: confidence band (95 %), blue lines: prediction band (95 %).

Appendix C

Spatially Resolved Reactor Profiles: Data Evaluation

Conducting spatial profile measurements requires processing of a large amount of raw data. To guarantee successful profiles in a series of experiments it is necessary to evaluate the obtained raw data immediately after data acquisition. This allows for instantaneous judgement of the profile quality and/or problem diagnostic. A MATLAB script was written for data evaluation, which is reproduced in the following section. It allows complete profile evaluation from ASCII raw data in less than 60 s. The transcript is self-explanatory to everyone familiar with basic knowledge of MATLAB. However important steps are commented. The script works in three steps:

- Data reading: The MS, the thermocouple and pyrometer raw data are read from ASCII files. The user needs to provide the script with parameters defining the catalyst stack dimensions and the reactant feed composition. For the reactant/product quantification calibration data need to be given, as well as integration intervals to evaluate the MS analog scan data.
- Data evaluation: This is the peak integration of the MS analog scan data, followed by reactant/product quantification. Molar flow rates, mole fractions, mass balances and the correlation of the MS data with the thermocouple and pyrometer data in the spatial domain are calculated.
- Data output: The results obtained in the previous step are plotted and displayed for examination. If needed the results are saved as ASCII files and the plots are saved as JPG image files.

```

1  %-----
2  %Script for evaluation/plotting of species and temperature profiles
3  %-----
4  clear; clc;
5  format long g
6
7  tic
8
9  disp('PROGRAM FOR QUICK PROFILE EVALUATION')
10 disp('Processing, please wait.')
```

11

12

13 %% Input calculation parameters

14

15 %% Input filenames of ASCII raw data

16 MSfilename='ms_ptt_12037_9_profile_up2_10_1000ml_1.15bar.asc';

17 Pyfilename='Tpy_ptt_12037_9_profile_up2_10_1000ml_1.15bar.txt';

18 Tcfilename='Ttc_ptt_12037_9_profile_up2_10_1000ml_1.15bar.CSV';

19

20 %% Input of stack coordinates (!!!In counts relative to FHS bottom side!!!)

21 FHS_bottom=0;

22 FHS_top=585956;

23 BHS_bottom=3430400;

24 BHS_top=3970845;

25 translation_top=4255289;

26 translation_bottom=-284444;

27 translation_velocity=1000;

28 translation_direction=2; %"1" represents running down; "2" represents running up

29 start_MS=0; %Master time index in profile measurements [s]

30 start_Py=60; %Delay to master time index [s]

31 start_Tc=120; %Delay to master time index [s]

32 start_Motor=180; %Delay to master time index [s]

33

34 %% Integration limits for MS data evaluation !!!Have a look on the spectra!!!

35 IP=[1 0.91 1.56

36 2 1.56 2.69

37 3 2.69 3.62

38 4 3.62 4.62

39 5 NaN NaN

40 6 NaN NaN

41 7 NaN NaN

42 8 NaN NaN

43 9 NaN NaN

44 10 NaN NaN

45 11 NaN NaN

46 12 11.56 12.53

47 13 12.53 13.56

48 14 13.56 14.53

49 15 14.53 15.56

50 16 15.56 16.59

51 17 16.59 17.53

52 18 17.53 18.56

53 19 18.56 19.41

54 20 19.41 20.56

55 21 NaN NaN

56 22 21.56 22.44

57 23 NaN NaN

58 24 23.50 24.50

59 25 24.50 25.44

60 26 25.44 26.47

61 27 26.47 27.28

62 28 27.28 28.50

63 29 28.50 29.44

64 30 29.44 30.41

65 31 30.41 31.19

66 32 31.19 32.56

67 33 32.56 33.38

68 34 33.38 34.31

69 35 34.31 35.25

70 36 35.25 36.41

71 37 36.41 37.34

72 38 37.34 38.34

73 39 NaN NaN

74 40 38.44 40.50

75 41 40.50 41.34

76 42 NaN NaN

```

77     43 NaN NaN
78     44 43.06 44.41
79     45 44.41 45.31
80     46 45.31 46.31
81     47 NaN NaN
82     48 NaN NaN
83     49 NaN NaN
84     50 NaN NaN];
85
86 %% Gas feed composition [mln/min]
87 FCH4=600;
88 FO2=300;
89 FAr=92;
90
91 FCH4=FCH4/1000000; %Converted to SI system
92 FO2=FO2/1000000;
93 FAr=FAr/1000000;
94
95 %% MS calibration data (slope of calibration line)
96 %1. H2
97 mH2calib=8.35048;
98 %2. CH4
99 mCH4calib=1.10814;
100 %3. CO
101 mCOcalib=1.20395;
102 %4. O2
103 mO2calib=0.93258;
104 %5. CO2
105 mCO2calib=1.03190;
106
107 %% Other parameters/constant
108 R=8.31447215; %Universal gas constant [J*mol^-1*k^-1]
109 MScyclelength=3650/333; %Duration for a MS cycle [s]
110
111
112 %% Read raw data to workspace
113
114 %MS
115 data=dlmread(MSfilename, '\t');
116 [a,b]=size(data);
117 [c,d]=size(IP);
118
119 %Pyrometer
120 %1. Ignore header lines by search of header line end
121 [fid, message]=fopen(Pyfilename, 'rt');
122 if fid==-1, %File doesn't exist?
123     disp('Input file does not exist!');
124     return;
125 else %Ok it exists
126     i=1;
127     count=0;
128     while feof(fid)==0,
129         header=fgetl(fid);
130         count=count+1;
131         if findstr(header, 'Emi'), %Search for key word, i.e. the headers end
132             index(i)=count;
133             i=i+1;
134             offset=count; %Offset from key word
135         end
136     end
137 end
138
139 %2. Read relevant data to workspace
140 [c1, c2, c3, c4, c5, c6, c7]=textread(Pyfilename, '%d %s %s %f %f %s %s', 'delimiter',
    '\t', 'headerlines', offset);
141 [Tpy_rawdata]=[c1, c4, c5];
142 clear c1 c2 c3 c4 c5 c6 c7;
143 fclose(fid);
144
145 %3. Correction of Tpy_rawdata: Due to the problem that the time inter is set to zero at 12
    am the time inter has to be corrected after reading the data from file. Otherwise a
    stupid jump in negative spatial coordinate occurs in the data valuation for
    measurements crossing 12 am. It works simply by checking if the smallest time value
    observed is the first in the file. If it is like this evrything is ok. If it is not
    like this, the largest time value is added to the smallest and all following times
    resulting in a stepless time index.

```

```

146 h1=Tpy_rawdata(:,2);
147 if min(h1)==h1(1),
148 else
149     h2=min(h1);
150     for i=1:length(h1),
151         if h2==h1(i),
152             h3=i;
153         else
154             end
155         end
156         h4=h1(h3-1);
157         for i=h3:1:(length(h1)),
158             h1(i)=h1(i)+h4;
159         end
160         Tpy_rawdata(:, 2)=h1;
161         clear h1 h2 h3 h3 i;
162     end
163
164 %Thermocouple
165 [fid, message]=fopen(Tcfilename, 'rt');
166 if fid==-1, %File doesn't exist?
167     disp('Input file does not exist!');
168     return;
169 else %Ok it exists
170     i=1;
171     count=0;
172     while feof(fid)==0,
173         header=fgetl(fid);
174         count=count+1;
175         if findstr(header, 'COM9.ID001-2416.Operator.MAIN.PV'), %Search for key word, i.e.
176             the headers end
177             index(i)=count;
178             i=i+1;
179             offset=count; %Offset from key word
180         end
181     end
182 [c1, c2, c3, c4]=textread(Tcfilename, '%f %f %d %f', 'delimiter', ',', 'headerlines',
183     offset);
184 [Ttc_rawdata]=[c1, c2, c3, c4];
185 clear c1 c2 c3 c4;
186 fclose(fid);
187
188 %% Calculations
189 %% Integration of peak areas in given interval
190 for spectrum=1:(b-1),
191     for peak=1:c,
192         pos1=int2str(spectrum);
193         pos2=int2str(peak);
194         for l=1:a,
195             if data(l, 1)==IP(peak, 2);
196                 indexx0=l;
197             else
198                 end
199             end
200             for l=1:a,
201                 if data(l, 1)==IP(peak, 3),
202                     indexx1=l;
203                 else
204                     end
205             end
206             x=data(indexx0:indexx1, 1);
207             y=data(indexx0:indexx1, (spectrum+1));
208             MS_peakareas(spectrum, peak)=trapz(x, y);
209         end
210     end
211 clear IP a b c d data indexx0 indexx1 l peak pos1 pos2 spectrum x y;
212
213 %Calculate m/z ratios for reactants and products (H2 (2), CH4 (15), H2O (18), CO (28), O2
214     (32), Ar (40), CO2 (44))
215 H2Ar=MS_peakareas(:, 2)./MS_peakareas(:, 40);
216 CH4Ar=MS_peakareas(:, 15)./MS_peakareas(:, 40);
217 H2OAr=MS_peakareas(:, 18)./MS_peakareas(:, 40);
218 COAr=MS_peakareas(:, 28)./MS_peakareas(:, 40);
219 O2Ar=MS_peakareas(:, 32)./MS_peakareas(:, 40);

```

```

219 CO2Ar=MS_peakareas(:, 44)./MS_peakareas(:, 40);
220
221 %% Calculate species molecular flow with respect to calibration data
222 %1. H2
223 if translation_direction==1,
224     h1=(translation_top-translation_bottom)/translation_velocity; %Time until full
        profile run completed [s]
225     h2=round(h1/MScyclelength); %Number (integer) of MS cycles in a full profile run
226     h3=(FHS_bottom-translation_bottom)/translation_velocity; %Time until distance
        translation_bottom to FHS_bottom takes [s]
227     h4=round(h3/MScyclelength); %Number (integer) of MS cycles from translation_bottom
        position to FHS_bottom position
228     blank=0;
229     for i=h2-6:1:h2; %Seven cycles from sampling position at the edge to the FHS and in
        flow direction
230         blank=blank+H2Ar(i);
231     end
232     blank=blank/7;
233     H2profile=((H2Ar-blank)./mH2calib).*(101325*FAr/R/298.15); %[mol/min]
234 elseif translation_direction==2,
235     h1=(translation_top-translation_bottom)/translation_velocity; %Time until full
        profile run completed [s]
236     h2=round(h1/MScyclelength); %Number (integer) of MS cycles in a full profile run
237     h3=(FHS_bottom-translation_bottom)/translation_velocity; %Time until distance
        translation_bottom to FHS_bottom takes [s]
238     h4=round(h3/MScyclelength); %Number (integer) of MS cycles from translation_bottom
        position to FHS_bottom position
239     blank=0;
240     for i=2+h4:1:8+h4, %Seven cycles, first cycle is neglected, sampling position in or
        prior to the FHS
241         blank=blank+H2Ar(i);
242     end
243     blank=blank/7;
244     H2profile=((H2Ar-blank)./mH2calib).*(101325*FAr/R/298.15); %[mol/min]
245 else
246     end
247
248 %2. CH4
249 %CH4profile=(CH4Ar./mCH4calib).*(101325*FAr/R/298.15); %[mol/min]
250 %
251 %Alternatively calculated with one point calibration from gas feed composition and
        blank in front heat shield
252 %
253 if translation_direction==1,
254     h1=(translation_top-translation_bottom)/translation_velocity; %Time until full
        profile run completed [s]
255     h2=round(h1/MScyclelength); %Number (integer) of MS cycles in a full profile run
256     h3=(FHS_bottom-translation_bottom)/translation_velocity; %Time until distance
        translation_bottom to FHS_bottom takes [s]
257     h4=round(h3/MScyclelength); %Number (integer) of MS cycles from translation_bottom
        position to FHS_bottom position
258     blank=0;
259     for i=h2-6:1:h2; %Seven cycles from sampling position at the edge to the FHS and in
        flow direction
260         blank=blank+CH4Ar(i);
261     end
262     blank=blank/7;
263     CH4profile=CH4Ar.*(FCH4*101325/R/298.15/blank); temp1=CH4Ar; temp2=blank;
264 elseif translation_direction==2,
265     h1=(translation_top-translation_bottom)/translation_velocity; %Time until full
        profile run completed [s]
266     h2=round(h1/MScyclelength); %Number (integer) of MS cycles in a full profile run
267     h3=(FHS_bottom-translation_bottom)/translation_velocity; %Time until distance
        translation_bottom to FHS_bottom takes [s]
268     h4=round(h3/MScyclelength); %Number (integer) of MS cycles from translation_bottom
        position to FHS_bottom position
269     blank=0;
270     for i=2+h4:1:8+h4, %Seven cycles, first cycle is neglected, sampling position in or
        prior to the FHS
271         blank=blank+CH4Ar(i);
272     end
273     blank=blank/7;
274     CH4profile=CH4Ar.*(FCH4*101325/R/298.15/blank);
275 else
276     end
277

```

```

278 %3. CO
279 if translation_direction==1,
280     h1=(translation_top-translation_bottom)/translation_velocity; %Time until full
        profile run completed [s]
281     h2=round(h1/MScyclelength); %Number (integer) of MS cycles in a full profile run
282     h3=(FHS_bottom-translation_bottom)/translation_velocity; %Time until distance
        translation_bottom to FHS_bottom takes [s]
283     h4=round(h3/MScyclelength); %Number (integer) of MS cycles from translation_bottom
        position to FHS_bottom position
284     blank=0;
285     for i=h2-6:1:h2; %Seven cycles from sampling position at the edge to the FHS and in
        flow direction
286         blank=blank+COAr(i);
287     end
288     blank=blank/7;
289     COprofile=((COAr-blank)./mCOcalib).*(101325*FAr/R/298.15); %[mol/min]
290 elseif translation_direction==2,
291     h1=(translation_top-translation_bottom)/translation_velocity; %Time until full
        profile run completed [s]
292     h2=round(h1/MScyclelength); %Number (integer) of MS cycles in a full profile run
293     h3=(FHS_bottom-translation_bottom)/translation_velocity; %Time until distance
        translation_bottom to FHS_bottom takes [s]
294     h4=round(h3/MScyclelength); %Number (integer) of MS cycles from translation_bottom
        position to FHS_bottom position
295     blank=0;
296     for i=2+h4:1:8+h4; %Seven cycles, first cycle is neglected, sampling position in or
        prior to the FHS
297         blank=blank+COAr(i);
298     end
299     blank=blank/7;
300     COprofile=((COAr-blank)./mCOcalib).*(101325*FAr/R/298.15); %[mol/min]
301 else
302     end
303
304 %4. O2
305 %O2profile=(O2Ar./mO2calib).*(101325*FAr/R/298.15); %[mol/min]
306 %-----
307 %Alternatively calculated with one point calibration from gas feed composition and
        blank in front heat shield
308 %-----
309 if translation_direction==1,
310     h1=(translation_top-translation_bottom)/translation_velocity; %Time until full
        profile run completed [s]
311     h2=round(h1/MScyclelength); %Number (integer) of MS cycles in a full profile run
312     h3=(FHS_bottom-translation_bottom)/translation_velocity; %Time until distance
        translation_bottom to FHS_bottom takes [s]
313     h4=round(h3/MScyclelength); %Number (integer) of MS cycles from translation_bottom
        position to FHS_bottom position
314     blank=0;
315     for i=h2-6:1:h2; %Seven cycles from the end of profile run, i.e. sampling position
        in or prior to the FHS
316         blank=blank+O2Ar(i);
317     end
318     blank=blank/7;
319     O2profile=O2Ar.*(FO2*101325/R/298.15/blank);
320 elseif translation_direction==2,
321     h1=(translation_top-translation_bottom)/translation_velocity; %Time until full
        profile run completed [s]
322     h2=round(h1/MScyclelength); %Number (integer) of MS cycles in a full profile run
323     h3=(FHS_bottom-translation_bottom)/translation_velocity; %Time until distance
        translation_bottom to FHS_bottom takes [s]
324     h4=round(h3/MScyclelength); %Number (integer) of MS cycles from translation_bottom
        position to FHS_bottom position
325     blank=0;
326     for i=2:1:8; %Seven cycles, first cycle is neglected, sampling position in or prior
        to the FHS
327         blank=blank+O2Ar(i);
328     end
329     blank=blank/7;
330     O2profile=O2Ar.*(FO2*101325/R/298.15/blank);
331 else
332     end
333
334 %5. CO2
335 if translation_direction==1,

```



```

336     h1=(translation_top-translation_bottom)/translation_velocity; %Time until full
        profile run completed [s]
337     h2=round(h1/MScyclelength); %Number (integer) of MS cycles in a full profile run
338     h3=(FHS_bottom-translation_bottom)/translation_velocity; %Time until distance
        translation_bottom to FHS_bottom takes [s]
339     h4=round(h3/MScyclelength); %Number (integer) of MS cycles from translation_bottom
        position to FHS_bottom position
340     blank=0;
341     for i=h2-6:1:h2; %Seven cycles from sampling position at the edge to the FHS and in
        flow direction
342         blank=blank+CO2Ar(i);
343     end
344     blank=blank/7;
345     CO2profile=((CO2Ar-blank)./mCO2calib).*(101325*FAr/R/298.15); %[mol/min]
346 elseif translation_direction==2,
347     h1=(translation_top-translation_bottom)/translation_velocity; %Time until full
        profile run completed [s]
348     h2=round(h1/MScyclelength); %Number (integer) of MS cycles in a full profile run
349     h3=(FHS_bottom-translation_bottom)/translation_velocity; %Time until distance
        translation_bottom to FHS_bottom takes [s]
350     h4=round(h3/MScyclelength); %Number (integer) of MS cycles from translation_bottom
        position to FHS_bottom position
351     blank=0;
352     for i=2+h4:1:8+h4, %Seven cycles, first cycle is neglected, sampling position in or
        prior to the FHS
353         blank=blank+CO2Ar(i);
354     end
355     blank=blank/7;
356     CO2profile=((CO2Ar-blank)./mCO2calib).*(101325*FAr/R/298.15); %[mol/min]
357 else
358 end
359
360 %6. H2O calculation from O balance
361 i=length(MS_peakareas(:, 1));
362 h1=ones(i, 1);
363 H2Oprofile=(2*(FO2*101325/R/298.15)*h1)-COprofile-2*O2profile-2*CO2profile; %[mol/min]
364
365 %clear CH4Ar CO2Ar COAr H2Ar H2OAr MS_peakareas O2Ar blank i mCH4calib mCO2calib mCOcalib
        mH2calib mO2calib;
366
367 %% Calculate mass balances
368 %1. C
369 Cbalance((((101325*FCH4/R/298.15)*h1)-CH4profile-COprofile-CO2profile)
        ./ (101325*FCH4/R/298.15).*100); %[%]
370
371 %2. H
372 Hbalance((((4*(101325*FCH4/R/298.15)*h1)-2*H2profile-4*CH4profile
        -2*H2Oprofile)./(4*(101325*FCH4/R/298.15)).*100); %[%]
373
374 %3. O
375 Obalance((((2*(101325*FO2/R/298.15)*h1)-COprofile-2*O2profile-2*CO2profile
        -H2Oprofile)./(2*(101325*FO2/R/298.15)).*100); %[%]
376
377 clear h1 h2 h3 h4;
378
379 %% Calculate mole fraction of all species from molar flow rates
380 tmp=ones(length(O2profile), 1);
381 Arprofile=tmp.*((FAr*101325)/(R*298.15));
382 Heprofile=tmp.*(((FAr/0.92)-FAr)*101325)/(R*298.15); %In case the Ar/He mixture with 8%
        He is used
383 Sumprofile=Arprofile+Heprofile+COprofile+CO2profile+O2profile
        +H2Oprofile+H2profile+CH4profile;
384
385 XArprofile=Arprofile./Sumprofile;
386 XHeprofile=Heprofile./Sumprofile;
387 XCOprofile=COprofile./Sumprofile;
388 XCO2profile=CO2profile./Sumprofile;
389 XO2profile=O2profile./Sumprofile;
390 XH2Oprofile=H2Oprofile./Sumprofile;
391 XH2profile=H2profile./Sumprofile;
392 XCH4profile=CH4profile./Sumprofile;
393 CheckSum=XArprofile+XHeprofile+XCOprofile+XCO2profile+XO2profile
        +XH2Oprofile+XH2profile+XCH4profile;
394
395 %% Transform time coordinate to spatial coordinate and plot results
396

```

```

397 %% 1. Pyrometer
398 if translation_direction==1,
399     i=length(Tpy_rawdata(:, 1));
400     h1=ones(i, 1); h3=h1;
401     h1=h1*Tpy_rawdata(1, 2);
402     h2=Tpy_rawdata(:, 2)-h1;
403     h4=(((translation_top*h3)-(h2-(h3*(start_Motor-start_Py)))
         *translation_velocity)+(h3*(FHS_bottom-FHS_top)))/56.88889; %This formula is:
         Uppermost position - velocity * time (pyrometer time index - delay to master time
         index) + corrected to zero position to begin at the catalyst bed bottom divided by
         number of counts per micrometer
404     clear h1 h2 h3;
405 elseif translation_direction==2, %now comes exactly the same as in case of down movement
         with one difference the starting position of the movement is the lowest spatial position
406     i=length(Tpy_rawdata(:, 1));
407     h1=ones(i, 1); h3=h1;
408     h1=h1*Tpy_rawdata(1, 2);
409     h2=Tpy_rawdata(:, 2)-h1;
410     h4=(((translation_bottom*h3)+(h2-(h3*(start_Motor-start_Py)))
         *translation_velocity)+(h3*(FHS_bottom-FHS_top)))/56.88889; %This formula is:
         Uppermost position + velocity * time (pyrometer time index - delay to master time
         index) + corrected to zero position to begin at the catalyst bed bottom divided by
         number of counts per micrometer
411     clear h1 h2 h3;
412 else
413 end
414
415 % Reduction of temperature datapoint number for CHEMKIN input (1/1000 of the original
         number of data points)
416 reducedTpy=[];
417 h5=[];
418 for i=1:1500:length(Tpy_rawdata(:, 1)),
419     h5=[h5; h4(i)];
420     reducedTpy=[reducedTpy; Tpy_rawdata(i, 3)];
421 end
422
423 % Plot results - pyrometer
424 figure;
425 plot(h4, Tpy_rawdata(:,3), 'r-', h5, reducedTpy, 'bo');
426 legend('T', 'T (reduced datapoint number)');
427 axis([(FHS_bottom-FHS_top)/56.88889, (BHS_top+FHS_bottom-FHS_top)/56.88889, 350,
         max(Tpy_rawdata(:, 3)+100)]);
428 xlabel('sampling position [um]');
429 ylabel('pyrometer temperature [°C]');
430 line([0, 0], ylim, 'color', [0, 0, 0]); %Line at catalyst bed beginning
431 line([(BHS_bottom+FHS_bottom-FHS_top)/56.88889,
         (BHS_bottom+FHS_bottom-FHS_top)/56.88889], ylim, 'color', [0, 0, 0]); %Line at
         catalyst bed end
432 resultPy=[h4, Tpy_rawdata(:, 3)];
433 resultPyLabel=[cellstr('axial position pyrometer / um'), cellstr('T pyrometer / °C')];
         %For storage of result data
434 resultreducedPy=[h5, reducedTpy]; %For storage of result data
435 clear h4 h5;
436
437 %% 2. Thermocouple
438 if translation_direction==1,
439     i=length(Ttc_rawdata(:, 1));
440     h1=ones(i, 1); h3=h1;
441     h1=h1*Ttc_rawdata(1, 1);
442     h2=(Ttc_rawdata(:, 1)-h1)*86400;
443     h4=(((translation_top*h3)-(h2-(h3*(start_Motor-start_Tc)))
         *translation_velocity)+(h3*(FHS_bottom-FHS_top)))/56.88889; %This formula is:
         Uppermost position - velocity * time (pyrometer time index - delay to master time
         index) + corrected to zero position to begin at the catalyst bed bottom divided by
         number of counts per micrometer
444     clear h1 h2 h3;
445 elseif translation_direction==2, %now comes exactly the same as in case of down movement
         with one difference the starting position of the movement is the lowest spatial position
446     i=length(Ttc_rawdata(:, 1));
447     h1=ones(i, 1); h3=h1;
448     h1=h1*Ttc_rawdata(1, 1);
449     h2=(Ttc_rawdata(:, 1)-h1)*86400;
450     h4=(((translation_bottom*h3)+(h2-(h3*(start_Motor-start_Tc)))
         *translation_velocity)+(h3*(FHS_bottom-FHS_top)))/56.88889; %This formula is:
         Uppermost position + velocity * time (pyrometer time index - delay to master time
         index) + corrected to zero position to begin at the catalyst bed bottom divided by

```

```

        number of counts per micrometer
451 clear h1 h2 h3;
452 else
453 end
454
455 % Plot results - Thermocouple
456 figure;
457 plot(h4, Ttc_rawdata(:, 2), 'r');
458 axis([(FHS_bottom-FHS_top)/56.88889, (BHS_top+FHS_bottom-FHS_top)/56.88889,
        min(Ttc_rawdata(:, 2)-100), max(Ttc_rawdata(:, 2)+100)]);
459 xlabel('sampling position [um]');
460 ylabel('thermocouple temperature [°C]');
461 line([0, 0], ylim, 'color', [0, 0, 0]); %Line at catalyst bed beginning
462 line([(BHS_bottom+FHS_bottom-FHS_top)/56.88889,
        (BHS_bottom+FHS_bottom-FHS_top)/56.88889], ylim, 'color', [0, 0, 0]); %Line at
        catalyst bed end
463 resultTc=[h4, Ttc_rawdata(:, 2)]; resultTcLabel=[cellstr('axial position thermocouple /
        um'), cellstr('T thermocouple / °C')]; %For storage of result data
464 clear h4;
465
466 %% 3. Species & balances
467 if translation_direction==1,
468     h1=[1:length(H2profile)-1, 1];
469     h1=reshape(h1, [], 1);
470     h2=(h1*MScyclelength);
471     h3=ones(length(H2profile), 1);
472     h4=((translation_top*h3)-(h2-(h3*(start_Motor-start_MS)))
        *translation_velocity)+(h3*(FHS_bottom-FHS_top))/56.88889;
473     clear h1 h2 h3;
474 elseif translation_direction==2,
475     h1=[1:length(H2profile)-1, 1];
476     h1=reshape(h1, [], 1);
477     h2=(h1*MScyclelength);
478     h3=ones(length(H2profile), 1);
479     h4=((translation_bottom*h3)+(h2-(h3*(start_Motor-start_MS)))
        *translation_velocity)+(h3*(FHS_bottom-FHS_top))/56.88889;
480     clear h1 h2 h3;
481 else
482 end
483
484 % Plot results - Species
485 figure;
486 plot(h4, H2profile, 'o', h4, CH4profile, 'o', h4, H2Oprofile, 'o', h4, COprofile, 'o', h4,
        O2profile, 'o', h4, CO2profile, 'o');
487 legend('H_2', 'CH_4', 'H_2O', 'CO', 'O_2', 'CO_2');
488 axis([(FHS_bottom-FHS_top)/56.88889, (BHS_top+FHS_bottom-FHS_top)/56.88889, -0.01,
        max(CH4profile)*2.25]);
489 xlabel('sampling position [um]');
490 ylabel('molar flow rate [mol/min]');
491 line([0, 0], ylim, 'color', [0, 0, 0]);
492 line([(BHS_bottom+FHS_bottom-FHS_top)/56.88889, (BHS_bottom+FHS_bottom-FHS_top)/56.88889],
        ylim, 'color', [0, 0, 0]);
493
494 % Plot results - Balances
495 figure;
496 plot(h4, Cbalance, h4, Hbalance, h4, Obalance);
497 legend('carbon balance', 'hydrogen balance', 'oxygen balance');
498 axis([(FHS_bottom-FHS_top)/56.88889, (BHS_top+FHS_bottom-FHS_top)/56.88889, -100, +100]);
499 xlabel('sampling position [um]');
500 ylabel('deviation from closed mass balance [%]');
501 line([0, 0], ylim, 'color', [0, 0, 0]);
502 line([(BHS_bottom+FHS_bottom-FHS_top)/56.88889, (BHS_bottom+FHS_bottom-FHS_top)/56.88889],
        ylim, 'color', [0, 0, 0]);
503
504 % Plot results - Mole fractions (all)
505 figure;
506 plot(h4, XArprofile, 'o', h4, XHeprofile, 'o', h4, XCOprofile, 'o', h4, XO2profile, 'o',
        h4, XCO2profile, 'o', h4, XH2Oprofile, 'o', h4, XH2profile, 'o', h4, XCH4profile, 'o',
        h4, CheckSum, 'o');
507 legend('Ar', 'He', 'CO', 'O_2', 'CO_2', 'H_2O', 'H_2', 'CH_4', 'Sum X_i');
508 axis([(FHS_bottom-FHS_top)/56.88889, (BHS_top+FHS_bottom-FHS_top)/56.88889, -0.01, 1.01]);
509 xlabel('sampling position [um]');
510 ylabel('mole fraction');
511 line([0, 0], ylim, 'color', [0, 0, 0]);
512 line([(BHS_bottom+FHS_bottom-FHS_top)/56.88889, (BHS_bottom+FHS_bottom-FHS_top)/56.88889],
        ylim, 'color', [0, 0, 0]);

```

```

513
514 resultSpeciesBalancesMoleFractions=[h4, COprofile, O2profile, CO2profile, Cbalance,
    Hbalance, Obalance, XArprofile, XHeprofile, XCOprofile, XO2profile, XCO2profile,
    XH2Oprofile, XH2profile, XCH4profile, CheckSum]; %For storage of result data
515 resultSpeciesBalancesMoleFractionsLabel=[cellstr('axial position / um'), cellstr('F CO /
    mol min-1'), cellstr('F O2 / mol min-1'), cellstr('F CO2 / mol min-1'), cellstr('C
    balance / err percent'), cellstr('H balance / err percent'), cellstr('O balance / err
    percent'), cellstr('X_Ar'), cellstr('X_He'), cellstr('X_CO'), cellstr('X_O2'),
    cellstr('X_CO2'), cellstr('X_H2O'), cellstr('X_H2'), cellstr('X_CH4'), cellstr('Sum
    X_i')]; %For storage of result data
516
517 clear h4;
518
519 disp('Done. ');
520
521 toc
522
523 disp('-----');
524
525 %% Write all results in one result file (ASCII)
526 h1=input('Do you wanna store data to file? (Y/N)', 's');
527
528 tic
529
530 if h1=='Y',
531     dlmwrite('MS.txt', resultSpeciesBalancesMoleFractions);
532     fid=fopen('MSlabel.txt', 'w');
533     for k=1:length(resultSpeciesBalancesMoleFractionsLabel),
534         if k<length(resultSpeciesBalancesMoleFractionsLabel),
535             fprintf(fid, [cell2mat(resultSpeciesBalancesMoleFractionsLabel(k)) ', ']);
536         else
537             fprintf(fid, [cell2mat(resultSpeciesBalancesMoleFractionsLabel(k)) '\n']);
538         end
539     end
540     fclose(fid);
541     !copy MSlabel.txt+MS.txt result_MS.txt;
542     delete MS.txt MSlabel.txt;
543
544     dlmwrite('Py.txt', resultPy);
545     fid=fopen('Pylabel.txt', 'w');
546     for k=1:length(resultPyLabel),
547         if k<length(resultPyLabel),
548             fprintf(fid, [cell2mat(resultPyLabel(k)) ', ']);
549         else
550             fprintf(fid, [cell2mat(resultPyLabel(k)) '\n']);
551         end
552     end
553     fclose(fid);
554     !copy Pylabel.txt+Py.txt result_Py.txt;
555     delete Py.txt Pylabel.txt;
556
557     dlmwrite('Py_reduced.txt', resultreducedPy);
558     fid=fopen('Pylabel.txt', 'w');
559     for k=1:length(resultPyLabel),
560         if k<length(resultPyLabel),
561             fprintf(fid, [cell2mat(resultPyLabel(k)) ', ']);
562         else
563             fprintf(fid, [cell2mat(resultPyLabel(k)) '\n']);
564         end
565     end
566     fclose(fid);
567     !copy Pylabel.txt+Py_reduced.txt result_Py_reduced.txt;
568     delete Py_reduced.txt Pylabel.txt;
569
570     dlmwrite('Tc.txt', resultTc);
571     fid=fopen('Tclabel.txt', 'w');
572     for k=1:length(resultTcLabel),
573         if k<length(resultTcLabel),
574             fprintf(fid, [cell2mat(resultTcLabel(k)) ', ']);
575         else
576             fprintf(fid, [cell2mat(resultTcLabel(k)) '\n']);
577         end
578     end
579     fclose(fid);
580     !copy Tclabel.txt+Tc.txt result_Tc.txt;
581     delete Tc.txt Tclabel.txt;

```

```

582     saveas(gcf-4, 'Tpy.jpg');
583     saveas(gcf-3, 'Tc.jpg');
584     saveas(gcf-2, 'Molar flow rates.jpg');
585     saveas(gcf-1, 'Mass balances.jpg');
586     saveas(gcf, 'Mole fractions.jpg');
587 elseif h1=='y',
588     dlmwrite('MS.txt', resultSpeciesBalancesMoleFractions);
589     fid=fopen('MSlabel.txt', 'w');
590     for k=1:length(resultSpeciesBalancesMoleFractionsLabel),
591         if k<length(resultSpeciesBalancesMoleFractionsLabel),
592             fprintf(fid, [cell2mat(resultSpeciesBalancesMoleFractionsLabel(k)) ',']);
593         else
594             fprintf(fid, [cell2mat(resultSpeciesBalancesMoleFractionsLabel(k)) '\n']);
595         end
596     end
597 end
598 fclose(fid);
599 !copy MSlabel.txt+MS.txt result_MS.txt;
600 delete MS.txt MSlabel.txt;
601
602 dlmwrite('Py.txt', resultPy);
603 fid=fopen('Pylabel.txt', 'w');
604 for k=1:length(resultPyLabel),
605     if k<length(resultPyLabel),
606         fprintf(fid, [cell2mat(resultPyLabel(k)) ',']);
607     else
608         fprintf(fid, [cell2mat(resultPyLabel(k)) '\n']);
609     end
610 end
611 fclose(fid);
612 !copy Pylabel.txt+Py.txt result_Py.txt;
613 delete Py.txt Pylabel.txt;
614
615 dlmwrite('Py_reduced.txt', resultreducedPy);
616 fid=fopen('Pylabel.txt', 'w');
617 for k=1:length(resultPyLabel),
618     if k<length(resultPyLabel),
619         fprintf(fid, [cell2mat(resultPyLabel(k)) ',']);
620     else
621         fprintf(fid, [cell2mat(resultPyLabel(k)) '\n']);
622     end
623 end
624 fclose(fid);
625 !copy Pylabel.txt+Py_reduced.txt result_Py_reduced.txt;
626 delete Py_reduced.txt Pylabel.txt;
627
628 dlmwrite('Tc.txt', resultTc);
629 fid=fopen('Tclabel.txt', 'w');
630 for k=1:length(resultTcLabel),
631     if k<length(resultTcLabel),
632         fprintf(fid, [cell2mat(resultTcLabel(k)) ',']);
633     else
634         fprintf(fid, [cell2mat(resultTcLabel(k)) '\n']);
635     end
636 end
637 fclose(fid);
638 !copy Tclabel.txt+Tc.txt result_Tc.txt;
639 delete Tc.txt Tclabel.txt;
640
641     saveas(gcf-4, 'Tpy.jpg');
642     saveas(gcf-3, 'Tc.jpg');
643     saveas(gcf-2, 'Molar flow rates.jpg');
644     saveas(gcf-1, 'Mass balances.jpg');
645     saveas(gcf, 'Mole fractions.jpg');
646 else
647     disp('OK');
648 end
649
650 disp('Done. ');
651 toc
652
653 disp('-----');

```


Appendix D

Raman Spectroscopy: Continuum Background Correction

As was described in Chapter 8 the Raman spectra recorded during the high-temperature in-situ experiments, e.g. methane CPO on a polycrystalline Pt foil, exhibit a strong background caused by thermal radiation. For quantitative analysis of the carbon bands overlapping with these background it was necessary to separate the background signal without affecting the Raman bands of interest. The following section elucidates the correction algorithm that is adapted from the work of Gornushkin et al. [201]. The transcript is self-explanatory to everyone familiar with basic knowledge of MATLAB. However important steps in the code are commented.

The background correction is done in two steps. In the first step, viz. script in Section D.1, the Raman raw data spectrum is analyzed and the background is fitted by a suited polynomial. To do so the script needs to separate Raman bands from the continuum background and find a suitable fit for the continuum background.

It needs to be kept in mind that the CCD camera used in this work has an array of 512×2048 light sensitive cells. The observed Raman shift corresponds to a given stack/bin of cells along the long CCD axis, with its absolute values depending on the position of the dispersing gratings.

The algorithm uses two convoluted loops. The outer loop divides the Raman spectrum in a certain amount of smaller sub-spectra, $2 \leq N \leq 64$, i.e. beginning with two sub-spectra of 1024 pixels length increasing the sub-spectra number until 64 sub-spectra of 32 pixels length are allocated. Raman bands are identified within the sub-spectra by selecting the $\frac{1}{16}$ of pixels with least intensity within each sub-spectrum. Fig. D.1 illustrated an example, where $N = 5$. The lower x-axis gives the 2048 bins, the upper x-axis gives the corresponding Raman shift. By dotted lines the limits of the seven sub-spectra are labeled. The grey trace is the Raman raw data spectrum and the hollow black circles mark the 128 minima in the seven groups. As can be seen in Fig. D.1 only data point are selected, which do not belong to real Raman bands.

The inner loop now fits polynomials of 1st to 10th order (P) to these minima resulting in fits of different quality to the overall continuum background. In Fig. D.1 the polynomial is of 5th order (red trace). The quality of each fit is determined by selecting a new set of minima that includes the firstly selected minima and all data points of the original raw data that lay in the triple standard deviation of the firstly selected minima. The deviation of the new minima set from the fit polynomial is the quality criterion stored in a matrix and allows identification of the best N and P parameter set to describe the continuum background properly. Fig. D.2 depicts the result of screening for best fitting parameters exemplarily. To assure the parameter set selection is correct it is recommended to fit a Raman spectrum recorded without laser excitation of the investigated sample. Since no Raman peaks are present in such a blank, the "real" background shape can be determined for a given temperature window and the operator can select the N and P combination of choice.

In the second step, viz. script in Section D.2, the selected set of P and N is used to fit the background signal in the apparent Raman spectrum and subtract the background fraction. Fig. D.1 (blue trace) gives the corrected Raman spectrum for the intermediate example case. It has to mentioned that the script works best for rather sharp Raman peaks. In cases of very broad peaks, the background correction can lead to an overestimation of the background fraction. To avoid this effect it is possible to preselect a window around the broad peak of interest. The green area in Fig. D.1 is an example of such a preselection. The fit function used to eliminate the continuum background has no physical interpretation. Very good results have been obtained by this method.

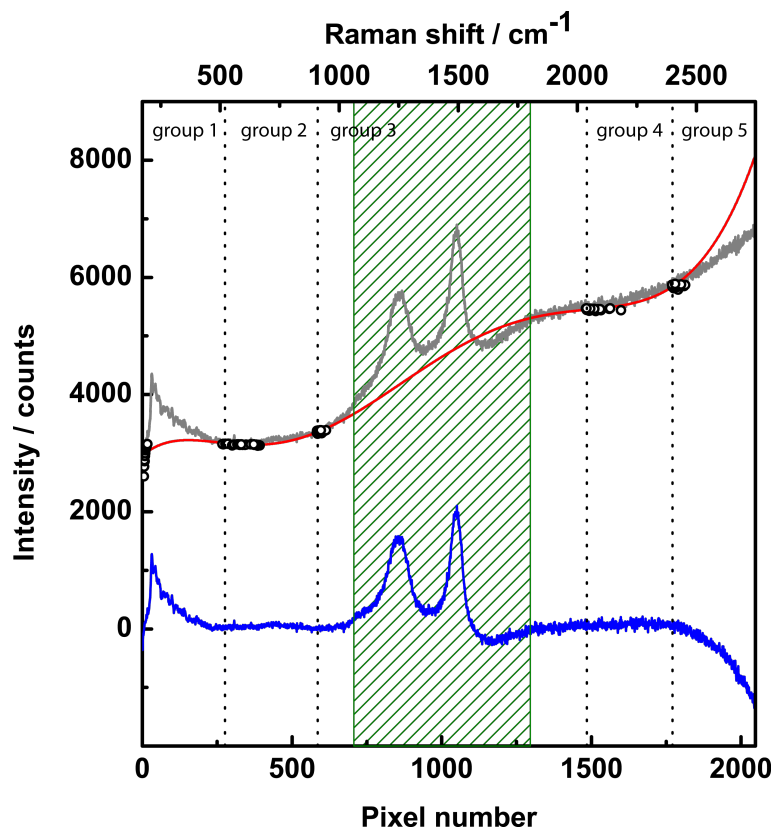


Figure D.1: Example of continuum background correction, intermediate solution with $N = 5$ and $P = 5$. All five sub-spectra/groups are of equal size. Note preselected green area, not considered for background estimation, divides Group 3. Grey trace: Raman raw data, Open black circles: Background data points selected for fitting procedure, Red trace: Estimated continuum background, Blue trace: Background corrected Raman spectrum.

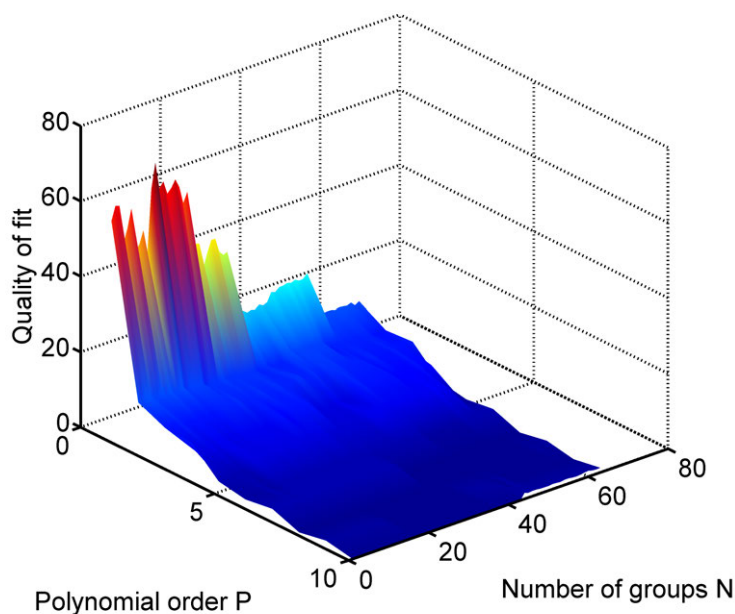


Figure D.2: Result of screening the parameter space of the background correction algorithm. Quality of fit from all background data points as function of P and N .

D.1 Screening for Best Parameter Set

```

1  %Program for removing the continuum background of Raman spectrum – Finding the suitable
   polynomial and grouping (scans the whole parameter space)
2  tic
3  clear
4  format long e
5  %Reading spectral data from ASCII file
6  rawdata=dlmread('reaction_a_pos36_cycle180.1.txt');
7  sigma_N=[]; %Return of this program
8  %Break spectrum in N groups, N_max=64
9  for N=2:1:64, %Number of groups !!! This loop runs to vary group number 2<=N<=64
10     %Selecting the spectral data and storing it in variables
11     xdata=[];
12     ydata=[];
13     xdata(:,1)=rawdata(:, 1);
14     ydata(:,1)=rawdata(:, 3);
15     h=mod(size(xdata, 1), N); %Find remainder
16     if h~=0,
17         xdata(end-h+1:end)=[]; %Delete spare elements x
18         ydata(end-h+1:end)=[]; %Delete spare elements y
19     end
20     x=reshape(xdata, [], N); %Grouping x
21     y=reshape(ydata, [], N); %Grouping y
22     %Find background points (major minima)
23     h=size(y,1); %Find out length of each column in matrix
24     k=floor(h*1/16); %Find integer number of points to select as minimum in each column
25     majormin_x=[];
26     majormin_y=[];
27     for i=1:1:k,
28         [minimum,index]=min(y); %Minimum in matrix y
29         majormin_y=[majormin_y; minimum]; %Store minima in majormin_y
30         tempvector=[];
31         for j=1:1:N, %Store corresponding x values to majormin_x
32             tempvector(:, j)=x(index(:, j), j);
33         end
34         majormin_x=[majormin_x; tempvector];
35         tempmatrix=[];
36         for j=1:1:N, %Delete stored major minima from x and store in temporary matrix
37             tempvector=x(:, j);
38             tempvector(index(j))=[];
39             tempmatrix=[tempmatrix, tempvector];
40         end
41         x=tempmatrix;
42         tempmatrix=[];
43         for j=1:1:N, %Delete stored major minima from y and store in temporary matrix
44             tempvector=y(:, j);
45             tempvector(index(j))=[];
46             tempmatrix=[tempmatrix, tempvector];
47         end
48         y=tempmatrix;
49     end
50     %Restore original groups including major minima
51     x=[x; majormin_x];
52     y=[y; majormin_y];
53     %Draw polynomial of selected power (1–10) through major minima
54     for P=1:1:10; %Power of polynomial !!! This loop runs to vary the power of the
   polynomial 1<=P<=10
55         fit=polyfit(majormin_x, majormin_y, P);
56         fity=polyval(fit, xdata);
57         fity_rest_in_dataset=polyval(fit, x);
58         plot(majormin_x, majormin_y, 'ko', xdata, fity, 'r-'); pause(0.125); %Plot
   background fit function with respect to raw data
59     %Find minor minima in each group which are within 3 std dev from major minima
60     sigma_majormin_y=std(majormin_y); %Standard deviation
61     threesigma_majormin_y=3.*sigma_majormin_y; %3xStandard deviation
62     h=size(y, 1); %Find out length of each column in matrix (remaining point from
   dataset)
63     allminormin_x=[];
64     allminormin_y=[];
65     for i=1:1:N,
66         for j=1:1:h,
67             if y(j, i)<=fity_rest_in_dataset(j, i) +threesigma_majormin_y & y(j,
   i)>=fity_rest_in_dataset(j, i) -threesigma_majormin_y,
68                 allminormin_y=[allminormin_y;y(j, i)];
69                 allminormin_x=[allminormin_x;x(j, i)];

```

```

70         end
71     end
72 end
73 % Calculate std dev of chosen polynomial with respect to minor minima sigma_N
74 h=size(allminormin_y, 1);
75 fity=polyval(fit,allminormin_x); %Calculate the fit value to each selected minor
    minimum
76 j=0;
77 for i=1:1:h,
78     j=j+(allminormin_y(i)-fity(i)).^2;
79 end
80 sigma_N=[sigma_N;sqrt(j/(h-1))];
81 end
82 end
83 sigma_N=reshape(sigma_N, [], 10);
84 %Plot quality of fit as function of number of groups
85 figure; surf(sigma_N); view(50, 30); shading interp;
86 toc

```

D.2 Removing Background Fraction from Raman Spectra with Parameter Set Selected with Respect to Section

```

1 %Program for removing the continuum background of Raman spectrum (Removes for the selected
    number of groups N and power of polynomial P the continuum background)
2 tic
3 clear
4 format long e
5 %Reading spectral data from ASCII file
6 rawdata=dlmread('reaction_b_pos1_cycle260_1.txt');
7 sigma_N=[]; %Return of this program
8 %Break spectrum in N groups, N_max=64
9 N=42; %Number of groups !!! 2<=N<=64 selection after screening
10 %Selecting the spectral data and storing it in variables
11 xdata=[];
12 ydata=[];
13 xdata(:, 1)=rawdata(:, 1);
14 ydata(:, 1)=rawdata(:, 3);
15
16 xdatabackup=[];
17 ydatabackup=[];
18 xdatabackup(:, 1)=rawdata(:, 1);
19 ydatabackup(:, 1)=rawdata(:, 3);
20
21 %Delete part of the spectra that shall be ignored in the fitting procedure
22
23 xdata(700:1200)=[];
24 ydata(700:1200)=[];
25
26 h=mod(size(xdata, 1), N); %Find remainder
27 if h~=0,
28     xdata(end-h+1:end)=[]; %Delete spare elements x
29     ydata(end-h+1:end)=[]; %Delete spare elements y
30 end
31 x=reshape(xdata, [], N); %Grouping x
32 y=reshape(ydata, [], N); %Grouping y
33 %Find background points (major minima)
34 h=size(y,1); %Find out length of each column in matrix
35 k=floor(h*1/16); %Find integer number of points to select as minimum in each column
36 majormin_x=[];
37 majormin_y=[];
38 for i=1:1:k,
39     [minimum,index]=min(y); %Minimum in matrix y
40     majormin_y=[majormin_y; minimum]; %Store minima in majormin_y
41     tempvector=[];
42     for j=1:1:N, %Store corresponding x values to majormin_x
43         tempvector(:, j)=x(index(:, j), j);
44     end
45     majormin_x=[majormin_x; tempvector];
46     tempmatrix=[];
47     for j=1:1:N, %Delete stored major minima from x and store in temporary matrix
48         tempvector=x(:, j);
49         tempvector(index(j))=[];
50         tempmatrix=[tempmatrix, tempvector];

```

```

51     end
52     x=tempmatrix;
53     tempmatrix=[];
54     for j=1:1:N, %Delete stored major minima from y and store in temporary matrix
55         tempvector=y(:, j);
56         tempvector(index(j))=[];
57         tempmatrix=[tempmatrix, tempvector];
58     end
59     y=tempmatrix;
60 end
61 %Restore original groups including major minima
62 x=[x; majormin_x];
63 y=[y; majormin_y];
64 %Draw polynomial of selected power (1-10) through major minima
65 P=9; %Power of polynomial !!! 1<=P<=10 selection after screening
66     fit=polyfit(majormin_x, majormin_y, P);
67     yfit=polyval(fit, xdatabackup)
68 ycorrdata=ydatabackup-yfit;
69 M=[xdatabackup, ydatabackup, yfit, ycorrdata];
70 dlmwrite('reaction_b_pos1_cycle260_1_corr.txt', M, '\t')
71 figure; plot(xdatabackup, ydatabackup, 'o', xdatabackup, yfit, '-', xdatabackup, ycorrdata,
72             '-');
73 toc

```


Appendix E

Reactor Profile Library

Table E.1: Summary of catalyst properties investigated in this thesis.

FHI ID	m [g]	m_{Pt} [wt%]	PD [ppi]	A_g [m ² m ⁻³]	A_{Kr-BET} [m ² g]	A_{Pt} [m ² g ⁻¹]	D_{Pt}	Crystallite size LVol-IB^d [nm]
#10253 ^a	3.90	1.09 ^c , 1.1 ^d	80	4650 ^e	-	0.015 ^f	0.006	42(3)
#10254 ^a	3.85	1.18 ^c , 1.1 ^d	80	3410 ^e	-	0.041 ^f	0.014	50(3)
#10255 ^a	2.97	1.04 ^c , 1.1 ^d	45	2550 ^e	-	0.021 ^f	0.008	73(5)
#10256 ^a	3.20	1.11 ^c , 1.0 ^d	45	2780 ^e	-	0.012 ^f	0.004	61(4)
#10774 ^a	3.99	0.96 ^c , 0.9 ^d	80	-	-	0.034 ^f , 0.035 ^g	0.007	44(3)
#10775	1.64	0.95 ^c	80	-	-	-	-	-
#10776	2.01	0.98 ^c	80	-	-	-	-	-
#12036	3.33	100	-	909	-	-	-	-
#12037 ^b	3.28	100	-	909	-	-	-	-
#12357 ^a	3.51	1.05 ^c , 1.0 ^d	80	-	0.159	0.062 ^f , 0.070 ^g	0.024	60(4)
#12358 ^a	3.99	1.17 ^c , 1.1 ^d	80	-	-	-	-	46(10)
#12359 ^a	3.52	1.12 ^c , 1.1 ^d	80	-	-	-	-	30(2)
#12360 ^a	2.87	1.05 ^c , 1.1 ^d	45	-	0.097	0.011 ^f	0.004	49(3)
#12979 ^a	3.00	0	80	-	0.160	-	-	-
#12980 ^a	3.00	0	45	-	0.094	-	-	-

^aFoam is now crushed and/or powdered for characterization.

^bTube is cut in two halves.

^cDetermined by gravimetric method (as prepared).

^dDetermined by XRD (after reaction tests).

^eDetermined by x-ray μ -CT.

^fDetermined by hydrogen chemisorption.

^gDetermined by carbon monoxide chemisorption in microcalorimetric experiment.

Table E.2: Gas feeds for catalytic testing at a given total flow rate.

\dot{V}_{total} [mln min ⁻¹]	C/O	\dot{V}_{CH_4} [mln min ⁻¹]	\dot{V}_{O_2} [mln min ⁻¹]	\dot{V}_{inert}^c [mln min ⁻¹]
500 ^a	2.0	229	57	214
	1.8	216	60	224
	1.6	201	63	236
	1.4	185	66	249
	1.2	168	70	262
	1.0	148	74	278
	0.8	126	79	295
1000 ^a	2.0	457	114	429
	1.8	431	120	449
	1.6	402	126	472
	1.4	370	132	498
	1.2	335	140	525
	1.0	296	148	556
	0.8	252	157	591
2000 ^b	2.0	913	228	859
	1.8	861	239	900
	1.6	803	251	946
	1.4	740	264	996
	1.2	670	279	1051
	1.0	592	296	1112
	0.8	502	314	1184
4000 ^b	0.6	402	335	1261
	2.0	1826	457	1717
	1.8	1722	478	1800
	1.6	1606	502	1892
	1.4	1480	528	1992
	1.2	1340	558	2102
	1.0	1184	592	2224
0.8	1004	628	2368	
0.6	804	670	2522	

E.1 Reactor Profiles Through Catalyst Foam #10253

Table E.3: List of profiles of foam monolith #10253

C/O	p	$\dot{V}_{\text{total}} = 2000$ mln min ⁻¹	$\dot{V}_{\text{total}} = 4000$ mln min ⁻¹
2.0	1 atm	Fig. E.4 bottom	Fig. E.8 bottom
1.8	1 atm	Fig. E.4 top	Fig. E.8 top
1.6	1 atm	Fig. E.3 bottom	Fig. E.7 bottom
1.4	1 atm	Fig. E.3 top	Fig. E.7 top
1.2	1 atm	Fig. E.2 bottom	Fig. E.6 bottom
1.0	1 atm	Fig. E.2 top	Fig. E.6 top
0.8	1 atm	Fig. E.1 bottom	Fig. E.5 bottom
0.6	1 atm	Fig. E.1 top	Fig. E.5 top

^aGas feeds used in catalytic testing of Pt tube, i.e. catalytic wall reactors.^bGas feeds used in catalytic testing of foam monoliths.^cThe inert component of the gas feed was either pure Ar or a mixture of 8 vol% He in Ar.

E.1.1 $\dot{V}_{\text{total}} = 2000 \text{ mln min}^{-1}$ - C/O Variation at Ambient Pressure

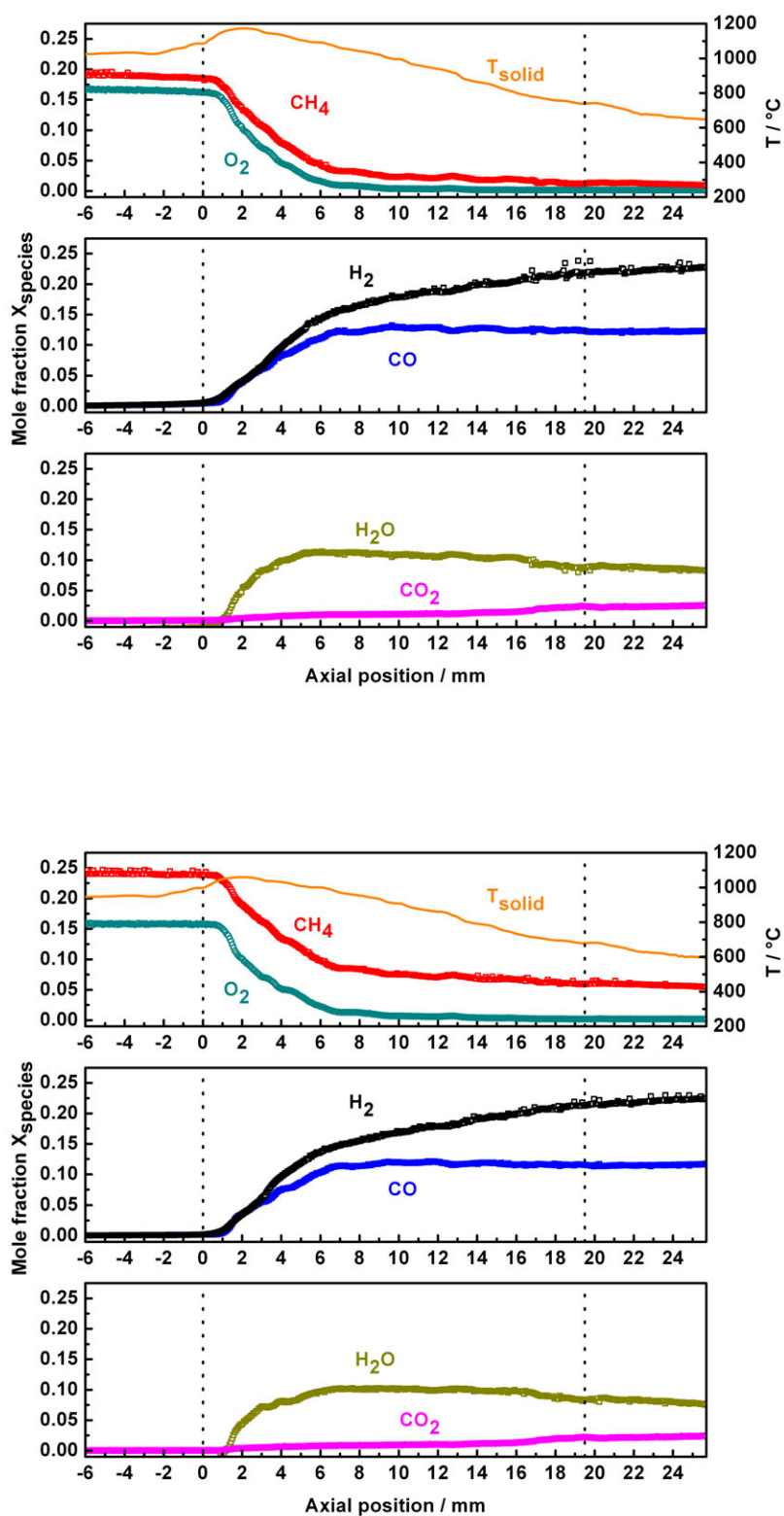


Figure E.1: Spatial reactor profile of surface temperature and species evolution. In between the dotted lines: catalyst foam monolith, left and right from the dotted lines: front and back heat shield respectively. Total gas feed of $2000 \text{ mln min}^{-1}$ @ C/O = 0.6 (top) and 0.8 (bottom) (both in auto thermal operation). For detailed information about the catalyst and reaction conditions see Tables E.1 and E.2.

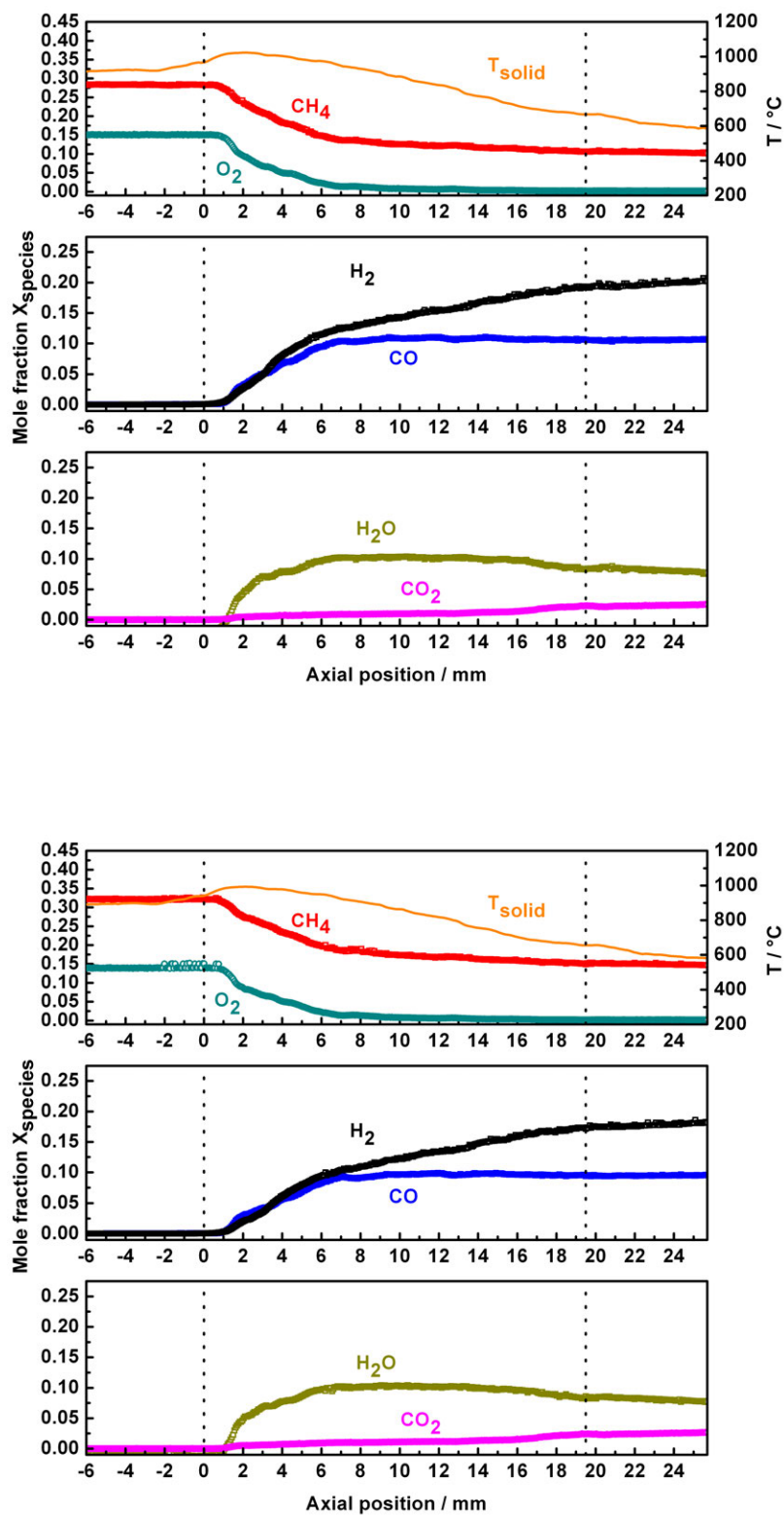


Figure E.2: Spatial reactor profile of surface temperature and species evolution. In between the dotted lines: catalyst foam monolith, left and right from the dotted lines: front and back heat shield respectively. Total gas feed of $2000 \text{ mln min}^{-1}$ @ $C/O = 1.0$ (top) and 1.2 (bottom) (both in auto thermal operation). For detailed information about the catalyst and reaction conditions see Tables E.1 and E.2.

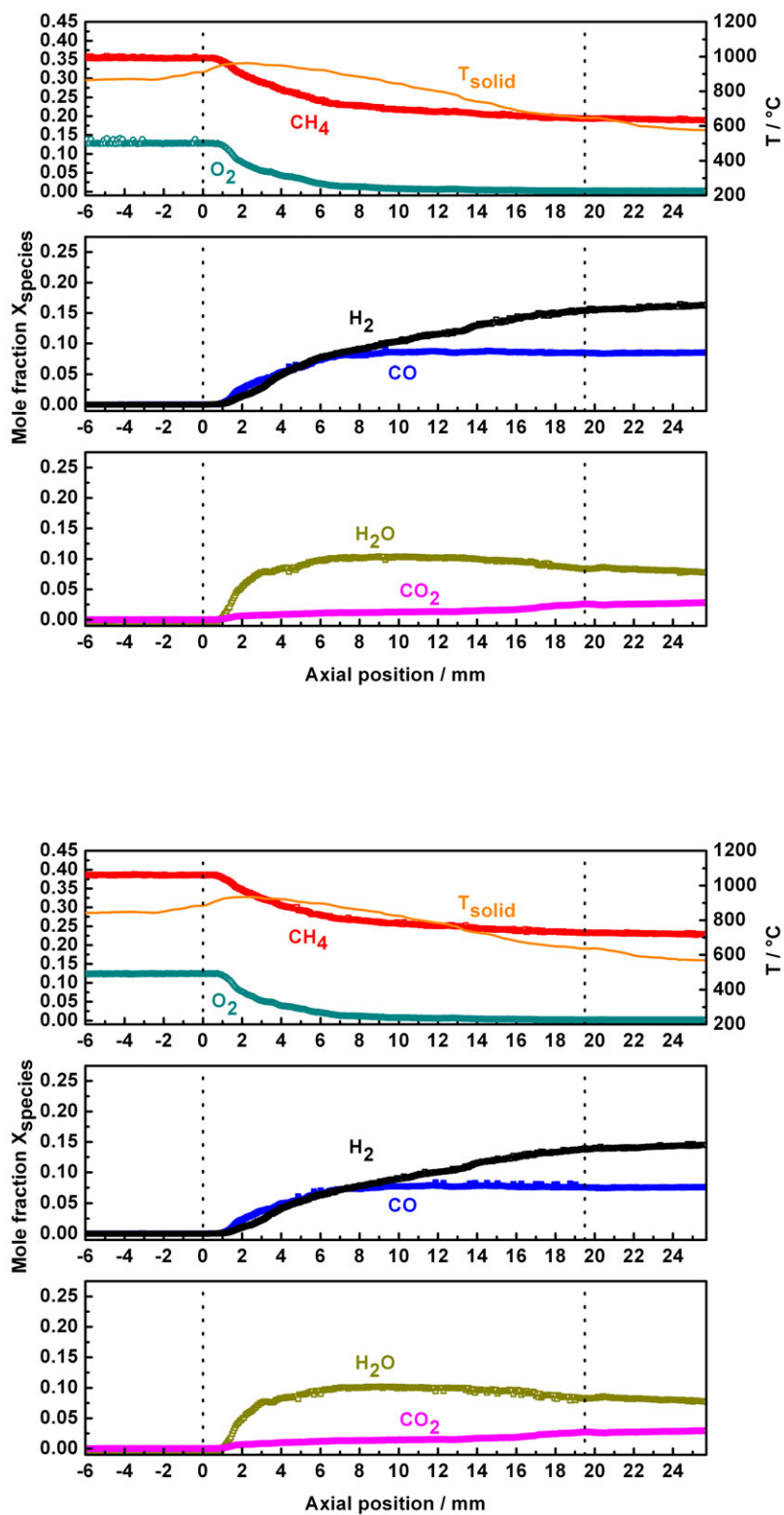


Figure E.3: Spatial reactor profile of surface temperature and species evolution. In between the dotted lines: catalyst foam monolith, left and right from the dotted lines: front and back heat shield respectively. Total gas feed of $2000 \text{ mln min}^{-1}$ @ $C/O = 1.4$ (top) and 1.6 (bottom) (both in auto thermal operation). For detailed information about the catalyst and reaction conditions see Tables E.1 and E.2.

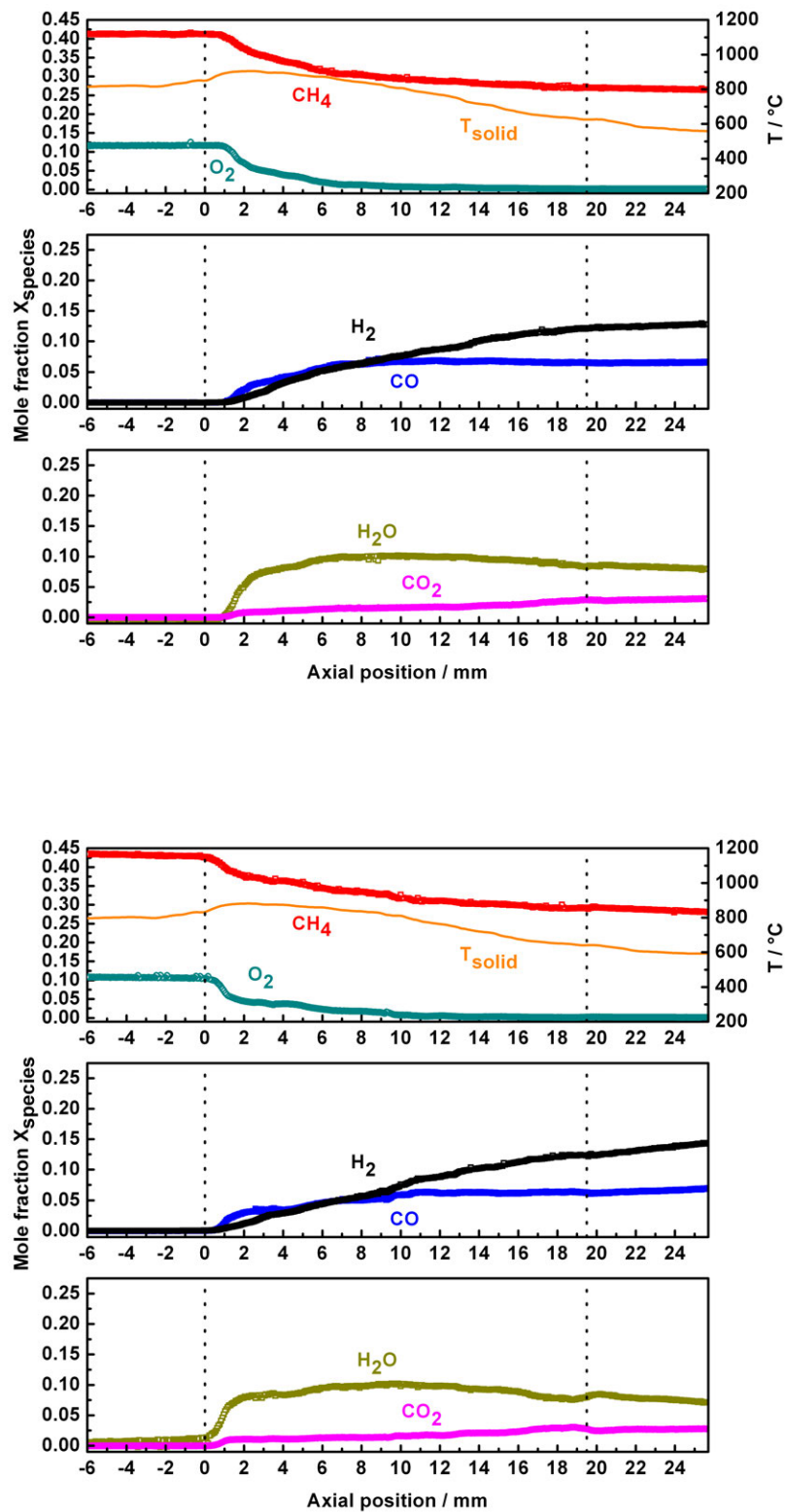


Figure E.4: Spatial reactor profile of surface temperature and species evolution. In between the dotted lines: catalyst foam monolith, left and right from the dotted lines: front and back heat shield respectively. Total gas feed of $2000 \text{ mln min}^{-1}$ @ $C/O = 1.8$ (top) and 2.0 (bottom) (both in auto thermal operation). For detailed information about the catalyst and reaction conditions see Tables E.1 and E.2.

E.1.2 $\dot{V}_{\text{total}} = 4000 \text{ mln min}^{-1}$ - C/O Variation at Ambient Pressure

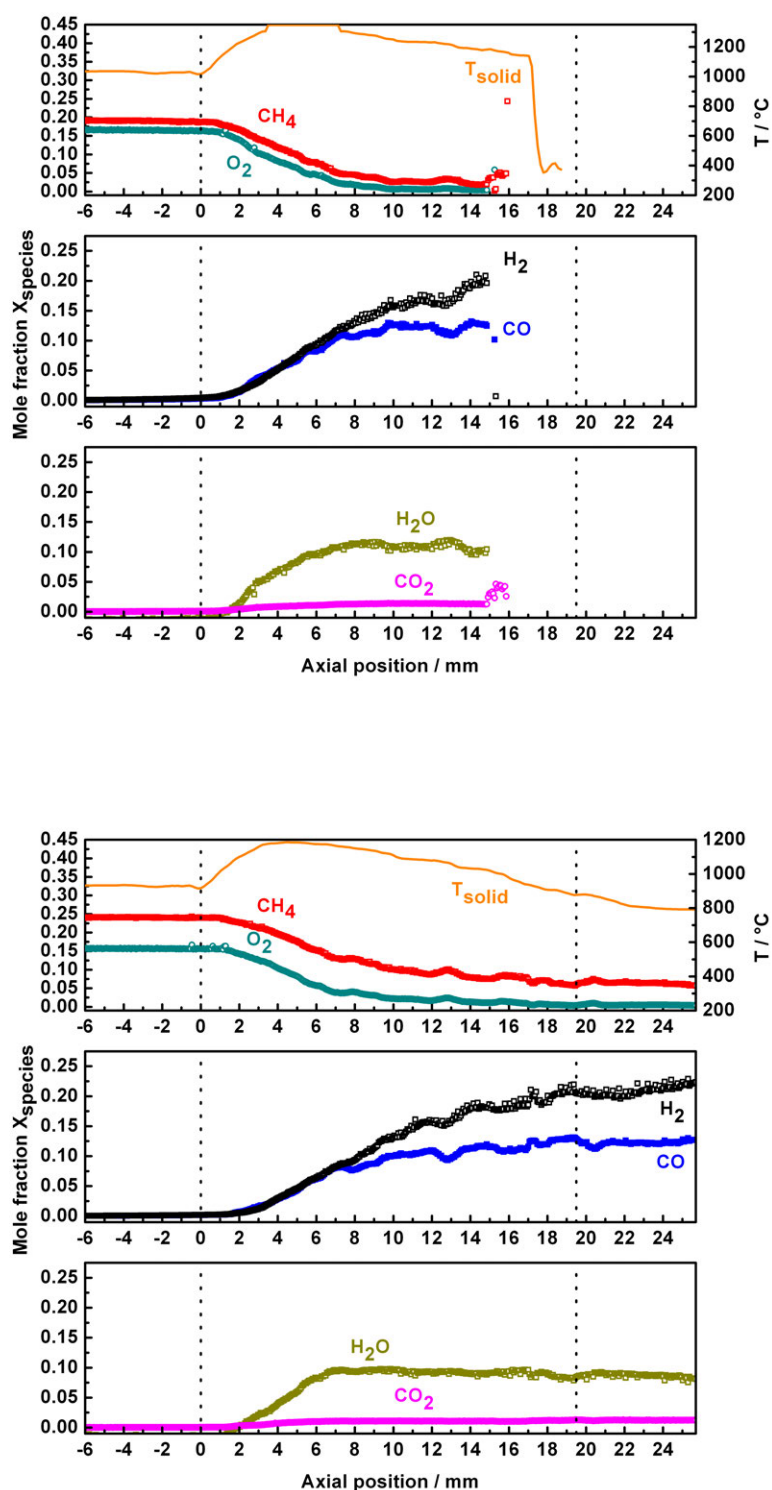


Figure E.5: Spatial reactor profile of surface temperature and species evolution. In between the dotted lines: catalyst foam monolith, left and right from the dotted lines: front and back heat shield respectively. Total gas feed of $4000 \text{ mln min}^{-1}$ @ C/O = 0.6 (top) and 0.8 (bottom) (both in auto thermal operation). For detailed information about the catalyst and reaction conditions see Tables E.1 and E.2. The profile at a C/O of 0.6 is interrupted at about 15 mm because the sampling system was blocked by melt down of the quartz capillary/pyrometer fiber probe at the harsh reaction conditions, with catalyst temperatures exceeding $1300 \text{ }^\circ\text{C}$.

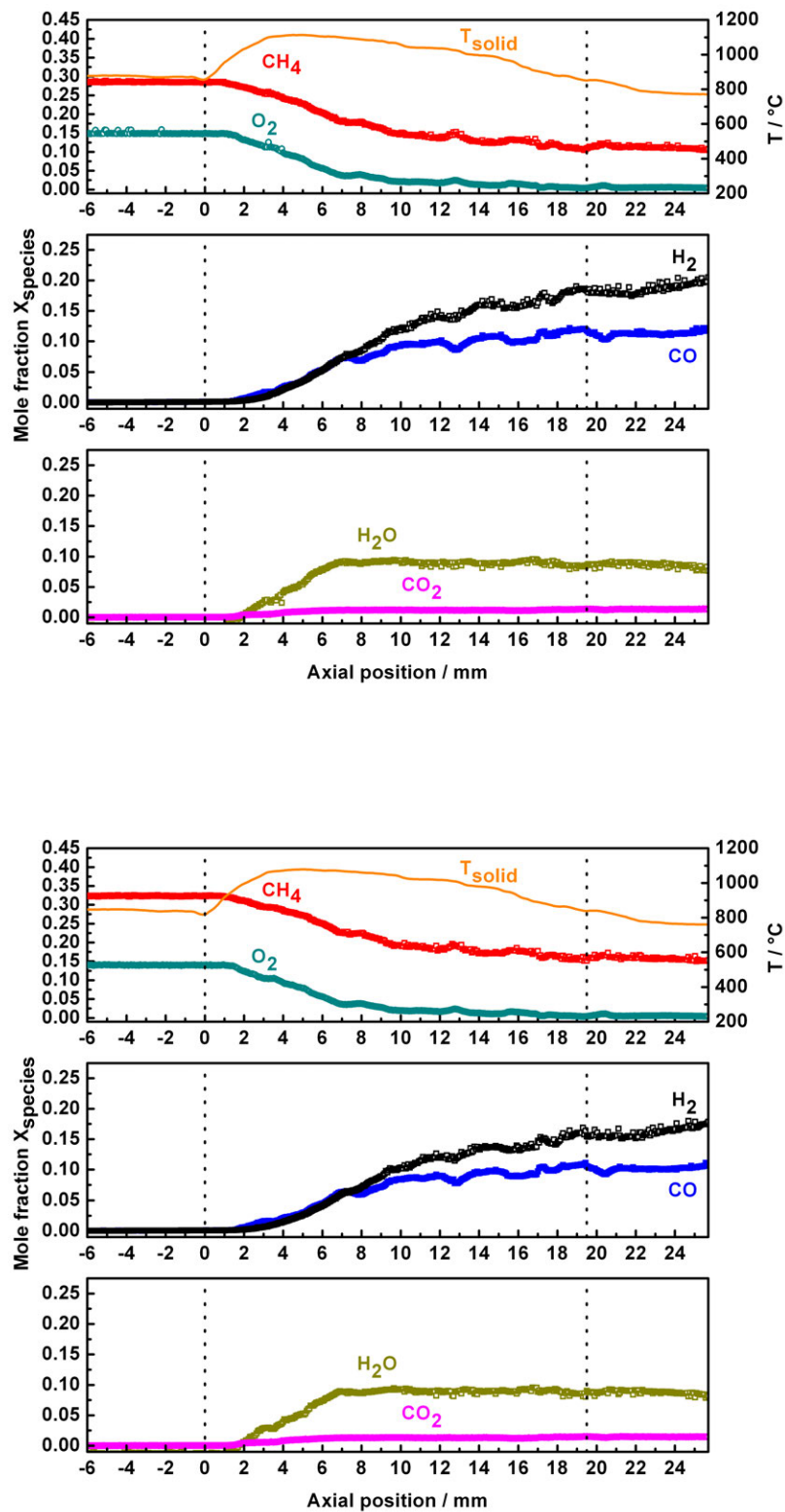


Figure E.6: Spatial reactor profile of surface temperature and species evolution. In between the dotted lines: catalyst foam monolith, left and right from the dotted lines: front and back heat shield respectively. Total gas feed of $4000 \text{ mln min}^{-1}$ @ $C/O = 1.0$ (top) and 1.2 (bottom) (both in auto thermal operation). For detailed information about the catalyst and reaction conditions see Tables E.1 and E.2.

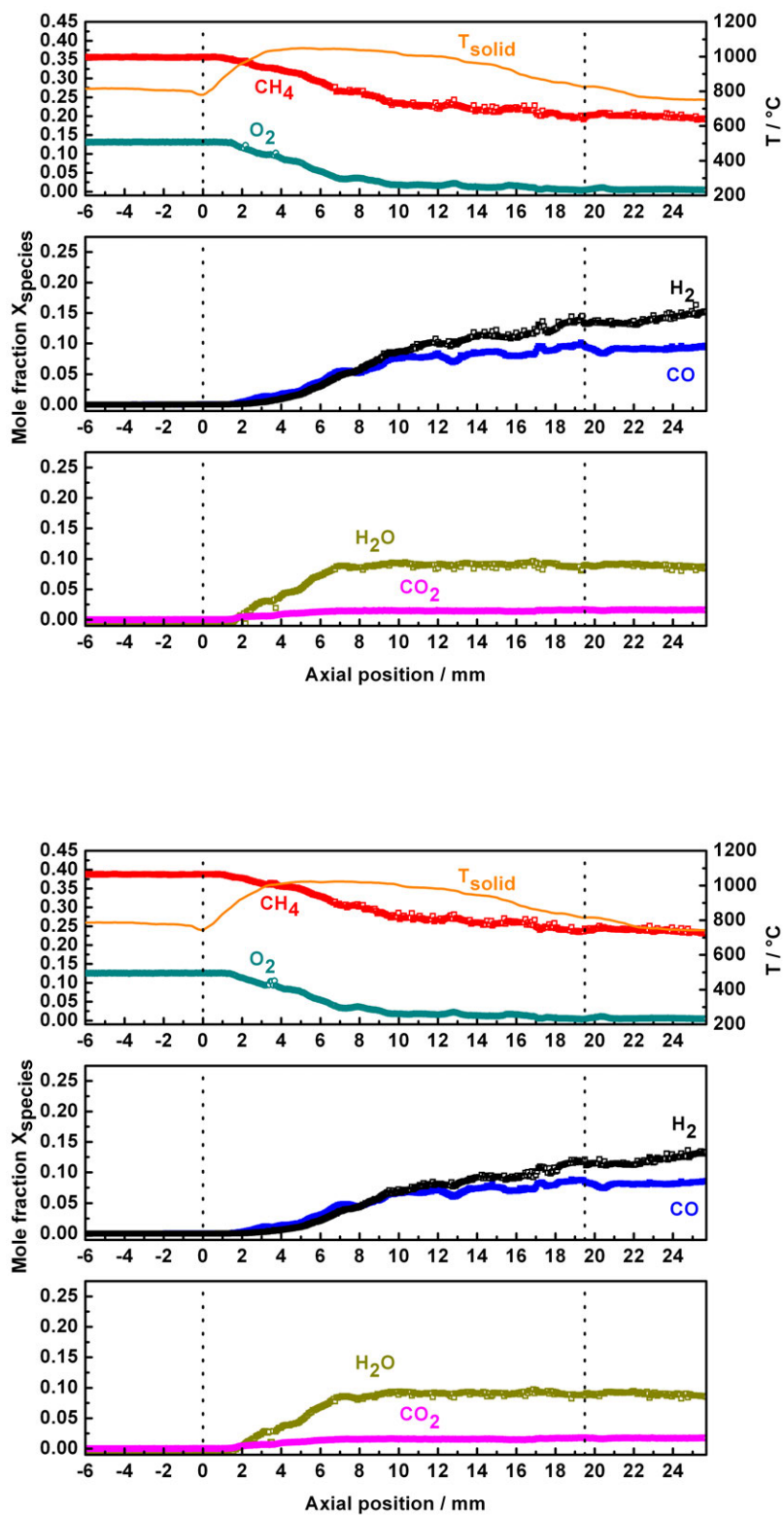


Figure E.7: Spatial reactor profile of surface temperature and species evolution. In between the dotted lines: catalyst foam monolith, left and right from the dotted lines: front and back heat shield respectively. Total gas feed of $4000 \text{ mln min}^{-1}$ @ $C/O = 1.4$ (top) and 1.6 (bottom) (both in auto thermal operation). For detailed information about the catalyst and reaction conditions see Tables E.1 and E.2.

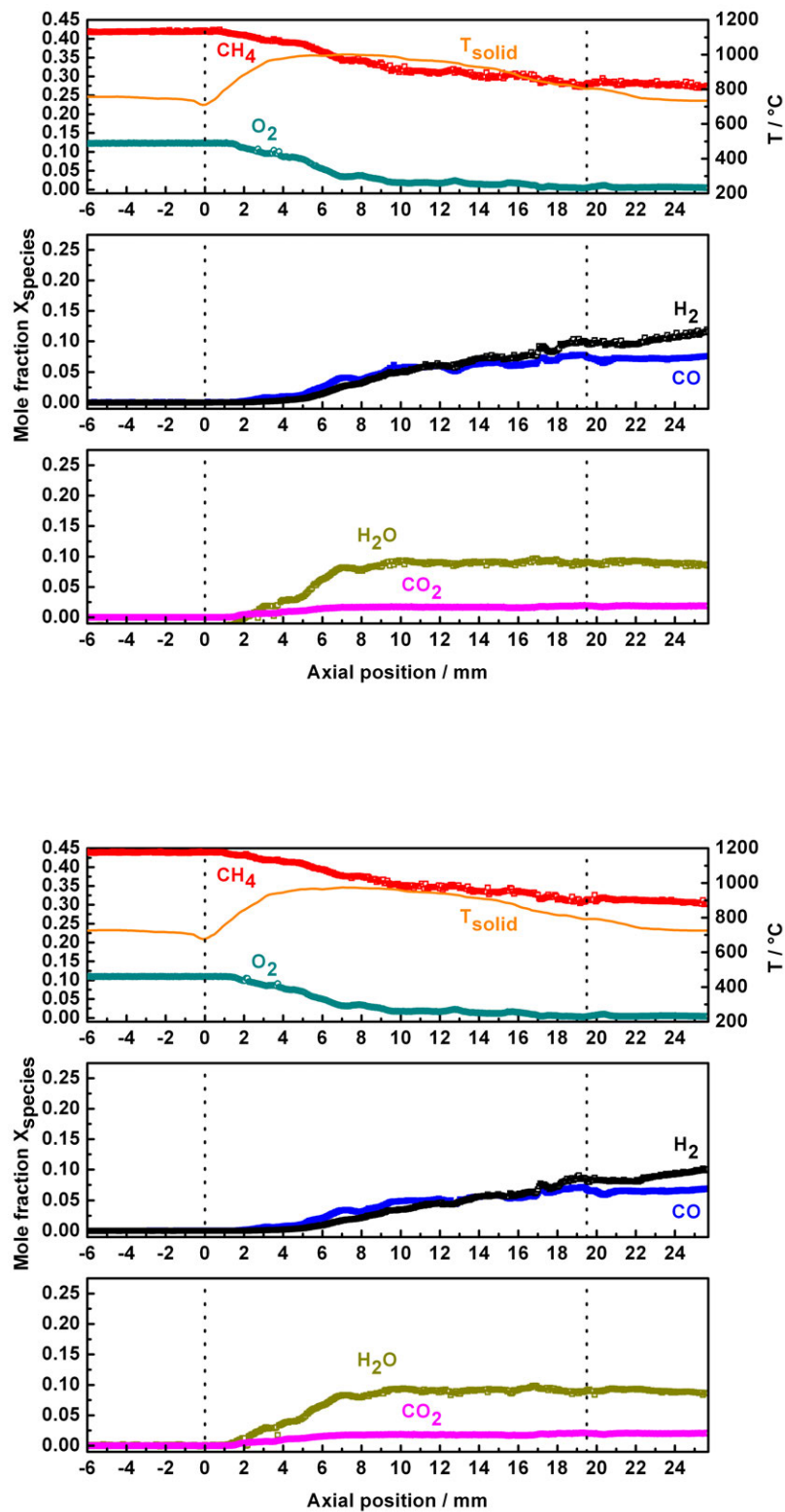


Figure E.8: Spatial reactor profile of surface temperature and species evolution. In between the dotted lines: catalyst foam monolith, left and right from the dotted lines: front and back heat shield respectively. Total gas feed of $4000 \text{ mln min}^{-1}$ @ $C/O = 1.8$ (top) and 2.0 (bottom) (both in auto thermal operation). For detailed information about the catalyst and reaction conditions see Tables E.1 and E.2.

E.2 Reactor Profiles Through Catalyst Foam #10255

Table E.4: List of profiles of foam monolith #10255.

C/O	p	$\dot{V}_{\text{total}} = 2000 \text{ mln min}^{-1}$	$\dot{V}_{\text{total}} = 4000 \text{ mln min}^{-1}$
2.0	1 atm	Fig. E.12 bottom	Fig. E.16 bottom
2.0	1 atm	Fig. E.17 top	-
2.0	5 bar	Fig. E.17 bottom	-
2.0	10 bar	Fig. E.18 top	-
2.0	15 bar	Fig. E.18 bottom	-
1.8	1 atm	Fig. E.12 top	Fig. E.16 top
1.6	1 atm	Fig. E.11 bottom	Fig. E.15 bottom
1.4	1 atm	Fig. E.11 top	Fig. E.15 top
1.2	1 atm	Fig. E.10 bottom	Fig. E.14 bottom
1.0	1 atm	Fig. E.10 top	Fig. E.14 top
0.8	1 atm	Fig. E.9	Fig. E.13

E.2.1 $\dot{V}_{\text{total}} = 2000 \text{ mln min}^{-1}$ - C/O Variation at Ambient Pressure

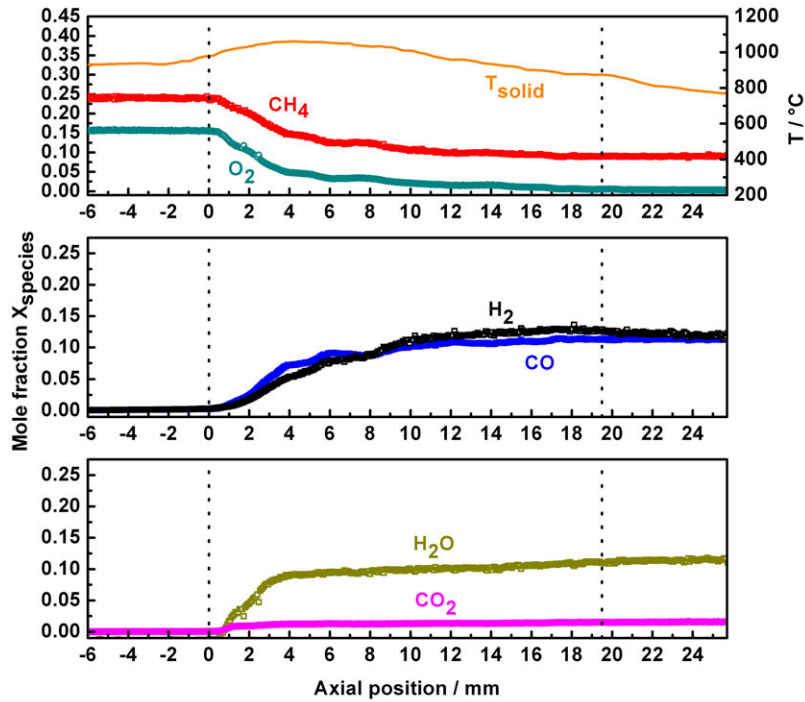


Figure E.9: Spatial reactor profile of surface temperature and species evolution. In between the dotted lines: catalyst foam monolith, left and right from the dotted lines: front and back heat shield respectively. Total gas feed of $2000 \text{ mln min}^{-1}$ @ C/O = 0.8 (top) (auto thermal operation). For detailed information about the catalyst and reaction conditions see Tables E.1 and E.2.

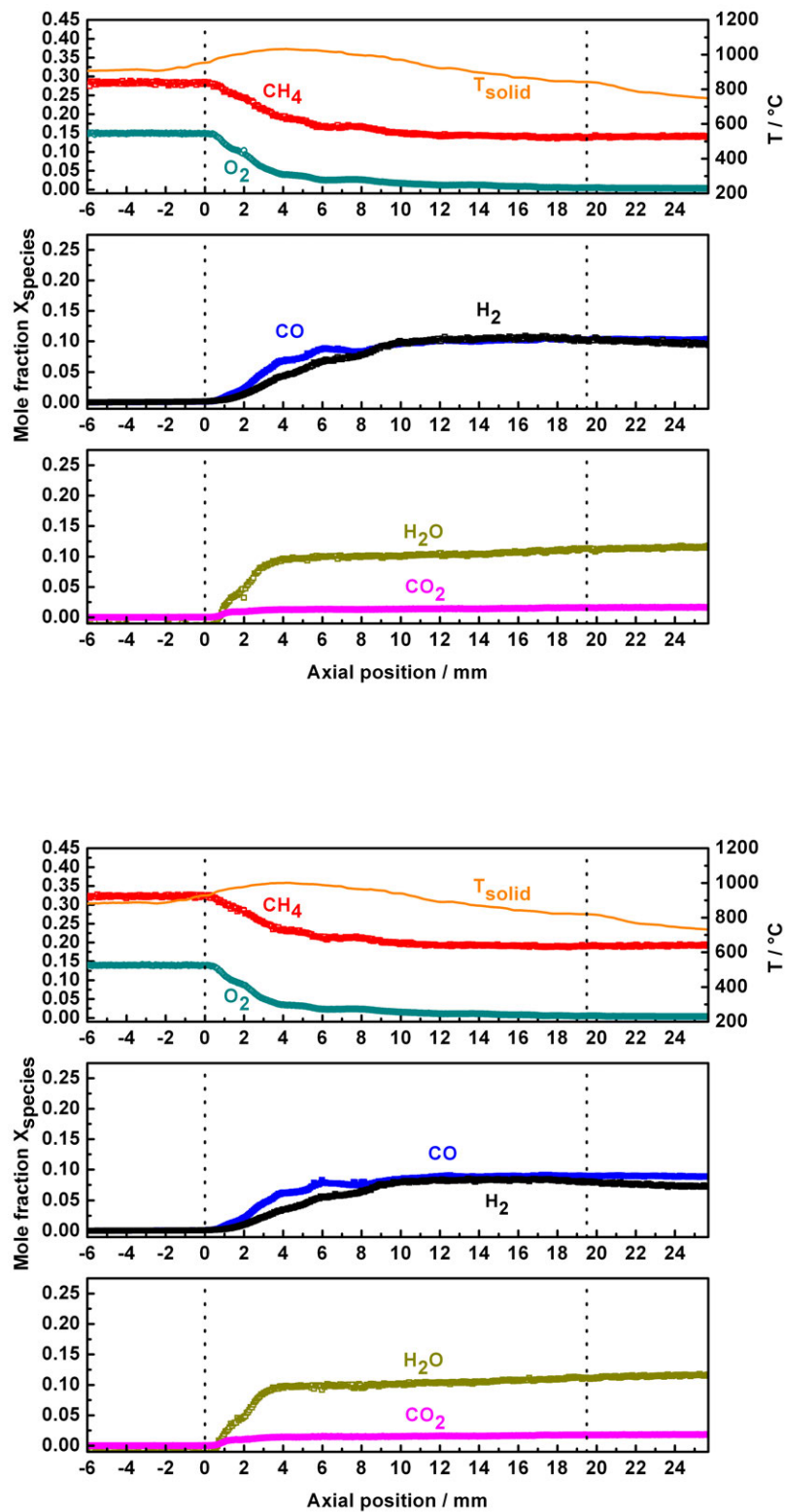


Figure E.10: Spatial reactor profile of surface temperature and species evolution. In between the dotted lines: catalyst foam monolith, left and right from the dotted lines: front and back heat shield respectively. Total gas feed of $2000 \text{ mln min}^{-1}$ @ $C/O = 1.0$ (top) and 1.2 (bottom) (both in auto thermal operation). For detailed information about the catalyst and reaction conditions see Tables E.1 and E.2.

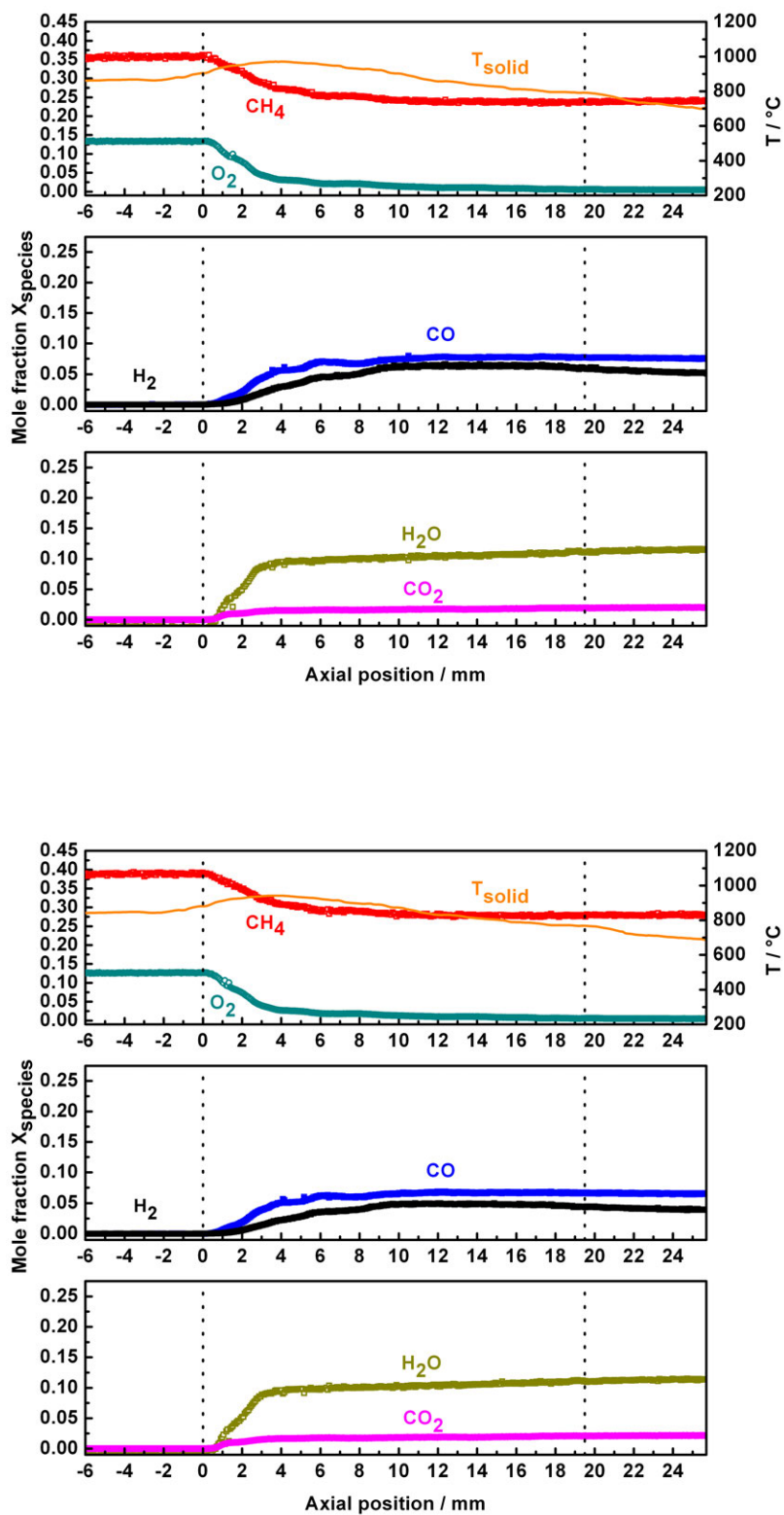


Figure E.11: Spatial reactor profile of surface temperature and species evolution. In between the dotted lines: catalyst foam monolith, left and right from the dotted lines: front and back heat shield respectively. Total gas feed of $2000 \text{ mln min}^{-1}$ @ $\text{C/O} = 1.4$ (top) and 1.6 (bottom) (both in auto thermal operation). For detailed information about the catalyst and reaction conditions see Tables E.1 and E.2.

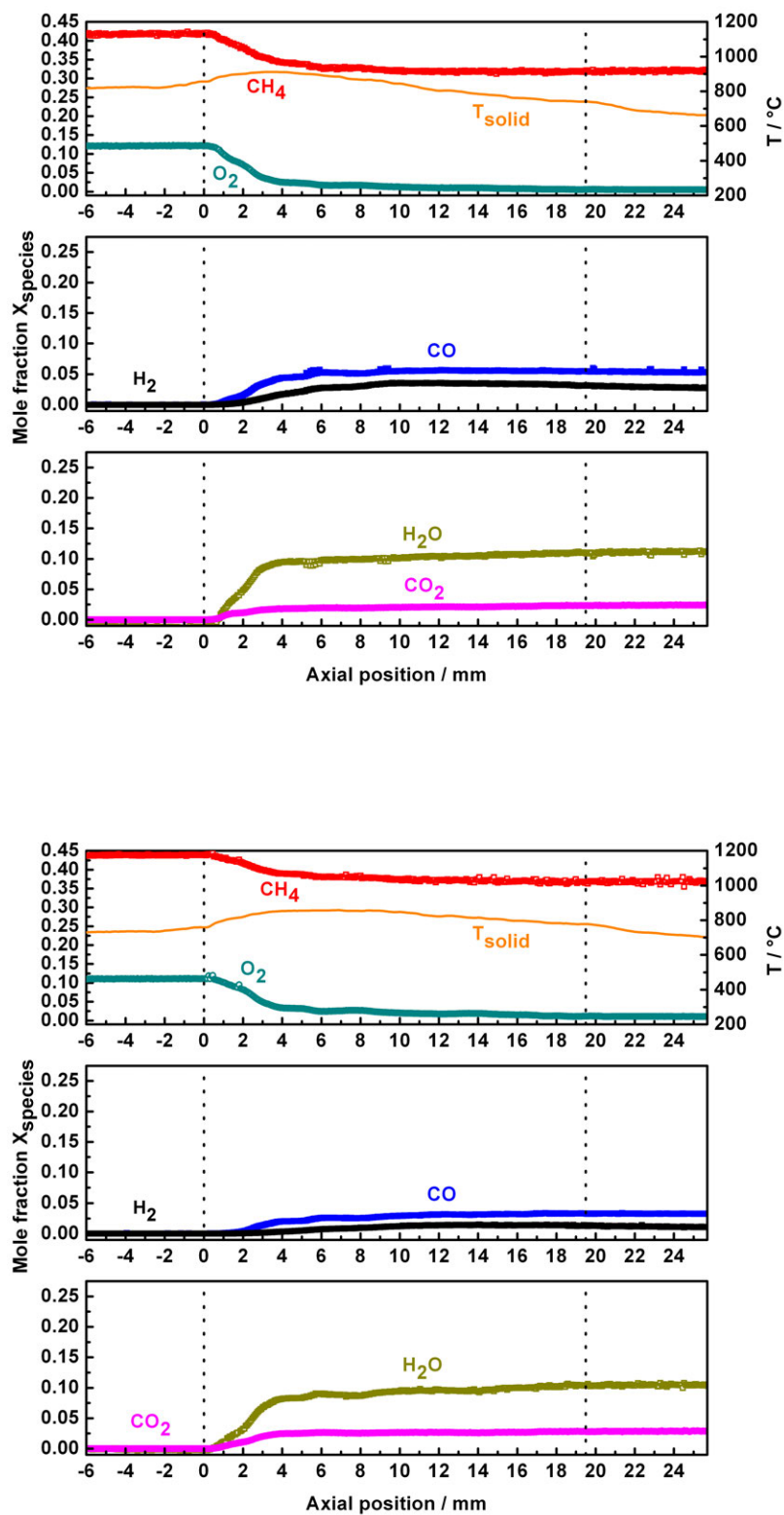


Figure E.12: Spatial reactor profile of surface temperature and species evolution. In between the dotted lines: catalyst foam monolith, left and right from the dotted lines: front and back heat shield respectively. Total gas feed of $2000 \text{ mln min}^{-1}$ @ $C/O = 1.8$ (top) and 2.0 (bottom) (both in auto thermal operation). For detailed information about the catalyst and reaction conditions see Tables E.1 and E.2.

E.2.2 $\dot{V}_{\text{total}} = 4000 \text{ mln min}^{-1}$ - C/O Variation at Ambient Pressure

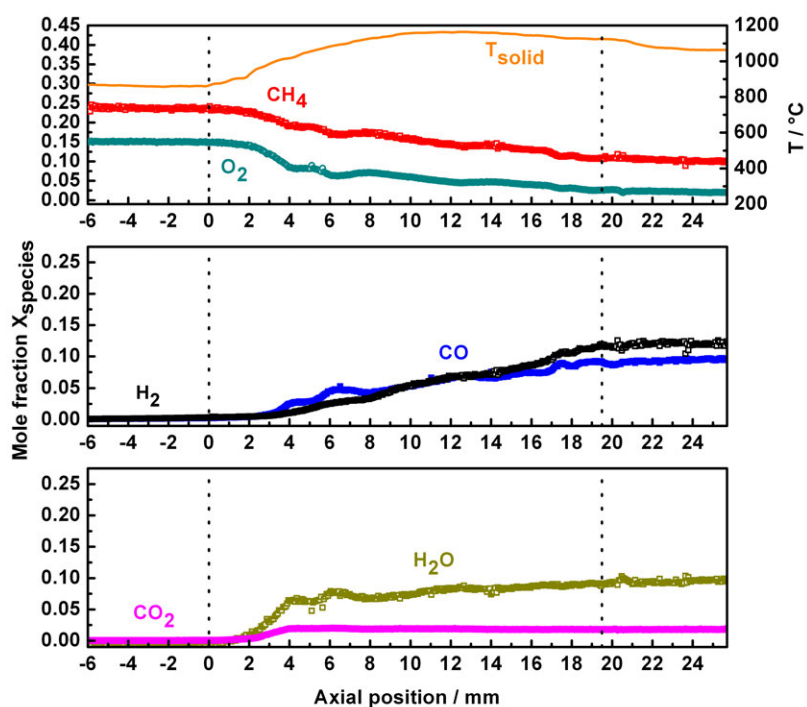


Figure E.13: Spatial reactor profile of surface temperature and species evolution. In between the dotted lines: catalyst foam monolith, left and right from the dotted lines: front and back heat shield respectively. Total gas feed of $4000 \text{ mln min}^{-1}$ @ $C/O = 0.8$ (top) (auto thermal operation). For detailed information about the catalyst and reaction conditions see Tables E.1 and E.2.

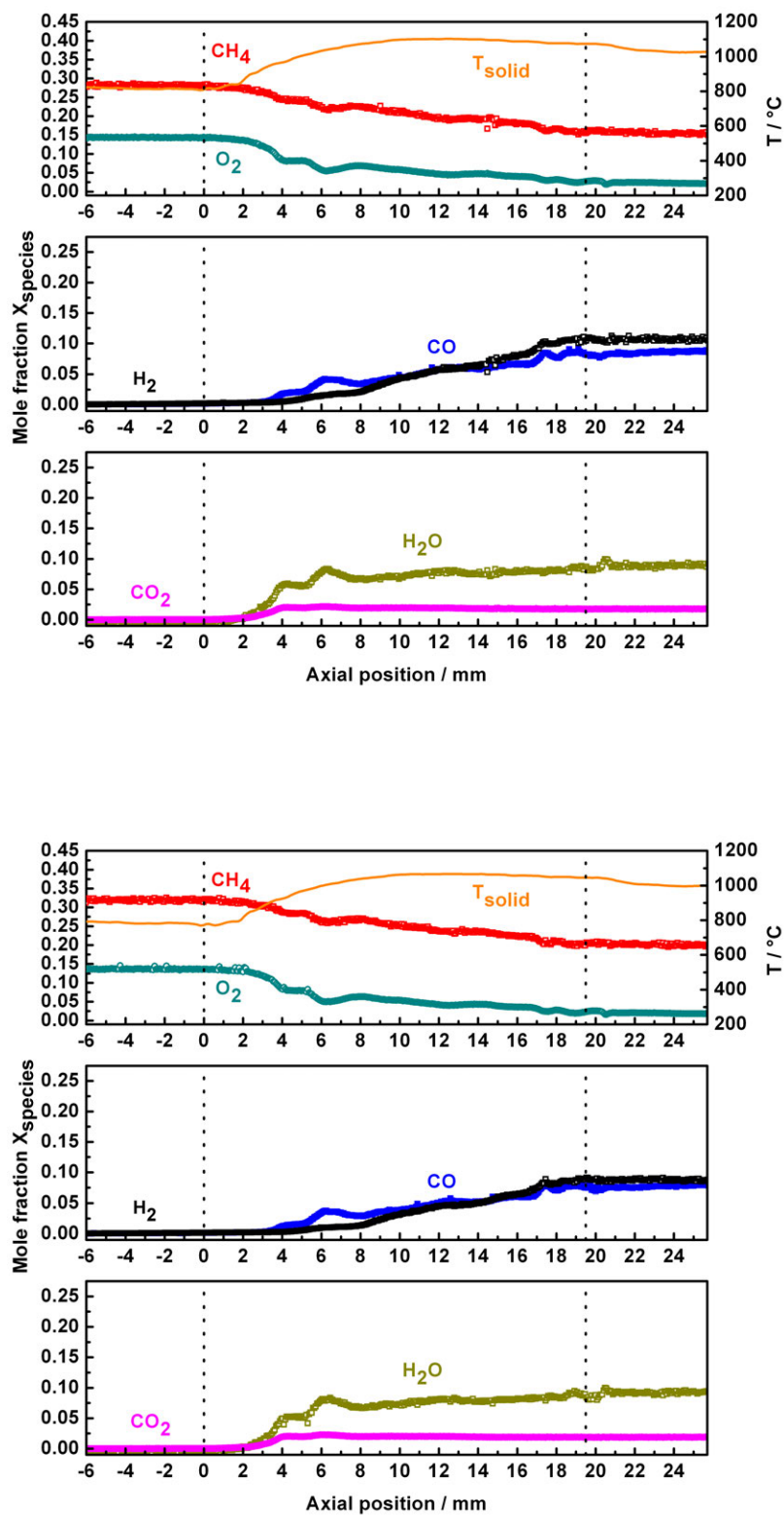


Figure E.14: Spatial reactor profile of surface temperature and species evolution. In between the dotted lines: catalyst foam monolith, left and right from the dotted lines: front and back heat shield respectively. Total gas feed of $4000 \text{ mln min}^{-1}$ @ $C/O = 1.0$ (top) and 1.2 (bottom) (both in auto thermal operation). For detailed information about the catalyst and reaction conditions see Tables E.1 and E.2.

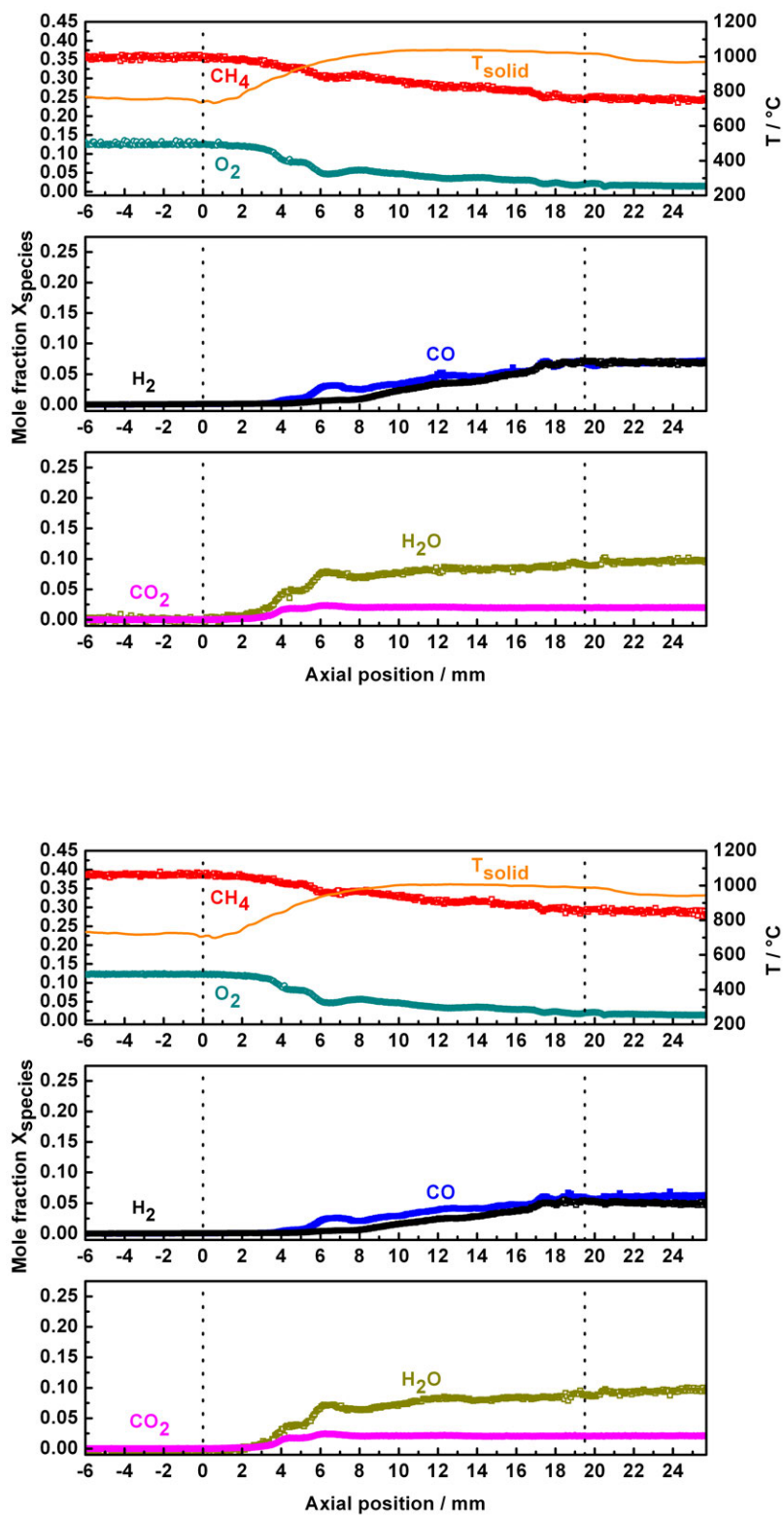


Figure E.15: Spatial reactor profile of surface temperature and species evolution. In between the dotted lines: catalyst foam monolith, left and right from the dotted lines: front and back heat shield respectively. Total gas feed of $4000 \text{ mln min}^{-1}$ @ $C/O = 1.4$ (top) and 1.6 (bottom) (both in auto thermal operation). For detailed information about the catalyst and reaction conditions see Tables E.1 and E.2.

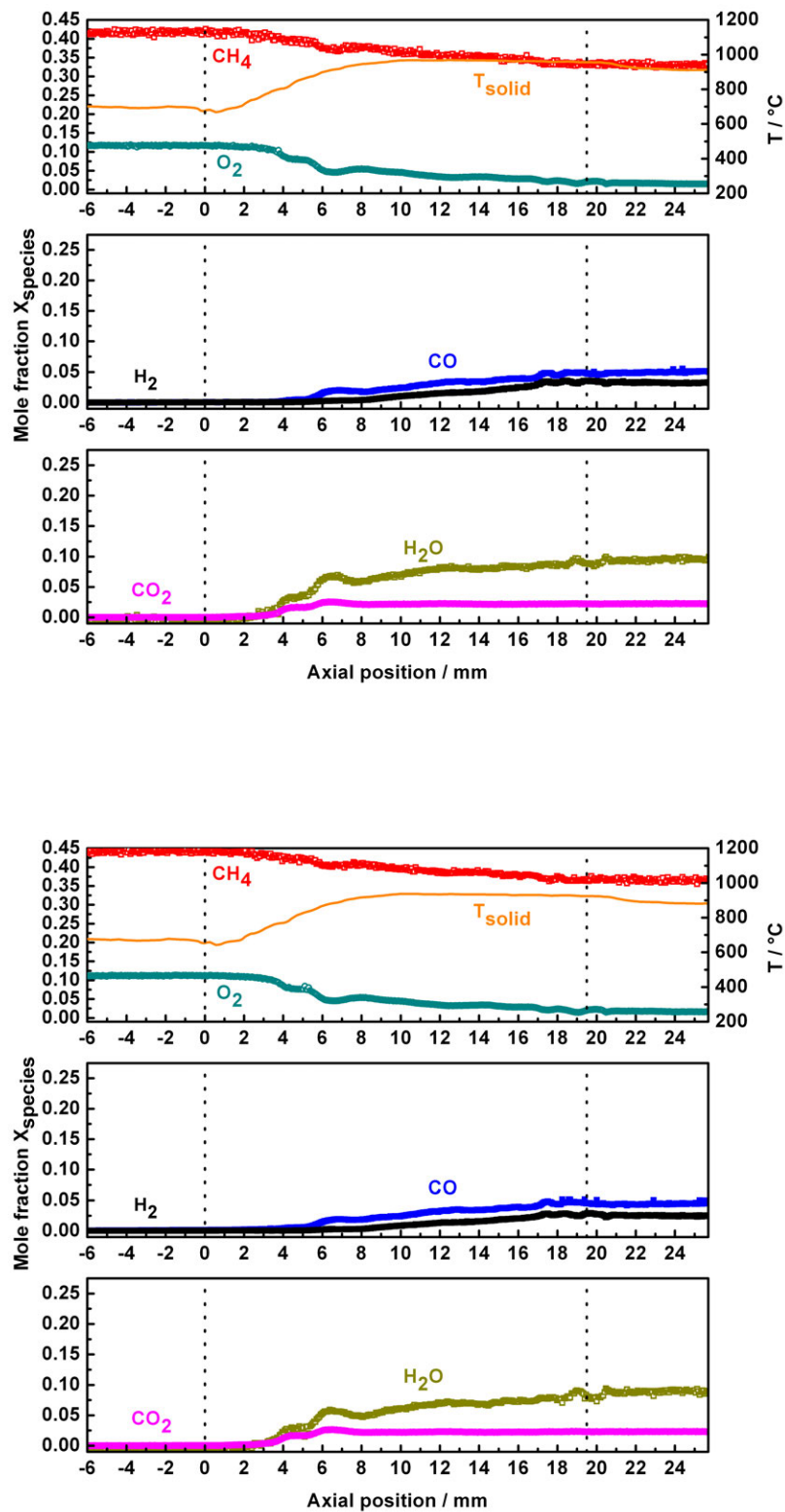


Figure E.16: Spatial reactor profile of surface temperature and species evolution. In between the dotted lines: catalyst foam monolith, left and right from the dotted lines: front and back heat shield respectively. Total gas feed of $4000 \text{ mln min}^{-1}$ @ $\text{C/O} = 1.8$ (top) and 2.0 (bottom) (both in auto thermal operation). For detailed information about the catalyst and reaction conditions see Tables E.1 and E.2.

E.2.3 $\dot{V}_{\text{total}} = 2000 \text{ mln min}^{-1}$ - Pressure Variation

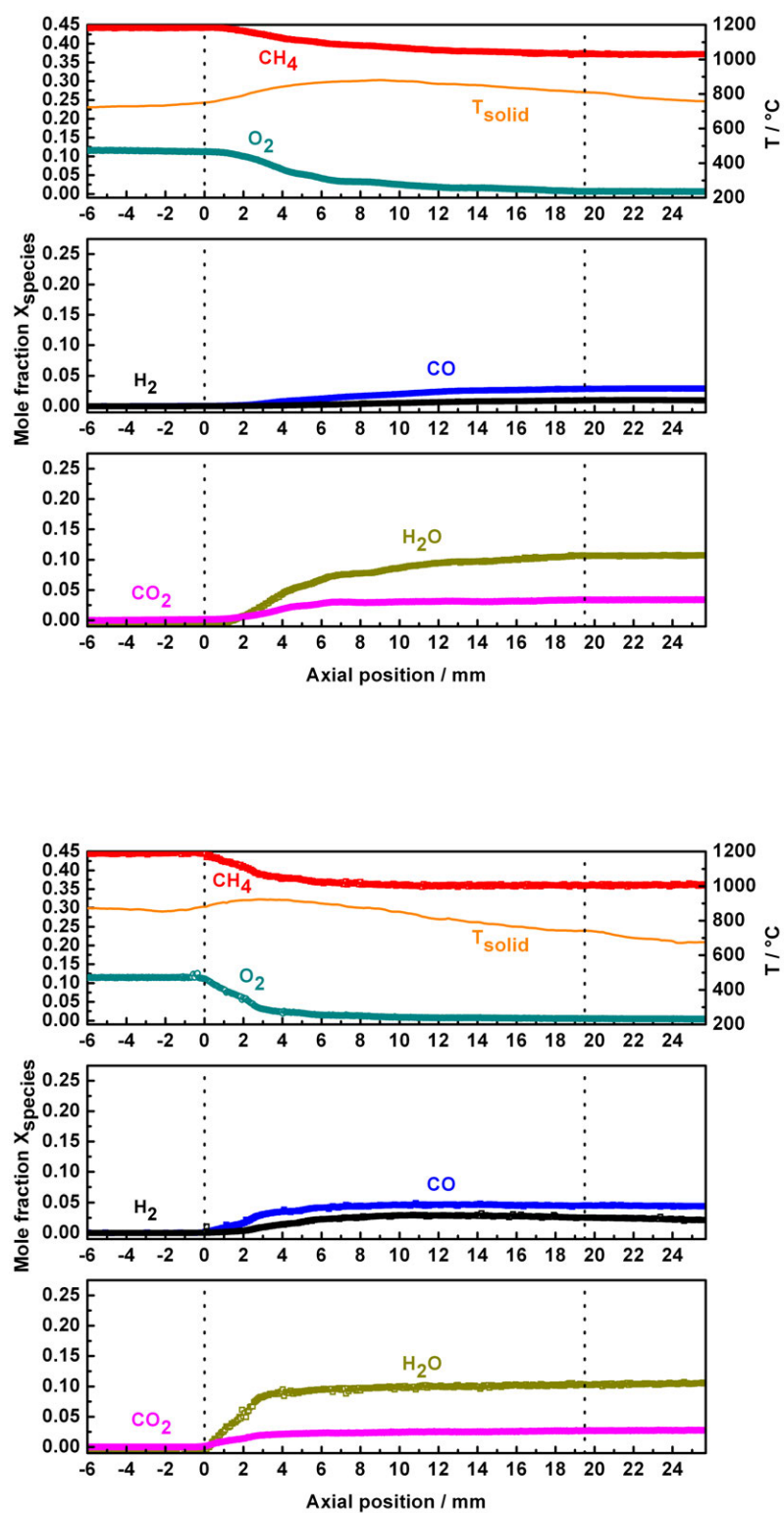


Figure E.17: Spatial reactor profile of surface temperature and species evolution. In between the dotted lines: catalyst foam monolith, left and right from the dotted lines: front and back heat shield respectively. Total gas feed of $2000 \text{ mln min}^{-1}$ @ $\text{C/O} = 2.0$ (both in auto thermal operation). Top: ambient pressure, Bottom: 5 bar reactor pressure. For detailed information about the catalyst and reaction conditions see Tables E.1 and E.2.

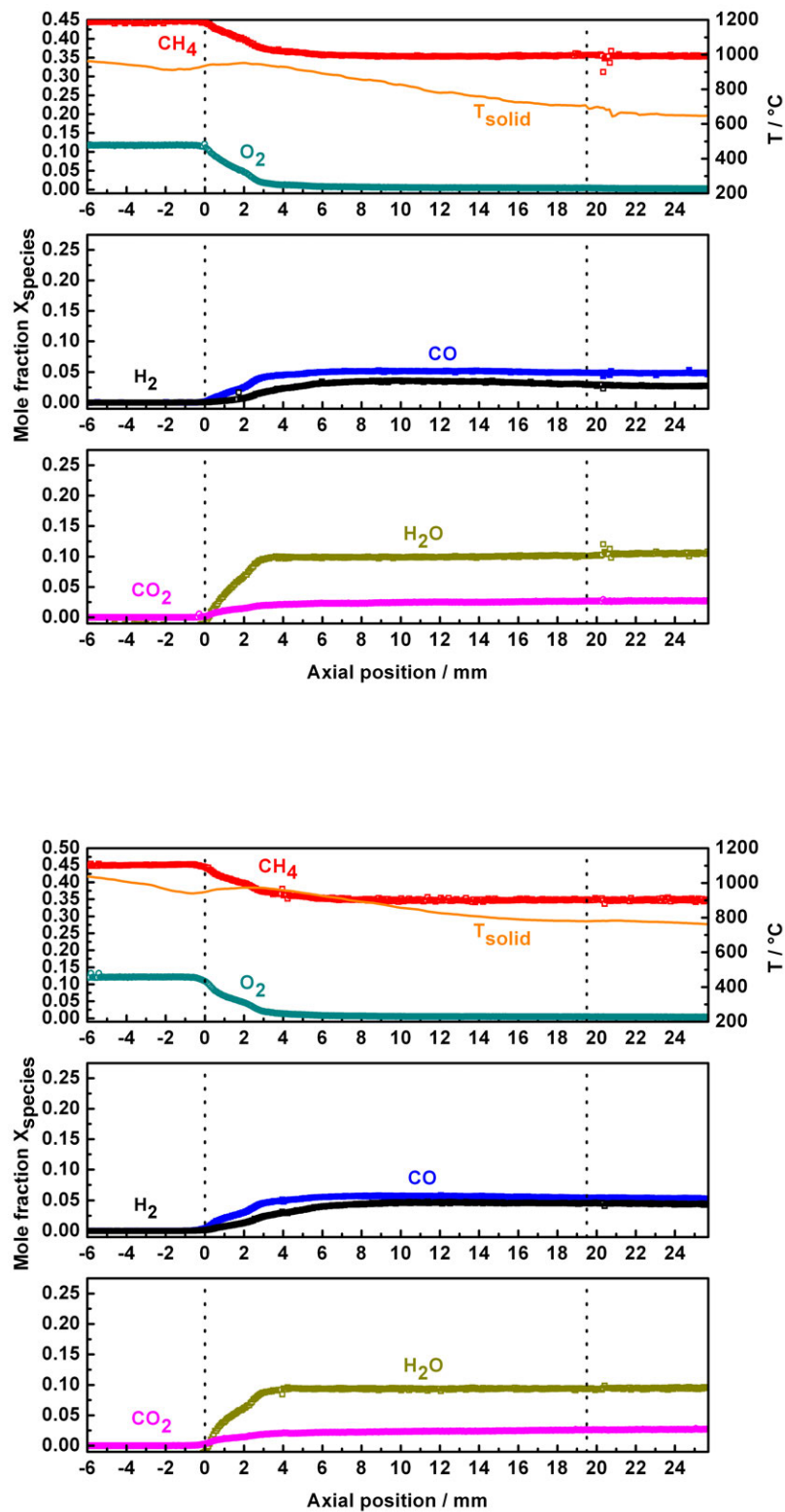


Figure E.18: Spatial reactor profile of surface temperature and species evolution. In between the dotted lines: catalyst foam monolith, left and right from the dotted lines: front and back heat shield respectively. Total gas feed of $2000 \text{ mln min}^{-1}$ @ $C/O = 2.0$ (both in auto thermal operation). Top: 10 bar reactor pressure, Bottom: 15 bar reactor pressure. For detailed information about the catalyst and reaction conditions see Tables E.1 and E.2.

E.3 Reactor Profiles Through Catalyst Foam #10256

Table E.5: List of profiles of foam monolith #10256.

C/O	p	$\bar{V}_{\text{total}} = 2000 \text{ mln min}^{-1}$	$\bar{V}_{\text{total}} = 4000 \text{ mln min}^{-1}$
2.0	1 atm	Fig. E.19 top	-
2.0	5 bar	Fig. E.19 bottom	-
2.0	10 bar	Fig. E.20 top	-
2.0	15 bar	Fig. E.20 bottom	-

E.3.1 $\dot{V}_{\text{total}} = 4000 \text{ mln min}^{-1}$ - Pressure Variation

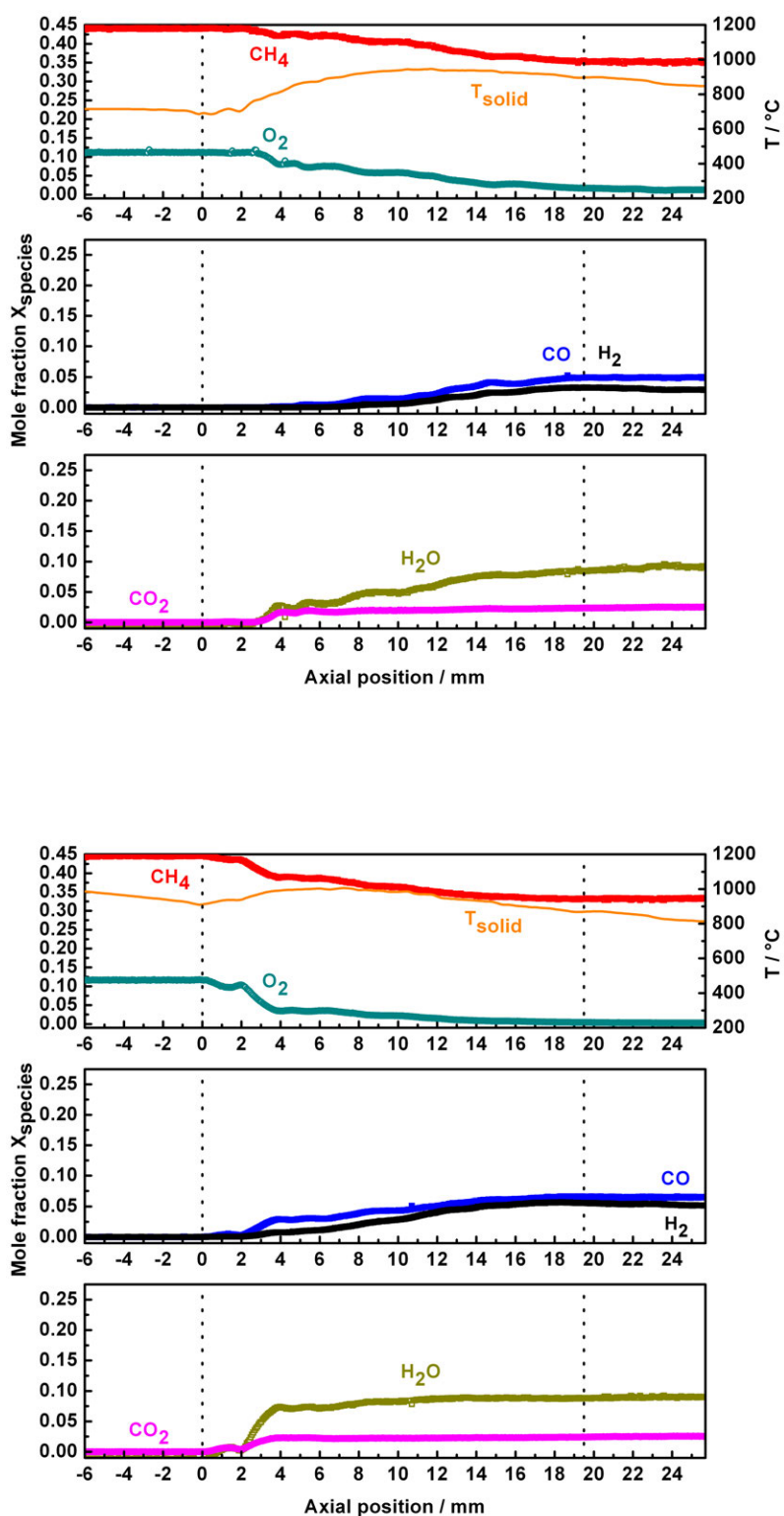


Figure E.19: Spatial reactor profile of surface temperature and species evolution. In between the dotted lines: catalyst foam monolith, left and right from the dotted lines: front and back heat shield respectively. Total gas feed of $4000 \text{ mln min}^{-1}$ @ $C/O = 2.0$ (both in auto thermal operation). Top: ambient pressure, Bottom: 5 bar reactor pressure. For detailed information about the catalyst and reaction conditions see Tables E.1 and E.2.

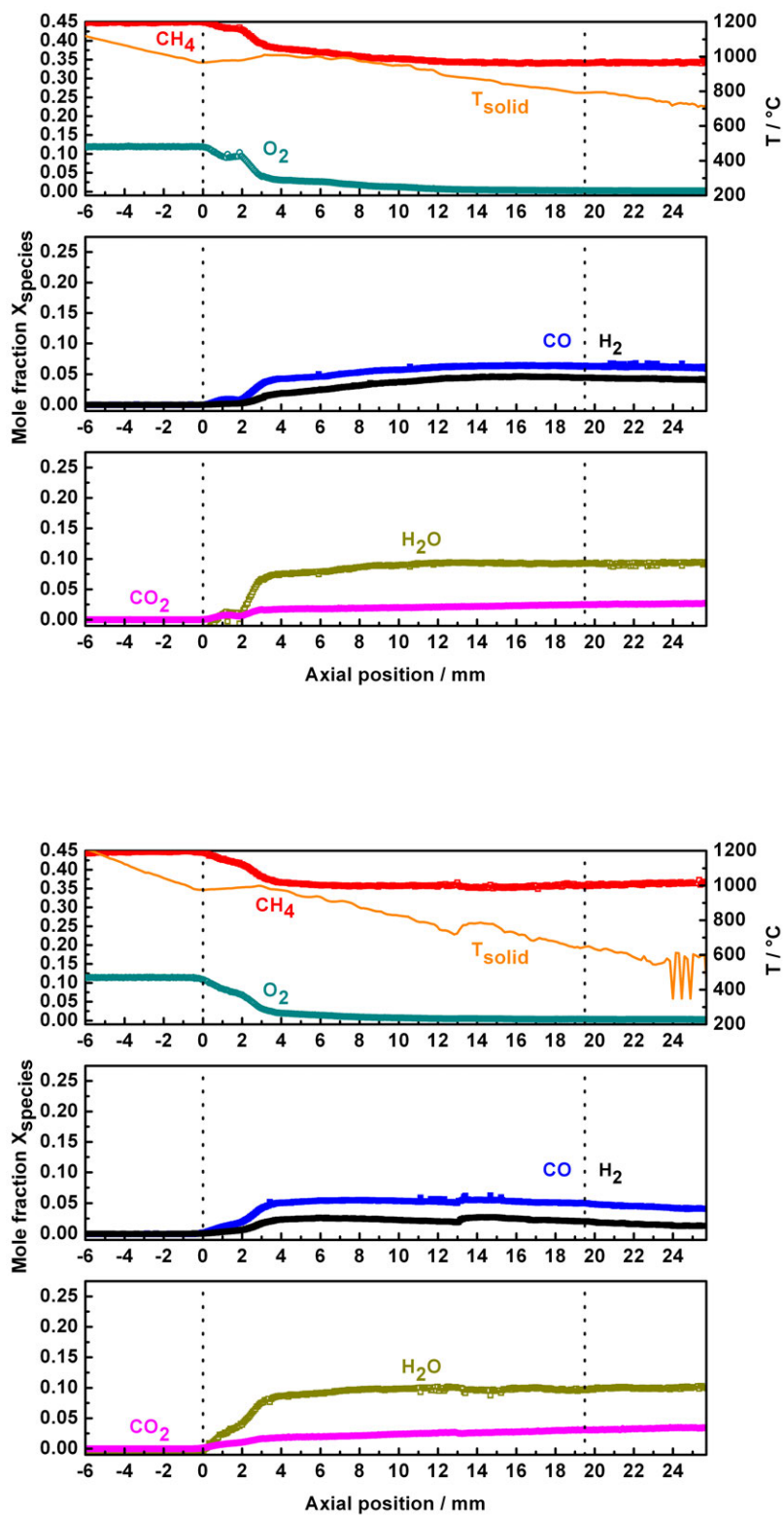


Figure E.20: Spatial reactor profile of surface temperature and species evolution. In between the dotted lines: catalyst foam monolith, left and right from the dotted lines: front and back heat shield respectively. Total gas feed of $4000 \text{ mln min}^{-1}$ @ $C/O = 2.0$ (both in auto thermal operation). Top: 10 bar reactor pressure, Bottom: 15 bar reactor pressure. For detailed information about the catalyst and reaction conditions see Tables E.1 and E.2.

E.4 Reactor Profiles Through Catalyst Foam #10774

Table E.6: List of profiles of foam monolith #10774.

C/O	p	$\dot{V}_{\text{total}} = 2000 \text{ mln min}^{-1}$	$\dot{V}_{\text{total}} = 4000 \text{ mln min}^{-1}$
2.0	1 atm	Fig. E.24 bottom	Fig. E.28 bottom
2.0	1 atm	Fig. E.29 top	Fig. E.31 top
2.0	5 bar	Fig. E.29 bottom	Fig. E.31 bottom
2.0	10 bar	Fig. E.30 top	Fig. E.32 top
2.0	15 bar	Fig. E.30 bottom	Fig. E.32 bottom
1.8	1 atm	Fig. E.24 top	Fig. E.28 top
1.6	1 atm	Fig. E.23 bottom	Fig. E.27 bottom
1.4	1 atm	Fig. E.23 top	Fig. E.27 top
1.2	1 atm	Fig. E.22 bottom	Fig. E.26 bottom
1.0	1 atm	Fig. E.22 top	Fig. E.26 top
0.8	1 atm	Fig. E.21	Fig. E.25

E.4.1 $\dot{V}_{\text{total}} = 2000 \text{ mln min}^{-1}$ - C/O Variation at Ambient Pressure

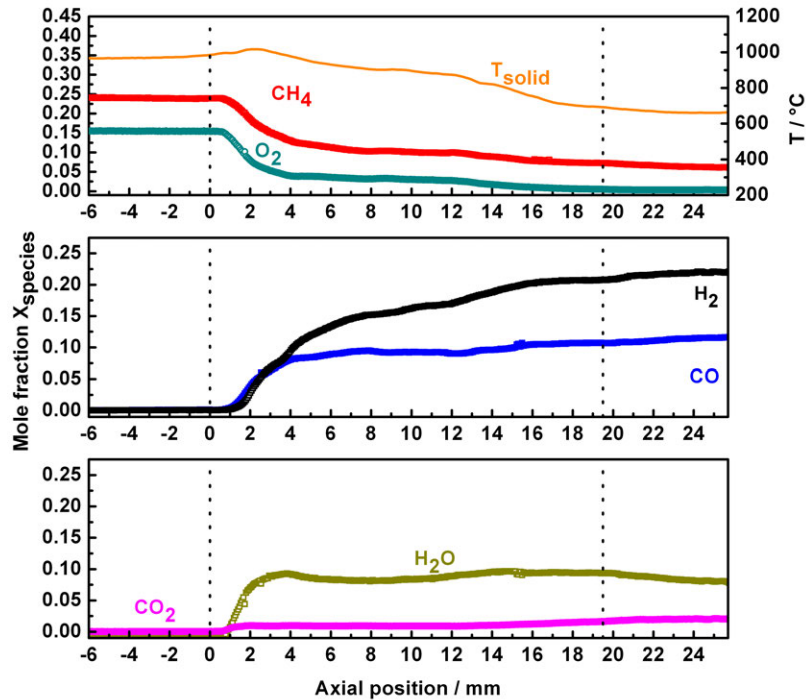


Figure E.21: Spatial reactor profile of surface temperature and species evolution. In between the dotted lines: catalyst foam monolith, left and right from the dotted lines: front and back heat shield respectively. Total gas feed of $2000 \text{ mln min}^{-1}$ @ C/O = 0.8 (auto thermal operation). For detailed information about the catalyst and reaction conditions see Tables E.1 and E.2.

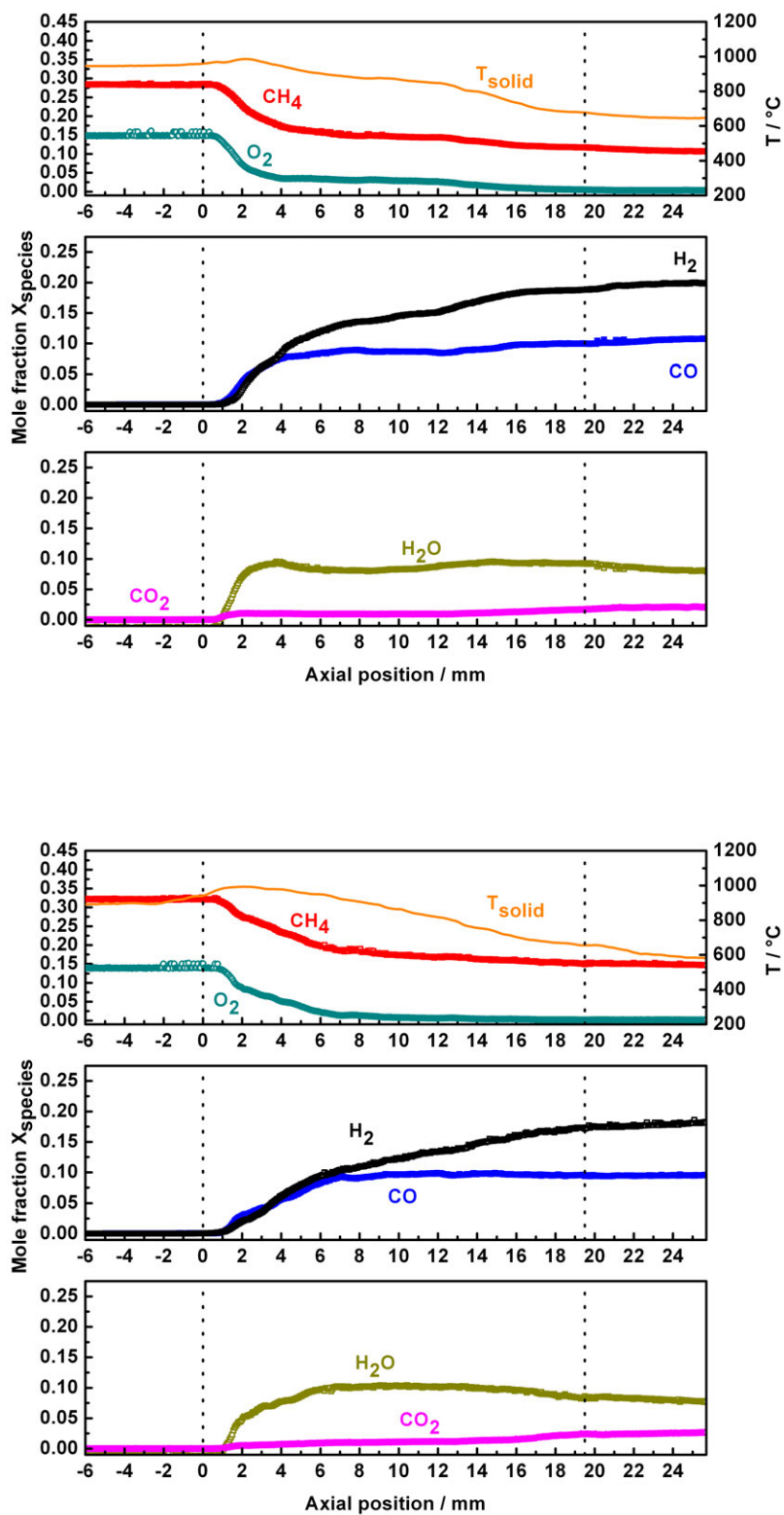


Figure E.22: Spatial reactor profile of surface temperature and species evolution. In between the dotted lines: catalyst foam monolith, left and right from the dotted lines: front and back heat shield respectively. Total gas feed of $2000 \text{ mln min}^{-1}$ @ $C/O = 1.0$ (top) and 1.2 (bottom) (both in auto thermal operation). For detailed information about the catalyst and reaction conditions see Tables E.1 and E.2.

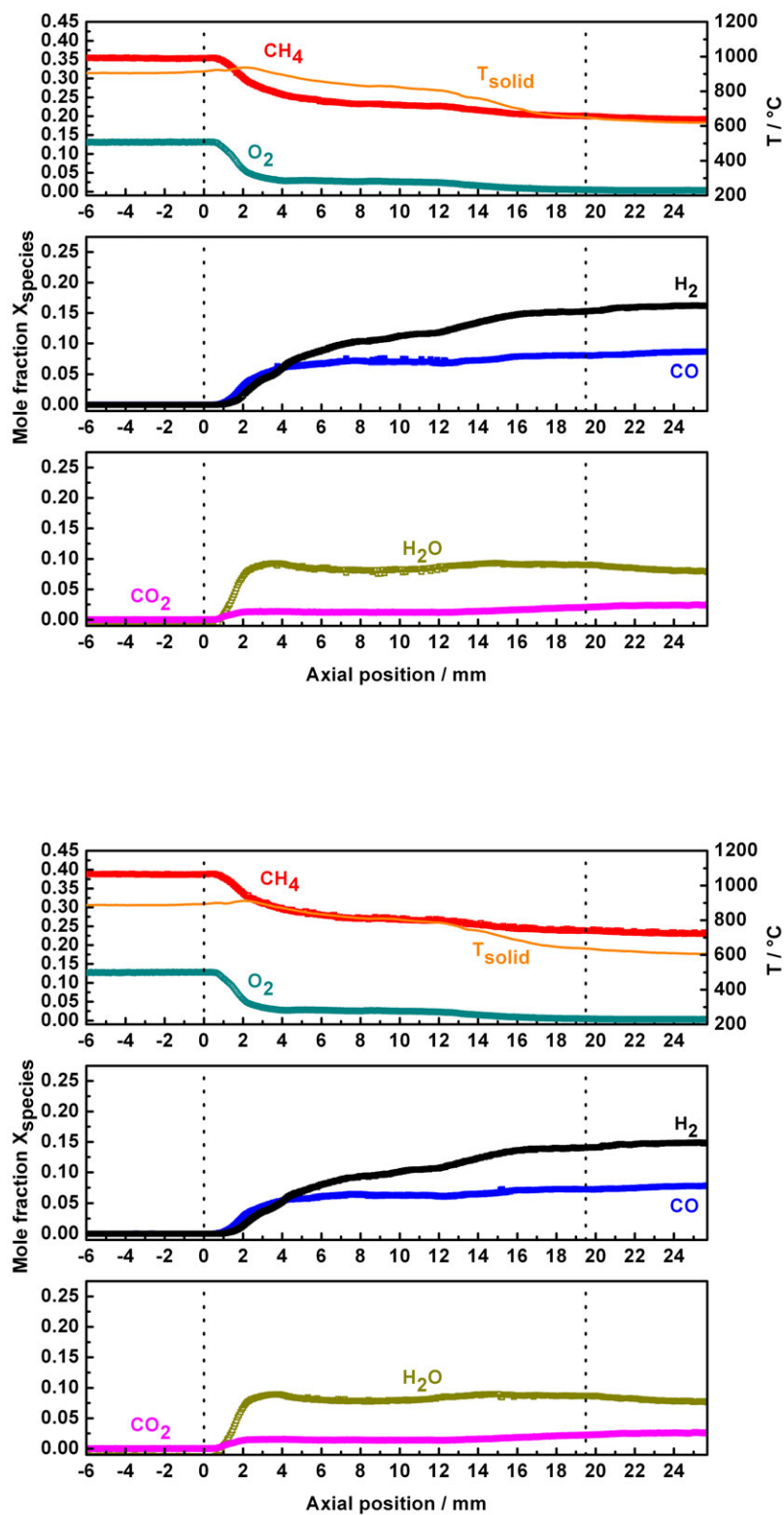


Figure E.23: Spatial reactor profile of surface temperature and species evolution. In between the dotted lines: catalyst foam monolith, left and right from the dotted lines: front and back heat shield respectively. Total gas feed of $2000 \text{ mln min}^{-1}$ @ $C/O = 1.4$ (top) and 1.6 (bottom) (both in auto thermal operation). For detailed information about the catalyst and reaction conditions see Tables E.1 and E.2.

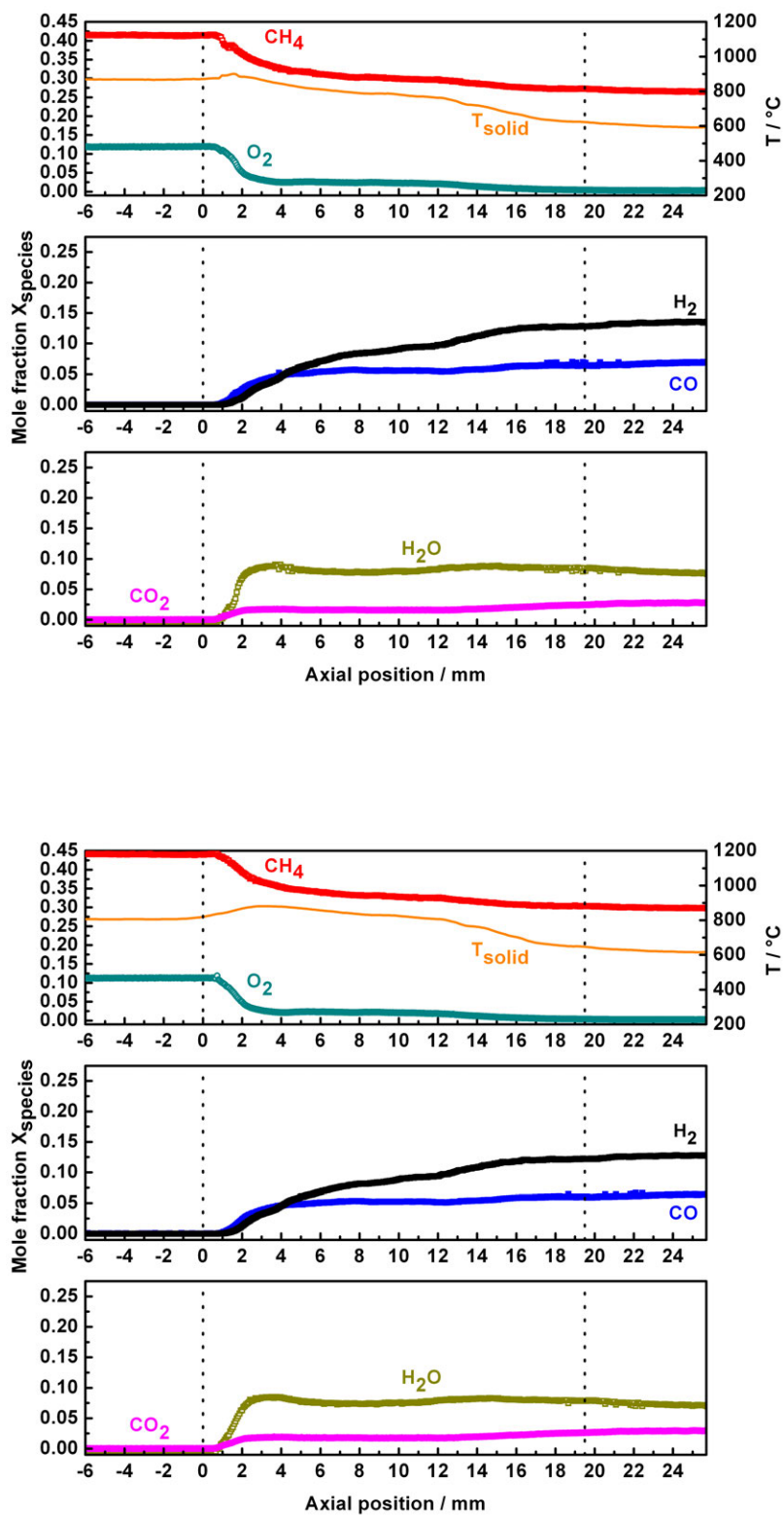


Figure E.24: Spatial reactor profile of surface temperature and species evolution. In between the dotted lines: catalyst foam monolith, left and right from the dotted lines: front and back heat shield respectively. Total gas feed of $2000 \text{ mln min}^{-1}$ @ $C/O = 1.8$ (top) and 2.0 (bottom) (both in auto thermal operation). For detailed information about the catalyst and reaction conditions see Tables E.1 and E.2.

E.4.2 $\dot{V}_{\text{total}} = 4000 \text{ mln min}^{-1}$ - C/O Variation at Ambient Pressure

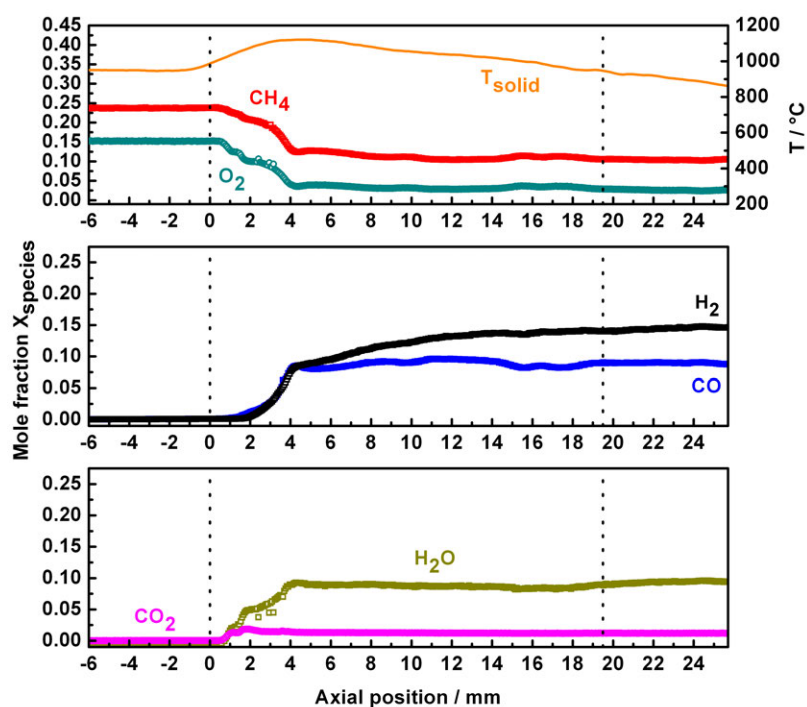


Figure E.25: Spatial reactor profile of surface temperature and species evolution. In between the dotted lines: catalyst foam monolith, left and right from the dotted lines: front and back heat shield respectively. Total gas feed of $4000 \text{ mln min}^{-1}$ @ C/O = 0.8 (auto thermal operation). For detailed information about the catalyst and reaction conditions see Tables E.1 and E.2.

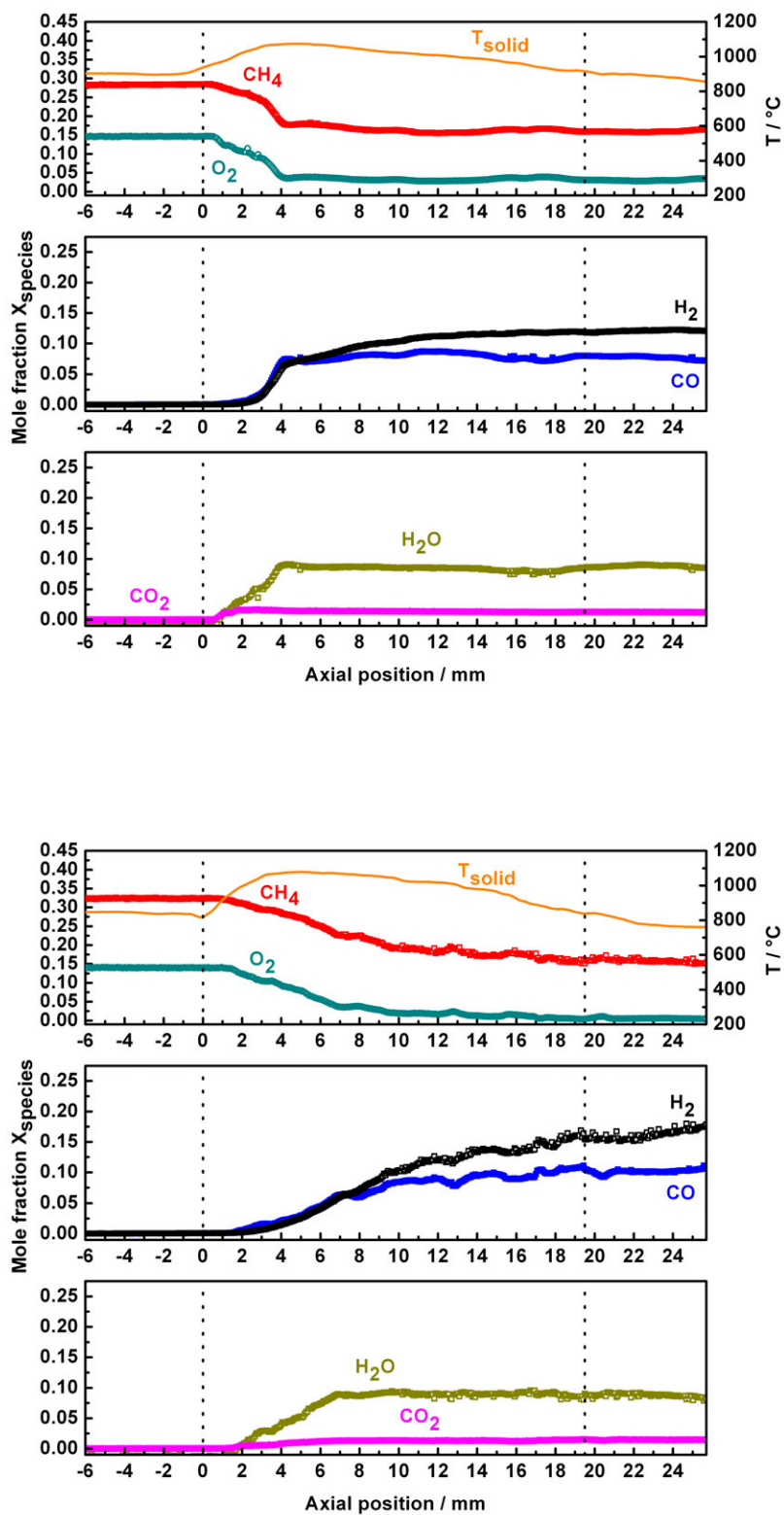


Figure E.26: Spatial reactor profile of surface temperature and species evolution. In between the dotted lines: catalyst foam monolith, left and right from the dotted lines: front and back heat shield respectively. Total gas feed of $4000 \text{ mln min}^{-1}$ @ $C/O = 1.0$ (top) and 1.2 (bottom) (both in auto thermal operation). For detailed information about the catalyst and reaction conditions see Tables E.1 and E.2.

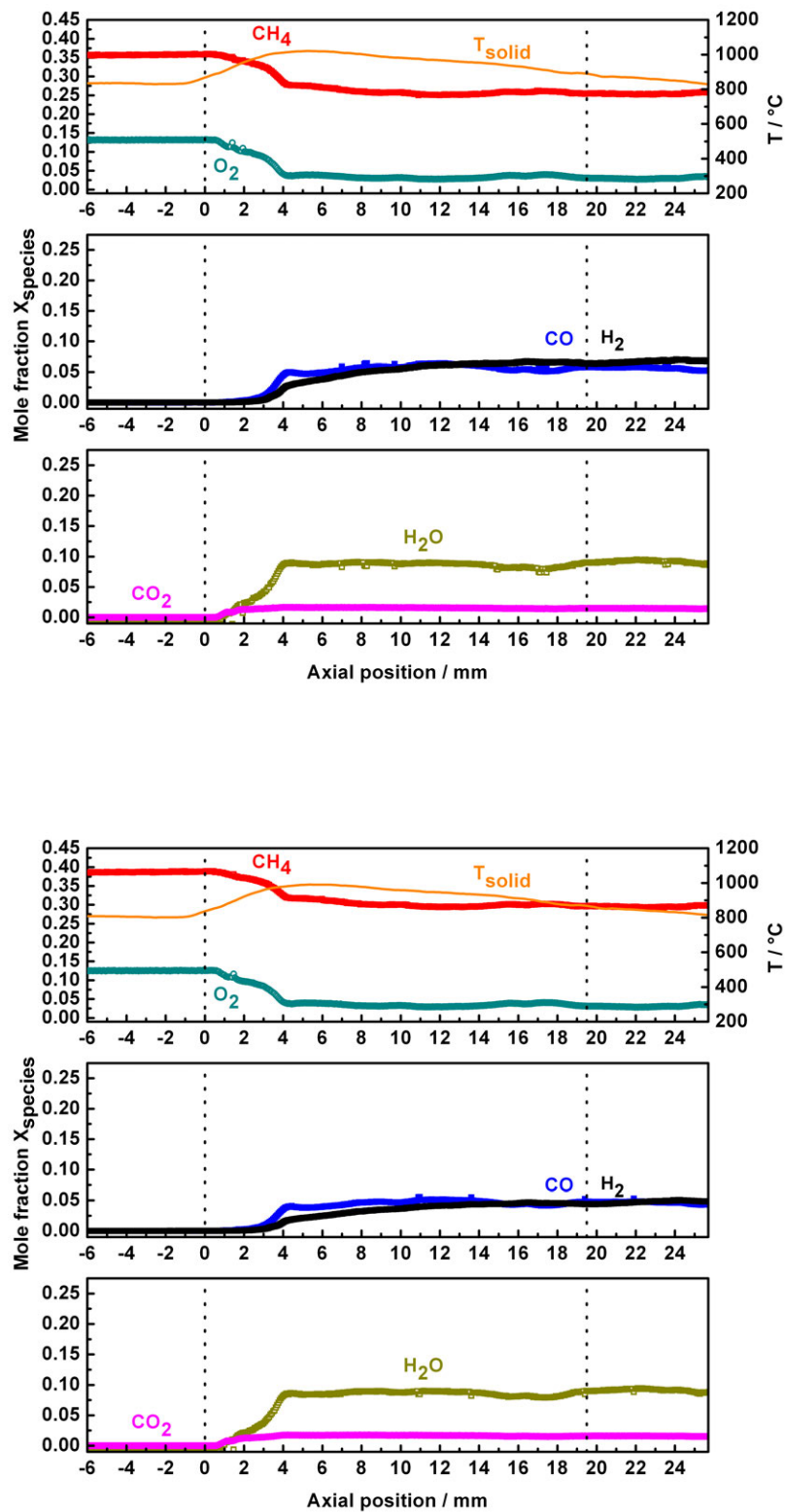


Figure E.27: Spatial reactor profile of surface temperature and species evolution. In between the dotted lines: catalyst foam monolith, left and right from the dotted lines: front and back heat shield respectively. Total gas feed of $4000 \text{ mln min}^{-1}$ @ $C/O = 1.4$ (top) and 1.6 (bottom) (both in auto thermal operation). For detailed information about the catalyst and reaction conditions see Tables E.1 and E.2.

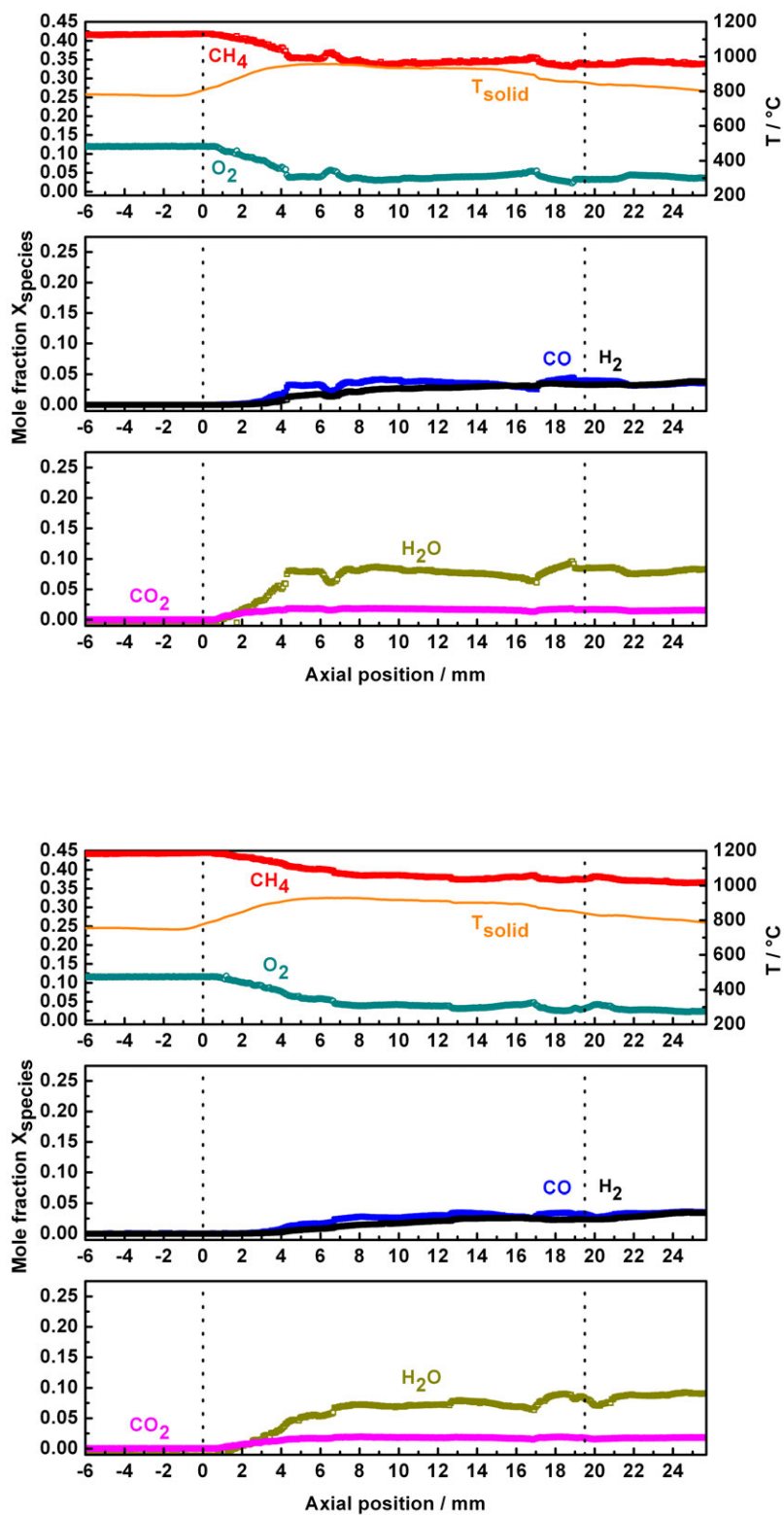


Figure E.28: Spatial reactor profile of surface temperature and species evolution. In between the dotted lines: catalyst foam monolith, left and right from the dotted lines: front and back heat shield respectively. Total gas feed of $4000 \text{ mln min}^{-1}$ @ $C/O = 1.8$ (top) and 2.0 (bottom) (both in auto thermal operation). For detailed information about the catalyst and reaction conditions see Tables E.1 and E.2.

E.4.3 $\dot{V}_{\text{total}} = 2000 \text{ mln min}^{-1}$ - Pressure Variation

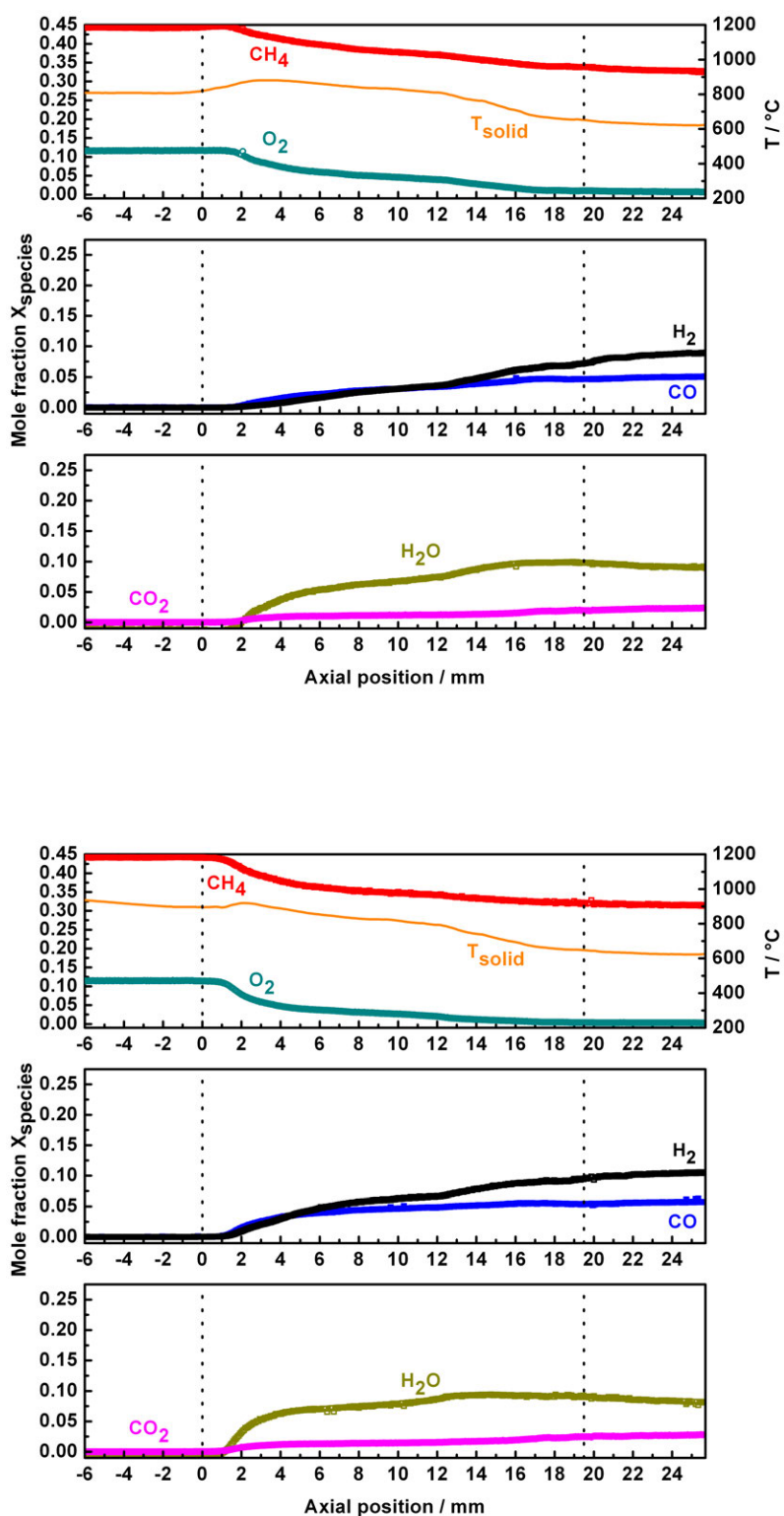


Figure E.29: Spatial reactor profile of surface temperature and species evolution. In between the dotted lines: catalyst foam monolith, left and right from the dotted lines: front and back heat shield respectively. Total gas feed of $2000 \text{ mln min}^{-1}$ @ $C/O = 2.0$ (both in auto thermal operation). Top: ambient pressure, Bottom: 5 bar reactor pressure. For detailed information about the catalyst and reaction conditions see Tables E.1 and E.2.

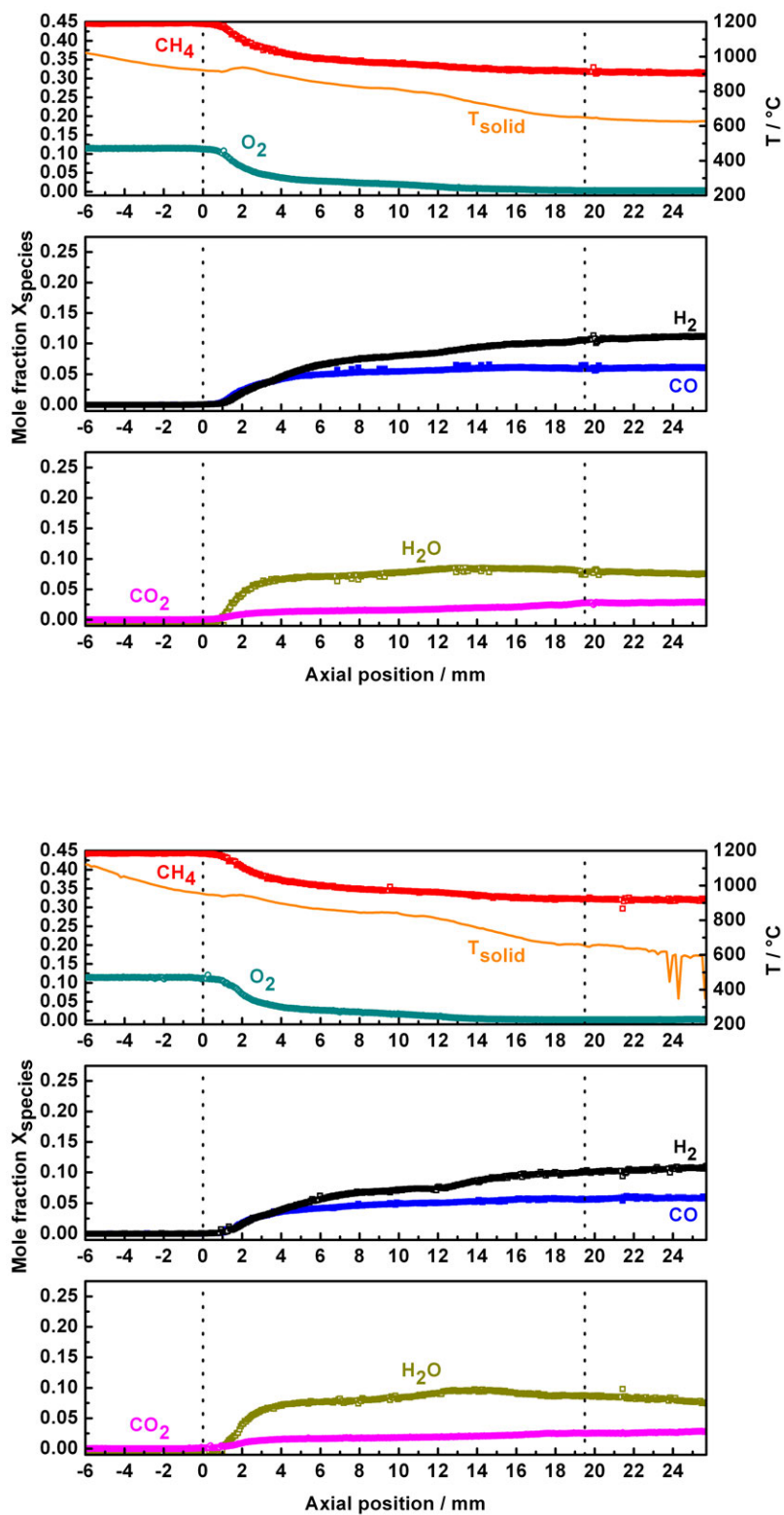


Figure E.30: Spatial reactor profile of surface temperature and species evolution. In between the dotted lines: catalyst foam monolith, left and right from the dotted lines: front and back heat shield respectively. Total gas feed of $2000 \text{ mln min}^{-1}$ @ $C/O = 2.0$ (both in auto thermal operation). Top: 10 bar reactor pressure, Bottom: 15 bar reactor pressure. For detailed information about the catalyst and reaction conditions see Tables E.1 and E.2.

E.4.4 $\dot{V}_{\text{total}} = 4000 \text{ mln min}^{-1}$ - Pressure Variation

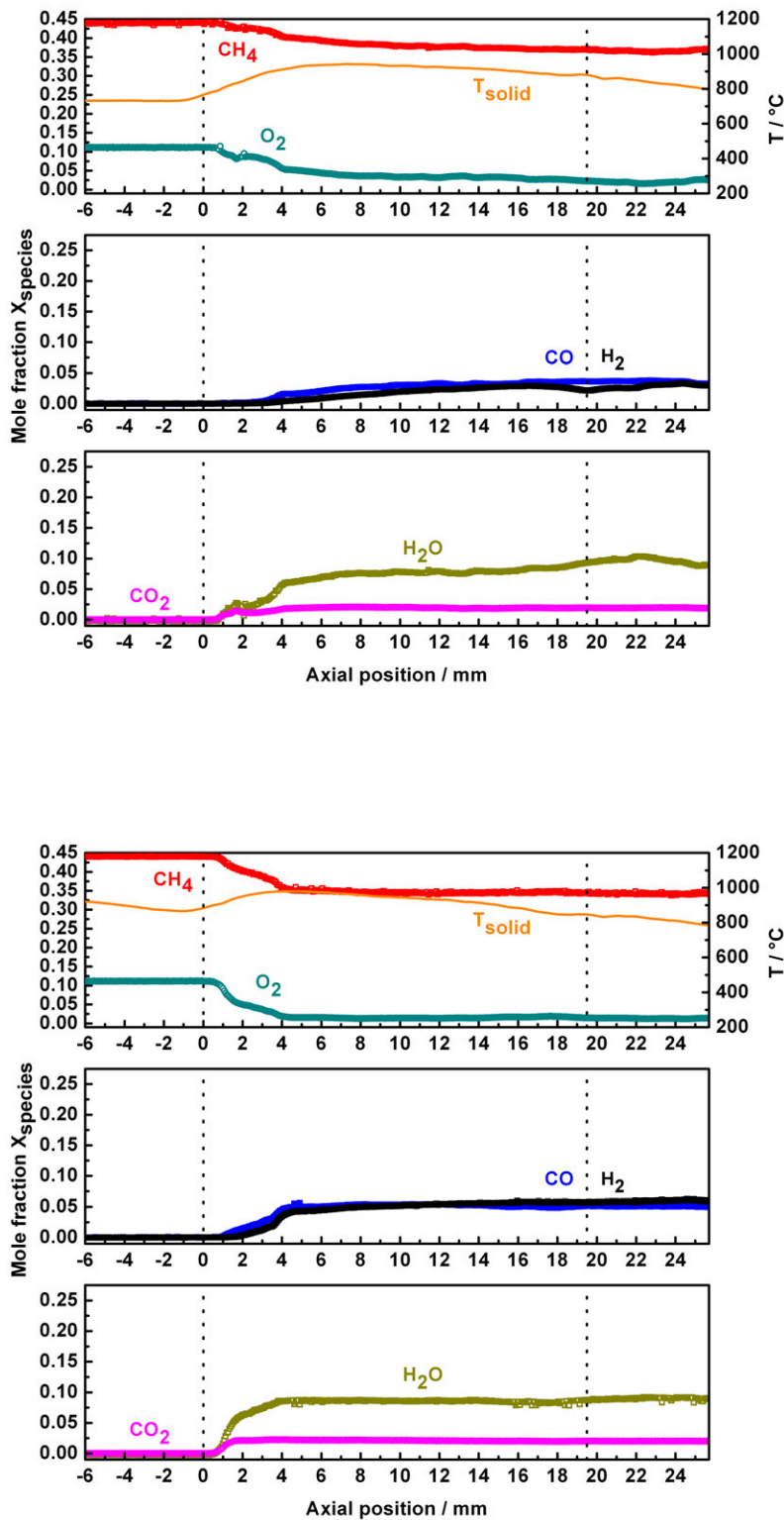


Figure E.31: Spatial reactor profile of surface temperature and species evolution. In between the dotted lines: catalyst foam monolith, left and right from the dotted lines: front and back heat shield respectively. Total gas feed of $4000 \text{ mln min}^{-1}$ @ $C/O = 2.0$ (both in auto thermal operation). Top: ambient pressure, Bottom: 5 bar reactor pressure. For detailed information about the catalyst and reaction conditions see Tables E.1 and E.2.

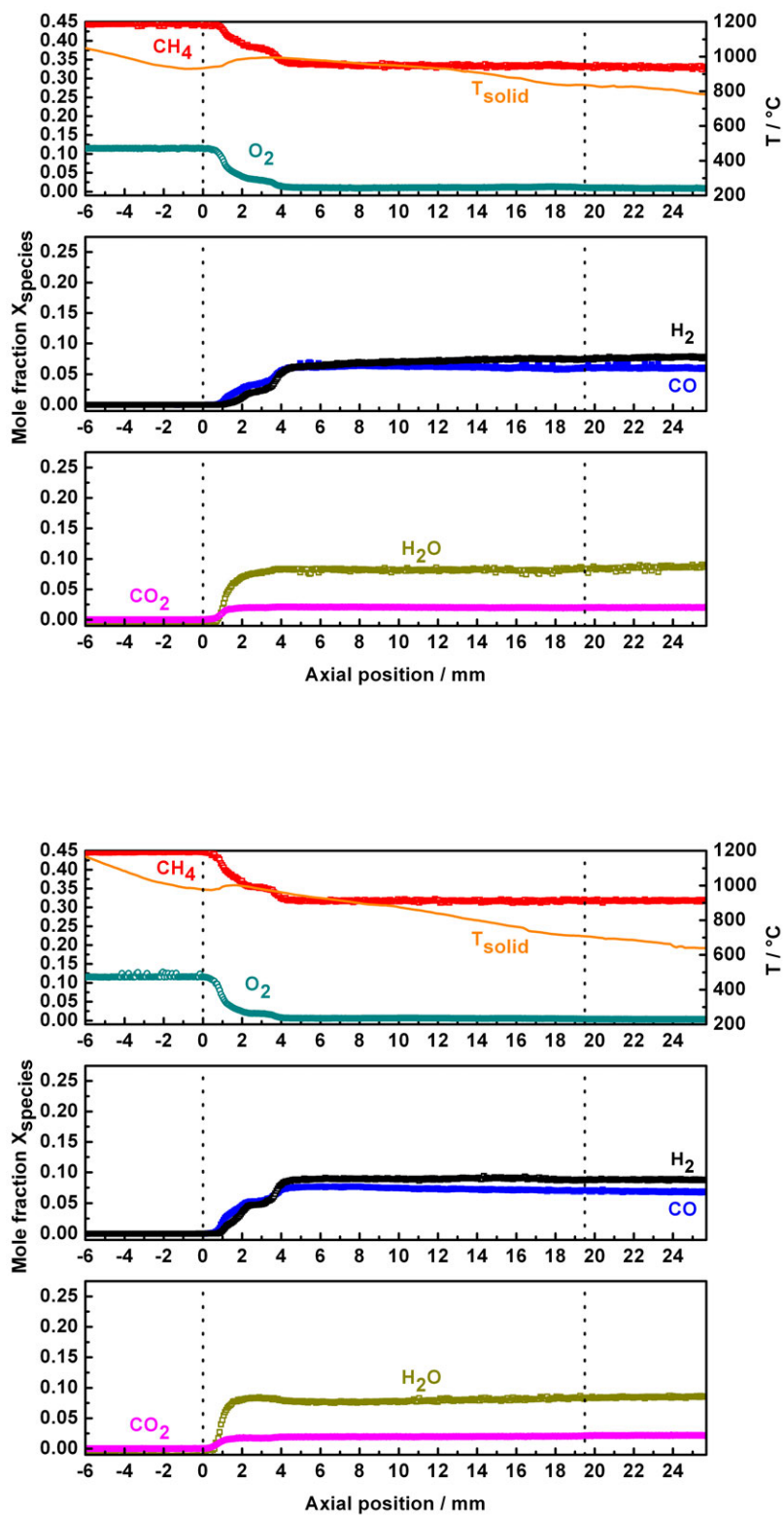


Figure E.32: Spatial reactor profile of surface temperature and species evolution. In between the dotted lines: catalyst foam monolith, left and right from the dotted lines: front and back heat shield respectively. Total gas feed of $4000 \text{ mln min}^{-1}$ @ $C/O = 2.0$ (both in auto thermal operation). Top: 10 bar reactor pressure, Bottom: 15 bar reactor pressure. For detailed information about the catalyst and reaction conditions see Tables E.1 and E.2.

E.5 Reactor Profiles Through Catalyst Foam #12036

Table E.7: List of profiles of Pt catalytic wall reactor #12036.

C/O	p	$\dot{V}_{\text{total}} = 500 \text{ mln min}^{-1}$	$\dot{V}_{\text{total}} = 1000 \text{ mln min}^{-1}$
2.0	1 atm	Fig. E.36 bottom	Fig. E.40 bottom
1.8	1 atm	Fig. E.36 top	Fig. E.40 top
1.6	1 atm	Fig. E.35 bottom	Fig. E.39 bottom
1.4	1 atm	Fig. E.35 top	Fig. E.39 top
1.2	1 atm	Fig. E.34 bottom	Fig. E.38 bottom
1.0	1 atm	Fig. E.34 top	Fig. E.38 top
0.8	1 atm	Fig. E.33	Fig. E.37

E.5.1 $\dot{V}_{\text{total}} = 500 \text{ mln min}^{-1}$ - C/O Variation at Ambient Pressure

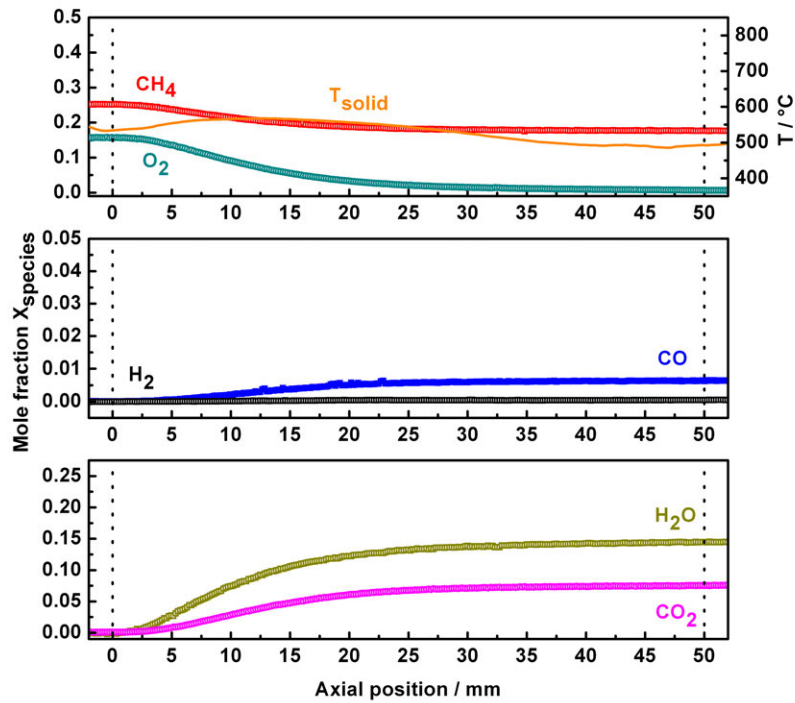


Figure E.33: Spatial reactor profile of surface temperature and species evolution. In between the dotted lines: Pt tube (OD = 5 mm, ID = 4.4 mm), left and right from the dotted lines: alumina-ceramic tube mount. Total gas feed of 500 mln min^{-1} @ C/O = 0.8 (auto thermal operation). For detailed information about the catalyst and reaction conditions see Tables E.1 and E.2.

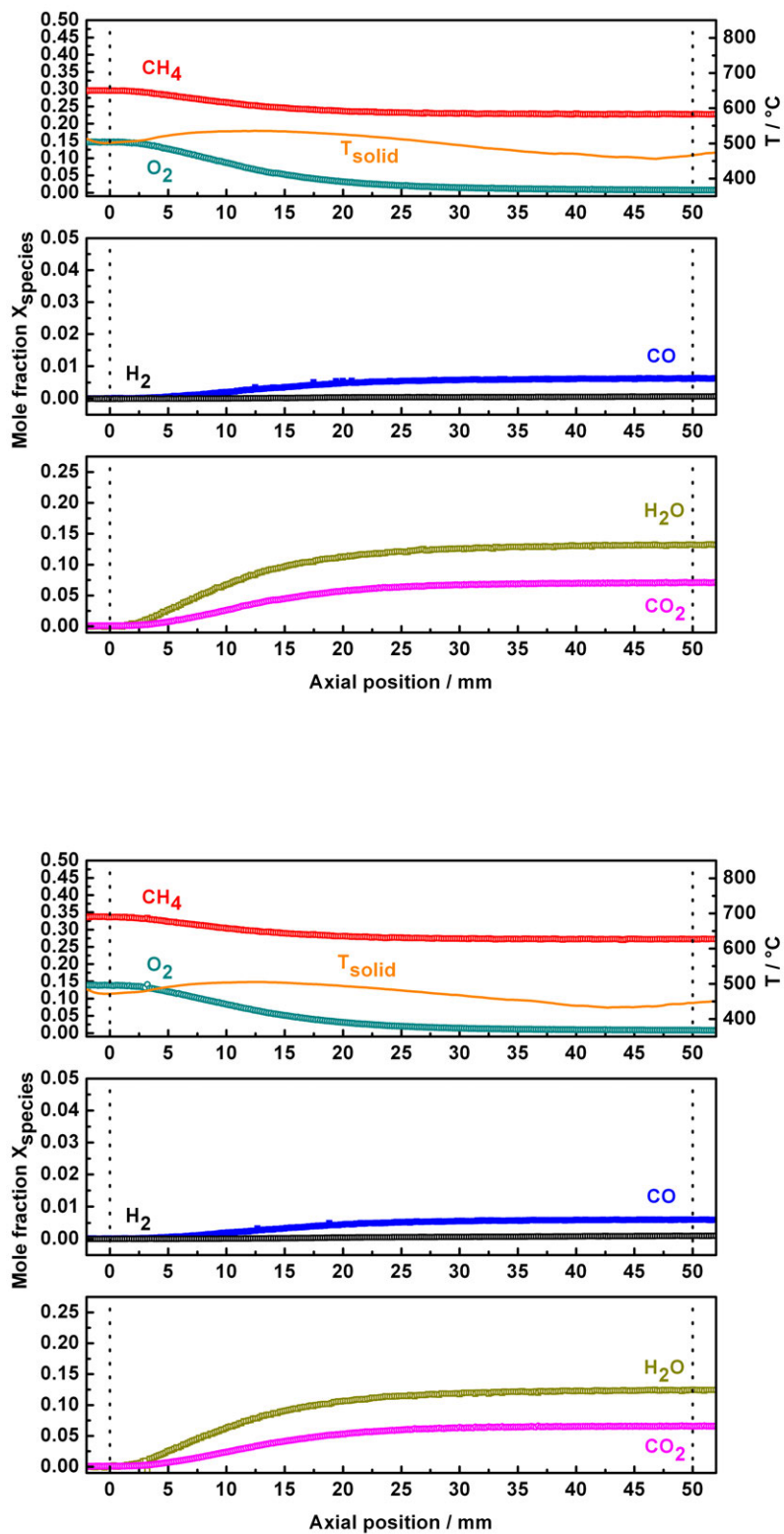


Figure E.34: Spatial reactor profile of surface temperature and species evolution. In between the dotted lines: Pt tube (OD = 5 mm, ID = 4.4 mm), left and right from the dotted lines: alumina-ceramic tube mount. Total gas feed of 500 mln min^{-1} @ C/O = 1.0 (top) and 1.2 (bottom) (both in auto thermal operation). For detailed information about the catalyst and reaction conditions see Tables E.1 and E.2.

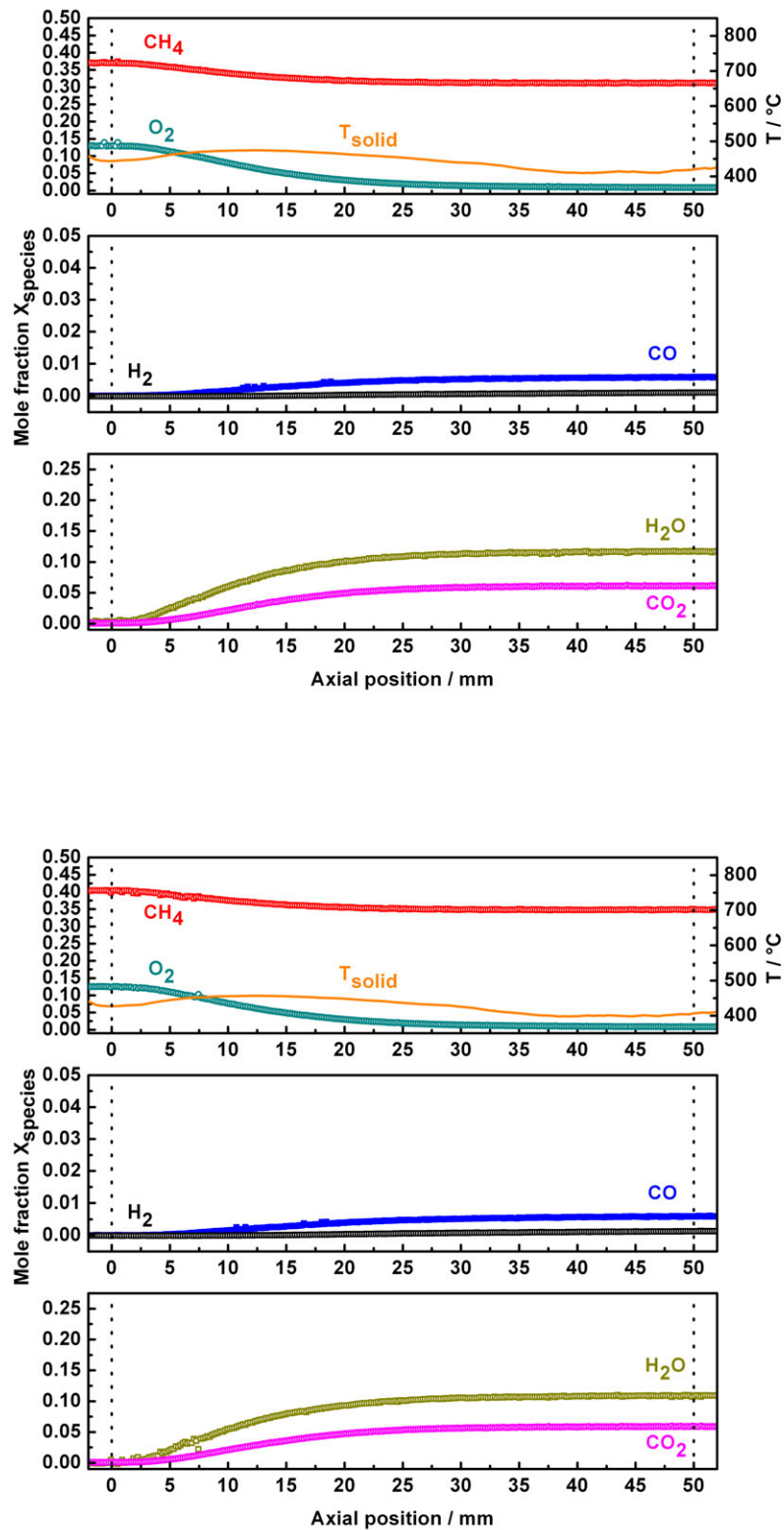


Figure E.35: Spatial reactor profile of surface temperature and species evolution. In between the dotted lines: Pt tube (OD = 5 mm, ID = 4.4 mm), left and right from the dotted lines: alumina-ceramic tube mount. Total gas feed of 500 mln min^{-1} @ C/O = 1.4 (top) and 1.6 (bottom) (both in auto thermal operation). For detailed information about the catalyst and reaction conditions see Tables E.1 and E.2.

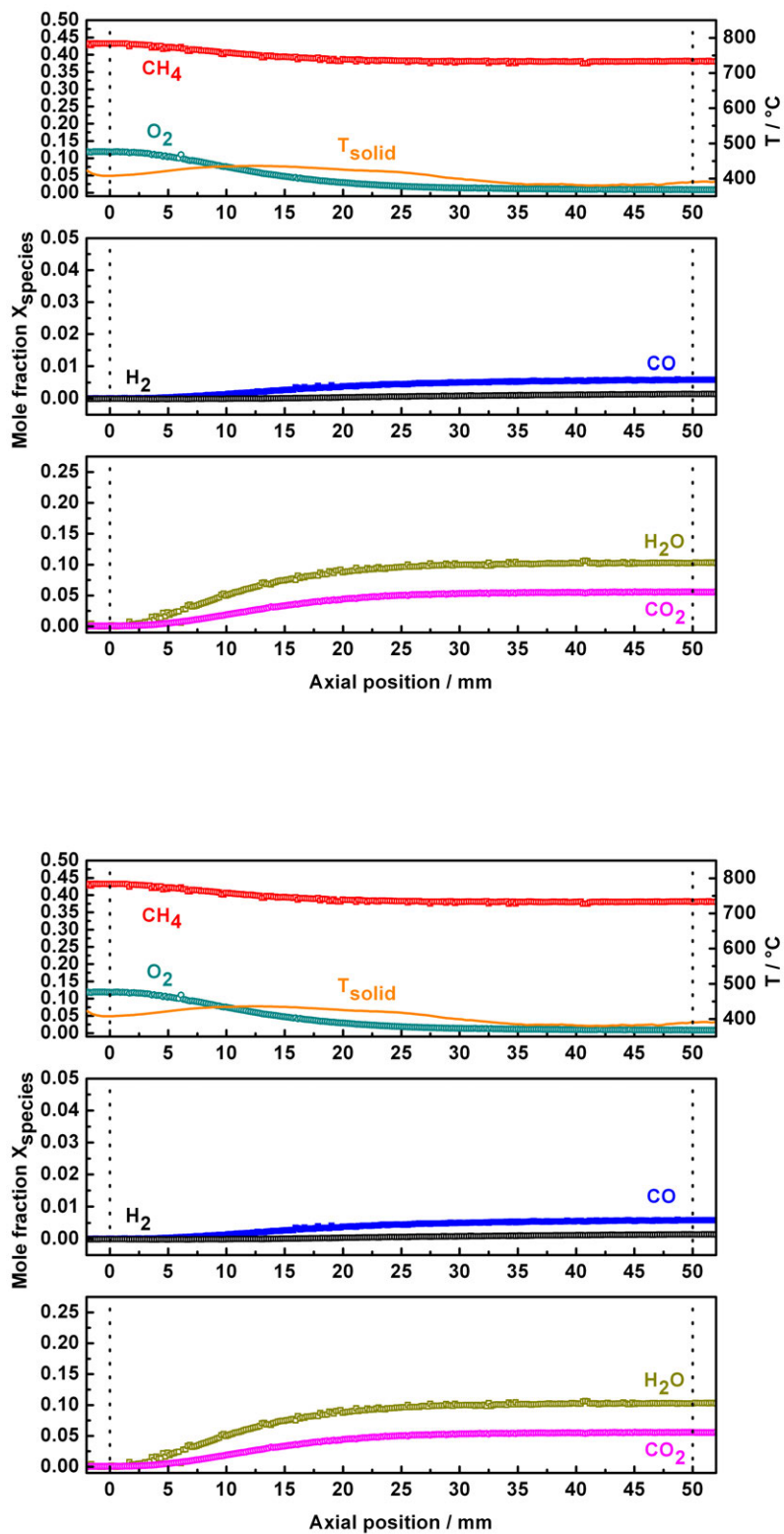


Figure E.36: Spatial reactor profile of surface temperature and species evolution. In between the dotted lines: Pt tube (OD = 5 mm, ID = 4.4 mm), left and right from the dotted lines: alumina-ceramic tube mount. Total gas feed of 500 mln min^{-1} @ C/O = 1.8 (top) and 2.0 (bottom) (both in auto thermal operation). For detailed information about the catalyst and reaction conditions see Tables E.1 and E.2.

E.5.2 $\dot{V}_{\text{total}} = 1000 \text{ mln min}^{-1}$ - C/O Variation at Ambient Pressure

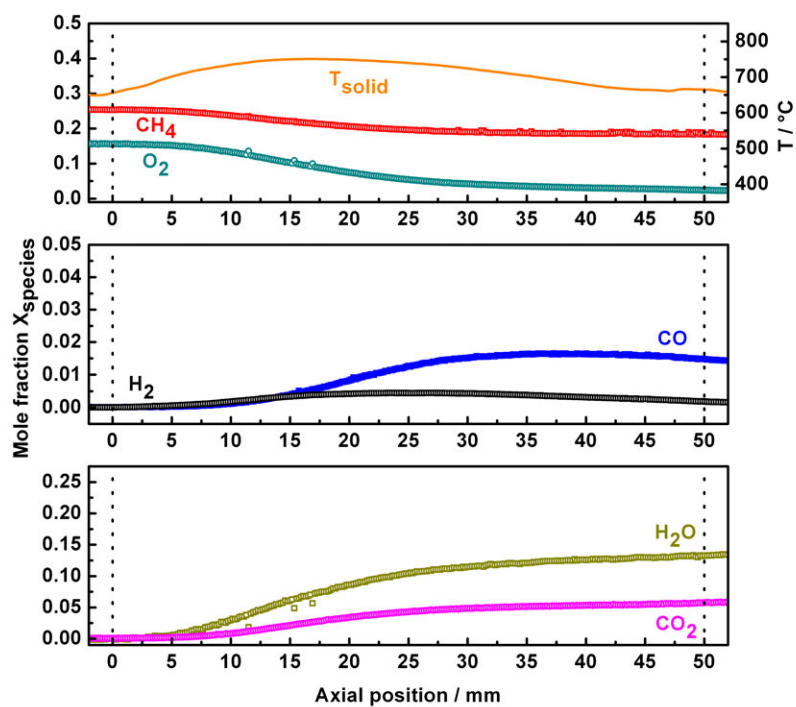


Figure E.37: Spatial reactor profile of surface temperature and species evolution. In between the dotted lines: Pt tube (OD = 5 mm, ID = 4.4 mm), left and right from the dotted lines: alumina-ceramic tube mount. Total gas feed of $1000 \text{ mln min}^{-1}$ @ C/O = 0.8 (auto thermal operation). For detailed information about the catalyst and reaction conditions see Tables E.1 and E.2.

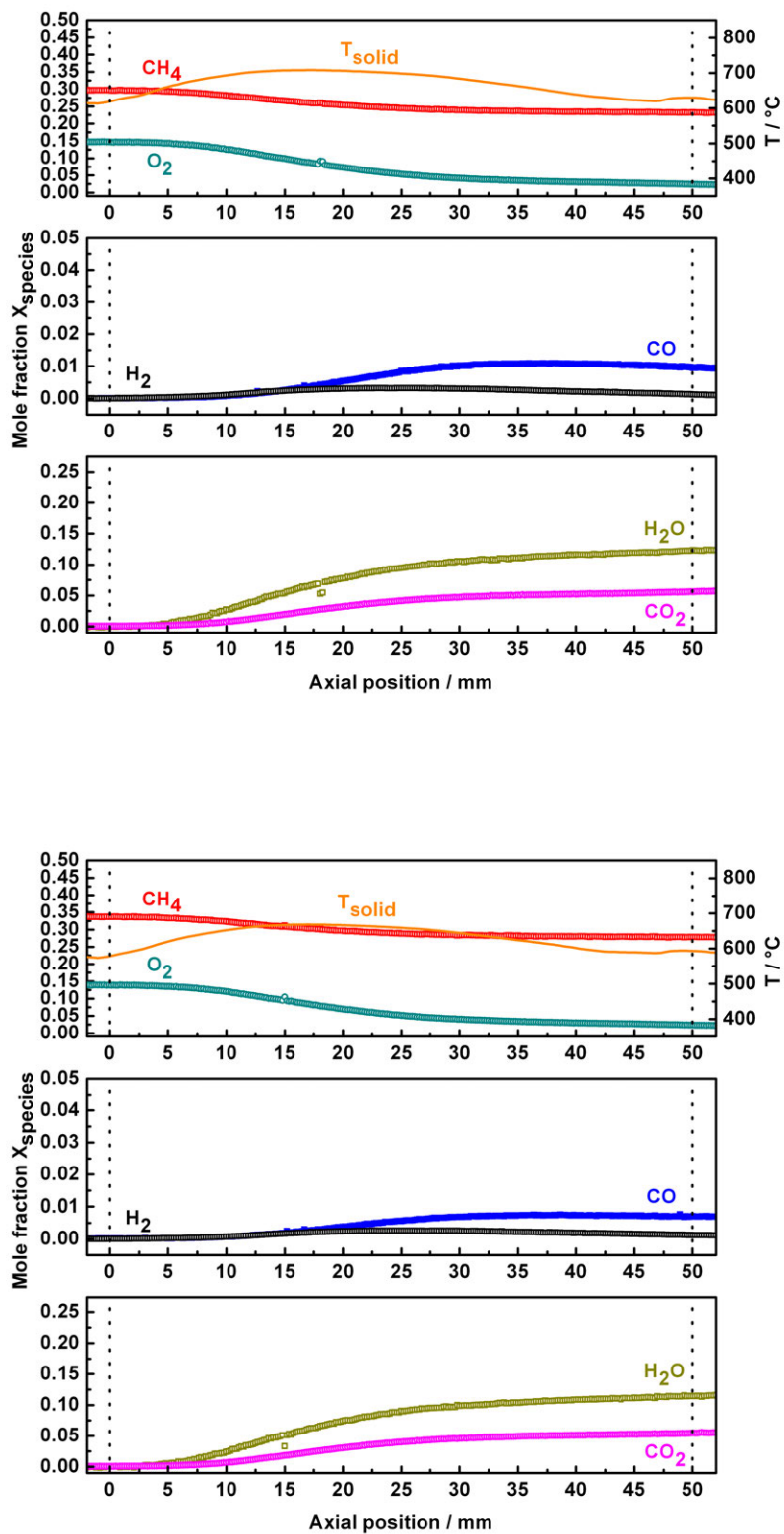


Figure E.38: Spatial reactor profile of surface temperature and species evolution. In between the dotted lines: Pt tube (OD = 5 mm, ID = 4.4 mm), left and right from the dotted lines: alumina-ceramic tube mount. Total gas feed of $1000 \text{ mln min}^{-1}$ @ C/O = 1.0 (top) and 1.2 (bottom) (both in auto thermal operation). For detailed information about the catalyst and reaction conditions see Tables E.1 and E.2.

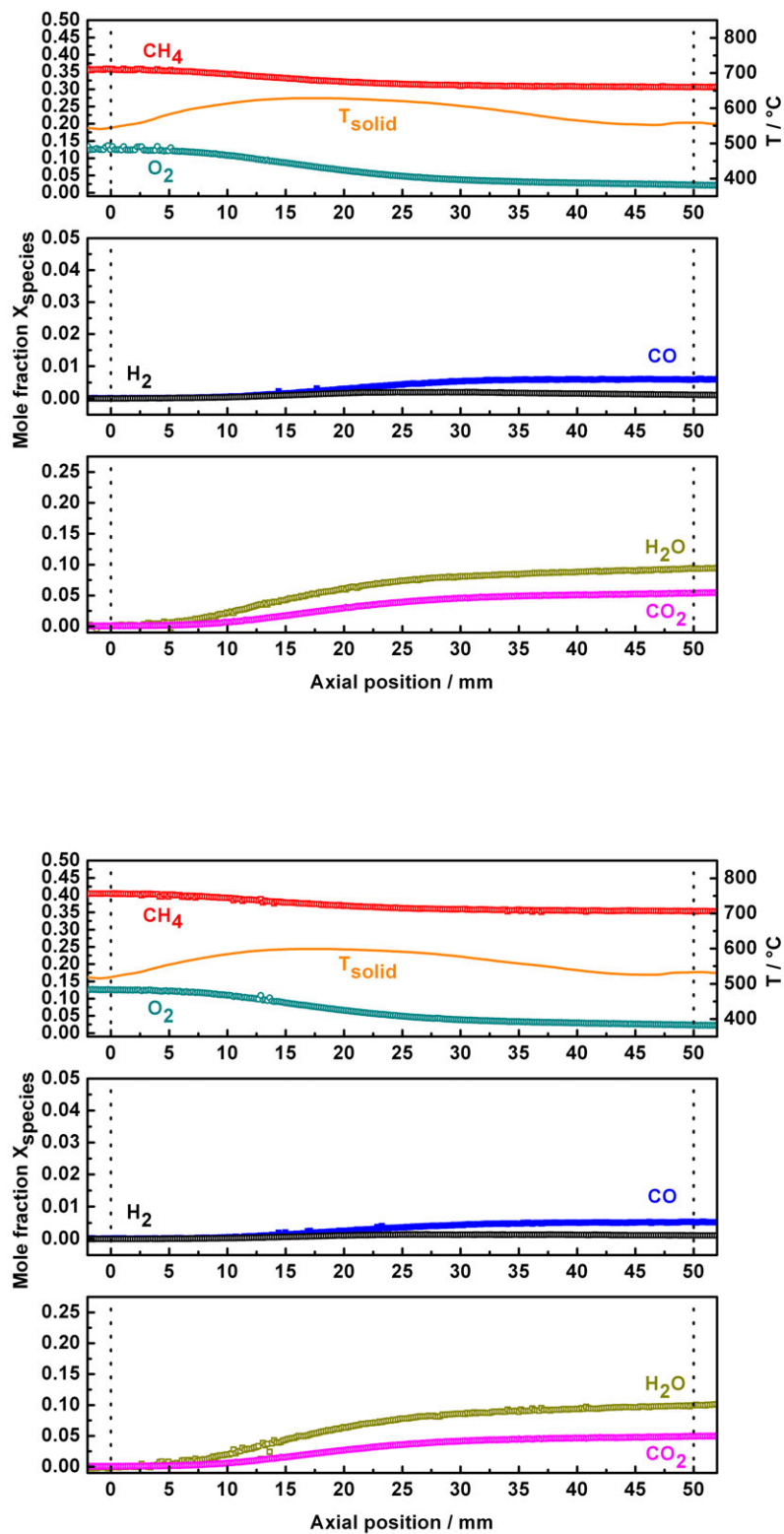


Figure E.39: Spatial reactor profile of surface temperature and species evolution. In between the dotted lines: Pt tube (OD = 5 mm, ID = 4.4 mm), left and right from the dotted lines: alumina-ceramic tube mount. Total gas feed of $1000 \text{ mln min}^{-1}$ @ C/O = 1.4 (top) and 1.6 (bottom) (both in auto thermal operation). For detailed information about the catalyst and reaction conditions see Tables E.1 and E.2.

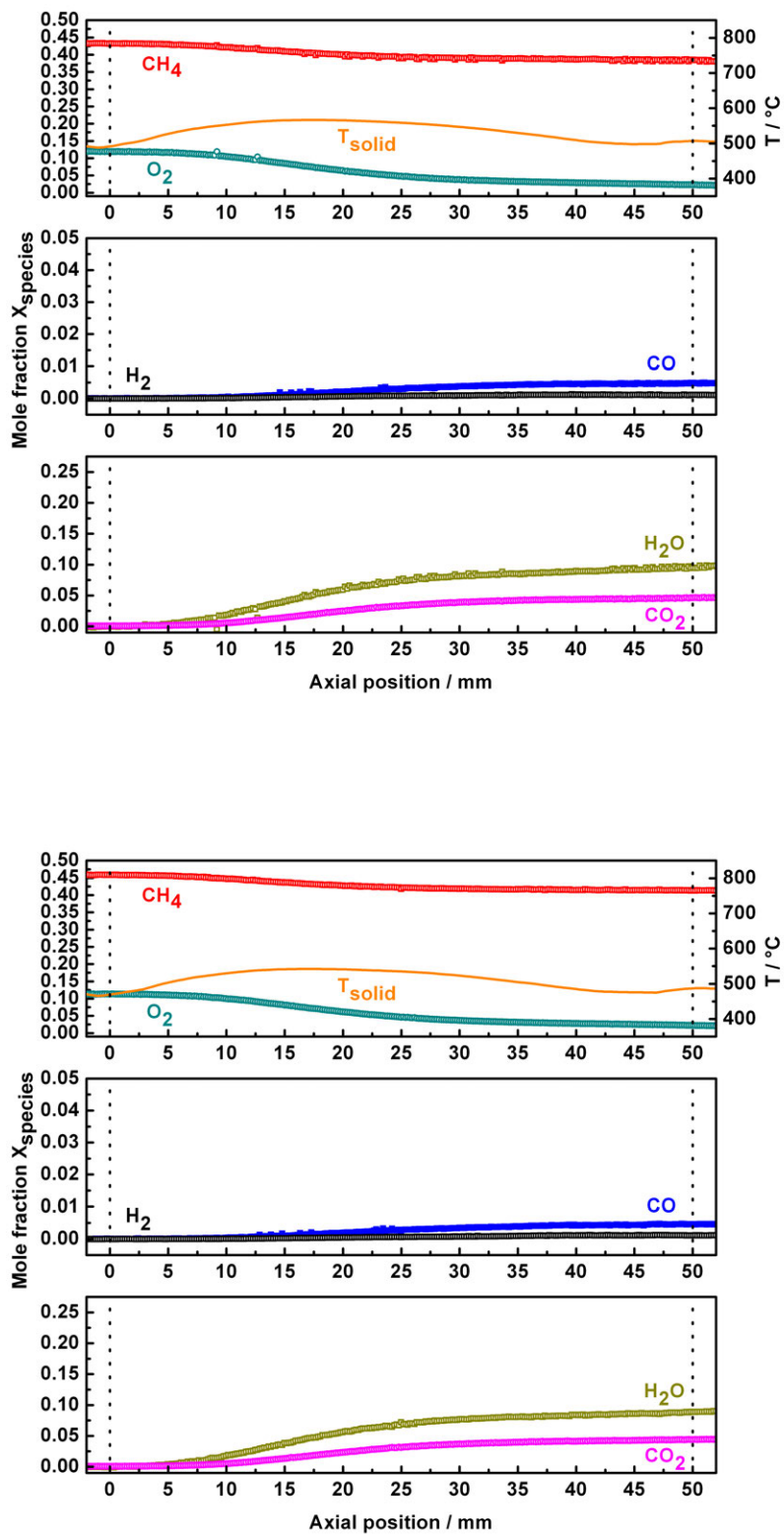


Figure E.40: Spatial reactor profile of surface temperature and species evolution. In between the dotted lines: Pt tube (OD = 5 mm, ID = 4.4 mm), left and right from the dotted lines: alumina-ceramic tube mount. Total gas feed of $1000 \text{ mln min}^{-1}$ @ C/O = 1.8 (top) and 2.0 (bottom) (both in auto thermal operation). For detailed information about the catalyst and reaction conditions see Tables E.1 and E.2.

List of Abbreviations

Abbreviation	Explanation
BET	Adsorption isotherm model of Brunauer, Emmet and Teller
BF	Bright-Field Image (TEM)
BHS	Back Heat Shield
BJH	Pore volume determination after Barrett, Joyner, and Halenda
BOE	Barrel of Oil Equivalent
BSE	Backscattered Electrons
BTU	British Thermal Unit
CCD	Charge-Coupled Device
CFD	Computational Fluid Dynamics
CM	Conventional Method
CPO	Catalytic Partial Oxidation
CRR	Combustion and Reforming Reactions Mechanism
DC	Direct Current
DF	Dark-Field Image (TEM)
DRIFTS	Diffuse Reflectance Infrared Fourier Transform Spectroscopy
DPO	Direct Partial Oxidation Mechanism
DSC	Differential Scanning Calorimetry
EI	Electron ionization
EDX	Energy Dispersive X-ray Spectroscopy
EM	Electron Microscopy or Electron Microscope
FEG	Field Emission Gun
FHS	Front Heat Shield
Fig.	Figure
FWHM	Full Width at Half Maximum
fcc	Face Centered Cubic
GC	Gas Chromatography
GRI	Gas Research Institute
GTL	Gas-to-Liquids
HPLC	High-Performance Liquid Chromatography
HRTEM	High Resolution Transmission Electron Microscopy
ID	Inner Diameter
IE	Ionization Energy
IR	Infrared Spectroscopy
IUPAC	International Union of Pure and Applied Chemistry
LMCT	Ligand to Metal Charge Transfer
LPG	Liquefied Petroleum Gas
LVol-IB	Integral breadth-based volume weighted means crystallite size
MACS	Microwave-Assisted Combustion Synthesis
MCP	Multi Channel Plate
MO	Microwave Oven
MS	Mass Spectrometry, Mass Spectrometer
MW	Microwave
NIR	Near-Infrared
OCM	Oxydative Coupling of Methane
ODH	Oxydative Dehydrogenation
OD	Outer Diameter
PDF	Powder Diffractogram File

RF	Radio Frequency
SE	Secondary Electrons
SEM	Scanning Electron Microscopy
SEM	Secondary Electron Multiplier
SGP	Shell Gasification Process
SSITKA	Steady State Isotopic Transient Kinetic Analysis
STP	Standard Pressure
TAP	Temporal Analysis of Products
TEM	Transmission Electron Microscopy
TG(A)	Thermogravimetry (analysis)
UV	Ultraviolet
UV/vis	Ultraviolet/Visible Spectroscopy
XRD	X-ray Diffraction

List of Symbols

Fundamental constant

Symbol	Explanation	Numerical value
c	Speed of light in vacuum	$299792458 \text{ m s}^{-1}$
c_1	1st Planck radiation constant	$2\pi hc^2 = 3.74177153(17) \cdot 10^{-16} \text{ W m}^2$
c_2	2nd Planck radiation constant	$hc/k_B = 1.4387770(13) \cdot 10^{-2} \text{ m K}$
e	Elementary charge	$1.602176565(35) \cdot 10^{-19} \text{ A s}$
h	Planck constant	$6.62606957(29) \cdot 10^{-34} \text{ J Hz}^{-1}$
k_B	Boltzmann constant	$R/N_A = 1.3806488(13) \cdot 10^{-23} \text{ J K}^{-1}$
N_A	Avogadro constant	$R/k_B = 6.02214129(27) \cdot 10^{23} \text{ mol}^{-1}$
π	mathematical constant Pi	3.141592654
R	Universal gas constant	$N_A k_B = 8.3144621(75) \text{ J K}^{-1} \text{ mol}^{-1}$

Specific Symbols

Symbol	Explanation	Unit
A_{BET}, A_M	BET surface area, metal surface area	$[A] = \text{m}^2 \text{ g}^{-1}$
a_c	Specific surface area	$[a_c] = \text{m}^2$
A_c	Cross sectional area	$[A_c] = \text{m}^2$
a_m	Molecular cross-sectional area	$[a_m] = \text{m}^2$
C_k	Molar concentration of component k	$[C] = \text{mol l}^{-1}$
c_p	Average heat capacity	$[c_p] = \text{J K}^{-1} \text{ kg}^{-1}$
C/O ratio	Ratio between atomic carbon and oxygen in gas feed	$[C/O] = 1$
d	Diameter	$[d] = \text{m}$
D	Metal dispersion	$[D] = 1$
D_{km}	Mixture-average diffusion coefficient for species k	$[D_{km}] = \text{m}^2 \text{ s}^{-1}$
δ	Boundary layer thickness	$[\delta] = \text{m}$
ΔH^\ominus	Standard enthalpy (298 K, 101.3 kPa)	$[\Delta H^\ominus] = \text{J}$
E_a	Activation energy	$[E_a] = \text{J mol}^{-1} \text{ or kcal mol}^{-1}$
E_λ	Spectral, hemispherical emissive power	$[E_\lambda] = \text{W m}^{-2} \mu\text{m}^{-1}$
ϵ	Emissivity	$[\epsilon] \leq 1$
ϵ	Porosity	$[\epsilon] \leq 1$
\vec{e}_z	Unit vector	$[\vec{e}_z] = 1$
F	Molar flow rate	$[F] = \text{mol min}^{-1}$
f_{active}	ratio of active metal surface area and support surface area	$f_{\text{active}} = \text{m}^2 \text{ m}^{-2}$
γ	Volume fraction of bulk gas	$[\gamma] = \text{m}^3 \text{ m}^{-3}$
Γ	Surface site density	$[\Gamma] = \text{mol m}^{-2}$
h_k	Enthalpy	$[h_k] = \text{J kg}^{-1}$
Φ	Electric potential	$[\Phi] = \text{V}$
j_k	Flux of species k due to molecular diffusion	$[j_k] = \text{kg m}^{-2} \text{ s}^{-1}$
κ	Extinction coefficient	$[\kappa] = \text{m}^{-1}$
k_i	Reaction rate of component i	$[k_i] = \text{mol s}^{-1} \text{ m}^{-1}$
K_k	Mass transfer coefficient	$[K_k] = \text{m s}^{-1}$
k_k^m	Mass transport coefficient of component k	$[k_k^m] = \text{m s}^{-1}$
K_T	Heat transfer coefficient	$[K_T] = \text{W m}^{-2} \text{ K}^{-1}$
I	Intensity	$[I] = \text{counts}$
l	Characterisitic length	$[l] = \text{m}$

L	Length	$[L] = \text{m}$
λ	Wavelength	$[\lambda] = \text{nm}$
λ	Average thermal conductivity	$[\lambda] = \text{W m}^{-1} \text{K}^{-1}$
LVol-IB	Integral breath-based volume weighted mean crystallite size	$[\text{LVol-IB}] = \text{m}$
m	Mass	$[m] = \text{kg}$
M	Molar mass	$[M] = \text{g mol}^{-1}$
m/e or m/z	Mass to charge ratio	$[m/e] = [m/z] = 1$
μ	Linear attenuation coefficient	$[\mu] = \text{cm}^{-1}$
μ	Average dynamic viscosity	$[\mu] = \text{kg m}^{-1} \text{s}^{-1}$
n	Amount of substance	$[n] = \text{mol}$
$\tilde{\nu}$	Wavenumber	$[\tilde{\nu}] = \text{cm}^{-1}$
ν_i	Stoichiometric coefficient of component i	$[\nu_i] = 1$
N_u	Nusselt number	$N_u = \frac{K_T l}{\lambda}$
ω	Angular frequency	$[\omega] = \text{s}^{-1}$
p	Pressure	$[p] = \text{Pa, atm, or bar}$
P_r	Prandtl number	$= \frac{\mu c_p}{\lambda}$
Q	Intensity ratio	$[Q] = 1$
r	Radius	$[r] = \text{m}$
Re	Reynolds number	$Re = \frac{\rho v_z l}{\mu}$
r_j	Reaction rate of component j	$[r_j] = \text{mol s}^{-1} \text{m}^{-1}$
R_i	Production rate of component i	$[R_i] = \text{mol s}^{-1} \text{m}^{-1}$
ρ	Density	$[\rho] = \text{kg m}^3$
S_{BET}	BET surface area	$[S] = \text{m}^2 \text{g}^{-1}$
S_c	Schmidt number	$S_c = \frac{\mu}{\rho D_{km}}$
S_h	Sherwood number	$S_h = \frac{K_k l}{D_k m}$
S_i	Selectivity to component i	$[S_i] = \%$
\dot{s}_k	Molar rate of production per unit area for species k due to surface chemistry	$[\dot{s}_k] = \text{mol m}^{-2} \text{s}^{-1}$
$\sigma_k(n)$	Number of sites occupied by k	$[\sigma_k(n)] = \text{mol mol}^{-1}$
S_v	Geometric foam surface area to total gas-phase volume	$[S_v] = \text{m}^{-1}$
t	Time	$[t] = \text{s}$
T	Temperature	$[T] = \text{K or } ^\circ\text{C}$
τ	Dimensionless parameter	$[\tau] = 1$
τ	Tortuosity of the foam	$[\tau] = \text{m m}^{-1}$
θ	Angle	$[\theta] = \text{sr}$
θ_k	Site fraction of species k on Pt surface	$[\theta] = \text{mol mol}^{-1}$
u	Velocity	$[u] = \text{m s}^{-1}$
U	Potential difference	$[U] = \text{V}$
V	RF voltage (quadrupole)	$[V] = \text{V}$
V	Volume	$[V] = \text{m}^3$
\dot{V}	Volume flow rate	$[\dot{V}] = \text{m}^3 \text{s}^{-1}$
v_m	Volume of adsorbed probe molecules per gramm sample	$[v_m] = \text{ml g}^{-1}$
v_z	Velocity in z direction	$[v_z] = \text{m s}^{-1}$
F	Chemisorption stoichiometry factor	$[F] = 1$
\dot{w}_k	Molar rate of production per unit volume of species k by homogeneous chemistry	$[\dot{w}_k] = \text{mol m}^{-3} \text{s}^{-1}$
\bar{W}	Average molecular weight	$[\bar{W}] = \text{kg mol}^{-1}$
W_k	Molecular mass of species k	$[W_k] = \text{kg kmol}^{-1}$
wt	Metal loading of a catalyst	$0 < [wt] \leq 1$
x	Cartesian coordinate	$[x] = 1$
x_k or X_k	Mole fraction of component k	$[x_k] = [X_k] = \text{mol mol}^{-1}$
X_k	Conversion of component k	$[X_k] = \%$
y	Cartesian coordinate	$[y] = 1$
y_k or Y_k	Mass fraction of species k	$[y_k] = [Y_k] = \text{kg kg}^{-1}$
z	Axial coordinate	$[z] = m$
z	Cartesian coordinate	$[z] = 1$

$Z_k(n)$ Site fraction of species k on surface n $[Z_k(n)] = \text{mol mol}^{-1}$

List of Figures

1.1	Suggested reaction pathways in methane CPO. Figure adapted from [52].	14
3.1	Nitrogen adsorption-desorption isotherms typical for the investigated catalyst systems. Top: A type II isotherm as it is observed for the α -Al ₂ O ₃ supported catalysts. Bottom: A type IV isotherm as it is observed for γ -Al ₂ O ₃ supported catalysts.	22
3.2	Typical chemisorption isotherms from CO adsorption at 40 °C. Black trace: first adsorption step (sum of reversible and irreversible chemisorption). Red trace: second adsorption step after evacuating at adsorption temperature (reversibly chemisorbed CO part). Green trace: irreversibly chemisorbed CO fraction, adsorbed volume can be read from the ordinate at the plateau.	24
3.3	Schematic illustration of the principle responses of an electron beam interacting with a sample in an EM. Figure adapted from [112]	26
3.4	Schematic of a linear quadrupole mass analyzer. Red: Illustration of the wobbling ion trajectory of a transmitting ion. Figure adapted from [117] (modified).	29
3.5	Schematic of a linear channel multiplier (single channel of a MCP) and a curved channel electron multiplier (channeltron). Figure adapted from [117] (modified).	30
4.1	Photos of the ceramic foams impregnated by glycerol-chelated Pt precursor: (a) snapshots recorded in time intervals of 20 s during microwave-assisted combustion synthesis; (b) thermographs recorded by an IR thermocamera (temperature range 25 – 370 °C) during the synthesis in a microwave oven operated at 700 W. (0 s) foam impregnated by the precursor solution, (30 s) foam coated by brownish gel-like film, (60 s) in situ carburized intermediate, and (130 s) Pt-coated ceramic foam.	40
4.2	Temperature profiles recorded by IR pyrometry (temperature range 350–1000 °C, fiber probe) during MACS after (a) one impregnation step with 0.6 wt% Pt loading, (b) two impregnation steps with 1.5 wt% Pt loading, and (c) three impregnation steps with 2.0 wt% Pt loading.	41
4.3	(a) UV/vis spectra of (a) initial transparent Pt(NH ₃) ₄ (NO ₃) ₂ /C ₃ H ₈ O ₃ precursor solution and (b) brownish gel-like films formed on corundum foam impregnated by the precursor after drying in a microwave oven at 700 W for 30 s. (b, c) TEM images of Pt nanoparticles in the brownish intermediate formed during the MACS process. (d) EDX spectrum of the nanoparticles identifying them clearly as Pt (Cu peaks stem from the TEM grid).	42
4.4	Low- and high-magnification SEM images of the carburized intermediate product obtained during the combustion synthesis by microwave heating for 1 min. The sample shows the formation of a uniform carbonaceous layer on Pt as revealed by the overview EDX spectra.	43
4.5	TG plots (in synthetic air) of as-prepared 2 % Pt/ α -Al ₂ O ₃ catalyst (top curve) and the carburized intermediate (bottom curve) during the microwave synthesis for 1 min. The heating rate is 2 °C min ⁻¹ . MS spectra (dashed lines) show evolved water ($m/e = 18$) and CO ₂ ($m/e = 44$) during the decomposition of the carburized intermediate.	44
4.6	Schematic representation of the sequence of events during MACS catalyst synthesis.	45
4.7	Representative pictures of (a-c) uncoated ceramic foams (Reticel Hi-Tech Ceramics), (d-f) 0.6 % Pt/ α -Al ₂ O ₃ -coated foam prepared by conventional wet impregnation [172]; (g-j) 0.6 % Pt/ α -Al ₂ O ₃ foam catalyst prepared by the MACS method during 3 min. (e, h) BSE images: Pt-bright, Al ₂ O ₃ -gray. (k) Overview EDX spectra and (l) particle size distribution histogram of the corresponding catalyst prepared by the MACS method.	46
4.8	HRTEM micrographs and EDX spectrum (powder preparation) of the 0.6 % Pt/ α -Al ₂ O ₃ foam catalyst prepared by the MACS method during 3 min. The copper peaks in the EDX spectrum stem from the TEM grid used.	47
4.9	Comparison of XRD patterns with Rietveld fitting of 0.6 % Pt/ α -Al ₂ O ₃ foam catalysts prepared by (a) the MACS method during 6 min and (b) wet impregnation from Pt(NH ₃) ₄ (NO ₃) ₂ followed by drying, conventional calcination, and reduction at 600 °C [172].	48

5.1	Principle of spatially resolved measurement of i) kinetic data, ii) gas temperature and iii) solid temperature.	52
5.2	Annotated 3D reactor drawing.	53
5.3	Spatial profile measurements for methane oxidation on 0.6 wt% Pt coated 45 ppi α -Al ₂ O ₃ foam catalysts. Gas flow: 911 ml min ⁻¹ CH ₄ , 228 ml min ⁻¹ O ₂ , 858 ml min ⁻¹ Ar. C/O = 2.0. Autothermal operation. Front heat shield -10000 μ m \rightarrow 0 μ m, catalyst section 0 μ m \rightarrow 10240 μ m (Pt foam 1) and 10240 μ m \rightarrow 20460 μ m (Pt foam 2), back heat shield 20460 μ m \rightarrow 30000 μ m.	56
5.4	Oxygen profiles from Fig. 5.3 superimposed. Linearity and pressure independence indicate zeroth order kinetics in the oxidation zone.	57
5.5	Spatial profile measurements for methane oxidative coupling on Li/MgO. Catalyst section formed by two 0.8 wt% Li/MgO coated α -Al ₂ O ₃ foams. Gas flow CH ₄ /O ₂ /Ar = 25.6/6.4/8.0 ml min ⁻¹ . Reactor temperature by external heating 780 °C.	58
6.1	Schematic of spatial profile measurements.	60
6.2	Surface temperature and species profiles through a catalyst bed of 1 wt% Pt-coated γ -alumina spheres (sphere diameter: 2.5 mm; gas feed: CH ₄ /O ₂ /Ar = 2010/628/2362 mln min ⁻¹ ; C/O = 1.6; reactor pressure of 1 bar).	61
6.3	Surface temperature and species profiles through a catalyst stack of two 0.6 wt% Pt-coated α -alumina foams (80 ppi, each 10 mm length, OD = 16.5 mm diameter; gas feed: CH ₄ /O ₂ /Ar = 911/228/858 mln min ⁻¹ ; C/O = 2.0; reactor pressure of 15 bar.	62
6.4	Surface temperature and species profiles through a polycrystalline Pt tube of 100 mm length, ID = 4.4 mm, OD = 5 mm (gas feed: CH ₄ /O ₂ /Ar = 600/300/100 mln min ⁻¹ ; C/O = 2.0; reactor pressure of 1 bar).	62
7.1	Conventional 'in-out' measurements in a continuous flow tubular reactor.	66
7.2	Principle of species, temperature and spectroscopic profile measurements in a continuous flow tubular reactor.	68
7.3	Laser drilled side sampling orifice in 700 μ m fused silica capillary.	68
7.4	Illumination and angular acceptance of a properly beveled optical fiber for spatially resolved Raman spectroscopy.	70
7.5	Species and gas temperature profiles for methane CPO on a 5 wt% Rh coated 80 ppi foam catalyst (α -Al ₂ O ₃). Total inlet gas stream $\dot{V}_{\text{CH}_4} + \dot{V}_{\text{O}_2} + \dot{V}_{\text{Ar}} = 4700$ mln min ⁻¹ at 273 K. Inlet stoichiometry C/O = $\dot{V}_{\text{CH}_4}/(2 \cdot \dot{V}_{\text{O}_2}) = 1.0$ and $\dot{V}_{\text{Ar}}/\dot{V}_{\text{O}_2} = 3.76$ (80 ppi, $L_f = 9.6$ mm, $d_f = 17$ mm, porosity $\varepsilon = 0.7$). Catalyst foam between dotted lines.	71
7.6	Spatial surface temperature profiles and species evolution through an α -Al ₂ O ₃ foam monolith coated with 1 wt% Pt (80 ppi, $L_f = 19.4$ mm, $d_f = 15.5$ mm, porosity $\varepsilon = 0.7$). Effect of reactor pressure. A: 1 bar, B: 15 bar. Gas feed of $\dot{V}_{\text{Ar}}/\text{CH}_4/\text{O}_2 = 1718/1826/456$ mln min ⁻¹ , respectively a total gas feed of $\dot{V}_{\text{total}} = 4000$ mln min ⁻¹	72
7.7	Determination of $k_c \cdot a_c$ by fitting Eq. 7.14 to the experimental data in Fig. 7.5.	73
7.8	Spatial surface temperature profiles and species evolution through a 1 wt% Pt coated α -Al ₂ O ₃ foam monolith at constant reactor pressure of $p = 1$ bar. Effect of flow rate. Gas feeds: A: $\dot{V}_{\text{Ar}}/\text{CH}_4/\text{O}_2 = 1112/592/296$ mln min ⁻¹ , i.e. total gas feed of $\dot{V}_A = 2000$ mln min ⁻¹ ; B: $\dot{V}_{\text{Ar}}/\text{CH}_4/\text{O}_2 = 2224/1184/592$ mln min ⁻¹ , i.e. total gas feed of $\dot{V}_B = 4000$ mln min ⁻¹ . The shape of the temperature profile in (A) is probably somewhat distorted by irregularities in the pore structure along the scan line.	77
7.9	Microscopic picture of Pt foil section prior reaction light-off (A) and after reaction light-off (B). C: In-situ Raman spectra of D and G band of carbonaceous surface deposits formed after reaction light-off.	78
7.10	Experimental reactor profiles (scatter) and boundary layer numerical simulations (dashed lines) of gas phase methane oxidative coupling. Reactor pressure $p = 8$ bar, reactant stoichiometric C/O = 4.0, $\dot{V}_{\text{CH}_4} = 3200$ mln min ⁻¹ , $\dot{V}_{\text{O}_2} = 400$ mln min ⁻¹ , $\dot{V}_{\text{Ar}} = 400$ mln min ⁻¹ , $\dot{V}_{\text{total}} = 4000$ mln min ⁻¹	79
7.11	Left: Species and catalyst temperature profiles for ethane ODH on MoO _x coated α -Al ₂ O ₃ spheres. Feed gas: $\dot{V}_{\text{C}_2\text{H}_6} = 4$ mln min ⁻¹ , $\dot{V}_{\text{O}_2} = 4$ mln min ⁻¹ , $\dot{V}_{\text{Ar}} = 58$ mln min ⁻¹ . Reactor pressure $p = 1$ bar. Right: Photograph of the sphere bed after 3 h time on stream.	80
7.12	A: Graphite and sulfur cylinders for demonstrating the principle of spatially resolved Raman spectroscopy. B: Optical fiber sticking out of the sampling capillary which was inserted in the graphite - sulfur stack. C: Assembly mounted in the profile reactor. D: Spatially resolved Raman in operation - fiber tip in the center of the sulfur cylinder.	81

7.13	Left: Single Raman spectra of the fiber tip in air (blank measurement, dotted line). Raman spectrum with fiber tip positioned in the sulfur cylinder (solid line). Raman spectrum of sulfur calculated as difference (inset). Right: Background corrected Raman spectra measured around the graphite – sulfur transition.	82
7.14	Determination of position accuracy and resolution of spatially resolved Raman measurements. Upper Panels: Peak areas of Raman peaks at 446 cm ⁻¹ and 480 cm ⁻¹ plotted against tip position with the fiber tip outside of the sampling capillary (left) and inside of the sampling capillary (right). Lower panels: First derivatives (points) fitted by a Gaussian function (solid line).	83
8.1	Comparison of two spatially resolved species and gas phase temperature profiles for methane CPO on rhodium and platinum. Top: 5 wt% Rh supported on an 80 ppi α -alumina foam monolith of about ~ 10 mm length. Bottom: 5 wt% Pt supported on an analog foam monolith. Total inlet gas feed in both cases $\dot{V}_{\text{CH}_4} + \dot{V}_{\text{O}_2} + \dot{V}_{\text{Ar}} = 4700$ mln min ⁻¹ at 273 K. Inlet stoichiometry $C/O = \dot{V}_{\text{CH}_4}/(2 \cdot \dot{V}_{\text{O}_2}) = 1.0$ and $\dot{V}_{\text{Ar}}/\dot{V}_{\text{O}_2} = 3.76$. Catalyst foam between first and last dotted line. Length of oxidation zone indicated by second dotted line. Data reproduced from [7] with permission by Elsevier.	87
8.2	Background correction of in-situ Raman spectra of carbonaceous deposits on a platinum foil during CPO of methane recorded at 800 °C reactor temperature. Black: Raman raw data, Red: estimated polynomial for continuum background by black body radiation from the sample adapted from Gornushkin et al. [201] and Blue: background corrected Raman spectrum.	88
8.3	Top: Fit of two baseline separated carbon peaks by two Lorentzian-shaped bands [202]. Bottom: Fit of two broad overlapping peaks by combination of four Lorentzian-shaped and one Gaussian-shaped bands after Sadezky et al. [90].	89
8.4	Light-optical micrograph of the polycrystalline platinum foil serving as model catalyst in methane CPO. The bright laser spots indicate the Raman sampling positions. Top: Platinum foil after oxidative and reductive cleaning as described in Section 8.2. Bottom: Platinum foil under CPO conditions at T = 800 °C reactor cell temperature.	91
8.5	Molar flow rates of reactants and products during temperature programmed methane CPO. Dotted lines indicate reactor temperature set points. Dashed lines indicate time coordinates where a corresponding Raman spectra was recorded.	92
8.6	Evolution of carbon Raman bands as function of reactor cell temperature. Dots: normalized measured Raman intensity, lines: fit according to Sadezky et al. [90].	92
8.7	Reactant and product molar flow rates measured during the in-situ Raman mapping experiment under methane CPO conditions. Dotted vertical lines indicate the time coordinate where Raman spectra were recorded. Positions correlate with Fig. 8.4.	96
8.8	Top: Selected in-situ Raman spectra recorded during methane CPO on a polycrystalline platinum foil. Spectra are normalized to the G band maximum for better comparability. Bottom: Cloud plot of relative D band intensity as a function of observed gray level in the light-optical micrographs of Fig. 8.4 right. Positions correlate with Fig. 8.4.	98
9.1	Left: Photograph of catalyst stack before reaction test, with one half foam monolith showing the centerline channel. Right: Foam structure visualization of the reconstruction of an intact foam monolith from X-ray μ -CT (overview and intermediate cut). For better visualization μ -CTs from a 45 ppi foam are shown.	102
9.2	Sketch of volume element illustrating the modeling domains. δ strongly exaggerated for illustration purpose ($\delta \ll r_h$).	103
9.3	Mole fractions of CH ₄ and O ₂ with catalyst surface temperatures (top panels), mole fractions of H ₂ and CO (center panels), and mole fractions of H ₂ O and CO ₂ (bottom panels) comparing prediction of the microkinetic models (dashed lines) of Mechanism 1 [70, 71, 89] (left panels) and Mechanism 2 [72, 73] (right panels) with experimental reactor profiles (symbols). Reactor in autothermal operation with a gas feed of CH ₄ /O ₂ /Ar = 592/296/1112 mln min ⁻¹ (C/O = 1.0).	108
9.4	Mole fractions of CH ₄ and O ₂ with catalyst surface temperatures (top panels), mole fractions of H ₂ and CO (center panels), and mole fractions of H ₂ O and CO ₂ (bottom panels) comparing prediction of the microkinetic models (dashed lines) of Mechanism 1 [70, 71, 89] (left panels) and Mechanism 2 [72, 73] (right panels) with experimental reactor profiles (symbols). Reactor in autothermal operation with a gas feed of CH ₄ /O ₂ /Ar = 1184/592/2224 mln min ⁻¹ (C/O = 1.0).	109

9.5	Surface mole fractions of Pt(s), CO(s), and CO ₂ (s) (top panels), surface mole fractions of C(s), CH(s), CH ₂ (s), and CH ₃ (center panels), and surface mole fractions of O(s) and OH(s) (bottom panel) comparing the predictions of the microkinetic models (dashed lines) of Mechanism 1 [70,71,89] (left panels) and Mechanism 2 [72,73]. Corresponding gas phase species and reaction conditions in Fig. 9.3.	110
9.6	Surface mole fractions of Pt(s), CO(s), and CO ₂ (s) (top panels), surface mole fractions of C(s), CH(s), CH ₂ (s), and CH ₃ (center panels), and surface mole fractions of O(s) and OH(s) (bottom panel) comparing the predictions of the microkinetic models (dashed lines) of Mechanism 1 [70,71,89] (left panels) and Mechanism 2 [72,73]. Corresponding gas phase species and reaction conditions in Fig. 9.4.	111
9.7	Mole fractions of CH ₄ and O ₂ with catalyst surface temperatures (top panel), mole fractions of H ₂ and CO (center panel), and mole fractions of H ₂ O and CO ₂ (bottom panel). Reactor in autothermal operation with a gas feed of CH ₄ /O ₂ /Ar = 592/296/1112 mln min ⁻¹ (C/O = 1.0).	112
9.8	Detection of carbonaceous deposits by Raman microscopy after reaction test of two half monoliths. Axial position z along the capillary channel centerline.	113
9.9	Electron micrographs comparing the as prepared Pt coated foam monolith with the monolith after reaction test at an axial position of about 4 mm. A: SE image (HV, 5 kV) as prepared. B: SE image (HV, 1 kV) as prepared. C: SE image (HV, 5 kV) after reaction test. D: BSE image (Low vacuum (60 Pa H ₂ O), 15 kV) after reaction test.	114
9.10	Plot of particle size distributions for Fig. 9.11D, 9.11G, and 9.11J with a bin width of 5 nm.	115
9.11	Selected electron micrographs from the centerline channel of a half monolith. A: Overview composite picture of the centerline channel with axial position (BSE image, Low vacuum (60 Pa H ₂ O), 15 kV). B: SE image (HV, 1.5 kV) of the end section of the catalyst foam. Filament-like and agglomerated carbonaceous deposits covering the catalyst surface. C, D: Magnified SE/BSE image (Low vacuum (60 Pa H ₂ O), 15 kV) of some of the agglomerated carbon deposits. E: SE image (HV, 1.5 kV) of the middle section of the catalyst bed. Filament-like structured carbon covering the catalyst surface. F, G: Magnified SE/BSE image (Low vacuum (60 Pa H ₂ O), 15 kV) of some of the filament-like carbon deposits. H: SE image (HV, 1.5 kV) of the front section of the catalyst foam, prior to the kink position. I, J: Magnified SE/BSE image (Low vacuum (60 Pa H ₂ O), 15 kV) of clean catalyst surface. No carbon species visible.	117
A.1	Setup for pyrometer calibration to thermocouple in a graphite monolith inside the isothermal zone of a tube furnace.	123
A.2	Top: Temperature reading of the pyrometer T_{py} by variation of k at a given graphite monolith temperature measured by a type K thermocouple T_{tc} . Bottom: k optimal in the temperature range of $400 \leq T \leq 1100$ °C.	124
A.3	Top: Photograph of test stack assembly to verify independence of the pyrometer from spectral emissivity after calibration. Upper and lower monolith made from graphite. Center monolith made from alumina. Bottom: Temperature profile along the monolith intersection from alumina to graphite in the furnace center zone. Furnace power set 450 W.	125
B.1	MS calibration line for CH ₄ . Black symbols: Measured ratio between methane and argon peak area ($(m/z = 15)/(m/z = 40)$), red line: linear regression of measured data, green lines: confidence band (95 %), blue lines: prediction band (95 %).	128
B.2	MS calibration line for H ₂ (top) and O ₂ (bottom). Black symbols: Measured ratio between analyte and argon peak area (m/z values see at ordinate), red line: linear regression of measured data, green lines: confidence band (95 %), blue lines: prediction band (95 %).	129
B.3	MS calibration line for CO (top) and CO ₂ (bottom). Black symbols: Measured ratio between analyte and argon peak area (m/z values see at ordinate), red line: linear regression of measured data, green lines: confidence band (95 %), blue lines: prediction band (95 %).	130
D.1	Example of continuum background correction, intermediate solution with $N = 5$ and $P = 5$. All five sub-spectra/groups are of equal size. Note preselected green area, not considered for background estimation, divides Group 3. Grey trace: Raman raw data, Open black circles: Background data points selected for fitting procedure, Red trace: Estimated continuum background, Blue trace: Background corrected Raman spectrum.	144
D.2	Result of screening the parameter space of the background correction algorithm. Quality of fit from all background data points as function of P and N	144

E.1	Reactor profile of #10253: Total gas feed of 2000 mln min ⁻¹ @ C/O = 0.6 (top) and 0.8 (bottom)	151
E.2	Reactor profile of #10253: Total gas feed of 2000 mln min ⁻¹ @ C/O = 1.0 (top) and 1.2 (bottom)	152
E.3	Reactor profile of #10253: Total gas feed of 2000 mln min ⁻¹ @ C/O = 1.4 (top) and 1.6 (bottom)	153
E.4	Reactor profile of #10253: Total gas feed of 2000 mln min ⁻¹ @ C/O = 1.8 (top) and 2.0 (bottom)	154
E.5	Reactor profile of #10253: Total gas feed of 4000 mln min ⁻¹ @ C/O = 0.6 (top) and 0.8 (bottom)	155
E.6	Reactor profile of #10253: Total gas feed of 4000 mln min ⁻¹ @ C/O = 1.0 (top) and 1.2 (bottom)	156
E.7	Reactor profile of #10253: Total gas feed of 4000 mln min ⁻¹ @ C/O = 1.4 (top) and 1.6 (bottom)	157
E.8	Reactor profile of #10253: Total gas feed of 4000 mln min ⁻¹ @ C/O = 1.8 (top) and 2.0 (bottom)	158
E.9	Reactor profile of #10255: Total gas feed of 2000 mln min ⁻¹ @ C/O = 0.8	159
E.10	Reactor profile of #10255: Total gas feed of 2000 mln min ⁻¹ @ C/O = 1.0 (top) and 1.2 (bottom)	160
E.11	Reactor profile of #10255: Total gas feed of 2000 mln min ⁻¹ @ C/O = 1.4 (top) and 1.6 (bottom)	161
E.12	Reactor profile of #10255: Total gas feed of 2000 mln min ⁻¹ @ C/O = 1.8 (top) and 2.0 (bottom)	162
E.13	Reactor profile of #10255: Total gas feed of 4000 mln min ⁻¹ @ C/O = 0.8	163
E.14	Reactor profile of #10255: Total gas feed of 4000 mln min ⁻¹ @ C/O = 1.0 (top) and 1.2 (bottom)	164
E.15	Reactor profile of #10255: Total gas feed of 4000 mln min ⁻¹ @ C/O = 1.4 (top) and 1.6 (bottom)	165
E.16	Reactor profile of #10255: Total gas feed of 4000 mln min ⁻¹ @ C/O = 1.8 (top) and 2.0 (bottom)	166
E.17	Reactor profile of #10255: Total gas feed of 2000 mln min ⁻¹ @ C/O = 2.0 and a reactor pressure of 1 atm (top) and 5 bar (bottom)	167
E.18	Reactor profile of #10255: Total gas feed of 2000 mln min ⁻¹ @ C/O = 2.0 and a reactor pressure of 10 bar (top) and 15 bar (bottom)	168
E.19	Reactor profile of #10256: Total gas feed of 4000 mln min ⁻¹ @ C/O = 2.0 and a reactor pressure of 1 atm (top) and 5 bar (bottom)	170
E.20	Reactor profile of #10256: Total gas feed of 4000 mln min ⁻¹ @ C/O = 2.0 and a reactor pressure of 10 bar (top) and 15 bar (bottom)	171
E.21	Reactor profile of #10774: Total gas feed of 2000 mln min ⁻¹ @ C/O = 0.8	172
E.22	Reactor profile of #10774: Total gas feed of 2000 mln min ⁻¹ @ C/O = 1.0 (top) and 1.2 (bottom)	173
E.23	Reactor profile of #10774: Total gas feed of 2000 mln min ⁻¹ @ C/O = 1.4 (top) and 1.6 (bottom)	174
E.24	Reactor profile of #10774: Total gas feed of 2000 mln min ⁻¹ @ C/O = 1.8 (top) and 2.0 (bottom)	175
E.25	Reactor profile of #10774: Total gas feed of 4000 mln min ⁻¹ @ C/O = 0.8	176
E.26	Reactor profile of #10774: Total gas feed of 4000 mln min ⁻¹ @ C/O = 1.0 (top) and 1.2 (bottom)	177
E.27	Reactor profile of #10774: Total gas feed of 4000 mln min ⁻¹ @ C/O = 1.4 (top) and 1.6 (bottom)	178
E.28	Reactor profile of #10774: Total gas feed of 2000 mln min ⁻¹ @ C/O = 1.8 (top) and 2.0 (bottom)	179
E.29	Reactor profile of #10774: Total gas feed of 2000 mln min ⁻¹ @ C/O = 2.0 and a reactor pressure of 1 atm (top) and 5 bar (bottom)	180
E.30	Reactor profile of #10774: Total gas feed of 2000 mln min ⁻¹ @ C/O = 2.0 and a reactor pressure of 10 bar (top) and 15 bar (bottom)	181
E.31	Reactor profile of #10774: Total gas feed of 4000 mln min ⁻¹ @ C/O = 2.0 and a reactor pressure of 1 atm (top) and 5 bar (bottom)	182
E.32	Reactor profile of #10774: Total gas feed of 4000 mln min ⁻¹ @ C/O = 2.0 and a reactor pressure of 1 bar (top) and 15 bar (bottom)	183
E.33	Reactor profile of #12036: Total gas feed of 500 mln min ⁻¹ @ C/O = 0.8	184

E.34	Reactor profile of #12036: Total gas feed of 500 mln min ⁻¹ @ C/O = 1.0 (top) and 1.2 (bottom)	185
E.35	Reactor profile of #12036: Total gas feed of 500 mln min ⁻¹ @ C/O = 1.4 (top) and 1.6 (bottom)	186
E.36	Reactor profile of #12036: Total gas feed of 500 mln min ⁻¹ @ C/O = 1.8 (top) and 2.0 (bottom)	187
E.37	Reactor profile of #12036: Total gas feed of 1000 mln min ⁻¹ @ C/O = 0.8	188
E.38	Reactor profile of #12036: Total gas feed of 1000 mln min ⁻¹ @ C/O = 1.0 (top) and 1.2 (bottom)	189
E.39	Reactor profile of #12036: Total gas feed of 1000 mln min ⁻¹ @ C/O = 1.4 (top) and 1.6 (bottom)	190
E.40	Reactor profile of #12036: Total gas feed of 500 mln min ⁻¹ @ C/O = 1.8 (top) and 2.0 (bottom)	191

List of Tables

1.1	Energy density of some important fuels taken from [35,36].	12
4.1	Characterization of Pt Deposited on 80 ppi Corundum Foams by the Conventional Method (CM) and MACS Preparation with Various Synthesis Times and Pt Loadings.	41
7.1	Estimation of the relative impact of O ₂ film transport limitation on methane CPO in Rh and Pt foam catalysts.	75
7.2	H ₂ selectivity at 50 % O ₂ conversion determined from the spatial reactor profiles.	75
8.1	Fitting parameters for quantitative spectral analysis of carbon Raman bands formed during temperature programmed methane CPO on a platinum foil according to the five band fitting procedure proposed by Sadezky et al. [90].	94
9.1	Catalyst characterization.	105
9.2	Product selectivities of experimental and simulated reactor performance at catalyst bed end (axial position of 20 mm).	106
9.3	Integral breadth-based volume weighted mean Pt crystallite size of powdered foam monoliths with a nominal Pt loading of 1 wt%. XRD analysis after reaction tests.	115
9.4	Deutschmann surface reaction mechanism of C1 oxidation on Pt adopted from [70, 71, 89], changed.	118
9.5	Vlachos surface reaction mechanism of C1 oxidation on Pt adopted from [72, 73], changed.	119
E.1	Summary of catalyst properties investigated in this thesis.	149
E.2	Gas feeds for catalytic testing at a given total flow rate.	150
E.3	List of profiles of foam monolith #10253	150
E.4	List of profiles of foam monolith #10255.	159
E.5	List of profiles of foam monolith #10256.	169
E.6	List of profiles of foam monolith #10774.	172
E.7	List of profiles of Pt catalytic wall reactor #12036.	184

Bibliography

- [1] D. A. Hickman, L. D. Schmidt, Production of Syngas by Direct Catalytic Oxidation of Methane, *Science* 259 (5093) (1993) 343–346. doi:10.1126/science.259.5093.343.
- [2] D. Dalle Nogare, N. J. Degenstein, R. Horn, P. Canu, L. D. Schmidt, Modeling spatially resolved profiles of methane partial oxidation on a Rh foam catalyst with detailed chemistry, *J. Catal.* 258 (1) (2008) 131–142. doi:10.1016/j.jcat.2008.06.006.
- [3] D. Dalle Nogare, N. J. Degenstein, R. Horn, P. Canu, L. D. Schmidt, Modeling Spatially Resolved Data of Methane Catalytic Partial Oxidation on Rh Foam Catalyst at Different Inlet Compositions and Flow Rates, *J. Catal.* 277 (2) (2011) 134–148. doi:10.1016/j.jcat.2010.10.020.
- [4] A. Donazzi, M. Maestri, B. C. Michel, A. Beretta, P. Forzatti, G. Groppi, E. Tronconi, L. D. Schmidt, D. G. Vlachos, Microkinetic Modeling of Spatially Resolved Autothermal CH_4 Catalytic Partial Oxidation Experiments over *Rh*-coated Foams., *J. Catal.* 275 (2010) 270–279. doi:10.1016/j.jcat.2010.08.007.
- [5] R. Horn, N. J. Degenstein, K. A. Williams, L. D. Schmidt, Spatial and temporal profiles in millisecond partial oxidation processes, *Catal. Lett.* 110 (3-4) (2006) 169–178. doi:10.1007/s10562-006-0117-8.
- [6] R. Horn, K. A. Williams, N. J. Degenstein, L. D. Schmidt, Syngas by catalytic partial oxidation of methane on rhodium: Mechanistic conclusions from spatially resolved measurements and numerical simulations, *J. Catal.* 242 (1) (2006) 92–102. doi:10.1016/j.jcat.2006.05.008.
- [7] R. Horn, K. A. Williams, N. J. Degenstein, A. Bitsch-Larsen, D. Dalle Nogare, S. A. Tupy, L. D. Schmidt, Methane catalytic partial oxidation on autothermal Rh and Pt foam catalysts: Oxidation and reforming zones, transport effects, and approach to thermodynamic equilibrium, *J. Catal.* 249 (2) (2007) 380–393. doi:10.1016/j.jcat.2007.05.011.
- [8] R. Horn, K. A. Williams, N. J. Degenstein, L. D. Schmidt, Mechanism of H_2 and CO formation in the catalytic partial oxidation of CH_4 on Rh probed by steady state spatial profiles and spatially resolved transients, *Chem. Eng. Sci.* 62 (5) (2007) 1298–1307. doi:10.1016/j.ces.2006.11.030.
- [9] K. A. Williams, R. Horn, L. D. Schmidt, Performance of Mechanisms and Reactor Models for Methane Oxidation on Rh, *AIChE J.* 53 (8) (2007) 2097–2113. doi:10.1002/aic.11244.
- [10] A. Bitsch-Larsen, R. Horn, L. D. Schmidt, Catalytic partial oxidation of methane on rhodium and platinum: Spatial profiles at elevated pressure, *Appl. Catal., A* 348 (2) (2008) 165–172. doi:10.1016/j.apcata.2008.06.036.
- [11] O. Korup, R. Schlögl, R. Horn, Carbon formation in catalytic partial oxidation of methane on platinum: Model studies on a polycrystalline Pt foil, *Catal. Today* 181 (1) (2012) 177–183. doi:10.1016/j.cattod.2011.04.051.
- [12] G. Centi, F. Trifiro, F. Cavani, *Selective Oxidation by Heterogeneous Catalysis*, 1st Edition, Fundamental and Applied Catalysis, Kluwer Academic/Plenum Publishers, New York, 2001.
- [13] Organization of the Petroleum Exporting Countries (OPEC), *OPEC Annual Statistical Bulletin 2010/2011* (2011).
URL http://www.opec.org/opec_web/static_files_project/media/downloads/publications/ASB2010_2011.pdf
- [14] T. S. Ahlbrandt, *Fututre Petroleum Energy Resources of the World*, *Int. Geol. Rev.* 44 (12) (2002) 1092–1104. doi:10.2747/0020-6814.44.12.1092.

- [15] R. A. Kerr, Peak Oil Production May Already Be Here, *Science* 331 (6024) (2011) 1510–1511. doi:10.1126/science.331.6024.1510.
- [16] BP, BP Statistical Review of World Energy June 2011 (2011).
URL http://www.bp.com/assets/bp_internet/globalbp/globalbp_uk_english/reports_and_publications/statistical_energy_review_2011/STAGING/local_assets/pdf/statistical_review_of_world_energy_full_report_2011.pdf
- [17] United Nations, UNFCCC Kyoto Protocol to the United Nations Framework Convention on Climate Change, New York, 1997.
URL <http://unfccc.int>
- [18] W. M. Haynes (Ed.), CRC Handbook of Chemistry and Physics (Internet Version 2012), 92nd Edition, CRC Press Taylor & Francis Group, Boca Raton, FL, 2012.
URL <http://www.hbcernetbase.com/>
- [19] E. V. Kondratenko, M. Baerns, Handbook of Heterogeneous Catalysis, 2nd Edition, Vol. 6, Wiley-VCH Verlag GmbH & Co. KGaA, Weinheim, 2008, Ch. 13.17 Oxidative Coupling of Methane, pp. 3010–3023. doi:10.1002/9783527610044.hetc0152.
- [20] U. Zavyalova, M. Holena, R. Schlögl, M. Baerns, Statistical Analysis of Past Catalytic Data on Oxidative Methane Coupling for New Insights into the Composition of High-Performance Catalysts, *Chem-CatChem* 3 (12) (2011) 1935–1947. doi:10.1002/cctc.201100186.
- [21] G. A. Kovalenko, V. D. Sokolovskii, A novel approach to selective oxidation of gaseous hydrocarbons, *React. Kinet. Catal. Lett.* 48 (2) (1992) 447–453. doi:10.1007/BF02162693.
- [22] J. B. van Beilen, E. G. Funhoff, Expanding the alkane oxygenase toolbox: new enzymes and applications, *Curr. Opin. Biotechnol.* 16 (3) (2005) 308–314. doi:10.1016/j.copbio.2005.04.005.
- [23] R. A. Periana, D. J. Taube, E. R. Evitt, D. G. Löffler, P. R. Wentreck, G. Voss, T. Masuda, A Mercury-Catalysed, High-Yield System for the Oxidation of Methane to Methanol, *Science* 259 (5093) (1993) 340–343. doi:10.1126/science.259.5093.340.
- [24] I. M. Lorkovic, A. Yilmaz, G. A. Yilmaz, X.-P. Zhou, L. E. Laverman, S. Sun, D. J. Schaefer, M. Weiss, M. L. Noy, C. I. Cutler, J. H. Sherman, E. W. McFarland, G. D. Stucky, P. C. Ford, A novel integrated process for the functionalization of methane and ethane: bromine as mediator, *Catal. Today* 98 (4) (2004) 317–322. doi:10.1016/j.cattod.2004.09.013.
- [25] M. A. Vannice, The Catalytic Synthesis of Hydrocarbons from Carbon Monoxide and Hydrogen, *Catal. Rev. Sci. Eng.* 14 (1) (1976) 153–191. doi:10.1080/03602457608073410.
- [26] G. P. van der Laan, A. A. C. M. Beenckers, Kinetics and Selectivity of the Fischer–Tropsch Synthesis: A Literature Review, *Catal. Rev. Sci. Eng.* 41 (3-4) (1999) 255–318. doi:10.1081/CR-100101170.
- [27] E. Iglesia, Design, synthesis, and use of cobalt-based Fischer–Tropsch synthesis catalysts, *Appl. Catal., A* 161 (1-2) (1997) 59–78. doi:10.1016/S0926-860X(97)00186-5.
- [28] E. de Smit, B. M. Weckhuysen, The renaissance of iron-based Fischer–Tropsch synthesis: on the multifaceted catalyst deactivation behaviour, *Chem. Soc. Rev.* 37 (2008) 2758–2781. doi:10.1039/b805427d.
- [29] C. D. Chang, Hydrocarbons from Methanol, *Catal. Rev. Sci. Eng.* 25 (1) (1983) 1–118. doi:10.1080/01614948308078874.
- [30] M. Stöcker, Methanol-to-hydrocarbons: catalytic materials and their behavior, *Microporous Mesoporous Mater.* 29 (1-2) (1999) 3–48. doi:10.1016/S1387-1811(98)00319-9.
- [31] F. J. Keil, Methanol-to-hydrocarbons: process technology, *Microporous Mesoporous Mater.* 29 (1-2) (1999) 49–66. doi:10.1016/S1387-1811(98)00320-5.
- [32] Department of the Treasury, Internal Revenue Service, USA, Internal Revenue Bulletin No. 1999-16 (1999).
URL <http://www.irs.gov/pub/irs-irbs/irb99-16.pdf>
- [33] ISO 80000-5:2007, Quantities and units – Part 5: Thermodynamics, NORM (2007).

- [34] Royal Dutch Shell plc, Pearl GTL - an overview, online (2012).
URL http://www.shell.com/home/content/aboutshell/our_strategy/major_projects_2/pearl/
- [35] G. J. Hutchings, R. W. Joyner, Prospects for the partial oxidation of natural gas, *Chem. Ind.* 16 (1991) 575–578.
URL http://findarticles.com/p/articles/mi_hb5255/is_n16/ai_n28604912/
- [36] A. P. E. York, T.-c. Xiao, M. L. H. Green, J. B. Claridge, Methane Oxyforming for Synthesis Gas Production, *Catal. Rev. - Sci. Eng.* 47 (4) (2007) 511–560. doi:10.1080/01614940701583315.
- [37] S. S. Bharadwaj, L. D. Schmidt, Catalytic partial oxidation of natural gas to syngas, *Fuel Process. Technol.* 42 (2-3) (1995) 109–127. doi:10.1016/0378-3820(94)00098-E.
- [38] Y. H. Hu, E. Ruckenstein, Catalytic Conversion of Methane to Synthesis Gas by Partial Oxidation and CO₂ Reforming, *Advances in Catalysis* 48 (2004) 297–345. doi:10.1016/S0360-0564(04)48004-3.
- [39] J. R. Rostrup-Nielsen, *Catalytic Steam Reforming*, Vol. 5, Springer-Verlag Berlin Heidelberg New York, 1984, Ch. Catalytic Steam Reforming, pp. 1–117.
- [40] J. P. van Hook, Methane-Steam Reforming, *Catal. Rev. - Sci. Eng.* 21 (1) (1980) 1–51. doi:10.1080/03602458008068059.
- [41] J. N. Armor, The multiple roles for catalysis in the production of H₂, *Appl. Catal., A* 176 (2) (1999) 159–176. doi:10.1016/S0926-860X(98)00244-0.
- [42] T. Rostrup-Nielsen, Manufacture of hydrogen, *Catal. Today* 106 (1-4) (2005) 293–296. doi:10.1016/j.cattod.2005.07.149.
- [43] B. C. Enger, R. Lødeng, A. Holmen, A review of catalytic partial oxidation of methane to synthesis gas with emphasis on reaction mechanisms over transition metal catalysts, *Appl. Catal., A* 346 (1-2) (2008) 1–27. doi:10.1016/j.apcata.2008.05.018.
- [44] B. Neumann, K. Jacob, Die Gleichgewichtsverhältnisse bei der Methanbildung aus Kohlenoxyd und Wasserstoff, bzw. Kohlendioxyd und Wasserstoff, *Z. Elektrochem.* 30 (12) (1924) 557–576.
- [45] P. J. Byrne Jr., E. J. Gohr, N. J. Elizabeth, R. T. Haslam, Recent Progress in Hydrogenation of Petroleum, *Ind. Eng. Chem.* 24 (10) (1932) 1129–1135. doi:10.1021/ie50274a009.
- [46] A. M. Adris, B. B. Pruden, C. J. Lim, J. R. Grace, On the Reported Attempts to Radically Improve the Performance of the Steam Methane Reforming Reactor, *Can. J. Chem. Eng.* 74 (2) (1996) 177–186. doi:10.1002/cjce.5450740202.
- [47] C. H. Bartholomew, Carbon Deposition in Steam Reforming and Methanation, *Catal. Rev. Sci. Eng.* 24 (1) (1982) 67–112. doi:10.1080/03602458208079650.
- [48] J. R. Rostrup-Nielsen, J. H. Bak Hansen, CO₂-Reforming of Methane over Transition Metals, *J. Catal.* 144 (1) (1993) 38–49. doi:10.1006/jcat.1993.1312.
- [49] J. Eilers, S. A. Posthuma, S. T. Sie, The shell middle distillate synthesis process (SMDS), *Catal. Lett.* 7 (1-4) (1990) 253–269. doi:10.1007/BF00764507.
- [50] J. C. Mackie, Partial Oxidation of Methane: The Role of the Gas Phase Reactions, *Catal. Rev. - Sci. Eng.* 33 (1&2) (1991) 169–240. doi:10.1080/01614949108020299.
- [51] S. C. Tsang, J. B. Claridge, M. L. H. Green, Recent advances in the conversion of methane to synthesis gas, *Catal. Today* 23 (1) (1995) 3–15. doi:10.1016/0920-5861(94)00080-L.
- [52] A. P. E. York, T. Xiao, M. L. H. Green, Brief Overview of the Partial Oxidation of Methane to Synthesis Gas, *Top. Catal.* 22 (3-4) (2003) 345–358. doi:10.1023/A:1023552709642.
- [53] M. Prettre, C. Eichner, M. Perrin, The catalytic oxidation of methane to carbon monoxide and hydrogen, *Trans. Faraday Soc.* 42 (1946) 335–339. doi:10.1039/TF946420335b.
- [54] P. D. F. Vernon, M. L. H. Green, A. K. Cheetham, A. T. Ashcroft, Partial oxidation of methane to synthesis gas, *Catal. Lett.* 6 (2) (1990) 181–186. doi:10.1007/BF00774718.

- [55] D. Dissanayake, M. P. Rosynek, K. C. C. Kharas, J. H. Lunsford, Partial oxidation of methane to carbon monoxide and hydrogen over a Ni/Al₂O₃ catalyst, *J. Catal.* 132 (1) (1991) 117–127. doi:10.1016/0021-9517(91)90252-Y.
- [56] D. A. Hickman, L. D. Schmidt, Synthesis gas formation by direct oxidation of methane over Pt monoliths, *J. Catal.* 138 (1) (1992) 267–282. doi:10.1016/0021-9517(92)90022-A.
- [57] D. A. Hickman, L. D. Schmidt, Steps in CH₄ Oxidation on Pt and Rh Surfaces: High-Temperature Reactor Simulations, *AIChE J.* 39 (7) (1993) 1164–1177. doi:10.1002/aic.690390708.
- [58] D. A. Hickman, E. A. Hauptfear, L. D. Schmidt, Synthesis gas formation by direct oxidation of methane over Rh monoliths, *Catal. Lett.* 17 (3-4) (1993) 223–237. doi:10.1007/BF00766145.
- [59] D. A. Hickman, L. D. Schmidt, Synthesis Gas Formation by Direct Oxidation of Methane over Monoliths, *ACS Symp. Ser.* 523 (1993) 416–426. doi:10.1021/bk-1993-0523.ch032.
- [60] E. P. J. Mallens, J. H. B. J. Hoebink, G. B. Marin, An investigation on the reaction mechanism for the partial oxidation of methane to synthesis gas over platinum, *Catal. Lett.* 33 (3-4) (1995) 291–304. doi:10.1007/BF00814232.
- [61] D. Qin, J. Lapszewicz, X. Jiang, Comparison of Partial Oxidation and Steam-CO₂ Mixed Reforming of CH₄ to Syngas on MgO-Supported Metals, *J. Catal.* 159 (1) (1996) 140–149. doi:10.1006/jcat.1996.0073.
- [62] K. Heitnes Hofstad, T. Sperle, O. A. Rokstad, A. Holmen, Partial oxidation of methane to synthesis gas over a Pt/10% Rh gauze, *Catal. Lett.* 45 (1-2) (1997) 97–105. doi:10.1023/A:1019030604516.
- [63] K. Heitnes Hofstad, O. A. Rokstad, A. Holmen, Partial oxidation of methane over platinum metal gauze, *Catal. Lett.* 36 (1-2) (1996) 25–30. doi:10.1007/BF00807201.
- [64] O. V. Buyevskaya, D. Wolf, M. Baerns, Rhodium-catalyzed partial oxidation of methane to CO and H₂. Transient studies on its mechanism, *Catal. Lett.* 29 (1-2) (1994) 249–260. doi:10.1007/BF00814271.
- [65] K. Walter, O. V. Buyevskaya, D. Wolf, M. Baerns, Rhodium-catalyzed partial oxidation of methane to CO and H₂. In situ DRIFTS studies on surface intermediates, *Catal. Lett.* 29 (1-2) (1994) 261–270. doi:10.1007/BF00814272.
- [66] O. V. Buyevskaya, D. Wolf, M. Baerns, Primary reaction steps and active surface sites in the rhodium-catalyzed partial oxidation of methane to CO and H₂, *Catal. Lett.* 38 (1-2) (1996) 81–88. doi:10.1007/BF00806904.
- [67] D. Wolf, M. Höhenberger, M. Baerns, External Mass and Heat Transfer Limitations of the Partial Oxidation of Methane over a Pt/MgO Catalyst Consequences for Adiabatic Reactor Operation, *Ind. Eng. Chem. Res.* 36 (1997) 3345–3353. doi:10.1021/ie960739a.
- [68] D. Wolf, M. Barré-Chassonery, M. Höhenberger, A. van Veen, M. Baerns, Kinetic study of the water-gas shift reaction and its role in the conversion of methane to syngas over a Pt/MgO catalyst, *Catal. Today* 40 (2-3) (1998) 147–156. doi:10.1016/S0920-5861(98)00003-0.
- [69] A. G. Hansen, W. J. M. van Well, P. Stoltze, Microkinetic modeling as a tool in catalyst discovery, *Top. Catal.* 45 (1-2) (2007) 219–222. doi:10.1007/s11244-007-0269-9.
- [70] R. Quiceno, J. Pérez-Ramírez, J. Warnatz, O. Deutschmann, Modeling the high-temperature catalytic partial oxidation of methane over platinum gauze: Detailed gas-phase and surface chemistries coupled with 3D flow field simulations, *Appl. Catal., A* 303 (2006) 166–176. doi:10.1016/j.apcata.2006.01.041.
- [71] J. Koop, O. Deutschmann, Detailed surface reaction mechanism for Pt-catalyzed abatement of automotive exhaust gases, *Appl. Catal., B* 91 (1-2) (2009) 47–58. doi:10.1016/j.apcatb.2009.05.006.
- [72] A. B. Mhadeshwar, D. G. Vlachos, A Catalytic Reaction Mechanism for Methane Partial Oxidation at Short Contact Times, Reforming, and Combustion, and for Oxygenate Decomposition and Oxidation on Platinum., *Ind. Eng. Chem. Res.* 46 (16) (2007) 5310–5324. doi:10.1021/ie070322c.
- [73] W. Hauptmann, M. Votsmeier, H. Vogel, D. G. Vlachos, Modeling the simultaneous oxidation of CO and H₂ on Pt – Promoting effect of H₂ on the CO-light-off, *Appl. Catal., A* 397 (1-2) (2011) 174–182. doi:10.1016/j.apcata.2011.02.031.

- [74] G. P. Smith, D. M. Golden, M. Frenklach, N. W. Moriarty, B. Eiteneer, M. Goldenberg, C. T. Bowman, R. K. Hanson, S. Song, W. C. Gardiner, Jr., V. V. Lissianski, Z. Qin, GRI-Mech 3.0.
URL http://www.me.berkeley.edu/gri_mech/
- [75] D. A. Henning, L. D. Schmidt, Oxidative dehydrogenation of ethane at short contact times: species and temperature profiles within and after the catalyst, *Chem. Eng. Sci.* 57 (14) (2002) 2615–2625. doi:10.1016/S0009-2509(02)00155-0.
- [76] I. Tavazzi, A. Beretta, G. Groppi, P. Forzatti, Development of a molecular kinetic scheme for methane partial oxidation over a Rh/ α -Al₂O₃ catalyst, *J. Catal.* 241 (1) (2006) 1–13. doi:10.1016/j.jcat.2006.03.018.
- [77] W. P. Partridge, J. M. E. Storey, S. A. Lewis, R. W. Smithwick, G. L. Devault, M. J. Cunningham, N. W. Currier, T. M. Yonushonis, Time-Resolved Measurements of Emission Transients By Mass Spectrometry, *SAE Int. J. Fuels Lubr.* 109 (2000) 2992–2999. doi:10.4271/2000-01-2952.
- [78] B. West, S. Huff, J. Parks, S. Lewis, J.-S. Choi, W. Partridge, J. Storey, Assessing Reductant Chemistry During In-Cylinder Regeneration of Diesel Lean NOx Traps, *SAE Technical Paper* 40 (2) (2004) 3023. doi:10.4271/2004-01-3023.
- [79] J. Sá, D. L. Fernandes, F. Aiouache, A. Goguet, C. Hardacre, D. Lundie, W. Naeem, W. P. Partridge, C. Stere, SpaciMS: spatial and temporal operando resolution of reactions within catalytic monoliths, *Analyst* 135 (9) (2010) 2260–2272. doi:10.1039/COAN00303D.
- [80] M. Bosco, F. Vogel, Optically accessible channel reactor for the kinetic investigation of hydrocarbon reforming reactions, *Catal. Today* 116 (3) (2006) 348–353. doi:10.1016/j.cattod.2006.05.064.
- [81] O. Korup*, M. Geske, S. Mavlyankariev, R. Schlögl, R. Horn, Catalytic partial oxidation of methane on autothermally operated Pt catalysts: Reaction pathways, zoning effects, and impact of mass and heat transfer, in: ACS National Meeting Fall 2010, Boston MA, USA, August 22nd – 26th, 2010.
- [82] R. Horn, O. Korup, M. Geske, U. Zavyalova, I. Oprea, R. Schlögl, Reactor for In-Situ Measurements of Spatially Resolved Kinetic Data in Heterogeneous Catalysis, *Rev. Sci. Instrum.* 81 (6) (2010) 064102. doi:10.1063/1.3428727.
- [83] O. Korup, S. Mavlyankariev, M. Geske, C. F. Goldsmith, R. Horn, Measurement and analysis of spatial reactor profiles in high temperature catalysis research, *Chem. Eng. Process.* 50 (10) (2011) 998–1009. doi:10.1016/j.cep.2011.05.024.
- [84] M. Geske*, O. Korup, R. Schlögl, R. Horn, Using spatially resolved in-situ catalyst characterization methods and Raman spectroscopy for the ODH of ethane over MoO_x, in: EuropaCat X, Glasgow, UK August 28th - September 2th, 2011.
- [85] M. Geske*, O. Korup, R. Schlögl, R. Horn, Using spatially resolved in-situ catalyst characterization methods and Raman spectroscopy for the ODH of ethane over MoO_x, in: Bunsentagung 2011, Berlin, Germany, June 2nd – 4th, 2011.
- [86] M. Geske, O. Korup, R. Horn, Resolving Kinetics and Dynamics of a Catalytic Reaction Inside a Fixed Bed Reactor by Combined Kinetic and Spectroscopic Profiling, *Catal. Sci. Technol.* (2012) accepted manuscript. doi:10.1039/C2CY20489D.
- [87] U. Zavyalova, F. Girgsdies, O. Korup, R. Horn, R. Schlögl, Microwave-Assisted Self-Propagating Combustion Synthesis for Uniform Deposition of Metal Nanoparticles on Ceramic Monoliths, *J. Phys. Chem. C* 113 (40) (2009) 17493–17501. doi:10.1021/jp905692g.
- [88] O. Korup, M. Geske, S. Mavlyankariev, R. Schlögl, R. Horn, Catalytic partial oxidation of methane on autothermally operated Pt catalysts: Reaction pathways, zoning effects, and impact of mass and heat transport, *Prepr. Pap. - Am. Chem. Soc., Div. Fuel Chem.* 55 (2) (2010) 149–150.
- [89] D. K. Zerkle, M. D. Allendorf, M. Wolf, O. Deutschmann, Understanding Homogeneous and Heterogeneous Contributions to the Platinum-Catalyzed Partial Oxidation of Ethane in a Short-Contact-Time Reactor, *J. Catal.* 196 (1) (2000) 18–39. doi:10.1006/jcat.2000.3009.
- [90] A. Sadezky, H. Muckenhuber, H. Grothe, R. Niessner, U. Pöschl, Raman microspectroscopy of soot and related carbonaceous materials: Spectral analysis and structural information, *Carbon* 43 (5) (2005) 1731–1742. doi:10.1016/j.carbon.2005.02.018.

- [91] G. A. Somorjai, *Chemistry in Two Dimensions: Surfaces*, Cornell University Press, Ithaca and London, 1981, Ch. 9. Hydrocarbon Conversion on Platinum, pp. 479–515.
- [92] R. L. Burwell, Jr., *Manual of Symbols and Terminology for Physicochemical Quantities and Units - Appendix II. Definitions, Terminology and Symbols in Colloid and Surface Chemistry. Part II: Heterogeneous Catalysis*, *Pure & Appl. Chem.* 46 (1) (1976) 71–90. doi:10.1351/pac197646010071.
- [93] DIN ISO 9277:2003-05, Determination of the specific surface area of solids by gas adsorption using the bet method (iso 9277:1995), NORM (2003).
- [94] P. Kolbes, K. Meyer, R. G. Munro, Special Publication 960-17 / Porosity and Specific Surface Area Measurements for Solid Materials, NIST National Institute of Standards and Technology, Technology Administration, U.S. Department of Commerce (2006).
URL <http://www.ceramics.nist.gov/ftproot/SP960-17.pdf>
- [95] S. J. Gregg, K. S. W. Sing, *Adsorption, Surface Area and Porosity*, 2nd Edition, Academic Press, Inc. London, 1982.
- [96] S. Lowell, J. E. Shields, M. A. Thomas, M. Thommes, *Characterization of Porous Solids and Powders: Surface Area, Pore Size and Density*, 1st Edition, Kluwer Academic Publishers, 2004.
- [97] S. Brunauer, P. H. Emmett, E. Teller, Adsorption of Gases in Multimolecular Layers, *J. Am. Chem. Soc.* 60 (2) (1938) 309–319. doi:10.1021/ja01269a023.
- [98] K. S. W. Sing, D. H. Everett, R. A. W. Haul, L. Moscou, R. A. Pierotti, J. Rouquérol, T. Siemieniewska, Reporting physisorption data for gas/solid systems with special reference to the determination of surface area and porosity (Recommendations 1984), *Pure & Appl. Chem.* 57 (4) (1985) 603–619. doi:10.1351/pac198557040603.
- [99] S. Brunauer, L. S. Deming, W. E. Deming, E. Teller, On a theory of the van der Waals adsorption of gases, *J. Am. Chem. Soc.* 62 (7) (1940) 1723–1732. doi:10.1021/ja01864a025.
- [100] E. P. Barrett, L. G. Joyner, P. P. Halenda, The Determination of Pore Volume and Area Distributions in Porous Substances. I. Computations from Nitrogen Isotherms, *J. Am. Chem. Soc.* 73 (1) (1951) 373–380. doi:10.1021/ja01145a126.
- [101] L. G. Joyner, E. P. Barrett, R. Skold, The Determination of Pore Volume and Area Distributions in Porous Substances. II. Comparison between Nitrogen Isotherm and Mercury Porosimeter Methods, *J. Am. Chem. Soc.* 73 (7) (1951) 3155–3158. doi:10.1021/ja01151a046.
- [102] DIN 66134:1998-02, Determination of the pore size distribution and the specific surface area of mesoporous solids by means of nitrogen sorption - method of barrett, joyner and halenda (bjh), NORM (1998).
- [103] DIN 66136-1:2004-03, Determination of the dispersion degree of metals using gas chemisorption - part 1: Principles, NORM (2004).
- [104] DIN 66136-2:2007-01, Determination of the degree of dispersion of metals using chemisorption - part 2: Volumetric method, NORM (2007).
- [105] DIN 66136-3:2007-01, Determination of the degree of dispersion of metals using chemisorption - part 3: Flow method, NORM (2007).
- [106] DIN 66136-4:2009-05, Determination of the degree of dispersion of metals using chemisorption - part 4: Static-gravimetric method, NORM (2009).
- [107] L. Li, X. Wang, J. Shen, L. Zhou, T. Zhang, Study on chemisorption of H₂, O₂, CO and C₂H₄ on Pt-Ag/SiO₂ catalysts by microcalorimetry and FTIR, *J. Therm. Anal. Calorim.* 82 (1) (2005) 103–107. doi:10.1007/s10973-005-0848-6.
- [108] E. Calvet, H. Prat, *Microcalorimetry. Physical-chemical and biological applications*, Masson et Cie, Paris, 1956.
- [109] E. N. Coker, H. G. Karge, Novel high-temperature, high-vacuum, all-metal sample cells for microcalorimetric measurements of solids, *Rev. Sci. Instrum.* 68 (1997) 4521–4524. doi:10.1063/1.1148424.
- [110] R. Erni, M. D. Rossell, C. Kisielowski, U. Dahmen, Atomic-Resolution Imaging with a Sub-50-pm Electron Probe, *Phys. Rev. Lett.* 102 (9) (2009) 096101. doi:10.1103/PhysRevLett.102.096101.

- [111] S. Amelinckx, D. van Dyck, J. van Landuyt, G. van Tendeloo (Eds.), *Electron Microscopy: Principles and Fundamentals*, 1st Edition, VCH Verlagsgesellschaft mbH, Weinheim, Germany, 1997. doi:10.1002/9783527614561.
- [112] D. Vaughan, *Energy-Dispersive X-Ray Microanalysis - An Introduction*, NORAN Instruments, Inc., 2551 West Beltline Highway, Middleton, WI 53562, USA (1999).
URL <http://cime.epfl.ch/webdav/site/cime2/shared/Files/Teaching/EDX/Introduction%20to%20EDS.pdf>
- [113] B. Fultz, J. M. Howe, *Transmission Electron Microscopy and Diffractometry of Materials*, 3rd Edition, Springer-Verlag Berlin Heidelberg, 2008.
URL <http://dx.doi.org/10.1007/978-3-540-73886-2>
- [114] D. B. Williams, C. B. Carter, *Transmission Electron Microscopy - A Textbook for Material Science*, 2nd Edition, Springer Science+Business Media, Inc. New York, 2009.
URL <http://dx.doi.org/10.1007/978-0-387-76501-3>
- [115] B. Müller, U. Renz, Development of a fast fiber-optic two-color pyrometer for the temperature measurement of surfaces with varying emissivities, *Rev. Sci. Instrum.* 72 (2001) 3366–3374. doi:10.1063/1.1384448.
- [116] C. Dass, *Fundamentals of Contemporary Mass Spectrometry*, 1st Edition, John Wiley & Sons, Inc., Hoboken, New Jersey., 2007. doi:10.1002/0470118490.
- [117] J. H. Gross, *Mass Spectrometry*, 2nd Edition, Springer-Verlag, Berlin, Heidelberg, 2011. doi:10.1007/978-3-642-10711-5.
- [118] E. Mathieu, Mémoire sur le mouvement vibratoire d'une membrane de forme elliptique, *J. Math. Pures Appl. série 2^e* (13) (1868) 137–203.
URL http://portail.mathdoc.fr/JMPA/PDF/JMPA_1868_2_13_A8_0.pdf
- [119] K. L. Busch, The Electron Multiplier, *Spectroscopy* 15 (6) (2000) 28–33.
URL <http://web.ebscohost.com/ehost/detail?sid=cc377ee9-16b7-499b-8e63-174d35147870%40sessionmgr15&vid=1&hid=21&bdata=JnNpdGU9ZWhvc3QtbG12ZSZZY29wZT1zaXRl#db=aph&AN=6596134>
- [120] C. V. Raman, K. S. Krishnan, A New Type of Secondary Radiation, *Nature* 121 (3048) (1928) 501–502. doi:10.1038/121501c0.
- [121] C. V. Raman, K. S. Krishnan, The Optical Analogue of the Compton Effect, *Nature* 121 (3053) (1928) 711. doi:10.1038/121711a0.
- [122] M. von Laue, *Nobel Lectures, Physics 1922-1941*, Elsevier Publishing Company, Amsterdam, 1965, Ch. Nobel Lecture, December 11, 1930 - The molecular scattering of light, pp. 267–275.
URL http://www.nobelprize.org/nobel_prizes/physics/laureates/1930/raman-lecture.html
- [123] M. Czerny, A. F. Turner, Über den Astigmatismus bei Spiegelspektrometern, *Z. Phys. A - Hadron Nucl.* 61 (11-12) (1930) 792–797. doi:10.1007/BF01340206.
- [124] D. A. McQuarrie, J. D. Simon, *Physical Chemistry - A Molecular Approach*, University Science Books, Sausalito, California, 1997, Ch. Molecular Spectroscopy, pp. 495–545.
- [125] G. Wedler, *Lehrbuch der Physikalischen Chemie*, 5th Edition, Wiley-VCH Verlag GmbH & Co. KGaA, Weinheim, 2004, Ch. Wechselwirkung zwischen Strahlung und Molekülen, pp. 598–660.
- [126] T. Lehmann, *Unterlagen zum Spektroskopiekurs: UV/VIS-Spektroskopie*, Freie Universität Berlin, online (2009).
URL <http://userpage.chemie.fu-berlin.de/~tlehmann/gp/uv.pdf>
- [127] W. Friedrich, P. Knipping, M. von Laue, Interferenzerscheinungen bei Röntgenstrahlen, *Sitzb. kais. Akad. Wiss., München* (1912) 303–322.
- [128] W. Friedrich, P. Knipping, M. von Laue, Interferenzerscheinungen bei Röntgenstrahlen, *Ann. Phys.* 346 (10) (1913) 971–988. doi:10.1002/andp.19133461004.
- [129] M. von Laue, *Nobel Lectures, Physics 1901-1921*, Elsevier Publishing Company, Amsterdam, 1967, Ch. Nobel Lecture, November 12, 1915 - Concerning the detection of X-ray interferences, pp. 347–355.
URL http://www.nobelprize.org/nobel_prizes/physics/laureates/1914/laue-lecture.html

- [130] W. H. Bragg, W. L. Bragg, The Reflection of X-rays by Crystals, *Proc. R. Soc. Lond. A* 88 (605) (1913) 428–438. doi:10.1098/rspa.1913.0040.
- [131] W. H. Bragg, The Reflection of X-rays by Crystals (II.), *Proc. R. Soc. Lond. A* 89 (610) (1913) 246–248.
URL <http://www.jstor.org/stable/93487>
- [132] W. L. Bragg, The Structure of Some Crystals as Indicated by Their Diffraction of X-rays, *Proc. R. Soc. Lond. A* 89 (610) (1913) 248–277.
URL <http://www.jstor.org/stable/93488>
- [133] W. L. Bragg, Nobel Lectures, Physics 1901-1921, Elsevier Publishing Company, Amsterdam, 1967, Ch. Nobel Lecture, September 6, 1922 - The diffraction of X-rays by crystals, pp. 370–382.
URL http://www.nobelprize.org/nobel_prizes/physics/laureates/1915/wl-bragg-lecture.html
- [134] H. M. Rietveld, A profile refinement method for nuclear and magnetic structures, *J. Appl. Cryst.* 2 (2) (1969) 65–71. doi:10.1107/S0021889869006558.
- [135] BRUKER AXS GmbH, Karlsruhe, Germany, TOPAS Version 3.0 User's Manual, April 30, 2005 (2005).
- [136] W. C. Röntgen, Über eine neue Art von Strahlen, *Sitzungsber. Phys. Med. Ges. Würzburg* (1895) 132–141.
- [137] J. Banhart (Ed.), *Advanced Tomographic Methods in Materials Research and Engineering*, Oxford University Press, Oxford, New York, 2008. doi:10.1093/acprof:oso/9780199213245.001.0001.
- [138] K. Iniewski, *Medical Imaging: Principles, Detectors, and Electronics*, 1st Edition, John Wiley & Sons, Inc., Hoboken, New Jersey., 2009, Ch. X-Ray and Computed Tomography Imaging Principles, pp. 3–21. doi:10.1002/9780470451816.ch1.
- [139] G. N. Hounsfield, Computerized transverse axial scanning (tomography): Part 1. Description of system, *Br. J. Radiol.* 46 (552) (1973) 1016–1022. doi:10.1259/0007-1285-46-552-1016.
- [140] J. Radon, Über die Bestimmung von Funktionen durch ihre Integralwerte längs gewisser Mannigfaltigkeiten, *Ber. Verh. Saechs. Akad. Wiss. Leipzig Math. Phys.* 69 (1917) 262–277.
- [141] G. N. Ramachandran, A. V. Lakshminarayanan, Radiographs and Electron Micrographs: Application of Convolutions instead of Fourier Transforms, *Proc. Natl. Acad. Sci. U.S.A.* 68 (9) (1971) 2236–2240.
URL <http://www.pnas.org/content/68/9/2236.abstract>
- [142] F. García Moreno, M. Fromme, J. Banhart, Real-time X-ray Radioscopy on Metallic Foams Using a Compact Micro-Focus Source, *Adv. Eng. Mater.* 6 (6) (2004) 416–420. doi:10.1002/adem.200405143.
- [143] A. J. Meagher, M. Mukherjee, D. Weaire, S. Hutzler, J. Banhart, F. Garcia-Moreno, Analysis of the internal structure of monodisperse liquid foams by X-ray tomography, *Soft Matter* 7 (2011) 9881–9885. doi:10.1039/c1sm05495c.
- [144] M. V. Twigg, J. T. Richardson, Theory and Applications of Ceramic Foam Catalysts, *Trans. IChemE* 80 (2) (2002) 183–189. doi:10.1205/026387602753501906.
- [145] J. T. Richardson, D. Remue, J.-K. Hung, Properties of ceramic foam catalyst supports: mass and heat transfer, *Appl. Catal., A* 250 (2) (2003) 319–329. doi:10.1016/S0926-860X(03)00287-4.
- [146] R. M. Heck, S. Gulati, R. J. Farrauto, The application of monoliths for gas phase catalytic reactions, *Chem. Eng. J.* 82 (1-3) (2001) 149–156. doi:10.1016/S1385-8947(00)00365-X.
- [147] T. A. Nijhuis, A. E. W. Beers, T. Vergunst, I. Hoek, F. Kapteijn, J. A. Moulijn, Preparation of monolithic catalysts, *Catal. Rev. Sci. Eng.* 43 (4) (2001) 345–380.
- [148] V. Meille, Review on methods to deposit catalysts on structured surfaces, *Appl. Catal., A* 315 (2006) 1–17. doi:10.1016/j.apcata.2006.08.031.
- [149] X. Xu, J. A. Moulijn, *Structured Catalysts and Reactors*, 2nd Edition, CRC Press Taylor & Francis Group, Boca Raton, FL, 2005, Ch. 21. Transformation of a Structured Carrier into a Structured Catalyst, pp. 751–779.
URL www.crcpress.com/product/isbn/9780824723439

- [150] F. C. Moates, T. E. McMinn, J. T. Richardson, Radial reactor for trichloroethylene steam reforming, *AIChE J.* 45 (11) (1999) 2411–2418. doi:10.1002/aic.690451114.
- [151] T. Vergunst, F. Kapteijn, J. A. Moulijn, Monolithic catalysts — non-uniform active phase distribution by impregnation, *Appl. Catal., A* 213 (2) (2001) 179–187. doi:10.1016/S0926-860X(00)00896-6.
- [152] J. T. Richardson, M. Garrait, J.-K. Hung, Carbon dioxide reforming with Rh and Pt–Re catalysts dispersed on ceramic foam supports, *Appl. Catal., A* 255 (1) (2003) 69–82. doi:10.1016/S0926-860X(03)00645-8.
- [153] P. Avila, M. Montes, E. E. Miró, Monolithic reactors for environmental applications: A review on preparation technologies, *Chem. Eng. J.* 109 (1-3) (2005) 11–36. doi:10.1016/j.cej.2005.02.025.
- [154] S. Biamino, C. Badini, Combustion synthesis of lanthanum chromite starting from water solutions: Investigation of process mechanism by DTA–TGA–MS, *J. Eur. Ceram. Soc.* 24 (10-11) (2004) 3021–3034. doi:10.1016/j.jeurceramsoc.2003.10.005.
- [155] P. Bera, K. C. Patil, V. Jayaram, G. N. Subbanna, M. S. Hedge, Ionic Dispersion of Pt and Pd on CeO₂ by Combustion Method: Effect of Metal–Ceria Interaction on Catalytic Activities for NO Reduction and CO and Hydrocarbon Oxidation, *J. Catal.* 196 (2) (2000) 293–301. doi:10.1006/jcat.2000.3048.
- [156] P. Palmisano, N. Russo, P. Fino, D. Fino, C. Badini, High catalytic activity of SCS-synthesized ceria towards diesel soot combustion, *Appl. Catal., B* 69 (1-2) (2006) 85–92. doi:10.1016/j.apcatb.2006.06.002.
- [157] P. Panagiotopoulou, J. Papavasiliou, G. Avgouropoulos, T. Ioannides, D. I. Kondarides, Water–gas shift activity of doped Pt/CeO₂ catalysts, *Chem. Eng. J.* 134 (1-3) (2007) 16–22. doi:10.1016/j.cej.2007.03.054.
- [158] P. Bera, S. Malwadkar, A. Gayen, C. V. V. Satyanatayana, B. S. Rao, M. S. Hedge, Low-Temperature Water Gas Shift Reaction on Combustion Synthesized Ce_{1-x}Pt_xO_{2-δ} Catalyst, *Catal. Lett.* 96 (3-4) (2004) 213–219. doi:10.1023/B:CATL.0000030123.41351.14.
- [159] P. Bera, K. C. Patil, V. Jayaram, M. S. Hedge, G. N. Subbanna, Combustion synthesis of nanometal particles supported on α-Al₂O₃: CO oxidation and NO reduction catalysts, *J. Mater. Chem.* 9 (1999) 1801–1806. doi:10.1039/A901826C.
- [160] P. Bera, M. S. Hedge, Characterization and Catalytic Properties of Combustion Synthesized Au/CeO₂ Catalyst, *Catal. Lett.* 79 (1-4) (2002) 75–81. doi:10.1023/A:1015352223861.
- [161] C. N. R. Rao, Chemical synthesis of solid inorganic materials, *Mater. Sci. Eng., B* 18 (1) (1993) 1–21. doi:10.1016/0921-5107(93)90109-Z.
- [162] G. Xanthopoulou, G. Vekinis, Deep oxidation of methane using catalysts and carriers produced by self-propagating high-temperature synthesis, *Appl. Catal., A* 199 (2) (2000) 227–238. doi:10.1016/S0926-860X(99)00562-1.
- [163] P. G. Tsyrlunikov, U. Zavyalova, N. B. Shitova, N. D. Ryshova, V. F. Tretyakov, RU Patent 2,284,219 (2005).
- [164] U. F. Zavyalova, V. F. Tretyakov, T. N. Burdeinaya, V. V. Lunin, N. B. Shitova, N. D. Ryzhova, A. N. Shmakov, A. I. Nizovskii, P. G. Tsyrlunikov, Self-Propagating Synthesis of Supported Oxide Catalysts for Deep Oxidation of CO and Hydrocarbons, *Kinet. Catal.* 46 (5) (2005) 752–757. doi:10.1007/s10975-005-0132-6.
- [165] S. Biamino, P. Fino, D. Fino, N. Russo, C. Badini, Catalyzed traps for diesel soot abatement: In situ processing and deposition of perovskite catalyst, *Appl. Catal., B* 61 (3-4) (2005) 297–305. doi:10.1016/j.apcatb.2005.05.010.
- [166] J. Papavasiliou, G. Avgouropoulos, T. Ioannides, In situ combustion synthesis of structured Cu–Ce–O and Cu–Mn–O catalysts for the production and purification of hydrogen, *Appl. Catal., B* 66 (3-4) (2006) 168–174. doi:10.1016/j.apcatb.2006.03.011.
- [167] H. S. Potdar, S. B. Deshpande, Y. B. Kholam, A. S. Deshpande, S. K. Date, Synthesis of nanosized Ce_{0.75}Zr_{0.25}O₂ porous powders via an autoignition: glycine nitrate process, *Mater. Lett.* 57 (5-6) (2003) 1066–1071. doi:10.1016/S0167-577X(02)00932-1.

- [168] U. Zavyalova, P. Scholz, B. Ondruschka, Influence of cobalt precursor and fuels on the performance of combustion synthesized $\text{Co}_3\text{O}_4/\gamma\text{-Al}_2\text{O}_3$ catalysts for total oxidation of methane, *Appl. Catal., A* 323 (2007) 226–232. doi:10.1016/j.apcata.2007.02.021.
- [169] U. Zavyalova, B. Nigrovski, K. Pollok, F. Langenhorst, B. Müller, P. Scholz, B. Ondruschka, Gel-combustion synthesis of nanocrystalline spinel catalysts for VOCs elimination, *Appl. Catal., B* 83 (3-4) (2008) 221–228. doi:10.1016/j.apcatb.2008.02.015.
- [170] A. Civera, M. Pavese, G. Saracco, V. Specchia, Combustion synthesis of perovskite-type catalysts for natural gas combustion, *Catal. Today* 83 (1-4) (2003) 199–221. doi:10.1016/S0920-5861(03)00220-7.
- [171] X. Wu, D. Weng, L. Xu, H. Li, Structure and performance of γ -alumina washcoat deposited by plasma spraying, *Surf. Coat. Technol.* 145 (1-3) (2001) 226–232. doi:10.1016/S0257-8972(01)01301-9.
- [172] J. R. Salge, G. A. Deluga, L. D. Schmidt, Catalytic partial oxidation of ethanol over noble metal catalysts, *J. Catal.* 235 (1) (2005) 69–78. doi:10.1016/j.jcat.2005.07.021.
- [173] K. J. Rao, B. Vaidhyanathan, M. Ganguli, P. A. Ramakrishnan, Synthesis of Inorganic Solids Using Microwaves, *Chem. Mater.* 11 (4) (1999) 882–895. doi:10.1021/cm9803859.
- [174] D. E. Clark, I. Ahmad, R. C. Dalton, Microwave ignition and combustion synthesis of composites, *Mater. Sci. Eng., A* 144 (1-2) (1991) 91–97. doi:10.1016/0921-5093(91)90213-7.
- [175] D. N. Furlong, A. Launikonis, W. H. F. Sasse, J. V. Sanders, Colloidal platinum sols. Preparation, characterization and stability towards salt, *J. Chem. Soc., Faraday Trans. I* 80 (1984) 571–588. doi:10.1039/F19848000571.
- [176] Y. Fernández, A. Arenillas, M. A. Díez, J. A. Menéndez, Pyrolysis of glycerol over activated carbons for syngas production, *J. Anal. Appl. Pyrolysis* 84 (2) (2009) 145–150. doi:10.1016/j.jaap.2009.01.004.
- [177] V. Subramanian, W. W. Burke, H. Zhu, B. Wei, Novel Microwave Synthesis of Nanocrystalline SnO_2 and Its Electrochemical Properties, *J. Phys. Chem. C* 112 (12) (2008) 4550–4556. doi:10.1021/jp711551p.
- [178] J. M. Berty, Reactor for vapor-phase catalytic studies, *Chem. Eng. Prog.* 70 (5) (1974) 78–85.
- [179] D. Farrusseng, High-throughput heterogeneous catalysis, *Surf. Sci. Rep.* 63 (11) (2008) 487–513. doi:10.1016/j.surfrep.2008.09.001.
- [180] J. H. Lunsford, The catalytic oxidative coupling of methane, *Angew. Chem., Int. Ed.* 34 (9) (1995) 970–980. doi:10.1002/anie.199509701.
- [181] R. J. Olsen, W. R. Williams, X. Song, L. D. Schmidt, R. Aris, Dynamics of homogeneous-heterogeneous reactors, *Chem. Eng. Sci.* 47 (9-11) (1992) 2505–2510. doi:10.1016/0009-2509(92)87084-4.
- [182] S. L. Shannon, J. G. Goodwin, Jr., Characterization of Catalytic Surfaces by Isotopic-Transient Kinetics during Steady-State Reaction, *Chem. Rev.* 95 (3) (1995) 677–695. doi:10.1021/cr00035a011.
- [183] J. T. Gleaves, J. R. Ebner, T. C. Kuechler, Catalyst Evaluation System with Submillisecond Time Resolution, *Catal. Rev. - Sci. Eng.* 30 (1) (1988) 49–116. doi:10.1080/01614948808078616.
- [184] J. T. Gleaves, G. Yablonsky, X. Zheng, R. Fushimi, P. L. Mills, Temporal analysis of products (TAP) – Recent advances in technology for kinetic analysis of multi-component catalysts, *J. Mol. Catal. A: Chem.* 315 (2) (2010) 108–134. doi:10.1016/j.molcata.2009.06.017.
- [185] M. Lyubovsky, S. Roychoudhury, R. LaPierre, Catalytic partial "oxidation of methane to syngas" at elevated pressures, *Catal. Lett.* 99 (3-4) (2005) 113–117. doi:10.1007/s10562-005-2103-y.
- [186] J. Kopyscinski, T. J. Schildhauer, F. Vogel, S. M. A. Biollaz, A. Wokaun, Applying spatially resolved concentration and temperature measurements in a catalytic plate reactor for the kinetic study of CO methanation, *J. Catal.* 271 (2) (2010) 262–279. doi:10.1016/j.jcat.2010.02.008.
- [187] C. Daniel, M.-O. Clarté, S.-P. Teh, O. Thinon, H. Provendier, A. C. Van Veen, B. J. Beccard, Y. Schuurman, C. Mirodatos, Spatially resolved catalysis in microstructured reactors by IR spectroscopy: CO oxidation over mono- and bifunctional Pt catalysts, *J. Catal.* 272 (1) (2010) 55–64. doi:10.1016/j.jcat.2010.03.012.

- [188] A. Urakawa, A. Baiker, Space-Resolved Profiling Relevant in Heterogeneous Catalysis, *Top. Catal.* 52 (10) (2009) 1312–1322. doi:10.1007/s11244-009-9312-3.
- [189] L. L. Raja, R. J. Kee, O. Deutschmann, J. Warnatz, L. D. Schmidt, A critical evaluation of Navier–Stokes, boundary-layer, and plug-flow models of the flow and chemistry in a catalytic-combustion monolith, *Catal. Today* 59 (1-2) (2000) 47–60. doi:10.1016/S0920-5861(00)00271-6.
- [190] G. Incera Garridoa, F. Patcas, S. Langa, B. Kraushaar-Czarnetzki, Mass transfer and pressure drop in ceramic foams: A description for different pore sizes and porosities, *Chem. Eng. Sci.* 63 (21) (2008) 5202–5217. doi:10.1016/j.ces.2008.06.015.
- [191] G. Groppi, L. Giani, E. Tronconi, Generalized Correlation for Gas/Solid Mass-Transfer Coefficients in Metallic and Ceramic Foams, *Ind. Eng. Chem. Res.* 46 (12) (2007) 3955–3958. doi:10.1021/ie061330g.
- [192] B. Dietrich, W. Schabel, M. Kind, H. Martin, Pressure drop measurements of ceramic sponges – Determining the hydraulic diameter, *Chem. Eng. Sci.* 64 (16) (2009) 3633–3640. doi:10.1016/j.ces.2009.05.005.
- [193] M.-L. Wang, H.-Z. Zheng, J.-M. Li, W.-Z. Weng, W.-S. Xia, C.-J. Huang, H.-L. Wan, In Situ Raman and Pulse Reaction Study on the Partial Oxidation of Methane to Synthesis Gas over a Pt/Al₂O₃ Catalyst, *Chemistry - An Asian Journal* 6 (2) (2011) 580–589. doi:10.1002/asia.201000580.
- [194] G. E. Keller, M. M. Bhasin, Synthesis of ethylene via oxidative coupling of methane: I. Determination of active catalysts, *J. Catal.* 73 (1) (1982) 9–19. doi:10.1016/0021-9517(82)90075-6.
- [195] A. M. Maitra, Critical performance evaluation of catalysts and mechanistic implications for oxidative coupling of methane, *Appl. Catal., A* 104 (1) (1993) 11–59. doi:10.1016/0926-860X(93)80209-9.
- [196] C. L. Rasmussen, J. G. Jakobsen, P. Glarborg, Experimental measurements and kinetic modeling of CH₄/O₂ and CH₄/C₂H₆/O₂ conversion at high pressure, *Int. J. Chem. Kinet.* 40 (12) (2008) 778–807. doi:10.1002/kin.20352.
- [197] Reaction Design: San Diego, Chemkin-pro 15101 (2011).
URL <http://www.reactiondesign.com>
- [198] H. Zanthoff, M. Baerns, Oxidative coupling of methane in the gas phase. Kinetic simulation and experimental verification, *Ind. Eng. Chem. Res.* 29 (1) (1990) 2–10. doi:10.1021/ie00097a001.
- [199] T. Blasco, J. M. López Nieto, Oxidative dyhydrogenation of short chain alkanes on supported vanadium oxide catalysts, *Appl. Catal., A* 157 (1-2) (1997) 117–142. doi:10.1016/S0926-860X(97)00029-X.
- [200] F. Cavani, N. Ballarini, A. Cericola, Oxidative dehydrogenation of ethane and propane: How far from commercial implementation?, *Catal. Today* 127 (1-4) (2007) 113–131. doi:10.1016/j.cattod.2007.05.009.
- [201] I. B. Gornushkin, P. E. Eagan, A. B. Novikov, B. W. Smith, J. D. Winefordner, Automatic Correction of Continuum Background in Laser-Induced Breakdown and Raman Spectrometry, *Appl. Spectrosc.* 57 (2) (2003) 197–207.
URL www.opticsinfobase.org/abstract.cfm?URI=as-57-2-197
- [202] A. C. Ferrari, J. Robertson, Interpretation of Raman spectra of disordered and amorphous carbon, *Phys. Rev. B* 61 (20) (2000) 14095–14107. doi:10.1103/PhysRevB.61.14095.
- [203] F. Tuinstra, J. L. Koenig, Raman Spectrum of Graphite, *J. Phys. Chem.* 53 (3) (1970) 1126–1130. doi:10.1063/1.1674108.
- [204] G. Katagiri, H. Ishida, A. Ishitani, Raman spectra of graphite edge planes, *Carbon* 26 (4) (1988) 565–571. doi:10.1016/0008-6223(88)90157-1.
- [205] Y. Wang, D. C. Alsmeyer, R. L. McCreery, Raman spectroscopy of carbon materials: structural basis of observed spectra, *Chem. Mater.* 2 (5) (1990) 557–563. doi:10.1021/cm00011a018.
- [206] N. P. Ivleva, U. McKeon, R. Niessner, U. Pöschl, Raman Microspectroscopic Analysis of Size-Resolved Atmospheric Aerosol Particle Samples Collected with an ELPI: Soot, Humic-Like Substances, and Inorganic Compounds, *Aerosol Sci. Technol.* 41 (7) (2007) 655–671. doi:10.1080/02786820701376391.

- [207] M. Knauer, M. E. Schuster, D. Su, R. Schlögl, R. Niessner, N. P. Ivleva, Soot Structure and Reactivity Analysis by Raman Microspectroscopy, Temperature-Programmed Oxidation, and High-Resolution Transmission Electron Microscopy, *J. Phys. Chem. A* 113 (50) (2009) 13871–13880. doi:10.1021/jp905639d.
- [208] B. Dippel, H. Jander, J. Heintzenberg, NIR FT Raman spectroscopic study of flame soot, *Phys. Chem. Chem. Phys.* 1 (1999) 4707–4712. doi:10.1039/A904529E.
- [209] B. Dippel, J. Heintzenberg, Soot characterization in atmospheric particles from different sources by NIR FT Raman spectroscopy, *J. Aerosol Sci.* 30 (1999) S907–S908. doi:10.1016/S0021-8502(99)80464-9.
- [210] A. Cuesta, P. Dhamelincourt, J. Laureyns, A. Martínez-Alonso, J. M. D. Tascón, Raman microprobe studies on carbon materials, *Carbon* 32 (8) (1994) 1523–1532. doi:10.1016/0008-6223(94)90148-1.
- [211] T. Jawhari, A. Roid, J. Casado, Raman spectroscopic characterization of some commercially available carbon black materials, *Carbon* 33 (11) (1995) 1561–1565. doi:10.1016/0008-6223(94)90148-1.
- [212] M. Dierick, B. Masschaele, L. Van Hoorebeke, Octopus, a fast and user-friendly tomographic reconstruction package developed in LabView®, *Meas. Sci. Technol.* 15 (7) (2004) 1366–1370. doi:10.1088/0957-0233/15/7/020.
- [213] Volume Graphics GmbH, Heidelberg, VGStudio MAX (2011).
URL <http://www.volumegraphics.com>
- [214] M. V. Twigg, J. T. Richardson, Fundamentals and Applications of Structured Ceramic Foam Catalysts, *Ind. Eng. Chem. Res.* 46 (12) (2007) 4166–4177. doi:10.1021/ie061122o.
- [215] O. Deutschmann, L. D. Schmidt, Modeling the partial oxidation of methane in a short-contact-time reactor, *AIChE J.* 44 (11) (1998) 2465–2477. doi:10.1002/aic.690441114.
- [216] R. S. Krishnan, Raman spectrum of alumina and the luminescence of ruby, *Nature* 160 (4053) (1947) 26. doi:10.1038/160026a0.
- [217] R. S. Krishnan, Raman spectrum of alumina and the luminescence of ruby, *Proceedings Mathematical Sciences* 26 (6) (1947) 450–459. doi:10.1007/BF03170901.
- [218] E. J. Nowak, Catalytic oxidation of ammonia on platinum, *Chem. Eng. Sci.* 21 (1) (1966) 19–27. doi:10.1016/0009-2509(66)80003-9.
- [219] R. W. McCabe, T. Pignet, L. D. Schmidt, Catalytic etching of platinum in NH₃ oxidation, *J. Catal.* 32 (1) (1974) 114–126. doi:10.1016/0021-9517(74)90165-1.
- [220] R. W. McCabe, G. D. W. Smith, A. S. Pratt, The Mechanism of Reconstruction of Rhodium-Platinum Catalyst Gauzes, *Platinum Metals Rev.* 30 (2) (1986) 54–62.
URL <http://www.platinummetalsreview.com/pdf/pmr-v30-i2-054-062.pdf>
- [221] V. W. Dean, M. Frenklach, J. Phillips, Catalytic etching of platinum foils and thin films in hydrogen-oxygen mixtures, *J. Phys. Chem.* 92 (20) (1988) 5731–5738. doi:10.1021/j100331a037.
- [222] C. F. Goldsmith, *Top. Catal.* (in press) (2012) (in press).

Acknowledgment

I express my gratitude to ...

- ... my supervisor Dr. Raimund Horn for his guidance during the development of this scientific work, and the helpful revision of this document. Many thanks for providing the amazing experimental setup.
- ... Prof. Dr. Robert Schlögl for giving me the opportunity to do this work in an excellent working environment in the Department of Inorganic Chemistry at the Fritz Haber Institute of the Max Planck Society, for offering an exciting research project, and for providing me with his scientific advice.
- ... Prof. Dr. Reinhard Schomäcker and Prof. Dr. Thomas Risse for referring this thesis.
- ... Prof. Dr. Thorsten Ressler for taking the chair of the examination board.
- ... my current and former colleagues from the High Temperature Catalysis Group for providing me with thoroughgoing help and inspiring discussions. Particular thanks go to Dr. Michael Geske for his skills in reanimating and/or replacing stubborn laboratory equipment. Thanks to everyone who ever was my 'second person in the lab' during one of the innumerable night shifts.
- ... all my colleagues, too numerous to name, in the Department of Inorganic Chemistry as well as the staff members of the different service groups at the Fritz Haber Institute of the Max Planck Society.
- ... my parents Britta and Karsten, and my sister Romina for their ongoing support and motivation.

Curriculum Vitae

Personal Data

Name	Oliver Korup
Date of Birth:	June 21st, 1981
Place of Birth:	Perleberg, Germany
Nationality:	German

Education

since Mar. 2008	PhD student at the Fritz-Haber-Institut der Max-Planck-Gesellschaft, Department of Inorganic Chemistry (director/supervisor: Prof. Dr. Robert Schlögl), Berlin, Germany. Member of the High Temperature Catalysis Group (group leader: Dr. Raimund Horn) Thesis title: "Methane Oxidation on Platinum Catalysts Investigated by Spatially Resolved Methods"
Apr. 2007 - Dec. 2007	Diploma thesis in physical chemistry at Humboldt-Universität zu Berlin, Berlin, Germany (supervisor: Prof. Dr. Klaus Rademann) Thesis title: "Supersonic Jet Expansion of Supercritical Fluids: Unexpectedly Cold Beams of Ethylene and Propane"
Mar. 2007	Final examination (Diplomhauptprüfung) in inorganic chemistry, organic chemistry, physical chemistry, and inorganic material science
Oct. 2002	Matriculation at the Humboldt-Universität zu Berlin, Berlin, Germany in the field of chemistry

List of Publications

- [1] O. Korup, C. F. Goldsmith, G. Weinberg, M. Geske, T. Kandemir, R. Schlögl, R. Horn, Catalytic Partial Oxidation of Methane on Platinum Investigated by Spatial Reactor Profiles, Spatially Resolved Spectroscopy, and Microkinetic Modeling, *J. Catal.* (2012) submitted.
- [2] M. Geske, O. Korup, R. Horn, Resolving Kinetics and Dynamics of a Catalytic Reaction Inside a Fixed Bed Reactor by Combined Kinetic and Spectroscopic Profiling, *Catal. Sci. Technol.* (2012) accepted manuscript. doi:10.1039/C2CY20489D.
- [3] O. Korup, R. Schlögl, R. Horn, Carbon formation in catalytic partial oxidation of methane on platinum: Model studies on a polycrystalline Pt foil, *Catal. Today* 181 (1) (2012) 177–183. doi:10.1016/j.cattod.2011.04.051.
- [4] O. Korup, S. Mavlyankariev, M. Geske, C. F. Goldsmith, R. Horn, Measurement and analysis of spatial reactor profiles in high temperature catalysis research, *Chem. Eng. Process.* 50 (10) (2011) 998–1009. doi:10.1016/j.cep.2011.05.024.
- [5] O. Korup, M. Geske, R. Schlögl, R. Horn, Carbon formation in catalytic partial oxidation of methane on platinum: Model studies on a polycrystalline Pt foil, *Bunsen-Magazin* 12 (5) (2011) 153, Note: Reprint of the poster abstract from Bunsentagung 2011 after been awarded a PCCP Hot Topic Prize. For the full paper see [11].
URL http://www.bunsen.de/bunsen_media/Downloads/BUNSEN_MAGAZIN/Erschienenene+BM/BM_5_2010_Homepage.pdf
- [6] O. Korup, M. Geske, S. Mavlyankariev, R. Schlögl, R. Horn, Catalytic partial oxidation of methane on autothermally operated Pt catalysts: Reaction pathways, zoning effects, and impact of mass and heat transport, *Prepr. Pap. - Am. Chem. Soc., Div. Fuel Chem.* 55 (2) (2010) 149–150.
- [7] R. Horn, O. Korup, M. Geske, U. Zavyalova, I. Oprea, R. Schlögl, Reactor for In-Situ Measurements of Spatially Resolved Kinetic Data in Heterogeneous Catalysis, *Rev. Sci. Instrum.* 81 (6) (2010) 064102. doi:10.1063/1.3428727.
- [8] U. Zavyalova, F. Girgsdies, O. Korup, R. Horn, R. Schlögl, Microwave-Assisted Self-Propagating Combustion Synthesis for Uniform Deposition of Metal Nanoparticles on Ceramic Monoliths, *J. Phys. Chem. C* 113 (40) (2009) 17493–17501. doi:10.1021/jp905692g.
- [9] G. Scholz, O. Korup, High-energy ball milling – a possible synthesis route for cryolite and chiolite, *Solid State Sci.* 8 (6) (2006) 678–684. doi:10.1016/j.solidstatesciences.2006.02.036.

List of Conference Talks as Presenter or Co-Author

- [1] M. Geske, O. Korup, R. Horn*, Spatially Resolved Raman Spectroscopy in Catalytic Packed Bed Reactors, in: 2011 AIChE Annual Meeting: Minneapolis, MN, USA, October 16th – 21st, 2011.
- [2] S. Mavlyankariev, O. Korup, M. Geske, R. Horn*, Gas Phase Methane Oxidative Coupling Studies by Spatial Reactor Profiles and Microkinetic Numerical Simulations, in: 2011 AIChE Annual Meeting: Minneapolis, MN, USA, October 16th – 21st, 2011.
- [3] O. Korup, C. F. Goldsmith, M. Geske, R. Horn*, Hydrogen Production by Catalytic Partial Oxidation of Methane on Reticulated Rhodium and Platinum Foam Catalysts, in: 2011 AIChE Annual Meeting: Minneapolis, MN, USA, October 16th – 21st, 2011.
- [4] O. Korup, S. Mavlyankariev, M. Geske, C. F. Goldsmith, R. Horn*, Spatial Reactor Profiles in Chemical Engineering Research, in: 8th European Congress of Chemical Engineering, Berlin, Germany, September 25th – 29th, 2011.
- [5] O. Korup*, M. Geske, C. F. Goldsmith, R. Schlögl, R. Horn, Autothermal Catalytic Partial Oxidation (CPO) of Methane on Platinum Investigated by High Resolution Spatial Reactor Profiles, in: 8th European Congress of Chemical Engineering, Berlin, Germany, September 25th – 29th, 2011.
- [6] O. Korup, C. F. Goldsmith, R. Schlögl, R. Horn*, Syngas Formation by Catalytic Partial Oxidation of Methane on Rhodium and Platinum Catalysts: A Mechanistic Study by Spatial Reactor Profiles, In Situ Raman Spectroscopy and Microkinetic Numerical Simulations, in: EuropaCat X, Glasgow, UK August 28th - September 2th, 2011.
- [7] O. Korup*, M. Geske, C. F. Goldsmith, R. Schlögl, R. Horn, Autothermal Catalytic Partial Oxidation (CPO) of Methane on Platinum Investigated by High Resolution Spatial Reactor Profiles, in: EuropaCat X, Glasgow, UK August 28th - September 2th, 2011.
- [8] O. Korup, S. Mavlyankariev, M. Geske, R. Schlögl, R. Horn*, Spatial Reactor Profiles in Heterogeneous Catalysis Research, in: Bunsentagung 2011, Berlin, Germany, June 2nd - 4th, 2011.
- [9] R. Horn*, O. Korup, R. Schlögl, Hydrogen Production by Catalytic Partial Oxidation of Methane on Rhodium and Platinum Catalysts, in: 1st International Symposium on Chemistry of Energy Conversion and Storage, Berlin, Germany, February 27th – March 2nd, 2011.
- [10] R. Horn*, O. Korup, S. Mavlyankariev, M. Geske, R. Schlögl, Spatially resolved reactor profiles as novel tool for in situ catalysis research, in: ACS National Meeting Fall 2010, Boston MA, USA, August 22nd – 26th, 2010.
- [11] O. Korup*, M. Geske, S. Mavlyankariev, R. Schlögl, R. Horn, Catalytic partial oxidation of methane on autothermally operated Pt catalysts: Reaction pathways, zoning effects, and impact of mass and heat transfer, in: ACS National Meeting Fall 2010, Boston MA, USA, August 22nd – 26th, 2010.
- [12] O. Korup*, R. Horn, M. Geske, R. Schlögl, Spatially Resolved Species and Temperature Profiles as Novel Tool to Study Mechanistic Details in Catalytic Methane Partial Oxidation on Platinum, in: 9th Novel Gas Conversion Symposium, Lyon, France, May 30th – June 3rd, 2010.
- [13] O. Korup, R. Schlögl, R. Horn*, High temperature catalytic methane oxidation on Pt coated catalysts, sphere beds and straight channels investigated by spatial profile measurements, in: Jahrestreffen Reaktionstechnik 2010, Würzburg, Germany, May 10th – 12th, 2010.

- [14] Y. Aksu, S. Arndt, M. Driess, H.-J. Freund, O. Görke, S. Heitz, R. Horn*, O. Korup, K. Kwapien, G. Laugel, S. Levchenko, S. Mavlyankariev, N. Nilius, I. Oprea, T. Risse, J. Sauer, R. Schlögl, R. Schomäcker, H. Schubert, U. Simon, U. Zavyalova, Li/MgO as catalyst for oxidative coupling of methane – what makes it work?, in: 43. Jahrestreffen Deutscher Katalytiker, Weimar, Germany, March 10th – 12th, 2010.
- [15] R. Horn*, O. Korup, M. Geske, U. Zavyalova, R. Schlögl, Spatially Resolved Reactor Profiles of Species and Temperatures as Novel Tool for Mechanistic Studies in High Temperature Oxidation Catalysis, in: 6th World Congress on Oxidation Catalysis, Lille, France, July 5th - 10th, 2009.

*presenting author

List of Posters as Presenter or Co-Author

- [1] S. Mavlyankariev, H. Petitjean, O. Korup, C. F. Goldsmith, M. Geske, R. Horn*, Gas phase methane oxidative coupling studied by spatial reactor profiles and microkinetic reactor simulations, in: Jahrestreffen Reaktionstechnik 2012, Würzburg, Germany, May 14th – 16th, 2012.
- [2] M. Geske*, O. Korup, R. Schlögl, R. Horn, Combined kinetic and spectroscopic measurements as novel research tool in the ODH of ethane over supported MoO₃, in: 45. Jahrestreffen Deutscher Katalytiker, Weimar, Germany, March 14th – 16th, 2012.
- [3] S. Mavlyankariev*, M. Geske, O. Korup, C. F. Goldsmith, R. Horn, Investigation of gas phase methane oxidative coupling by spatial profile measurements and microkinetic modelling, in: 8th European Congress of Chemical Engineering, Berlin, Germany, September 25th – 29th, 2011.
- [4] M. Geske*, O. Korup, R. Schlögl, R. Horn, Using spatially resolved in-situ catalyst characterization methods and Raman spectroscopy for the ODH of ethane over MoO_x, in: EuropaCat X, Glasgow, UK August 28th - September 2th, 2011.
- [5] O. Korup*, M. Geske, R. Schlögl, R. Horn, Carbon Formation in Catalytic Partial Oxidation of Methane on Platinum: Model Studies on a Polycrystalline Pt Foil, in: Bunsentagung 2011, Berlin, Germany, June 2nd - 4th, 2011, awarded with a *PCCP* Hot Topic Prize.
- [6] M. Geske*, O. Korup, R. Schlögl, R. Horn, Using spatially resolved in-situ catalyst characterization methods and Raman spectroscopy for the ODH of ethane over MoO_x, in: Bunsentagung 2011, Berlin, Germany, June 2nd – 4th, 2011.
- [7] O. Korup*, M. Geske, S. Mavlyankariev, R. Schlögl, R. Horn, Carbon Formation in Catalytic Partial Oxidation of Methane on Platinum: Model Studies on a Polycrystalline Pt Foil, in: 44. Jahrestreffen Deutscher Katalytiker, Weimar, Germany, March 16th – 18th, 2011.
- [8] S. Mavlyankariev*, M. Geske, O. Korup, C. F. Goldsmith, R. Abdallah, T. Mäurer, R. Schomäcker, R. Schlögl, R. Horn, Investigation of methane oxidative coupling in the gas phase by spatial profile measurements and microkinetic simulations, in: 44. Jahrestreffen Deutscher Katalytiker, Weimar, Germany, March 16th – 18th, 2011.
- [9] M. Geske*, O. Korup, S. Mavlyankariev, R. Schlögl, R. Horn, Mechanistic investigation of the ODH of ethane over a MoO_x catalyst using in-situ techniques and Raman spectroscopy, in: 44. Jahrestreffen Deutscher Katalytiker, Weimar, Germany, March 16th – 18th, 2011.
- [10] O. Korup*, R. Horn, M. Geske, R. Schlögl, Spatially resolved species and temperature profiles as novel tool to study mechanistic details in catalytic methane partial oxidation on platinum, in: 43. Jahrestreffen Deutscher Katalytiker, Weimar, Germany, March 10th – 12th, 2010.
- [11] R. Horn*, U. Zavyalova, M. Geske, O. Korup, I. Oprea, R. Schlögl, Oxidative coupling of methane on Li/MgO nanocrystalline coated monolith and granulated supports, in: EuropaCat IX, Salamanca, Spain August 30th – September 4th, 2009.
- [12] U. Zavyalova, R. Horn*, O. Korup, R. Schlögl, Microwave-Assisted Gel-Combustion Synthesis of Nanocrystalline Catalytic Metal Films, in: 6th World Congress on Oxidation Catalysis, Lille, France, July 5th - 10th, 2009.
- [13] R. Horn, O. Korup*, U. Zavyalova, R. Schlögl, Mechanism of methane catalytic partial oxidation to synthesis gas on Rh and Pt probed by spatial profile measurements, in: 42. Jahrestreffen Deutscher Katalytiker, Weimar, Germany, March 11th – 13th, 2009.

- [14] W. Christen, O. Korup*, K. Rademann, Überschallexpansion von überkritischen Fluiden: Ethen und Propan, in: Clustertreffen 2007, Berlin, Germany, September 23rd – 28th, 2007.

*presenting author